Dry Reforming of Methane Using Non-Thermal Plasma-Catalysis

A thesis submitted to The University of Manchester for the degree of Doctor of Philosophy in the Faculty of Engineering and Physical Sciences.

2010

Helen J. Gallon

School of Chemistry

Contents

Chapter 1. Methane Reforming

Chapter 2. Plasma-Catalysis and Analytical Techniques

Chapter 3. Dry Reforming of Methane: Effect of Packing Materials in a DBD Reactor

Chapter 5. Plasma-Reduction of NiO/Al_2O_3 in a Coaxial DBD Reactor

Chapter 6. Dry Reforming of Methane: Performance of Plasma-Reduced Ni/Al_2O_3 Catalysts in a Coaxial DBD Reactor

Chapter 7. Further Work

Appendices

Final Word Count: 53, 866

List of Figures

Chapter 1

Chapter 2

Chapter 3

Chapter 4

Chapter 5

Chapter 6

Chapter 7

List of Tables

Chapter 1

Chapter 2

Chapter 3

Chapter 4

Chapter 5

Chapter 6

Abstract

This thesis has studied CO_2 reforming of CH_4 in atmospheric pressure, non-thermal plasma discharges. The objective of this research was to improve the current understanding of plasma-catalytic interactions for methane reforming.

Chapter 1 introduces the existing and potential applications for methane reforming products. The industrial approaches to methane reforming and considerations for catalyst selection are discussed.

Chapter 2 introduces non-thermal plasma technology and plasma-catalysis. An introduction to the analytical techniques used throughout this thesis is given.

Chapter 3 investigates the effects of packing materials into the discharge gap. The materials were found to influence the reactant conversions for dry reforming of methane in the following order: quartz wool > no packing > Al_2O_3 > zeolite 3A > $BaTiO_3$ > TiO_2. In addition to the dielectric properties, the morphology and porosity of the materials was found to influence the reaction chemistry. The materials also affected the electrical properties of the plasma resulting in surface discharges, as opposed to a filamentary discharge mode.

Chapter 4 investigates the effects of variation in CH_4/CO_2 ratios on plasma-assisted dry reforming of CH_4. Differences in the reaction performance for different feed gas compositions are explained in terms of the possible reaction pathways and the electron energy distribution functions. A NiO/Al_2O_3 catalyst is introduced for plasma-catalytic dry reforming of CH_4, which was found to have no significant effect on the reaction performance at low specific input energies.

Chapter 5 presents the plasma-assisted reduction of a NiO/Al_2O_3 catalyst by CH_4 and H_2/Ar discharges. When reduced in a CH_4 discharge, the active Ni/Al_2O_3 catalyst was effective for plasma-catalytic methane decomposition to produce H_2 and solid carbon filaments. A decrease in the breakdown voltage was observed, following the catalyst reduction to the more conductive Ni phase.

Chapter 6 investigates the performance of the plasma-reduced Ni/Al_2O_3 catalysts for plasma-catalytic dry reforming of methane. Whilst the activity towards dry reforming of CH_4 was low, the CH_4 plasma-reduced catalyst was found to be effective for catalysing the decomposition of CH_4 into H_2 and solid carbon filaments; both potentially useful products.

Chapter 7 discusses further work relevant to this thesis.

Declaration

No portion of the work referred to in this thesis has been submitted in support of an application for another degree or qualification of this or any other university or other institute of learning.

Copyright Statement

i. The author of this thesis (including any appendices and/or schedules to this thesis) owns any copyright in it (the “Copyright”) and she has given The University of Manchester the right to use such Copyright for any administrative, promotional, educational and/or teaching purposes.

ii. Copies of this thesis, either in full or in extracts, may be made **only** in accordance with the regulations of the John Rylands University Library of Manchester. Details of these regulations may be obtained from the Librarian. This page must form part of any such copies made.

iii. The ownership of any patents, designs, trade marks and any and all other intellectual property rights except for the Copyright (the “Intellectual Property Rights” and any reproductions of copyright works, for example graphs and tables (“Reproductions”), which may be described in this thesis, may not be owned by the author and may be owned by third parties. Such Intellectual Property Rights and Reproductions cannot and must not be made available for use without the prior written permission of the owner(s) of the relevant Intellectual Property Rights and/or Reproductions.

iv. Further information on the conditions under which disclosure, publication and exploitation of this thesis, the Copyright and any Intellectual Property Rights and/or Reproductions described in it may take place is available from the Head of School of the School of Chemistry.

Acknowledgements

Firstly, I would like to thank my supervisor Prof. Christopher Whitehead, who has been a great source of help and encouragement throughout my Ph.D. His academic expertise, as well as his unfaltering optimism have been invaluable to me at every stage. I have always felt able to chat to him about any matter, and discussing new ideas for the research has made the last three years very enjoyable. I simply could not wish for a better supervisor.

Within our group at Manchester, I would like to thank Dr. Xin Tu for his help with the electrical measurements and for always having time to answer my unending questions. I also wish to thank Dr. Kui Zhang, a former group member and my unofficial mentor, for his great enthusiasm and support. As well as Maria Prantsidou, a Ph.D. student in the group who has made this last year all the more enjoyable.

I am sincerely grateful to Dr. Hyun-Ha Kim and Dr. Atsushi Ogata for their scientific expertise and generous hospitality in allowing me to use their facilities during my Summer Program fellowship. I am indebted to the Japan Society for the Promotion of Science for funding my research (and travel!) in Japan during the summer of 2009; an enjoyable and unforgettable experience.

Many thanks go to Dr. Martyn Twigg and Johnson Matthey, not only for supplying the catalyst that has formed an important part of this research, but also for being a fantastic source of knowledge and a pleasure to work with.

This research would not have been possible without the technical expertise of many of the staff in the School of Chemistry. In particular, my thanks go to Steve Mottley and Andy Sutherland for their work on the power supply, Peter Wilde and Malcolm Carroll for their innovation and efficiency in the mechanical workshop and to Dr. Peter Gorry for an excellent LabVIEW system that has greatly enhanced the value of my research.

Thanks also go to Supergen XIV, the EPSRC and the Joule Centre who have funded and supported this research.

I also wish to thank Arul for much laughter and happiness over the last year (and for the TPR measurements in Chapter 5!). Finally, a huge thank you must go to my Mum, Dad, Sarah and Holleigh for their endless support and encouragement.

List of Abbreviations

AC	Alternating current
ADC	Analogue to digital conversion
APPJ	Atmospheric pressure plasma jet
CCP	Capacitively coupled plasma
DBD	Dielectric barrier discharge
DC	Direct current
E_a	Activation energy
EEDF	Electron energy distribution function
(E)SEM	(Environmental) scanning electron microscopy
FID	Flame ionisation detector
F-T	Fischer-Tropsch
FTIR	Fourier transform infra-red
GC	Gas chromatography
ICCD	Intensified charge coupled device
ICE	Internal combustion engine
ICP	Inductively coupled plasma
IR	Infra-red
MFC	Mass flow controller
NO_x	Nitrogen oxides
PEM	Proton exchange membrane
POX	Partial oxidation of methane
RF	Radio frequency
SIE	Specific input energy
SMR	Steam methane reforming
SS	Stainless steel
Syngas	Synthesis gas (H_2 and CO)
TCD	Thermal conductivity detector
TEM	Transmission electron microscopy
TPR	Temperature programmed reduction
V_b	Breakdown voltage
VOCs	Volatile organic compounds
XRD	X-ray diffraction

1. Methane Reforming

1.1 Introduction

Methane is the predominant component of natural gas and has formed a major part of the energy market for many years. In Britain, the discovery of natural gas in the North Sea in 1965 meant that a cleaner form of gas became accessible. At that time, town gas manufactured from coal was supplied to homes by a national network until a program for conversion to natural gas was completed in 1976. To this date, natural gas is distributed to homes where it is combusted in a highly exothermic reaction (1.0) to provide energy for central heating, gas heating and cooking. It is also utilised in gas fired power stations to generate electricity for the national grid, where the energy released during combustion is used to drive a gas or steam turbine.

$$CH_4 + 2\ O_2 \rightarrow CO_2 + 2\ H_2O \qquad \Delta H° = -891\ kJ\ mol^{-1} \qquad (1.0)$$

The uses of methane are not restricted to the energy sector; many synthetic chemicals originate from methane such as methanol, ammonia, liquid fuels and other speciality chemicals. Methane is first converted into synthetic gas, or syngas as it is commonly abbreviated, in a process known as *methane reforming*. Syngas is a mixture of hydrogen and carbon monoxide and has a wide range of uses in synthetic chemistry (as its name suggests). Methane is a very stable molecule due to the high strength of the four C-H bonds, which have an average bond enthalpy of 413 kJ mol^{-1} [1]. Adverse reaction conditions are necessary in order to overcome the high activation energies required to break these bonds. Established industrial methods for methane reforming involve reacting CH_4 with steam or another oxidant under high temperatures, pressures and the presence of catalysts that are prone to sintering and deactivation under these harsh operating conditions. Frequent replacement of spent catalysts and high energy consumption add to the overall running costs of methane reforming processes. Many research efforts are focussed on the development of alternative technologies that allow methane reforming to proceed under milder reaction conditions, in attempt to make it a more economically favourable process.

This chapter discusses the existing and potential applications for methane reforming products, H_2 and CO. There are several different industrial approaches to methane reforming; the challenges associated with these methods are discussed in this chapter, which explains the motivation behind the research in this thesis.

1.2 Natural Gas

Methane is the main constituent of natural gas and is naturally abundant in many locations around the world. Natural gas and other fossil fuels are formed over millions of years, deep beneath the Earth's surface. Continued extraction of natural gas could eventually lead to depletion of the current sources. Figure 1.0 shows the geographical distribution of proven reserves of natural gas, of which significant proportions are found in Middle Eastern countries and Russia [2]. Environmental concerns as well as uncertainties surrounding the sustainability and cost of future sources of natural gas have led to considerable interest in alternative methane sources.

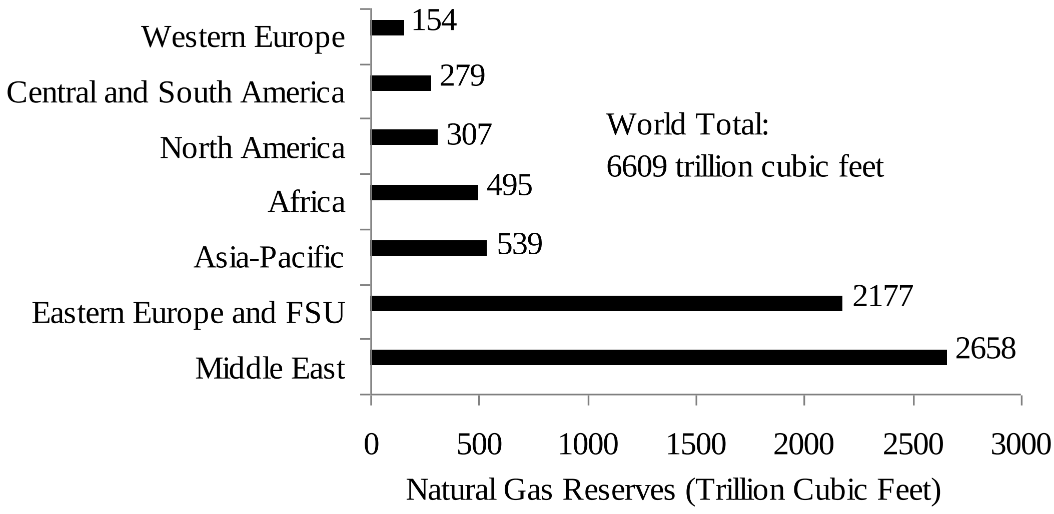

Figure 1.0: Proven world natural gas reserves by geographical region in 2010, FSU denotes the former soviet union (data taken from [2]).

1.2.1 Global Climate Change

The combustion of natural gas and other fossil fuels for domestic, industrial and automotive energy demands creates considerable emissions of CO_2. Carbon dioxide concentrations in the atmosphere have increased dramatically (past what could be considered a natural fluctuation) since the use of fossil fuels by industrialised nations became widespread. Figure 1.1 depicts the Earth's energy balancing mechanisms through incoming and outgoing radiation. Greenhouse gases exist naturally in the atmosphere and have a vital role in maintaining this energy balance, by absorbing and reflecting radiation back to the Earth's surface, a concept that is widely known as the *greenhouse effect*. Anthropogenic greenhouse gas emissions which include CO_2, methane, nitrous oxide (N_2O), sulphur hexafluoride (SF_6), chlorofluorocarbons (CFCs) and hydrochlorofluorocarbons (HCFCs) have led to an enhanced greenhouse effect, whereby increased levels of radiation are trapped in the Earth's atmosphere. This has resulted in increased average global temperatures, a decrease in the pH of the ocean surface and significant changes to local weather systems: collectively known as *global climate change*.

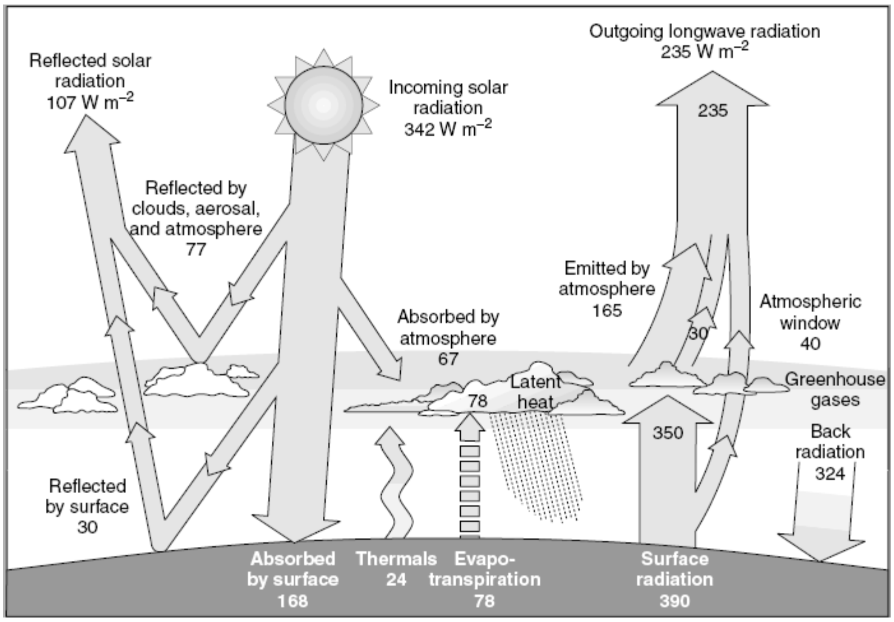

Figure 1.1: Schematic diagram showing the Earth's energy balance through incoming and outgoing radiation. All values are in W m^{-2} and represent the energy budget for the period of March 2000 to May 2004. The broad arrows indicate the flow of energy in proportion to their importance (taken from [3, 4]).

Carbon dioxide emissions from fossil fuel combustion are believed to be the most significant contributor to global climate change. This has been globally recognised in the 1997 Kyoto Protocol, an international agreement by United Nations member states that commits these industrialised nations to reducing their CO_2 emissions. Whilst the legally binding duration of this agreement is due to run out in 2012, member states are continuing the implementation of CO_2 reduction strategies by continued investment in renewable energy technologies.

1.3 Biogas

Biogas is a renewable source of methane and can be formed by the anaerobic decay of organic matter. Almost all organic matter can be used as a biogas feedstock. However, the use of waste products is particularly advantageous as it can prevent the unnecessary waste of useful energy sources and offers increased financial profits to plant operators. Industries that generate biogas from waste products could use it directly on-site as a fuel and/or for electricity generation that could be resold to the national grid [5]. Waste biomass sources that have potential for industrial biogas generation include:

Wastewater treatment – the treatment of wastewater inevitably generates sludge, which needs to be chemically treated and disposed of, in a process that incurs considerable financial cost. An alternative waste management strategy is the generation of biogas from wastewater sludge in anaerobic digestion tanks. This process has been considered economically feasible [5], which has led to the implementation of biogas generators at several sites across the U.K.

Animal manure – Manure has important uses in farming as a fertiliser, and recently also as a source for on-farm biogas generation. The usual practice is to store the manure for several months until it is needed. During this time, gases that are produced from the manure can be released straight into the atmosphere, if they are not properly collected. To make use of these gases, the manure can be transferred to an anaerobic digester for biogas generation. The remaining substrate after biogas production still contains nutrients that give it value as a fertiliser [6].

Food waste – Waste materials from food processing industries, agricultural processes and forestries all have the potential to generate biogas through the use of anaerobic digesters. In the U.K, several plants of this type are in operation including the use of brewery by-products, potato peelings, fish waste, sugar cane waste and other food wastes from kitchens.

Landfill gas – the organic fraction of municipal solid waste in landfill sites is biologically digested by micro-organisms, releasing a stream of methane-rich gas. Currently, landfill gas is often flared to prevent a risk of explosion on mixing with oxygen. Collection of this gas and subsequent use for energetic purposes could be a viable alternative [6, 7]. Challenges associated with landfill gas collection include inconsistent gas pressure and variable gas composition resulting from differences in local ecosystems within the landfill, as a result of the heterogeneous nature of the waste.

Other methods for biogas generation include the collection of biogas from large-scale cultivation of algae [8] and the growth and subsequent anaerobic digestion of dedicated energy crops such as rape. The latter method is more controversial as it requires the occupation of land that could otherwise be used for growing food as well as substantial energy expenditure associated with the farming of these crops [9].

The composition of biogas varies greatly depending on the biomass source, but it is always produced with a significant CO_2 component (≤ 50 %), in contrast to natural gas, where CO_2 is present in relatively low concentrations (≤ 8 %). Table 1.0 gives an approximation of the composition of natural gas and biogas generated from three different waste biomass sources for comparison. Water vapour, H_2 and trace compounds such as sulphides, siloxanes, aromatics and halogenated compounds may also be present in each of these gas sources [7]. Biogas can be upgraded to increase the methane concentration and remove corrosive H_2S and halogenated compounds. When biogas is upgraded to natural gas standard, it is known as *biomethane* and can be used as a natural gas substitute for electricity generation or as a fuel, particularly in the transport sector. The high expense of upgrading biogas and converting existing vehicles and infrastructure to use gas instead of liquid fuels (petrol and diesel) have prevented this transition [6].

	Natural Gas	Biogas sources		
		Municipal landfill sites	Waste water treatment plants	Animal manure
CH_4 (%)	70 – 90	47 – 62	60 – 67	55 – 70
CO_2 (%)	0 – 8	32 – 43	33 – 38	29 – 44
$C_2 – C_4+$ (%) hydrocarbons	0 – 20	-	-	-
O_2 (%)	0 – 0.2	< 1	< 1	< 1
N_2 (%)	0 – 5	< 1 – 17	< 2	< 1 – 2
H_2S (ppm)	0 – 5	27 – 500	< 1 – 4	3 – 1000

Table 1.0: Compositions of natural gas and biogas from three different sources, (-) denotes unknown concentrations (data taken from [7] and [10]).

While combustion of renewable methane sources does emit CO_2, it is more favourable than fossil fuel combustion. The carbon in biogas was originally absorbed from the atmosphere by plants during photosynthesis. Eventually, the same amount of carbon is returned to the atmosphere during combustion of the plant-derived fuel; therefore no additional carbon is introduced into the Earth's carbon cycle. Provided that the plant source is regenerated, the fuel can be considered *carbon-neutral*. This is in contrast to combustion of fossil fuels where carbon that has been removed from the carbon cycle for millions of years is reintroduced without an efficient removal mechanism.

1.4 Syngas Applications

Syngas has direct application as a fuel. It can be combusted in a gas turbine, internal combustion engine or boiler, in much the same way as natural gas. Most recently installed plants that generate electricity from syngas use an integrated gasification combined cycle (IGCC) system. This method generates syngas from the gasification of coal, petroleum coke, heavy oil or biomass. The syngas is then cleaned of sulphur compounds, ammonia, metals and particulates before it is used to drive a gas turbine that generates electricity [11]. If the syngas is generated from biomass sources, this method of electricity generation can be considered as a renewable and clean alternative to the use of fossil fuels.

Reforming of natural gas represents the lowest cost route to production of syngas [12], which has found a wide range of uses in synthetic chemical industries as shown in Figure 1.2. The H_2 and CO constituents can be separated and used individually for producing various chemicals such as ammonia (NH_3) in the case of H_2, or acids and other carbonylation products in the case of CO. Syngas can also be used in the direct reduction of iron ore (the DRI process) for industrial steel manufacture. Other processes use the mixture of H_2 and CO to react these two species directly using catalysts and elevated temperatures.

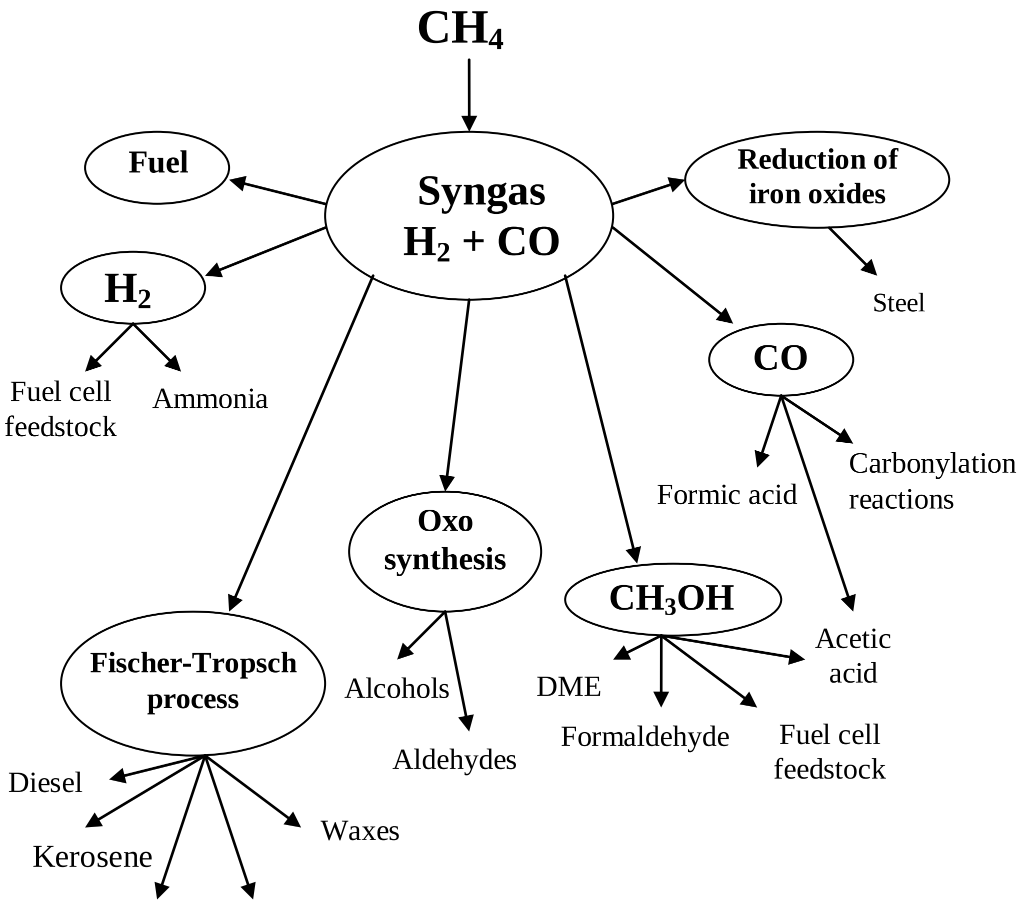

Figure 1.2: Schematic diagram showing the main applications of syngas.

1.4.1 Gas-to-Liquid Conversion

The conversion of syngas to liquid products is the main route to the synthesis of liquid fuels and many important oxygenated compounds such as methanol and dimethyl ether (DME). There are several key reactions for gas-to-liquid conversion (Fig. 1.2) such as the Fischer-Tropsch (F-T) process for production of liquid fuels, synthesis of methanol (CH_3OH) from the direct reaction between H_2 and CO and the oxo synthesis where alkenes of variable carbon number are reacted with syngas to produce alcohols and aldehydes with one additional carbon to the alkene reactant [13]. An important factor in determining the chemistry of syngas is the H_2/CO ratio; this can be adjusted using a water-gas shift reaction, downstream of the methane reformer.

A renewed interest in gas-to-liquid processes has been initiated by the increasing legislation for cleaner energy sources, which includes the production of liquid fuels from biomass-derived sources. Another reason for interest in these reactions comes from the natural gas industry, where gas-to-liquid conversions, if carried out at remote offshore locations could enable some governments to profit from stranded natural gas reserves at oil wells where the natural gas by-product is otherwise flared. There is little economic interest in transporting gas from remote locations due to the low volumetric energy content of natural gas compared with liquid oil [14, 15]. Natural gas is transported from several countries after liquefaction, by cooling to -162 °C at atmospheric pressure. It is then reheated to recover the gas when it reaches the destination. However, this is an expensive solution and it does not address the need for sustainable sources of energy.

1.4.2 Fischer-Tropsch (F-T) Process

The Fischer-Tropsch process was established in 1923 by German researchers, Franz Fischer and Hans Tropsch. They discovered that syngas could be converted into a mixture of linear and branched hydrocarbons and alcohols using various metal catalysts at elevated temperatures [16]. For commercial F-T synthesis, iron and cobalt catalysts are used at temperatures of 200 – 300 °C and pressures of 1000 – 6000 kPa. A syngas ratio of $H_2/CO = 2$ is generally required. Potassium and iron catalysts are used to promote the water-gas shift reaction which is used to modify the H_2/CO ratio [17]. The main reactions of F-T synthesis are shown in Table 1.1. Conventional refinery processes are used to separate and upgrade the syncrude mixture into useful products such as diesel, kerosene, naphtha and waxes. High quality liquid fuels can be produced by this method with very low aromaticity and zero sulphur impurities [18].

Main reactions	
1. Alkanes	$(2n +1) H_2 + n CO \rightarrow C_nH_{2n+2} + n H_2O$
2. Alkenes	$2n H_2 + n CO \rightarrow C_nH_{2n} + n H_2O$
3. Water-gas shift	$CO + H_2O \leftrightarrow CO_2 + H_2$
Side reactions	
4. Alcohols	$2n H_2 + n CO \rightarrow C_nH_{2n+2}O + (n -1) H_2O$
5. Boudouard reaction	$2 CO \rightarrow C + CO_2$
Catalyst Modifications	
6. Catalyst oxidation	$x M + y O_2 \leftrightarrow M_xO_{2y}$
7. Catalyst reduction	$M_xO_y + y H_2 \leftrightarrow y H_2O + x M$
8. Bulk carbide formation	$y C + x M \leftrightarrow M_xC_y$

Table 1.1: Major reactions in the Fischer-Tropsch synthesis, where n, x and y are integers and M represents a metal catalyst (modified from [17]).

F-T processes are a well-established set of reactions that have been improved greatly over the years with advances in catalysis and reactor design. However, further breakthroughs are necessary if the large scale manufacture of liquid fuels from biomass sources is to become viable for today’s energy markets [12]. Specific challenges arises from the high cost of syngas production and preparation including sulphur removal, partial oxidation or steam reforming of methane, heat recovery and the cooling of syngas; these processes have been estimated to induce 66 % of the total costs of the production of liquid fuels from natural gas [19].

1.5 H_2 Energy

The depletion of fossil fuel reserves and the adverse effects of global climate change have led to the emergence of several new energy technologies in recent years. One of which, is the use of H_2 as an energy carrier that can be used to generate electricity by combustion in an internal combustion engine (ICE) or by the use of fuel cells, where chemical energy is converted into electricity using an electrochemical cell. The latter is favourable, particularly for automotive applications, given that the transfer of chemical energy associated with fuel cells is more efficient than methods of combustion where loss of energy as heat is inevitable. Additionally, the use of H_2 as a fuel for ICEs would result in emissions of nitrogen oxides (NO_x) due to the combustion of hydrogen-air mixtures, thus fuel cells are preferable in terms of a cleaner air quality [20]. The oxidation of hydrogen produces zero harmful emissions; H_2O is the only by-product of both ICE and fuel cell applications. However, for H_2 to be considered as a clean source of energy it should be derived from renewable sources and not from fossil fuels.

As with any fuel, issues of safety must be addressed prior to endorsement. H_2 is a flammable gas over a wide range of concentrations (4 – 75 %) and burns with a colourless flame. The ignition temperature of H_2 is higher than petroleum-derived fuels and if allowed to leak, H_2 will quickly rise and disperse, lessening the risk of fire. Overall, safety concerns do not prevent the use of H_2 as a fuel [21].

1.5.1 Proton Exchange Membrane (PEM) Fuel Cells

The basic components of a PEM fuel cell are the anode, cathode and a proton exchange membrane sandwiched between layers of catalysts, as shown in Figure 1.3. At the anode, H_2 is oxidised and the resulting protons diffuse through the PEM layer. At the cathode, O_2 from air is reduced to form H_2O. The electrons released travel around an external circuit, providing electricity to the load. The PEM is most commonly a Nafion-based polymeric electrolyte. The membrane has hydrophilic pores of ~ 10 nm in size, which allow the passage of H^+ ions only through the membrane. The oxidation and reduction reactions in the fuel cell are promoted by Pt-based catalysts, which are more efficient at higher temperatures. However, the proton-conducting channels in the membrane are also strongly temperature dependent, with high temperatures causing the pore size to shrink, hindering the proton exchange mechanism [22]. These factors limit PEM fuel cells to working temperatures in the range of 80 – 100 °C; this requires the use of efficient cooling systems to prevent overheating of the cells. At these relatively low temperatures, any CO impurities (as low as 50 ppm) in the H_2 feed can cause poisoning of the catalysts due to a strong adsorption affinity of CO towards the Pt catalysts [20, 23]. Therefore, the purity of H_2 is critical for the operation of PEM fuel cells.

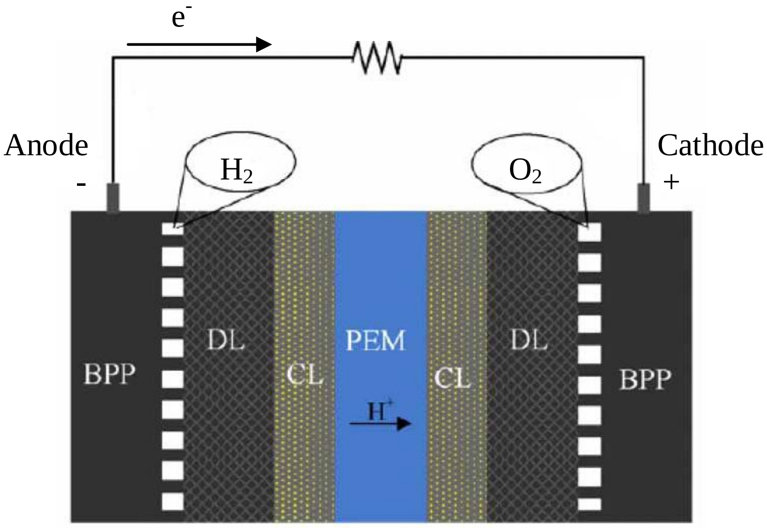

Figure 1.3: Schematic diagram of a PEM fuel cell, CL = catalyst layer, DL = diffusion layer and BPP = bipolar plate (taken from [20]).

To amplify the power generation from fuel cells, several units are arranged in series to form a fuel cell stack as illustrated in Figure 1.4, where three fuel cell units are integrated, sandwiched between bipolar plates. The bipolar plates act as gas separators between the adjacent cells and must be electrically conductive to assist the flow of current around the integrated circuit. Increasing the number of individual fuel cell units can allow the generation of several hundred volts of electricity. Several leading car manufacturers have developed PEM fuel cell technologies that are sufficiently advanced to be able to power motorised vehicles at acceptable speeds over a 300 mile range, meeting the criteria for commercial vehicles. The low operating temperatures offer a rapid response, which enables acceptable acceleration and braking to be met [24]. In addition, PEM fuel cells have been reported as 2 – 3 times more energy efficient than the currently employed petrol or diesel ICEs [20, 25].

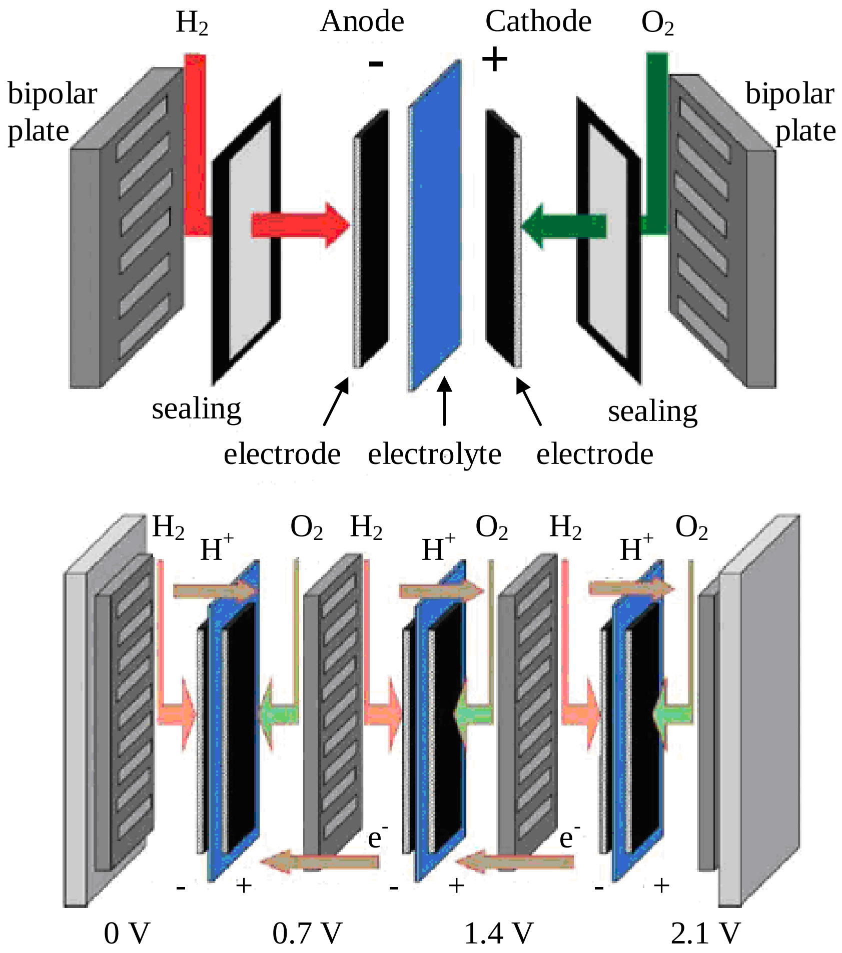

Figure 1.4: Schematic diagram of the components of a single fuel cell and their simplified integration into a fuel cell stack (taken from [20]).

1.5.2 Methods for Production of H_2

Unlike fossil fuels, H_2 cannot be extracted from underground; it must be produced from another source, as a secondary fuel. The annual production of H_2 has been estimated at around 65 million tons by the International Energy Agency in 2007, of which ~ 96 % comes from fossil fuels, either from reforming of natural gas, refinery/chemical off-gases or by coal gasification [26]. If a transition towards H_2 energy and fuel cells is to be made possible, large quantities of renewable H_2 will need to be produced from an abundant source and at a lower cost than offered by current methods. This has been internationally recognised by many governments, who currently have initiatives in place for the development of H_2 technologies. Brief descriptions of the key emerging technologies for H_2 production are given in this section.

Reforming of natural gas with carbon sequestration – The most established method for H_2 production is by reforming of natural gas; the existing methods for this are described in section 1.6. However, even if significant advances were to bring down the cost of methane reforming, there is still the issue of the carbon by-product. Carbon capture and sequestration (CCS) is a possible option, whereby the carbon dioxide product is liquefied and injected deep underground beneath imporous layers of rock or into the deep ocean where it would form CO_2 'lakes'. These technologies are currently at an experimental stage and have significant technological, economic and environmental issues which would need to be addressed before it could be implemented on a large scale.

Biogas reforming – Reforming of biogas from renewable sources is a potential route to syngas production, without the need for carbon sequestration. Since biogas contains CH_4 in conjunction with CO_2 there is no need for an additional oxidant. Dry reforming of CH_4 with CO_2 using thermal catalysis is discussed in section 1.6.4.

Biomass gasification/pyrolysis – This process is similar to the process of coal gasification, except that the organic matter comes from a renewable source, such as woody materials or waste organic products. Under conditions of high temperatures, catalysis and the presence of an oxidant (O_2, air or steam), a combination of reactions can take place including pyrolysis, partial oxidation and steam reforming of hydrocarbons, as well as methanation and the water-gas shift reaction. Optimisation of reaction conditions can maximise the yield of syngas production. Biomass gasification requires temperatures of ~ 700 °C; however, higher temperatures are usually favoured in order to reduce the formation of tar [27].

Electrolysis of water – Electricity from renewable sources can be used to split H_2O into H_2 and O_2. The electricity can be supplied from intermittent sources such as wind turbines, solar cells, hydroelectric or geothermal facilities; for each of these sources the electricity generation does not necessarily meet the demand at a given time. Since it is difficult to store excess electricity, the energy can be used in electrolysis of H_2O to produce H_2, which behaves as an energy carrier that can be converted back to electricity when it is needed. This method has the advantage that it does not coproduce CO, which is incompatible with fuel cells.

1.5.2 Hydrogen Infrastructure

Hydrogen energy could be used in stationary, portable and mobile applications. Large stationary power plants (~ 250 kW) could produce the electricity supply for buildings; initially this is likely to provide supplementary energy to larger sites such as hospitals, office buildings and factories. If this market proved to be successful, H_2 could be phased into use for residential areas from smaller plants (5 – 10 kW). Building regulations would need to be updated for the change of fuel, which could mean a costly modification of the existing infrastructure [24]. Portable applications such as laptop computers and mobile telephones require a lower power output (< 1 kW). This is possible with H_2 fuel cells but the size of the H_2 storage unit and fuel cell stack are likely to make these applications uncompetitive with the existing battery-powered technologies. The automotive market is considered to be the main application for H_2 energy. This transition would require the replacement of current vehicles and infrastructure with those capable of using H_2 as a fuel.

The technical challenges of H_2 storage and delivery to the consumer are a major barrier to the widespread use of hydrogen. Being the lightest chemical element, compressed H_2 gas has a very low energy per unit volume of 0.5 kW h dm^{-3} but the highest energy output per unit weight of any substance at 33.3 kW h kg^{-1}. Comparisons of the gravimetric and volumetric energy densities of the most common fuels are shown in Table 1.2. For automotive applications, storage of compressed H_2 gas is not feasible in most cases, where available space is insufficient for large H_2 tanks (buses and lorries being among the exceptions). Consequently, alternative methods for storing hydrogen in a liquid or solid form are being explored. Hydrogen can be stored as a cryogenic liquid in pressurised tanks by supercooling to < -253 °C at 1 bar. This increases the energy density to 2.4 kW h dm^{-3} but this is still relatively low and expensive to implement, since sophisticated insulation is required for the tanks and energy must be consumed during the compression. Storing hydrogen as a solid ionic-covalent hydride of light elements such as lithium, boron, sodium, magnesium and aluminium can increase the energy density further. However, solid storage methods must be able to rapidly absorb and desorb hydrogen at close to room temperature and pressure as well as being inexpensive to prepare and resistant to poisoning; conditions that are not met by current solid hydrogen storage methods [21]. The difficulties and cost of H_2 storage make it likely that production sites would need to be widespread to reduce the need for transporting H_2 over long distances. Compressed gas and cryogenic H_2 could be delivered to the locations where it is needed or transported in pipes to fuelling stations or homes, in a similar way to natural gas.

Fuel	Specific energy (kW h kg^{-1})	Energy density (kW h dm^{-3})
Liquid H_2	33.3	2.4
H_2 gas (200 bar)	33.3	0.5
Liquid natural gas	13.9	5.6
Natural gas (200 mbar)	13.9	2.3
Petrol	12.8	9.5
Diesel	12.6	10.6
Coal	8.2	7.6
$LiBH_4$	6.2	4.0
Methanol	5.5	4.4
Wood	4.2	3.0
Electricity (Li-ion battery)	0.6	1.7

Table 1.2: Gravimetric and volumetric energy content of fuels, excluding the weight and volume of the container (taken from [21]).

1.6 Industrial Approaches to Methane Reforming

In the absence of a breakthrough technology it is likely that H_2 will continue to be produced from fossil fuels for some time. This section describes the main industrial methods for reforming of methane. The method of reforming is often determined by the required H_2/CO ratio of the resulting syngas, depending on its end use and also on the scale of the required plant.

1.6.1 Steam Methane Reforming (SMR)

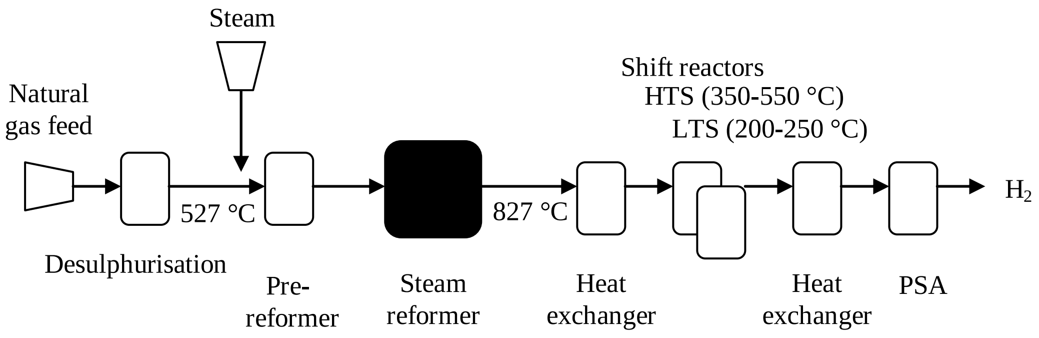

Figure 1.5: Schematic flow diagram of a conventional SMR process. HTS = high temperature shift, LTS = low temperature shift and PSA = pressure swing adsorption (taken from [28]).

A conventional set-up for SMR is shown in Figure 1.5. Firstly, the natural gas is desulphurised to prevent catalyst poisoning. It is then mixed with excess steam and fed into a pre-reformer at 527 °C. Steam reforming is a highly endothermic process as shown by equation 1.1. It is carried out over Ni-based catalysts in the temperature range 697 – 827 °C at 3.5 MPa to produce syngas and CO_2 [28]. A water-gas shift (1.2) is established to drive the equilibrium towards H_2 and CO_2 using high temperatures and oxide catalysts such as NiO, CaO and SiO_2 [16]. This is carried out over two stages; a high temperature shift that accomplishes most of the reaction and a low temperature shift over a more active catalyst, which minimises the remaining CO content in the feed gas.

$$CH_4 + H_2O \rightarrow CO + 3\,H_2 \qquad \Delta H^\circ = 241\ kJ\ mol^{-1} \qquad (1.1)$$

$$CO + H_2O \leftrightarrow CO_2 + H_2 \qquad \Delta H^\circ = -41\ kJ\ mol^{-1} \qquad (1.2)$$

A pressure swing adsorption stage purifies the H_2 product by using sorbents to selectively remove CO_2 from the gas stream at high pressure (as well as smaller amounts of H_2O, CH_4 and CO). A swing to low pressure is accompanied by desorption of the CO_2 from the sorbent material. Heat exchangers are used to recycle the excess energy by using it to heat water for the production of steam.

Challenges associated with SMR include the deactivation and sintering of catalysts, the need for adjustment of the H_2/CO syngas ratio and the disposal of unwanted by-products. Each of these factors contributes to the high capital costs of SMR.

1.6.1.1 Carbon Deposition

Carbon deposition is a major setback to SMR (and reforming of other hydrocarbon feedstocks). The formation of solid carbon ultimately forms a barrier on the surface of the catalyst that prevents reactant molecules from accessing the active sites, leading to deactivation. Carbon deposition can be attributed to two main reactions, direct methane decomposition and the disproportionation of carbon monoxide (1.3 and 1.4). The use of excess steam lowers the rate of carbon deposition but increases the H_2/CO ratio of the syngas produced. Usually a H_2-rich syngas is produced by SMR, where $H_2/CO = 3$ which is higher than the ideal starting mixture for the Fischer-Tropsch synthesis ($H_2/CO \approx 2$). The syngas ratio can be adjusted to a certain extent by modifying the CH_4/steam ratio and by the addition of CO_2 to the feed [29].

Methane decomposition: $CH_4 \rightarrow C + 2\,H_2 \qquad \Delta H° = 75\ kJ\ mol^{-1} \qquad (1.3)$

Boudouard reaction: $2\,CO \rightarrow C + CO_2 \qquad \Delta H° = -171\ kJ\ mol^{-1} \qquad (1.4)$

The thermodynamic potential for carbon formation for different CH_4/H_2O and CH_4/CO_2 ratios is shown in Figure 1.6. The carbon limit curve is calculated using the atomic O/C and H/C ratios in the feed stream and the temperature and pressure of the reformer outlet at conditions of 900 °C and 5 bar. The H_2/CO ratio corresponds to the equilibrated gas at the reformer outlet. Mixing ratios to the left side of the carbon limit curve have a thermodynamic potential for carbon formation whilst those on the right side of the curve do not. The shape of the curve indicates that flexible H_2/CO ratios can be obtained by changing the mixing ratios of the feed gas, at the expense of carbon deposition. For example, a H_2/CO ratio of 0.6 can be obtained but carbon deposition will almost certainly hinder the catalytic reaction under the range of conditions shown on the graph.

By working at conditions to the right side of the curve, carbon deposition can be reduced; however, this may increase the running costs due to higher steam and CO_2 requirements in the feed gas. Consequently, development of catalysts that can kinetically inhibit carbon formation and other advanced methods of methane reforming are the focus of many research groups with the aim of establishing reaction conditions that enable reforming reactions to proceed at conditions to the left of the carbon limit curve but with reduced carbon deposition.

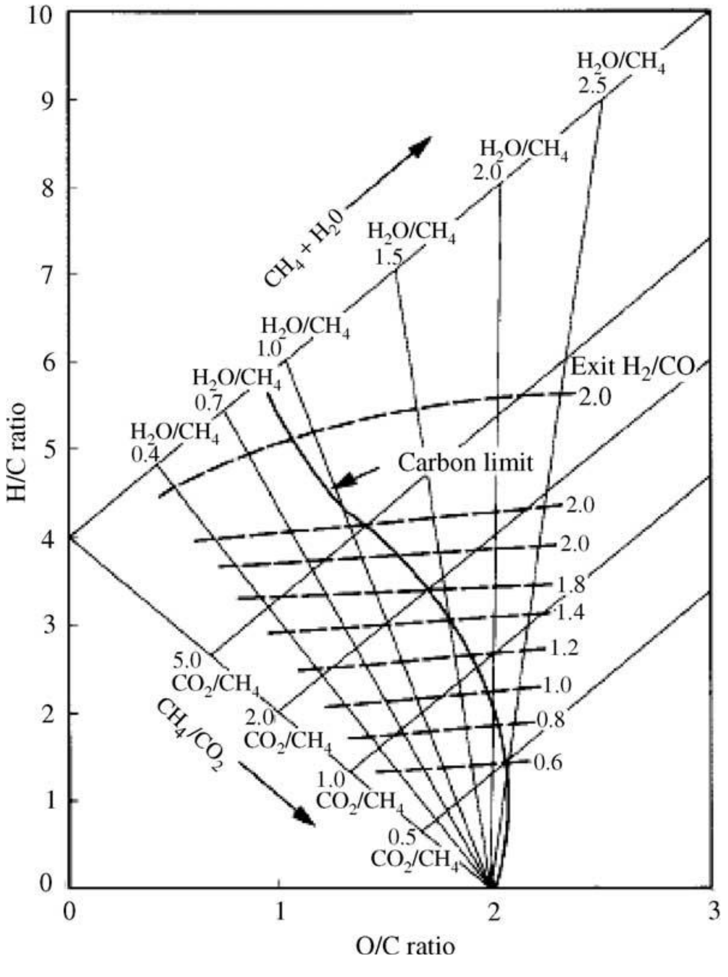

Figure 1.6: Carbon limit curve showing the relationship between the atomic H/C and O/C ratios in the feed and the equilibrated H_2/CO ratio at the reformer exit. Carbon deposition is thermodynamically favoured at conditions to the left of the curve (taken from [29]).

1.6.2 Partial Oxidation of Methane (POX)

$$CH_4 + \frac{1}{2} O_2 \rightarrow CO + 2 H_2 \qquad \Delta H^\circ = -36\ kJ\ mol^{-1} \qquad (1.5)$$

Partial oxidation of methane (1.5) can be achieved with or without the presence of catalysts. In non-catalytic POX, methane is mixed with excess O_2 and ignited. Temperatures of > 1127 °C and pressures of 50 – 70 atm are required to bring about large conversions of methane. Several types of catalysts have been investigated for POX including supported transition and noble metal oxides and various transition metal carbides, with the effect of lowering the operating temperatures to 727 – 927 °C. At these conditions some complete combustion of CH_4 will occur, as well as steam reforming and CO_2 reforming of methane [29]. The main advantages of POX are that it is a slightly exothermic reaction and therefore it requires less external heating and it produces syngas with a H_2/CO ratio of ~ 2 with very little CO_2 content, which is suitable for the F-T synthesis without further adjustment [30]. However, the high running costs of this process have made it uncompetitive with SMR. The main setbacks are due to the costs of separating the O_2 reactant from air and the need for a soot scrubber system downstream of the reformer, as well as the problems of high energy input, catalyst deactivation and sintering that also plague the SMR process.

1.6.3 Autothermal Reforming of Methane

$$CH_4 + x\ H_2O + (1 - x/2)\ O_2 \rightarrow CO_2 + (x + 2)\ H_2 \qquad (1.6)$$

Autothermal reforming of methane combines steam methane reforming and partial oxidation of methane in a single reactor. This method for syngas production was first developed by Haldor Topsøe and has been used in industry since the late 1950s. The autothermal reactor contains an upper combustion zone and a lower catalyst bed as shown in Figure 1.7. Separate streams of natural gas with steam and O_2 are mixed as they enter a turbulent diffusion flame, where the methane is oxidised by either H_2O or O_2. The overall exothermic reaction can be simplified as shown by equation 1.6. Gases exiting the combustion chamber are passed through a bed of $Ni/MgAl_2O_4$ catalysts where further equilibration of the gas mixture occurs. The resulting syngas ratio can be modified by changes to the adiabatic heat balance at the reactor outlet, which is influenced by the composition of the feed gas. Soot precursors are destroyed in the catalyst bed, allowing the soot-free production of syngas [29, 31].

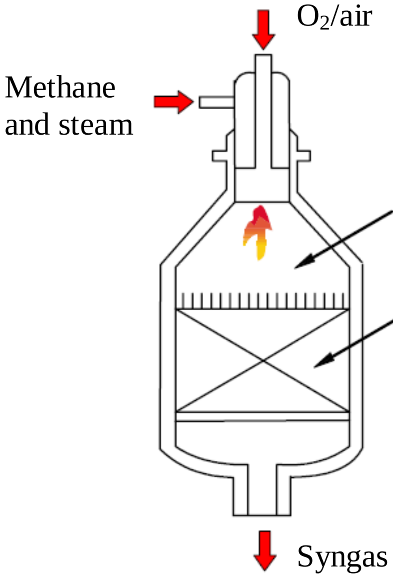

Figure 1.7: Schematic diagram of an autothermal reformer (taken from [29]).

1.6.4 CO_2 Reforming of Methane

Dry reforming of methane with CO_2 is an attractive process from an environmental perspective as it involves the destruction of two greenhouse gases (1.7) that can be renewably generated as biogas. Dry reforming may also be applicable to low-grade natural gas that contains a large amount of CO_2, such as is often found at oil wells. The recovery of CO_2 from flue gases for use as a reactant in dry reforming has been discussed by Kraus [15], who concluded that it is unfeasible due to the high energy input required for current methods of CO_2 recovery.

$$CH_4 + CO_2 \rightarrow 2\ CO + 2\ H_2 \qquad \Delta H° = 247\ kJ\ mol^{-1} \qquad (1.7)$$

Dry reforming of methane is strongly endothermic and therefore requires temperatures in excess of 640 °C and catalysis to bring about CH_4 conversions

[32]. At temperatures in the range 560 – 700 °C carbon formation is thermodynamically favoured by both decomposition of methane and the Boudouard reaction (1.3 and 1.4 respectively). To reduce carbon formation, dry reforming of CH_4 is usually carried out at temperatures > 750 °C, where carbon formation is less thermodynamically favourable [32]. The severity of carbon deposition is more pronounced in dry reforming of methane than for SMR or partial oxidation of methane due to the low O/C atomic ratio in the feed gas, which is made worse with higher CO_2 content [15]. Increasing the operating pressure above atmospheric may be preferable in industry to minimise reactor dimensions and improve reaction rates; however, this also increases the rate of carbon deposition.

There are several reviews in the literature that discuss the catalytic aspects of dry reforming of methane [15, 33-35]. In general, transition metals Fe, Co, Ni and Cu and noble metals Ru, Rh, Pd, Ir and Pt have shown the most promising catalytic activity (usually in the reduced form) [36]. Noble metals are generally more catalytically active towards dry reforming of methane; however, the use of noble metals is limited by their relatively high cost. Subsequently most catalytic investigations concentrate on the use of supported bimetallic catalysts or the use of metal promoters [32]. The metals are typically incorporated into an oxide support such as SiO_2, Al_2O_3, MgO,, CaO, CeO_2, ZrO_2 or La_2O_3 [15]. The support should maximise the surface area, provide a high dispersion of the active metal and be stable at high temperatures. Whilst most catalyst supports do not possess catalytic activity, they may have an interactive role in the chemistry. The acidity/basicity of the support is an important factor in influencing the carbon deposition. Carbon deposition is favoured on acidic supports such as SiO_2 whilst Lewis base supports such as Al_2O_3 have been reported to reduce carbon deposition [37]. Lewis bases have a high affinity for the chemisorption of CO_2 and it has been suggested that adsorbed CO_2 reacts with deposited carbon to form CO, thereby reducing coke formation [38]. However, the influence of acidic and basic supports on dry reforming of CH_4 has not been fully ascertained. The rate of catalysis can be enhanced by the use of smaller metal crystallites in order to maximise the metal surface area. Therefore, the use of nano-sized metal particles on basic supports is considered favourable for dry reforming of methane.

There are two advanced methods for CO_2 reforming of methane that have minimised the problem of carbon deposition, namely the Calcor process and the SPARG (sulphur-passivated reforming) process.

1.6.4.1 The Calcor Process

The Calcor process is used for the production of high purity CO at chemical manufacturing plants. The process is carried out on-site due to the high toxicity and associated risks of transporting carbon monoxide. In this case, dry reforming of methane has been optimised to reduce the H_2 content of the product gas. The reaction is carried out in excess CO_2 by passing a desulphurised feed through reformer tubes filled with unspecified catalysts of different activities and shapes at low pressure and high temperature [39].

1.6.4.2 The SPARG Process

The SPARG process works on the principle of 'promotion by poisoning' [40]. The active sites on the catalyst that promote carbon nucleation can be 'blocked' by the addition of H_2S to the feed gas. The chemisorption of sulphur to the catalytic sites is thermodynamically favoured over carbon growth. However, sufficient activity remains in the catalyst to obtain high conversions of methane. Variation of the CO_2 and steam concentrations in the feed gas allow production of syngas with a low H_2/CO ratio (< 1.8), under conditions to the left of the carbon limit curve (Fig. 1.6) which is usually prevented by carbon formation [29].

1.6.5 Thermocatalytic Decomposition of Methane

$$CH_4 \rightarrow C\ (s) + 2\ H_2 \qquad \Delta H° = 76\ kJ\ mol^{-1} \qquad (1.8)$$

An alternative technique is the direct decomposition of methane to produce H_2 and solid carbon as shown by equation 1.8. The reaction does not directly produce any CO_x by-products; however CO_2 emissions are associated with the energy input required for decomposition. The reaction can be performed in a fluidised bed reactor with periodic removal of the deposited carbon [41]. The carbon can be produced in various forms, such as amorphous, filamentous, graphitic or as carbon nanotubes, depending on the operating conditions. Solid carbon is easier to sequester than gaseous products and has many uses in industry for which it can be marketed, for example, as a pigment, a reducing agent in the metallurgic industries, a stiffening agent for car tyre production or as a reinforcing agent in the construction industry [42].

Methane decomposition can be achieved entirely thermally or with catalysis. Non-catalytic methane pyrolysis can produce a reasonable yield at temperatures > 1200 °C. The use of metal or carbonaceous catalysts can lower the required operating temperature. Catalysts such as supported nickel, iron or copper are effective for CH_4 conversion. However, these catalysts are prone to sintering and deactivation at high temperatures and the rates of methane conversion are thermodynamically limited at lower temperatures. Carbon catalysts such as activated carbon or carbon black can act as ‘seed carbons’ promoting further carbon growth. Seed carbons are also still prone to deactivation, as the deposited carbon has a lower surface area and activity compared to the original catalyst [41].

1.7 Plasma-Assisted Methane Reforming Technologies

The previously described challenges associated with conventional methods of methane reforming have led to a major interest in alternative reforming techniques in pursuit of milder reaction conditions, more durable catalysts and reduced energy costs. Plasma reformers have shown potential for H_2 production from methane either at fuelling stations or on-board vehicles, where the H_2 could be used directly as a feedstock for fuel cells. This would eliminate the need for H_2 storage and transport, as the existing infrastructure would be used to supply natural gas to fuelling stations. The feasibility of this concept is discussed by Petitpas et al. [43], together with a review of the existing technologies. In favour of plasma reformers is the low device weight, compactness, rapid response and low cost.

Bromberg et al. at the Massachusetts Institute of Technology have developed a series of thermal and non-thermal plasma reformers known as ‘plasmatrons’ [44-46]. The hydrocarbon feed is partially oxidised in air or water-air mixtures in a plasma discharge to produce a H_2-rich gas with low CO content (1.5 – 3 vol. % CO with ~ 40 % H_2 in the product gas) [44]. They have been used to reform natural gas, biofuels and heavy oil fractions. The main drawback of these reformers is their reliance on electrical power to achieve 50 – 300 W required to sustain the plasma. The efficiency could be improved by heat recycling, better thermal insulation and improved reactor design. Catalysts for NO_x removal and particulate traps would also need to be incorporated into the plasmatron design. However, the technology is in the early stages of development, further technological advances and investigations would need to be conducted before the technology could be suitably advanced for marketing. Another plasma process for H_2 production is the Kværner process; originally developed in Norway in the late 1980s and has been used industrially since 1992 for the decomposition of CH_4 into H_2 and a high-grade carbon black. The technology uses an arc plasma at temperatures of ~ 1600 °C [47]. The research in this thesis focuses on the use of a plasma technology for dry reforming methane, using model mixtures of CH_4 and CO_2 representative of the main components of biogas without its impurities. In particular, the interactions between plasma and catalysts are examined.

1.8 References

1. Atkins, P.W., *Physical Chemistry*. Vol. 1. 1978, Oxford: Oxford University Press.
2. *Worldwide Look at Reserves and Production.* Oil Gas J., 2008. **106**(48): p. 22-23.
3. Hardy, J.T., *Climate Change: Causes, Effects and Solutions*. 2003, Chichester: Wiley.
4. Trenberth, K.E., Fasullo, J.T.and Kiehl, J., *Earth's Global Energy Budget.* Bulletin of the American Meteorological Society, 2008.
5. Coffey, M., *Energy and Power Generation: Maximising Biogas Yields From Sludge.* Filtr. Separat., 2009. **46**(1): p. 12-15.
6. *European Biomass Association. A Biogas Road Map for Europe.* 2009.
7. Rasi, S., *Biogas Composition and Upgrading to Biomethane*. 2009, University of Jyväskylä, Finland.
8. Mann, G., Schlegel, M., Schumann, R.and Sakalauskas, A., *Biogas-Conditioning with Microalgae.* Agron. Res., 2009. **7**(1): p. 33-38.
9. Monbiot, G., *Heat. How to Stop the Planet Burning*. 2006: Penguin Books.
10. *NaturalGas.org [online]. Overview of Natural Gas* http://www.naturalgas.org/overview/background.asp. [cited 20/10/2010].

11. Whitty, K.J., Zhang, H.R.and Eddings, E.G., *Emissions from Syngas Combustion.* Combust. Sci. Technol., 2008. **180**(6): p. 1117-1136.
12. Wilhelm, D.J., Simbeck, D.R., Karp, A.D.and Dickenson, R.L., *Syngas Production for Gas-to-Liquids Applications: Technologies, Issues and Outlook.* Fuel Process. Technol., 2001. **71**: p. 139-148.
13. Wender, I., *Reactions of Synthesis Gas.* Fuel Process. Technol., 1996. **48**(3): p. 189-297.
14. Fleisch, T.H., Sills, R.A.and Briscoe, M.D., *2002 - Emergence of the Gas-to-Liquids Industry: a Review of Global GTL Developments.* J. Nat. Gas Chem., 2002. **11**: p. 1-14.
15. Kraus, M., *Catalytic CO_2 Reforming of Methane in a Dielectric-Barrier Discharge* 2001, Swiss Federal Institute of Technology: Zurich.
16. Bond, G.C., *Heterogeneous Catalysis: Principles and Applications*. 2nd ed. 1987, New York: Oxford Science Publications.
17. Van Der Laan, G.P., *Kinetics, Selectivity and Scale-Up of the Fischer-Tropsch Synthesis*. 1999, Rijksuniversiteit Groningen, The Netherlands.
18. Van Der Laan, G.P.and Beenackers, A.A.C.M., *Kinetics and Selectivity of the Fischer-Tropsch Synthesis: A Literature Review.* Catal. Rev., 1999. **41**(3): p. 255-318.
19. Choi, G.N., Kramer, S.J.and Tam, S.S. *Design and Economics of a Fischer-Tropsch Plant for Converting Natural Gas to Liquid Transportation Fuels*. in *Spring National Meeting, American Institute of Chemical Engineers*. 1996. Houston.
20. Mandal, T.K.and Gregory, D.H., *Hydrogen: a Future Energy Vector for Sustainable Development.* Proc. IMechE. Part C: J. Mechanical Engineering Science, 2010. **224**(3): p. 539-558.
21. Edwards, P.P., Kuznetsov, V.L.and David, W.I.F., *Hydrogen Energy.* Philos. T. Roy. Soc. A., 2007. **365**(1853): p. 1043-1056.
22. Buratto, S.K., *Fuel Cells: Engineering the Next Generation.* Nat. Nanotechnol., 2010. **5**: p. 176.
23. Yan, W.-M., Chu, H.-S., Lu, M.-X., Weng, F.-B., Jung, G.-B.and Lee, C.-Y., *Degradation of Proton Exchange Membrane Fuel Cells due to CO and CO_2 Poisoning.* J. Power Sources, 2009. **188**(1): p. 141-147.
24. Ralph, T.R., *Clean Fuel Cell Energy for Today. Developments in Proton Exchange Membrane Fuel Cells.* Platinum Met. Rev., 1999. **43**(1): p. 14-17.
25. Ogden, J., *High Hopes for Hydrogen.* Sci. Am., 2006. **295**(3): p. 94-101.
26. Simbolotti, G., *IEA Energy Technology Essentials - Hydrogen Production and Distribution.* 2007.
27. Tanksale, A., Beltramini, J.N.and Lu, G.M., *A Review of Catalytic Hydrogen Production Processes from Biomass.* Renew. Sust. Energ. Rev., 2010. **14**(1): p. 166-182.
28. Go, K.S., Son, S.R., Kim, S.D., Kang, K.S.and Park, C.S., *Hydrogen Production from Two-Step Steam Methane Reforming in a Fluidized Bed Reactor.* Int. J. Hydrogen Energ., 2009. **34**: p. 1301-1309.
29. Song, X.and Guo, Z., *Technologies for Direct Production of Flexible H_2/CO Synthesis Gas.* Energ. Convers. Manage., 2006. **47**(5): p. 560-569.
30. York, A.P.E., Xiao, T.and Green, M.L.H., *Brief Overview of the Partial Oxidation of Methane to Synthesis Gas.* Top. Catal., 2003. **22**(3-4): p. 345-358.

31. Aasberg-Petersen, K., Bak Hansen, J.H., Christensen, T.S., Dybkjaer, I., Christensen, P.S., Stub Nielsen, C., Winter Madsen, S.E.L.and Rostrup-Nielsen, J.R., *Technologies for Large-Scale Gas Conversion.* Appl. Cat. A: Gen., 2001. **221**(1-2): p. 379-387.
32. Fan, M.S., Abdullah, A.Z.and Bhatia, S., *Catalytic Technology for Carbon Dioxide Reforming of Methane to Synthesis Gas.* ChemCatChem, 2009. **1**(2): p. 192-208.
33. Bradford, M.C.J.and Vannice, M.A., *CO_2 Reforming of CH_4.* Catal. Rev., 1999. **41**(1): p. 1-42.
34. Edwards, J.H.and Maitra, A.M., *The Chemistry of Methane Reforming with Carbon Dioxide and its Current and Potential Applications.* Fuel Process. Technol., 1995. **42**: p. 269-289.
35. Moon, D.J., *Hydrogen Production by Catalytic Reforming of Gaseous Hydrocarbons (Methane & LPG).* Catal. Surv. Asia, 2008. **12**: p. 188-202.
36. Zhang, Z.L.and Verykios, X.E., *Carbon Dioxide Reforming of Methane to Synthesis Gas Over Supported Ni Catalysts.* Catal. Today, 1994. **21**(2-3): p. 589-595.
37. Ferreira-Aparicio, P., Rodríguez-Ramos, I., Anderson, J.A.and Guerrero-Ruiz, A., *Mechanistic Aspects of the Dry Reforming of Methane Over Ruthenium Catalysts.* Appl. Catal. A, 2000. **202**(2): p. 183-196.
38. Hu, Y.H., *Solid-Solution Catalysts for CO_2 Reforming of Methane.* Catal. Today, 2009. **148**(3-4): p. 206-211.
39. Teuner, S.C., Neumann, P.and Von Linde, F., *The Calcor Standard and Calcor Economy Processes*, in *Oil Gas European Magazine*. 2001. p. 44-46.
40. Rostrup-Nielsen, J., *40 Years in Catalysis.* Catal. Today, 2005. **111**: p. 4-11.
41. Abbas, H.F.and Wan Daud, W.M.A., *Hydrogen Production by Methane Decomposition: A Review.* Int. J. Hydrogen Energ., 2010. **35**(3): p. 1160-1190.
42. Muradov, N., Smith, F., Huang, C.and T-Raissi, A., *Autothermal Catalytic Pyrolysis of Methane as a new Route to Hydrogen Production with Reduced CO_2 Emissions.* Catal. Today, 2006. **116**(3): p. 281-288.
43. Petitpas, G., Rollier, J.D., Darmon, A., Gonzalez-Aguilar, J., Metkemeijer, R.and Fulcheri, L., *A Comparative Study of Non-Thermal Plasma Assisted Reforming Technologies.* Int. J. of Hydrogen Energ., 2007. **32**(14): p. 2848-2867.
44. Bromberg, L., Cohn, D.R., Rabinovich, A.and Alexeev, N., *Plasma Catalytic Reforming of Methane.* Int. J. Hydrogen Energ., 1999. **24**(12): p. 1131-1137.
45. Bromberg, L., Cohn, D.R., Rabinovich, A., Alexeev, N., Samokhin, A., Ramprasad, R.and Tamhankar, S., *System Optimization and Cost Analysis of Plasma Catalytic Reforming of Natural Gas.* Int. J. Hydrogen Energ., 2000. **25**(12): p. 1157-1161.
46. Bromberg, L., Cohn, D.R., Rabinovich, A.and Heywood, J., *Emissions Reductions Using Hydrogen From Plasmatron Fuel Converters.* Int. J. Hydrogen Energ., 2001. **26**(10): p. 1115-1121.
47. *AEA Technology, The Feasibility, Costs and Markets for Hydrogen Production.* 2002.

2. Plasma-Catalysis and Analytical Techniques

2.1 Introduction to Plasma

Plasma is a partially or wholly ionised gas. When energy is applied to a substance, the molecules become more energetic and transform through four distinct states of matter: solid, liquid, gas and finally plasma. Generally, this increased energetic state is associated with heating, however, plasma can also be generated from a gas by the application of an electric field, energetic beam or by adiabatic gas compression [1]. Under these conditions of increased energy, the gas molecules can become dissociated or ionised. This results in a 'soup' of freely moving charged particles and neutral gas species, sufficient to make the plasma electrically conductive; a property that distinguishes plasma from neutral gas which is an electrical insulator. Approximately equal concentrations of positive ions and electrons make the plasma quasi-neutral.

Plasma is naturally abundant throughout the universe and comprises ~ 99 % of the observable cosmos, including the solar corona, solar wind and nebula [2, 3]. Plasma is also present in the upper region of the Earth's atmosphere (at altitudes > 100 km) [3] where interactions with cosmic radiation lead to the dissociation of atmospheric gas molecules. This produces a region of ions and freely moving electrons, known as the ionosphere. Plasmas can be visible on Earth as naturally occurring phenomena including lightning, the Aurora Borealis and the Aurora Australis.

2.2 Applications of Plasma

Since the first investigations into electrical arcs in the early 19th century, several laboratory techniques have been developed for the generation of man-made plasma discharges. Pioneering studies by Siemens in the 1850s led to the first important industrial application of plasma: the synthesis of ozone (O_3) from an O_2 silent discharge for water purification [4]. However, it was not until the 1920s that Langmuir named this phenomenon as a 'plasma' [5]. In recent years, plasma technologies have progressed to include a wide range of applications across many industries. Some important applications at various stages of development are listed below:

- **Surface modification** – etching of semiconductors, ‘plasma hardening’ of metallic components for cars and aircrafts [2].
- **Thin film deposition** – anti-reflective coatings for lenses, hydrophilic and hydrophobic coatings for textiles [2], deposition of diamond and cubic boron nitride films for cutting tools [6].
- **Pollutant remediation** – destruction of volatile organic compounds (VOCs) from diesel exhausts and flue gases [4], destruction of odorous molecules [7].
- **Chemical synthesis** – O_3 generation [7], synthesis of acetylene (C_2H_2) [4].
- **Lighting** – excimer based UV and fluorescent lamps [4].
- **Biomedical techniques** – tissue engineering, blood coagulation, deactivation of micro-organisms, sterilisation of instruments and surfaces [3].
- **Plasma display panels –** large area flat-screen televisions [7].
- **Lasers –** CO_2 laser discharges for cutting and welding [7].

Although several of these plasma technologies are relatively advanced, the empirical focus has been on the development of deliverables, whilst a basic understanding of the plasma chemistry is still lacking in many cases [2].

2.3 Types of Plasma

There are two main types of plasma: high-temperature plasma (such as thermonuclear fusion plasmas or thermal arc torches) and low-temperature plasma. All plasmas consist of multiple components including electrons, excited molecules and atoms, ions, radicals, neutral gas species and photons. The extent to which these constituents have reached thermal equilibrium is used to further classify the plasma as thermal or non-thermal (which are also known as equilibrium and non-equilibrium plasmas respectively). These classifications are shown in Table 2.0.

Low-Temperature Plasma		**High Temperature Plasma**
Non-Thermal Plasma	Thermal Plasma	
$T_0 \approx T_i \approx T_r < T_v << T_e$ $\leq 10^5$ K	$T_0 \approx T_i \approx T_r \approx T_v \approx T_e$ $\leq 2 \times 10^4$ K	$T_0 \approx T_i \approx T_r \approx T_v \approx T_e$ $\geq 10^7$ K

Table 2.0: Subdivision of plasmas, where T_0 = gas temperature, T_i = ion temperature, T_r = rotational temperature, T_v = vibrational temperature and T_e = electron temperature (modified from [8]).

In thermal plasma, sufficient applied energy and time for equilibration has resulted in a plasma discharge that can be defined by a single temperature. In contrast, non-thermal plasmas are characterised by multiple temperatures relating to different plasma species. Highly energetic electrons (10^3 – 10^5 K) can exist together with species of substantially lower temperatures such as excited species, ions and neutral molecules. Heavy gas molecules usually exhibit the lowest temperatures in these systems and in many cases the bulk gas remains close to room temperature [3].

2.4 Generation of Non-Thermal Plasma by Electric Fields

The most widely used method for the formation of non-thermal plasma is by the application of an external electric field between two electrodes surrounded by a volume of gas. The plasma can be operated either at low pressures (1 – 10^3 Pa) or at atmospheric pressure and above.

The breakdown voltage (V_b) defines the minimum voltage required to breakdown a gas to form a plasma discharge. V_b is dependent on the gas pressure (p) and the distance between the electrodes (d). This relationship is described by Paschen’s Law (2.0), where a and b are constants that are dependent on the gas type [9].

$$V_b = \frac{a(pd)}{\ln(pd)+b} \qquad (2.0)$$

An applied voltage causes free electrons, that exist to some extent in a gas volume as a result of an interaction with cosmic radiation, to become accelerated. At the point where the breakdown voltage is reached, the current flow will increase sharply due to an intensive avalanche of electrons in the discharge gap between the electrodes. These high energy electrons will collide with gas molecules leading to the formation of new ‘active’ plasma species including excited molecules and atoms and their relevant degrees of freedom, radicals, ions and new stable gas molecules. These collision processes are shown in Table 2.1.

Electron/Molecular Reactions	
Excitation	$e^- + A_2 \rightarrow A_2^* + e^-$
Dissociation	$e^- + A_2 \rightarrow 2\,A + e^-$
Attachment	$e^- + A_2 \rightarrow A_2^-$
Dissociative attachment	$e^- + A_2 \rightarrow A^- + A$
Ionisation	$e^- + A_2 \rightarrow A_2^+ + 2\,e^-$
Dissociative ionisation	$e^- + A_2 \rightarrow A^+ + A + e^-$
Recombination	$e^- + A_2^+ \rightarrow A_2$
Detachment	$e^- + A_2^- \rightarrow A_2 + 2\,e^-$
Atomic/Molecular Reactions	
Penning dissociation	$M + A_2 \rightarrow 2\,A + M$
Penning ionisation	$M^* + A_2 \rightarrow A_2^+ + M + e^-$
Charge transfer	$A^\pm + B \rightarrow B^\pm + A$
Ion recombination	$A^- + B^+ \rightarrow AB$
Neutral recombination	$A + B + M \rightarrow AB + M$
Decomposition	
Electronic	$e^- + AB \rightarrow A + B + e^-$
Atomic	$A^* + B_2 \rightarrow AB + B$
Synthesis	
Electronic	$e^- + A \rightarrow A^* + e^-,\ A^* + B \rightarrow AB$
Atomic	$A + B \rightarrow AB$

Table 2.1: The main plasma processes. A and B represent atoms and M stands for a temporary collision partner (taken from [4]).

During collisions between electrons and heavy gas molecules only a small portion of the energy is transferred, due to the relative sizes of the species involved. In most non-thermal plasma systems for gas processing, the plasma is only weakly ionised. The degree of ionisation in the plasma can be defined as the ratio of the density of charged particles to the density of neutral species, this is generally in the range of $10^{-7} – 10^{-14}$ [3].

In addition to the plasma species shown in Table 2.1, photons are also generated in the plasma volume. In an electronically excited gas molecule or atom, an electron exists in a high energy orbital further from the nucleus, whilst an electron 'hole' exists in the lower energy orbital that it was originally excited from. This excited state is metastable and can spontaneously return to its more stable ground state. When an electron is de-excited back to its lower energy orbital, the excess energy is released in the form of a photon. This initiates a chain of reactive photon absorptions and emissions as molecules are excited and de-excited within the plasma. Consequently, the plasma can exhibit a visible glow if the energies of the emitted photons are in the visible region of the electromagnetic spectrum.

In plasma processing of gases, each of the plasma species may have different roles in the plasma chemistry. Electrons, being the first to receive energy from the electric field, distribute this energy through collisions, generating new reactive species. Vibrationally excited molecular states can transfer a significant proportion of energy into gas heating, which will accelerate chemical reactions in the plasma. Ions and radicals are able to make a significant contribution in plasma chemical synthesis due to their ability to react in plasma at lower temperatures than would be required by thermal reaction methods. Control over the complex chemical processes in a plasma by selection of appropriate gases, plasma type and operating conditions could allow the selective synthesis of the desired end products [3].

Several different types of non-thermal plasma can be formed depending on the type of applied electric field used to drive the plasma formation. This may be a continuous or pulsed direct current (DC) or an alternating current (AC) which may utilise radio frequencies (kHz – MHz) or microwave frequencies (GHz).

2.5 Continuous and Pulsed Direct Current Discharges

Several types of direct current (DC) discharge can be obtained depending on the voltage-current characteristics as depicted in Figure 2.0. The initial breakdown of a gas at low current is known as a Townsend discharge. The transition from Townsend discharge to corona, through to subnormal glow discharge and normal glow discharge is accompanied by an increase in current and simultaneous decrease in the applied voltage. A normal glow discharge can be characterised by a constant current density at the cathode surface, which is only partially covered by the discharge. As the current is increased with increasing voltage, an abnormal glow discharge develops which completely covers the cathode surface. At even higher currents, an irreversible glow-to-arc transition can occur. The arc is sustainable at low voltage and high current due to heating of the cathode to the point of thermionic emission (heat-induced current flow) [8].

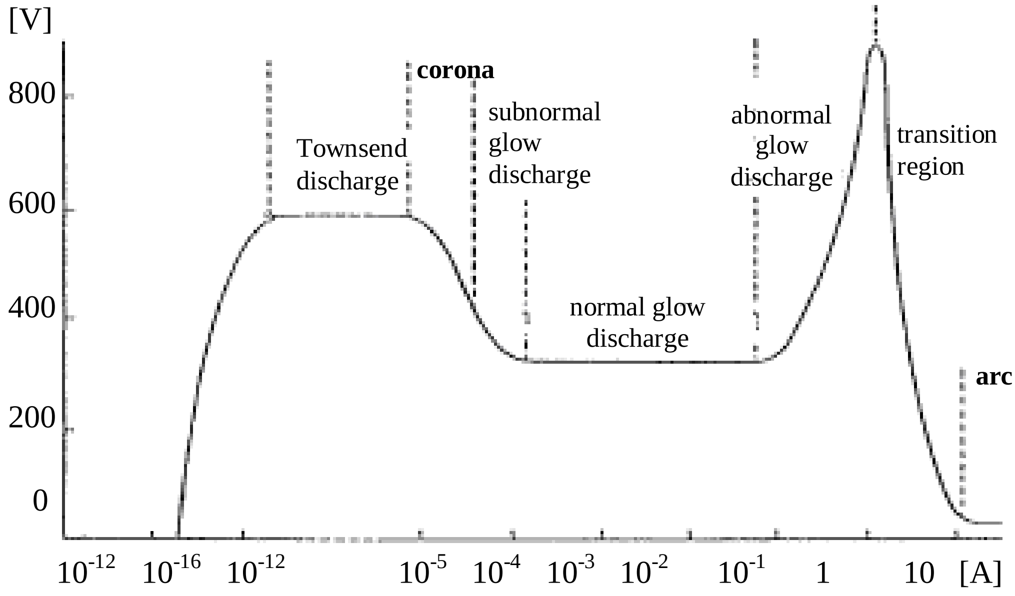

Figure 2.0: Voltage-current properties of different DC plasma discharges (taken from [1]).

The most widely used DC discharges in plasma processing of gases are the corona discharge and the gliding arc discharge, typical reactor configurations for these are described in the following sections.

2.5.1 Corona Discharges

Corona can occur at atmospheric pressure in regions of non-uniform electric fields. They appear when the field at one or both electrodes is stronger than in the surrounding gas. This is prevalent near sharp points, edges or thin wires. Coronas have frequently been observed at high voltage transmission lines, lightning rods and ships' masts during electrical storms, where the discharge takes the shape of a crown (from which corona takes its name) [10]. A corona discharge can be formed by applying either continuous or pulsed DC voltage between two electrodes. The electrodes are most commonly arranged as a grounded cylindrical outer electrode (e.g. a stainless steel tube) with a high voltage wire or rod inner electrode (Figure 2.1) or as a point-to-plate (Figure 2.2) or point-to-point electrode configuration. The area between the electrodes where the corona is formed is occupied by a continuous flow of gas.

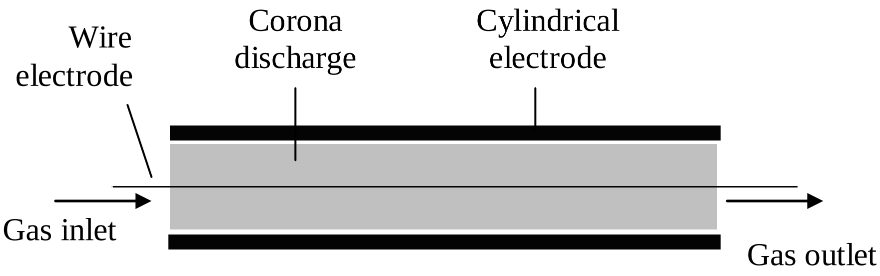

Figure 2.1: Schematic diagram of a corona discharge reactor in a coaxial wire-cylinder configuration.

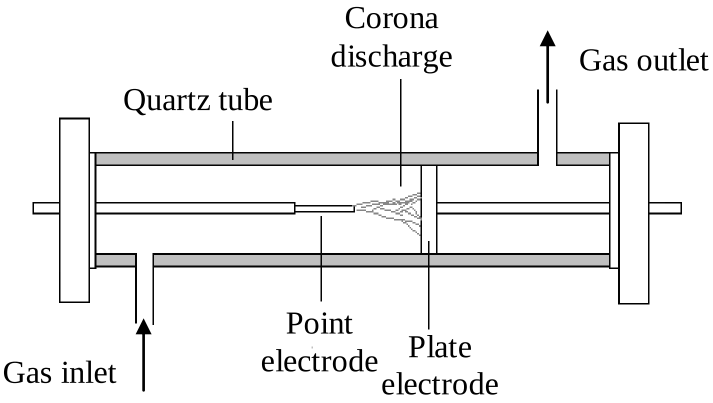

Figure 2.2: Schematic diagram of a corona discharge reactor in a point-to-plate configuration.

Corona discharges can take on several forms depending on the relative polarity of the electrodes. For a point-to-plate electrode configuration, the different types of corona discharge are shown in Figure 2.3, where the applied voltage increases from left to right. Positive corona is formed at a pointed anode, whilst negative corona is formed at a pointed cathode. In a positive corona, the initial breakdown of the gas produces a burst pulse, which is limited to the area immediately surrounding the electrode. The discharge is space-charge limited and therefore requires an increase in voltage to create additional charged species, leading to the formation of streamers. Streamers extend into the inter-electrode gap and several transient streamers can be observed at a given time. In this mode, the corona occupies a relatively large active volume and has a low temperature of ~ 27 °C [10].

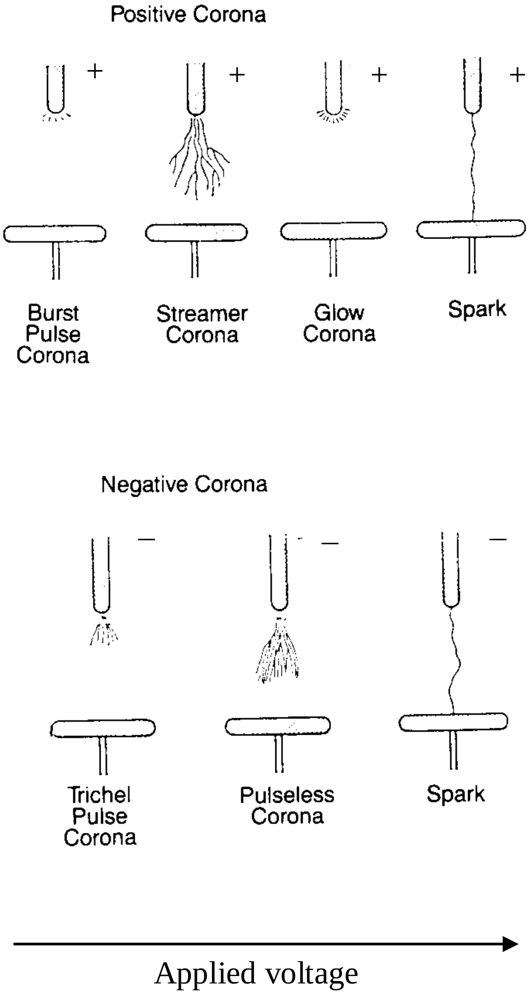

Figure 2.3: Schematic diagrams showing different forms of corona discharges in a point-to-plate electrode configuration (modified from [10]).

In both positive and negative corona, high current flow will result in complete breakdown and the formation of a single spark discharge that bridges the discharge gap. A spark discharge is confined to a narrow channel and produces an unsteady current. The spark is usually noisy and causes local heating in the channel in which it is formed and is therefore not a desirable outcome. The use of short DC pulses, typically of nanosecond duration can overcome the problem of unwanted spark formation. By varying between plasma pulses and plasma afterglow, the current flow can be controlled. This can improve the energy efficiency of the process and allow operation at higher powers [8].

2.5.2 Gliding Arc Discharges

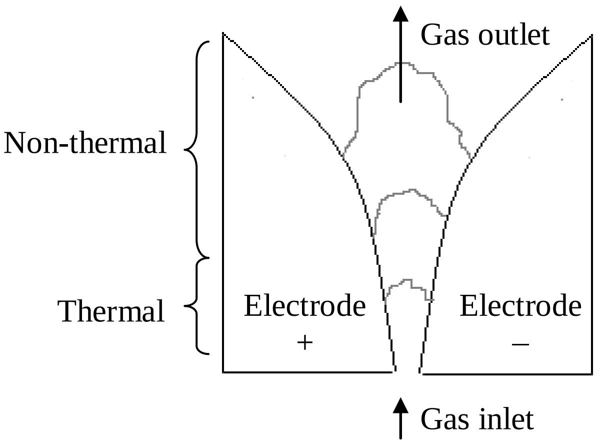

Figure 2.4: Schematic diagram of a gliding arc discharge reactor.

An atmospheric pressure gliding arc discharge can be formed between two flat knife-shaped electrodes with a gas flowing between them, as shown in Figure 2.4. The discharge is initially formed at the point where the discharge gap is narrowest and proceeds to ‘glide’ up the electrodes, pushed by the flow of gas. The arc grows in volume as it proceeds up the electrodes and then extinguishes when it reaches the top, where the electrodes diverge. The arc is immediately reignited at the shortest gap and the cycle continues. Gliding arcs may be thermal or non-thermal, depending on the applied power and gas flow rate. It is also possible to operate in the transitional regime, whereby the discharge has thermal characteristics in the lower part of the gliding-arc and evolves into a non-thermal discharge as it proceeds up the electrodes [3]. Gliding arc discharges are suitable for applications that require relatively large gas flows (several L min^{-1}) and can be either DC or AC driven.

2.6 Radio Frequency Discharges

Radio frequency (RF) electromagnetic fields can be used to generate weakly ionised plasma at low pressures, typically in the range $1 – 10^3$ Pa [1]. At higher pressures, the properties of the RF discharge will change as the collision frequency increases, leading to a discharge approaching a thermal regime when close to atmospheric pressure [4]. RF discharges usually operate at frequencies in the range 1 – 100 MHz corresponding to wavelengths in the range 300 – 3 m [1]. A frequency of 13.56 MHz ($\lambda = 22$ m) is particularly common for industrial applications. The large wavelength relative to the size of the discharge chamber allows relatively homogeneous plasmas to be formed by this method [4]. In order to maximise the energy efficiency of the system, the plasma reactor is usually connected to an RF generator with an impedance matching network. This matches the impedance of the generator to that of the plasma discharge and minimises reflected RF power [1, 3]. RF discharges are particularly advantageous for applications that require the electrodes to be outside of the discharge region, thereby preventing contamination with metal vapours given off at the electrodes [4]. The two main types of RF discharge are capacitively coupled plasmas (CCPs) and inductively coupled plasma (ICPs). Typical reactor designs for each of these configurations are shown in Figure 2.5.

Capacitively coupled plasmas can be formed by applying an RF voltage between two planar electrodes, which are usually spaced a few centimetres apart [1]. The electrodes can be located either inside or outside the discharge chamber (Figure 2.5 a and b respectively). When an RF voltage is applied across the discharge gap, a strong electric field is established resulting in the ignition of a plasma discharge. The electrons respond to the electric field by rapidly oscillating back and forth within a cloud of positively charged ions. Due to the relatively large size of the ions, they respond only to time-averaged electric fields [11].

Inductively coupled plasmas can be formed using an inductive solenoid coil that is wrapped around the discharge chamber or a planar coil that is situated adjacent to it (Figure 2.5 c and d). When an electric current passes through the induction coil, a strong magnetic field is established in the discharge gap which induces a low electric field (in contrast to CCP, which primarily produces an electric field). ICPs can achieve high electron densities and electrical conductivities and are less suited for creating non-thermal plasma at atmospheric pressure than the previously described CCP [3].

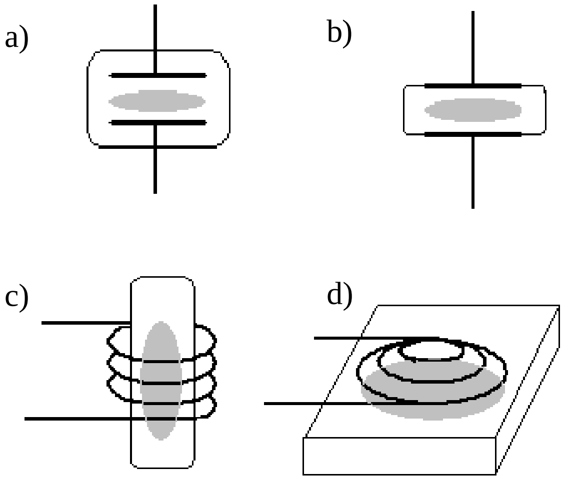

Figure 2.5: Electrode configurations for RF discharges a) CCP with the electrodes inside the gas chamber, b) CCP with the electrodes outside the gas chamber, c) ICP with the discharge located inside an inductive coil and d) ICP with the discharge located adjacent to an inductive coil (taken from [3]).

2.7 Atmospheric Pressure Plasma Jet

The atmospheric pressure plasma jet (APPJ) or atmospheric pressure glow discharge is a well-developed form of AC discharge that can sustain a non-thermal regime at atmospheric pressure. It requires an inert gas such as helium or argon. Various additive gases can be used in the discharge; however, the discharge can become unstable if the additive concentrations are too high, possibly due to the increase in breakdown voltage associated with non-inert gases. A coaxial APPJ set-up is shown in Figure 2.6. A high voltage inner electrode is surrounded by an outer electrode in the shape of a nozzle. The plasma is directed through the nozzle to form a plasma ‘jet’. Planar configurations are also possible, usually with discharge gaps of 1 – 2 mm [3]. Plasma jets have widespread use in the production of microelectronic devices and in surface treatment. More recently, the applications of this discharge for pre-treatment of catalysts has been investigated (this work is reviewed in Chapter 5 of this thesis).

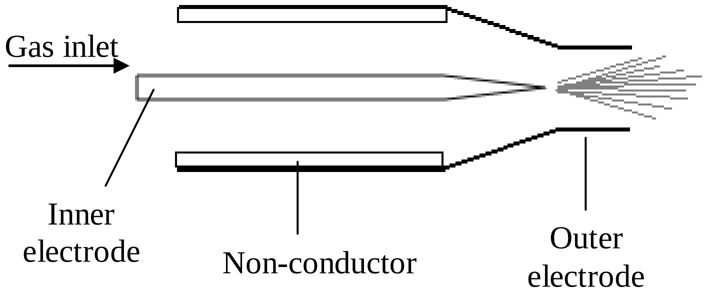

Figure 2.6: Schematic diagram of an atmospheric pressure plasma jet (taken from [12]).

2.8 Dielectric Barrier Discharges

The dielectric barrier discharge (DBD) or silent discharge (as it was originally known, due to a lack of noisy spark formation) is a strongly non-thermal plasma that can be operated at atmospheric pressure. It is driven by a sinusoidal AC voltage in the frequency range from 50 Hz to 500 kHz [7]. DBDs are able to form stable discharges in a range of different gases at relatively high discharge powers, making them particularly suitable for many industrial applications.

The DBD reactor consists of two electrodes with one or more dielectric barriers positioned in the discharge gap (in the path of current flow). Materials with high relative permittivity such as quartz, glass and ceramics are suitable for use as dielectric barriers. Several DBD configurations are possible including planar, cylindrical and surface discharges, as illustrated in Figure 2.7. The spacing in the discharge gap can vary from 0.1 mm to several centimetres. The DBD is a non-uniform plasma discharge, it consists of many tiny breakdown channels known as microdischarges or filaments that cover the entire surface of the dielectric material and extend across the discharge gap. The dielectric barrier limits the flow of current causing the microdischarges to become extinguished, leaving significant charge deposition on the dielectric surfaces. As the polarity of the electrodes is rapidly changing, the microdischarges are reformed at the point where the breakdown voltage is reached in the next half cycle of the AC voltage sine wave. This results in the continuous formation of nanosecond microdischarges at a frequency which is twice that of the applied frequency [7]. The microdischarges appear as ‘spikes’ on the current waveform. In appearance, the microdischarges are randomly distributed over the surface of the dielectric. In reality, the position of the microdischarge formation is dependent on the residual charge distribution on the dielectric surface [13, 14].

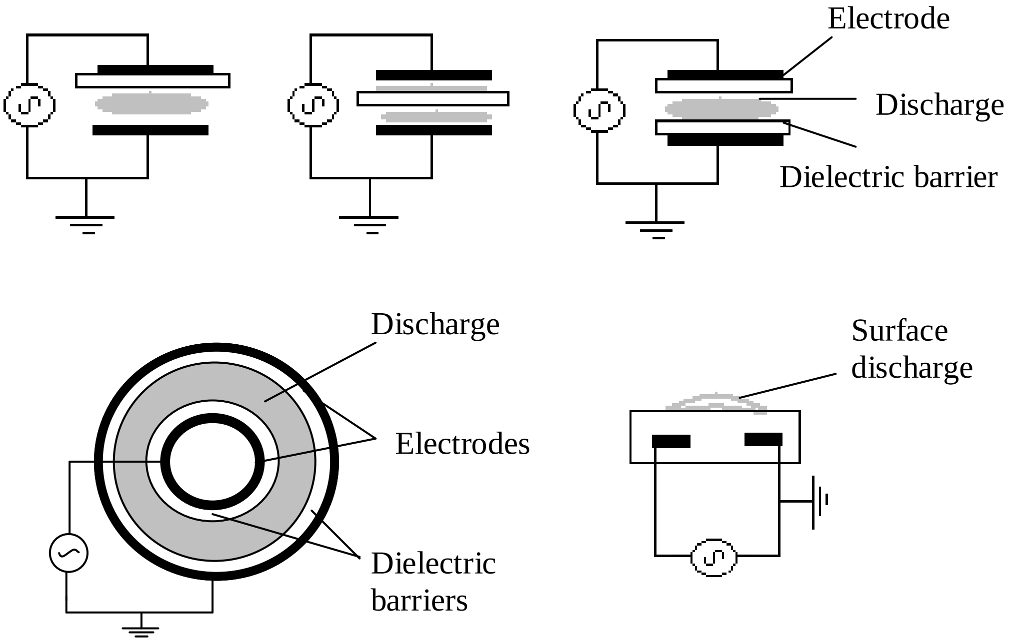

Figure 2.7: Schematic diagrams of planar, coaxial and surface DBD configurations (taken from [7]).

The terms ‘relative permittivity’ and ‘dielectric constant’ are synonymous, meaning the ability of a material to store electrical charge relative to a vacuum. Where DBD plasmas are concerned, exclusive use of the term ‘dielectric constant’ is used.

2.8.1 The Packed-Bed Reactor

A special modification to the DBD reactor exists in the form of the packed-bed DBD reactor (Figure 2.8). The gap between two parallel electrodes is packed with dielectric pellets, such as barium titanate beads ($BaTiO_3$). The dielectric pellets have an excellent ability to concentrate electrostatic lines of flux leading to enhanced electric fields at the contact points between the beads. As there are many contact points in close proximity, the average electric field strength can be enhanced and in turn electron energies increased, this is known as the *packed-bed effect*. The electric field strength can be enhanced by a factor of 10 to 250 depending on the dielectric constant, curvature and contact angle of the packing material [3]. Higher electric field strengths give rise to higher electron energies. As with conventional DBD reactors, the microdischarges are driven by an AC voltage. In the packed-bed configuration, relatively low applied voltages (< 30 kV) can ignite a discharge over a large electrode separation (~ 5 cm) [15].

Figure 2.8: Image of plasma generation in a packed-bed DBD reactor, showing microdischarges at the contact points between $BaTiO_3$ beads.

The use of both coaxial and packed-bed DBD reactors have been employed for experiments in this thesis due to the ability to form stable discharges at atmospheric pressure as well as the ease of combining DBD plasmas with catalysts.

2.9 Microwave Discharges

Microwave discharges are commonly generated using a frequency of 2.45 GHz, corresponding to a wavelength of 12.24 cm. At microwave frequencies (0.3 – 10 GHz), only the electrons are light enough to oscillate with the electric field, resulting in a discharge which is far from thermodynamic equilibrium [4]. As with RF discharges, microwave discharges can be operated at low pressures (10^3 – 10^4 Pa) or atmospheric pressure, where the properties can approach that of a thermal plasma. A typical experimental set-up for a microwave discharge reactor is shown in Figure 2.9. It consists of a waveguide that directs the microwaves towards the plasma load with optimised energy transfer and minimal reflected power. A continuous flow of gas occupies the region where the plasma is formed, which can be contained inside a quartz tube or other discharge chamber. The microwave power supply is connected to a circulator which protects the power supply from the reflected microwave energy [1].

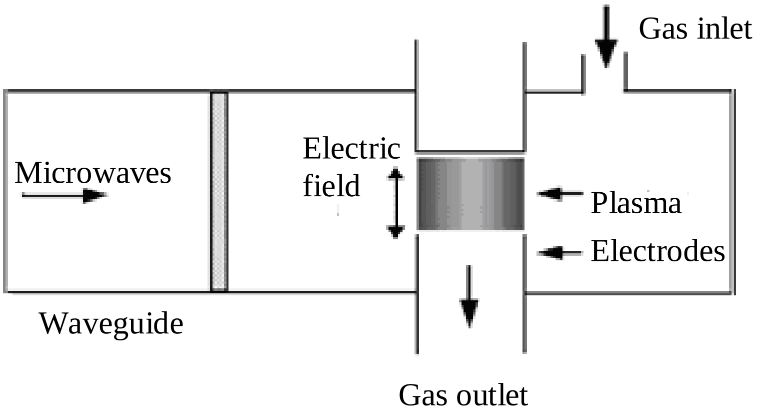

Figure 2.9: Schematic diagram of a microwave plasma reactor (taken from [15]).

2.10 Plasma-Catalysis

Several different types of plasma have been investigated for dry reforming of CH_4 over the last 15 years, most notably, DBDs [16-22], atmospheric pressure plasma jets [23-25], gliding arc discharges [26, 27], coronas [28-30] and a microwave discharge [31]. Whilst the use of a plasma discharge alone has shown that syngas can be generated at low temperature and atmospheric pressure, the selectivities towards the desired products are typically low. In addition to syngas, significant amounts of higher hydrocarbons (C_2 – C_4), oxygenates, liquid hydrocarbons and polymers can be formed [18, 32]. The use of plasma in combination with heterogeneous catalysis can provide an attractive solution, as it combines the low temperature activity, fast response and compactness of the plasma reactors with the high selectivity of catalytic reactions.

The two main applications for plasma-catalysis are for destruction of pollutant molecules and hydrocarbon reforming for production of syngas. Generally, plasma-catalytic reactors have been shown to be effective for clean-up of nitrogen oxides (NO_x), chlorofluorocarbons (CFCs) and other volatile organic compounds (VOCs). Typically, the pollutants are in low concentrations (< 1000 ppm) in waste gas streams. The choice of catalyst and reactor configuration can lead to selective removal of the unwanted species, whilst lowering the operating temperature and giving an overall increased energy efficiency [33-37]. Several challenges arise for plasma-catalytic hydrocarbon reforming, where bulk gas conversion is required in order to obtain significant yields of H_2. Hydrocarbon decomposition via electron impact processes requires highly energetic electrons, particularly in the case of methane where C-H bond strength is highest. The efficiency of the reactor configuration is therefore of increasing importance in this application, so as not to waste energy through ineffective collisions with electrons of insufficient energy. The majority of electron impact processes should ideally result in ionisation and dissociation of gas molecules.

High reactant conversions can be obtained for dry reforming of methane with the use of a carrier gas to dilute CH_4 and CO_2 [21, 38]. Inert carrier gases cannot be considered inert in the plasma state due to the presence of high densities of electrons and excited gas molecules. Gases such as helium and argon have low breakdown voltages in comparison with CH_4 and CO_2, which can have a significant effect on the reaction chemistry due to increased ionisation in the plasma discharge. However, inert gases are expensive and would require separating from the reaction products. For these reasons, dry reforming of methane in plasma with the use of a diluent gas is not considered industrially relevant. This thesis focuses on the undiluted dry reforming of methane using plasma-catalysis.

2.10.1 Plasma-Catalyst Configurations

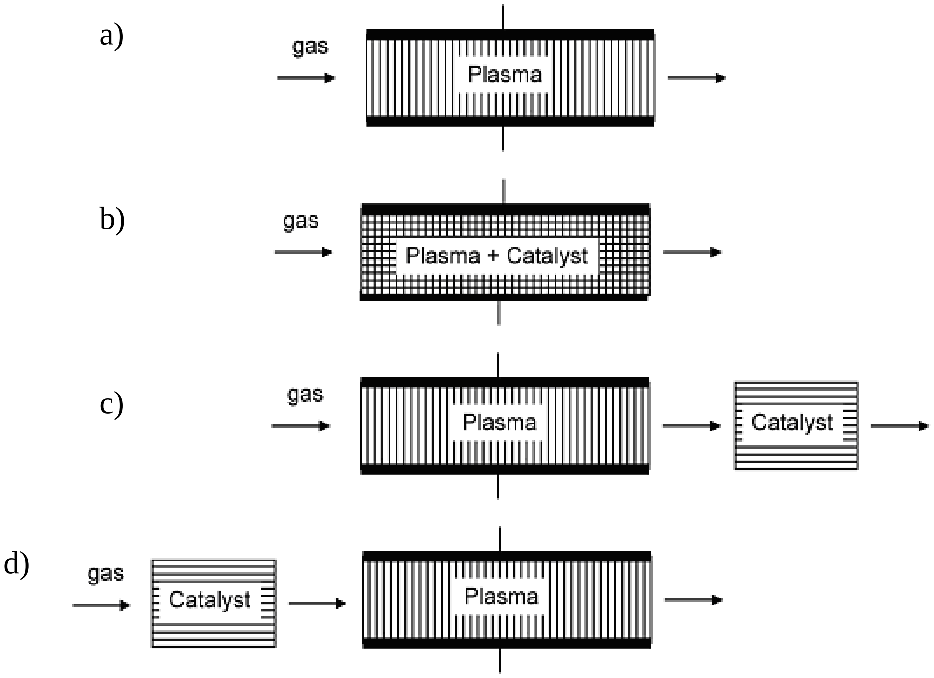

Figure 2.10: Schematic diagram of different plasma-catalyst configurations. Configuration (a) is a plasma-only system, (b) is a single-stage arrangement, (c) is a two-stage arrangement with plasma pre-processing and (d) is a two-stage process with plasma post-processing (modified from [36]).

Non-thermal plasma can be combined with catalysts in either single-stage or two-stage configurations, as illustrated in Figure 2.10. In a single-stage system, the catalyst is placed directly into the plasma discharge; this allows direct interaction between the plasma and catalyst. Reactions in this configuration will involve short-lived active species such as excited atoms and molecules, radicals, electrons and photons [36]. In a two-stage plasma-catalyst arrangement, the catalyst is positioned either downstream or upstream of the plasma discharge. The active species in these configurations are end products and/or long-lived intermediates resulting from the plasma or catalytic treatments in plasma pre-processing and post-processing respectively. The typical lifetimes of vibrationally excited species has been reported as 1 – 100 ns at atmospheric pressure, this is extremely short and therefore vibrational species would not be involved in reaction mechanisms involving a two-stage plasma-catalysis configuration [39]. For the purpose of the investigations in this thesis, plasma-catalysis refers to the single-stage process, where the catalysts are packed directly into the discharge gap of a coaxial DBD reactor.

2.10.2 Plasma-Catalyst Interactions

The interactions between plasma and catalyst become complex when the catalyst is placed directly in the plasma discharge. Both the chemical and physical properties of the plasma and catalyst can be modified by the presence of each other. A review by Chen et al. [33] considers each of these effects in detail. The influence of the catalyst on the plasma has been distinguished from the influence of the plasma on the catalyst. Figure 2.11 shows these effects, together with the potential enhancements to the reaction performance for VOC abatement. Similar enhancements are possible for plasma-catalytic dry reforming of CH_4.

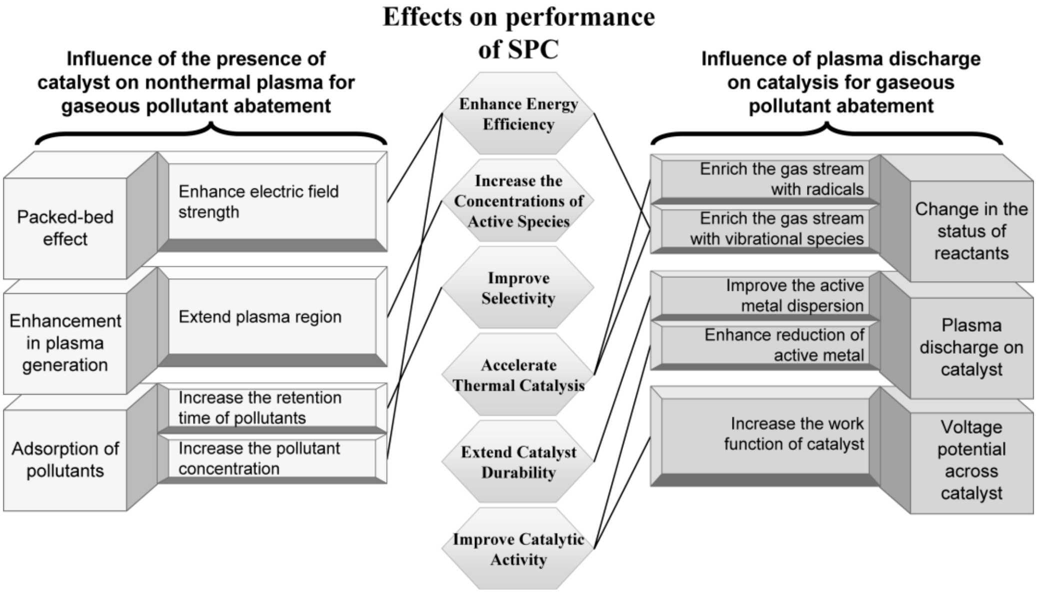

Figure 2.11: Diagram showing possible interactions in single-stage plasma-catalysis (SPC) with potential benefits for the reaction performance (taken from [33]).

Introducing catalyst pellets to a plasma discharge can have a similar effect to dielectric pellets in a packed-bed DBD reactor. If the dielectric properties and morphology of the selected catalyst are suitable, enhancement of the average electric field strength can occur, resulting in an enhanced efficiency of the chemical reactions taking place in the discharge. Catalyst surfaces can directly change the physical characteristics of the plasma discharge. Different discharge modes can be generated such as filamentary microdischarges and homogeneous surface discharges. This is discussed in detail in Chapter 3 of this thesis, where changes to the discharge modes are accompanied by changes to the dry reforming of CH_4 reaction performance. In addition, the plasma region can be extended if the discharge is able to propagate along a catalyst surface, this could lead to greater generation of active species in the plasma volume.

Surface adsorption within a plasma volume can have a significant contribution to improved reaction performance. When reactant gas molecules are adsorbed onto the catalyst surface, the retention time and concentration of those species in the plasma discharge will be enhanced. This could lead to an increased probability of reactive collisions with active species in the plasma volume. Appropriate selection of catalysts could therefore result in improved selectivities towards desired reaction products.

The plasma may facilitate catalytic surface reactions by enriching the gas stream with radicals and excited species. This is in contrast to thermal catalysis where gas molecules are mostly in the ground state when they are adsorbed onto a catalyst surface [39]. Non-thermal plasma produces ions, radicals and electronically excited species with internal energies that are often higher than the activation energies for thermal catalysis; these species can enhance plasma volume reactions. This can be attributed to the high threshold energies required to generate these species through electron impact processes. For ions and radicals, threshold energies of 5 – 20 eV are typically required and for electronically excited species, threshold energies are in the range of 1 – 10 eV. Vibrationally excited species are produced with lower threshold energies of 0.1 – 1 eV, hence the internal energies are too low to facilitate plasma volume reactions. However, activation energies for reactions involving vibrational species can be lowered when adsorbed to a catalyst surface. Consequently, the vibrational state can be a significant contributor to the acceleration of catalysis in a plasma system. This is not the case for relatively low energy rotationally excited species (0.01 – 0.1 eV), whose involvement in plasma-catalytic mechanisms can be disregarded. In addition, the energy required for surface adsorption of radical species may be lower than for adsorption of ground state gas molecules. This effect can also lead to enhancements in plasma-catalysis, in comparison with thermal catalysis where dissociative adsorption is often the rate-limiting step [39].

Exposure of a catalyst to a plasma discharge has been shown in many cases to modify the catalyst surface, this can be through reduction of the active metal and/or enhancements in metal dispersion. Studies in this area are reviewed in Chapter 5 of this thesis.

The integration of a catalyst in the plasma discharge results in a voltage potential across the catalyst bed. The voltage and resulting charges that accumulate on the surface could lead to changes in the work function of the metal catalyst. This effect has not been directly investigated in plasma systems. However, changes to the work function of metal films deposited on solid electrolytes have been shown to be strongly correlated with enhancements in catalytic activity. This effect has been investigated for several different metals in a technique known as electrochemical promotion of catalysis [39-41].

2.10.3 Synergistic Effects in Plasma-Catalysis

In several studies the combination of plasma and catalysts has been found to have synergistic effects. Figure 2.12 shows synergy in the plasma-catalytic dry reforming of CH_4 over Cu-Ni/γ-Al_2O_3 in a DBD reactor.

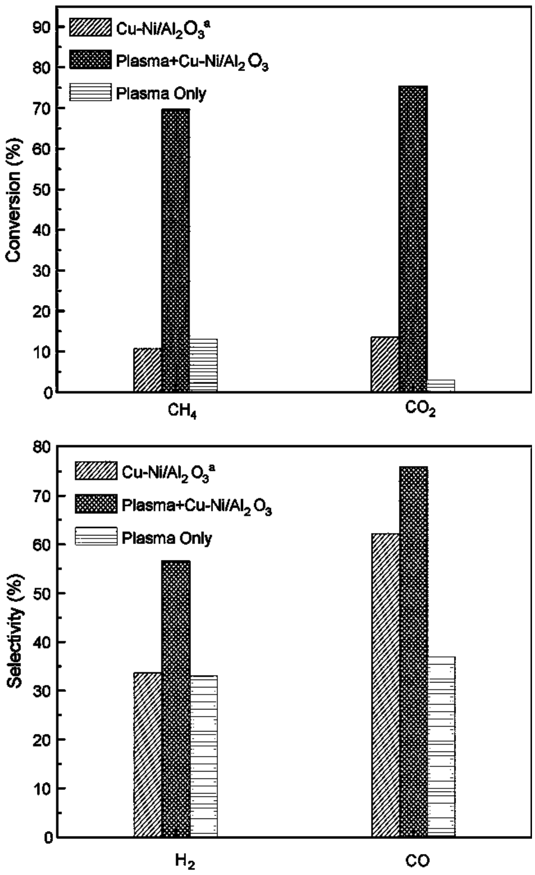

Figure 2.12: Results obtained by Zhang et al. [19] showing the synergistic effect of a DBD and catalyst on CO_2 reforming of CH_4 (total flow rate = 60 ml min^{-1}, CH_4:CO_2:Ar = 1:1:2, power = 60 W, 450 °C, (a) during catalyst only reaction, the catalyst bed was heated to 450 °C.

The effect was observed in the conversions of CH_4 and CO_2, where the result for the plasma-catalytic reaction was greater than the sum of the catalyst only or plasma only results. H_2 and CO selectivities were also enhanced by the use of plasma-catalysis. Synergy in plasma-catalysis has been demonstrated for several reactions including steam reforming of biogas over Ni/γ-Al_2O_3 catalysts [42], hydrogenation of CO_2 [43] and destruction of toluene [36], benzene [44] and hydrofluorocarbons [45]. However, the synergistic effect can not be generalised to all plasma-catalytic reactions as shown by contrasting results for the decomposition of dichloromethane, where the destruction in plasma-catalysis was displaced to lower temperatures in comparison with thermal catalysis, but a synergistic effect was not observed [46].

2.11 Plasma Power Measurement

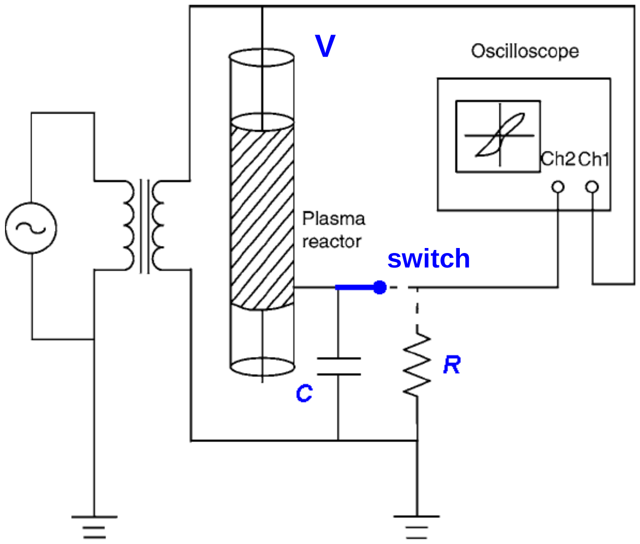

Figure 2.13: Schematic diagram of the circuit used for measuring the discharge power of a DBD reactor (taken from [47]).

There are two possible methods for determination of the discharge power in a plasma reactor. These require the measurement of the high voltage (V) and either the voltage across a resistor (R) or the voltage across a capacitor (C). Figure 2.13 shows the circuit used for measuring the discharge power throughout the work in this thesis, which is adaptable to both methods of power determination by the means of a switch.

<u>Current Method</u>

The first method measures the high voltage and the current through a resistor (hence, the current through the plasma reactor). Figure 2.14 shows typical waveforms for the high voltage and current in a DBD reactor, recorded using an oscilloscope. The spikes on the current waveform correspond to microdischarges of nanosecond duration.

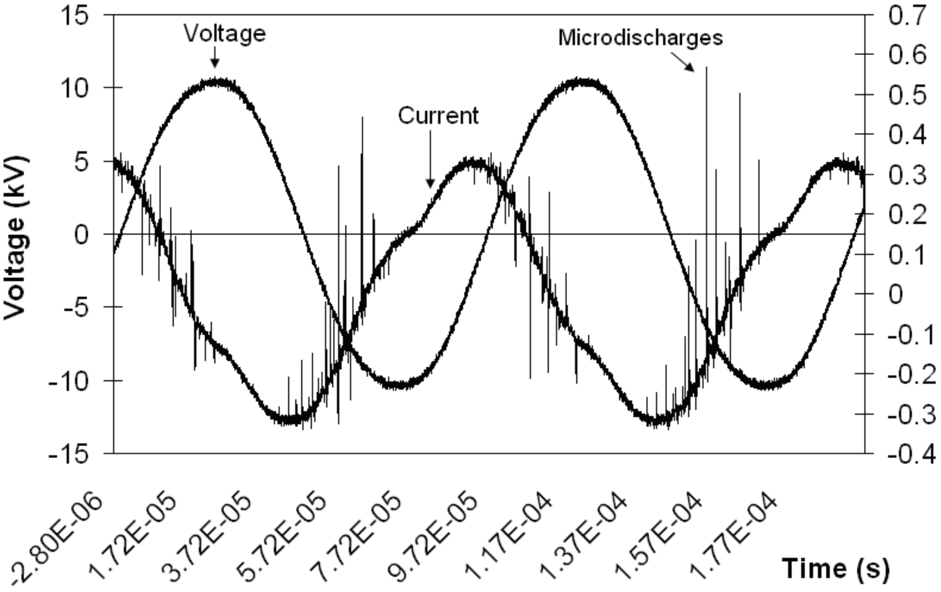

Figure 2.14: Voltage (V) and current (I) waveforms for a DBD.

The instantaneous power (p) at any given time can be calculated as shown in equation 2.1 by multiplying the voltage V(t) and current I(t). The current is found as shown in equation 2.2, where V_R is the voltage across the resistor and R is the resistance.

$$p = V(t) \times I(t) \qquad (2.1)$$

$$I(t) = \frac{V_R(t)}{R} \qquad (2.2)$$

The average power over a single period (T) can be found by integrating the discharge power over one cycle, where t_0 is the centre of the cycle:

$$P = \frac{1}{T}\int_{t_0-T/2}^{t_0+T/2} p \cdot dt = \frac{1}{T}\int_{t_0-T/2}^{t_0+T/2} V(t) \cdot I(t) \cdot dt = \frac{1}{T}\int_{t_0-T/2}^{t_0+T/2} \frac{V(t) \cdot V_R(t)}{R} \cdot dt \qquad (2.3)$$

This method is difficult to perform accurately due to the short duration of the microdischarge current pulses. Even when a high bandwidth sampling oscilloscope is used to record the current trace, overlap of the current spikes can lead to poor resolution and inaccurate power measurements [47].

Lissajous Method

This method was first described by Manley in 1943 [14] and is now considered to be the most accurate method for DBD power determination. It requires the measurement of the high voltage and the voltage (V_c) across a capacitor with an oscilloscope. This can be used to find the charge Q(t) accumulated as a result of current flow through the capacitor (of capacitance, C):

$$Q(t) = C \times V_c(t) \qquad (2.4)$$

By recording the values for Q(t) and V(t) over a series of regularly sampled points which capture the full cycle of the AC sine wave, we can plot the charge against high voltage (Fig. 2.14). The resulting plot is known as a Q-V Lissajous figure, the area of which is equal to the discharge power.

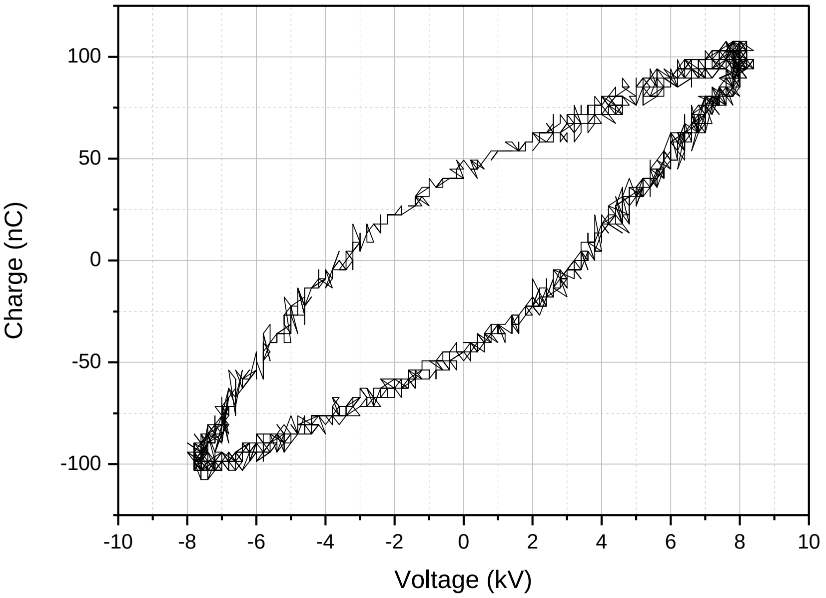

Figure 2.15: Q-V Lissajous figure.

The area of the Lissajous figure can be calculated as shown by the integration in equation 2.5 [14, 48]. The gradients and positions of the lines that make up the

Lissajous figure can be used to calculate some of the electrical parameters of the discharge, including the peak-peak charge, charge discharged, transferred charge and capacitance [14, 49-51].

$$W = \int_{t_0 - T/2}^{t_0 + T/2} V(t) \cdot C \cdot V_c(t) \cdot dt = \int_{t_0 - T/2}^{t_0 + T/2} V(t) \cdot dQ(t) \qquad (2.5)$$

This method has been employed throughout this work for accurate measurement of the discharge power and calculation of discharge electrical parameters. Details of these calculations can be found in Appendix B.

2.12 Gas Chromatography

Gas chromatography (GC) has been used for the analysis of complex gas mixtures during the experiments in this thesis. In general, chromatography refers to the chemical separation of mixtures into pure substances and can be used for both gases and liquids. Essentially, chromatography requires a ‘mobile phase’ (containing the mixture to be separated) and a ‘stationary phase’ through which the mobile phase can be eluted. In gas chromatography, the mobile phase is usually an inert carrier gas such as helium or argon. The carrier gas is continuously passed through a column containing the stationary phase.

GC columns originally consisted of a tube containing a packing of solid support material with various liquid or solid coatings depending on the type of mixture being separated. Most GCs now use capillary columns, which offer several advantages over packed columns. The stationary phase is coated uniformly on the inside of a capillary tube which eliminates problems associated with uneven packing. Capillary columns are made of a flexible material so that longer lengths can be wound into compact coils that allow for a better resolution of the separated gas mixture [52].

The mixture to be separated is injected into the column. Different gas species pass through the column at different rates depending on the strength of electrostatic interactions with the walls of the column. This causes the gas mixture to become separated into individual components that reach the end of the column and are detected at different times. By measuring the retention time of each species in the column, the component gases can be identified by comparison with chromatograms for known species. Retention times are affected by the gas concentration, flow rate and pressure as well as the column material and temperature [53], therefore selection of appropriate column materials and operating conditions are critical for resolution of the gas mixture.

The signal produced by each gas as it reaches the detector results in a peak on the chromatogram at a residence time that is characteristic for that gas. The peak area is proportional to the gas concentration. Examples of two gas chromatograms are shown in Figure 2.16.

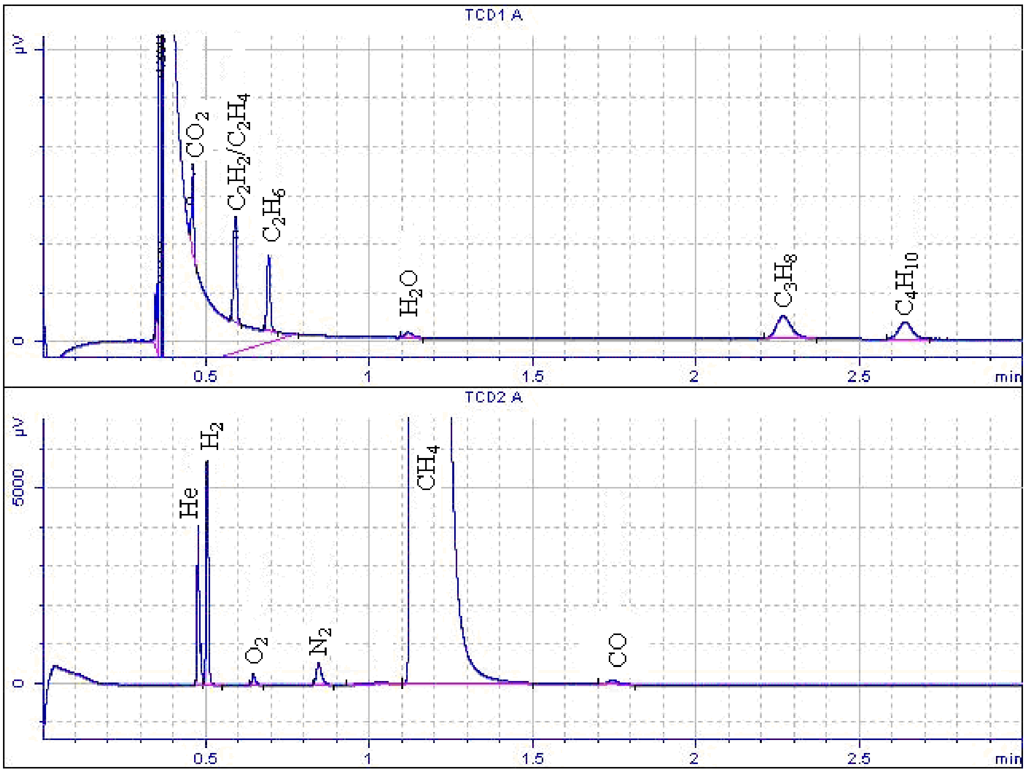

Figure 2.16: Gas chromatograms using Plot Q (top) and Molsieve 5A (bottom) columns in an Agilent 3000A micro-GC.

2.12.1 Micro-Gas Chromatography

Most of the gaseous analysis carried out in this thesis has used a micro-GC (Agilent 3000A with Cerity software) which is shown schematically in Figure 2.17. The micro-GC contains two columns of different materials that use different carrier gases. Both columns use thermal conductivity detection, allowing the analysis of the full range of gases present in the experiments (liquid products such as H_2O could not be measured by GC as they are damaging to the columns). Gas samples were pumped into the GC automatically and heated to a set temperature before reaching the temperature-controlled column. Micro-GCs have several advantages over conventional instruments, such as the small size of the required sample and of the instrument, which allow micro-GCs to be used for bench-top or portable applications. The run time for each sample is 3 minutes and samples can be run back to back without the need for column cool down, which is necessary with conventional GC instruments.

The micro-GC used for the experiments in this thesis was regularly calibrated over a wide range of concentrations for each of the gases of interest. CH_4 (10 – 100 %), CO_2 (10 – 60 %) and H_2 (1 – 100 %) were calibrated using dilutions of the pure gases (BOC Gases). CO (5 – 15 %) was calibrated using dilutions of a 15 % CO/N_2 mixture (SIP Analytical Ltd). C_2H_6 and C_3H_6 (1 – 10 %) were calibrated from dilution of the pure gases (Argo International Ltd). In addition, CO_2, H_2, CO, C_2, C_3 and C_4 hydrocarbons were regularly calibrated at concentrations of 0.05 % using a certified universal gas calibration standard (Agilent Technologies). Calibration curves (GC peak area vs. concentration) were plotted for each gas and were used to determine accurate gas concentrations from GC peak areas during the experiments.

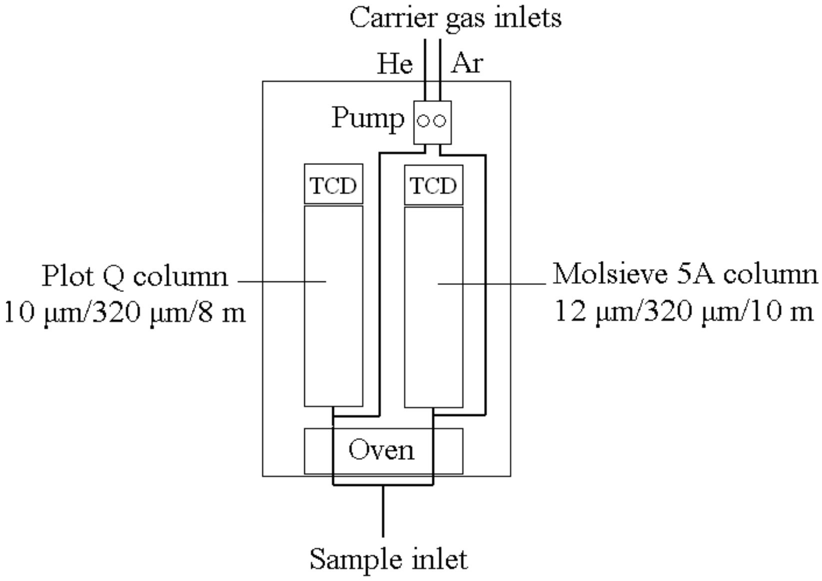

Figure 2.17: A schematic diagram of a two-channel Agilent 3000A micro-GC with thermal conductivity detection.

2.12.2 Thermal Conductivity Detection

Thermal conductivity detectors (TCD) can be used for the detection of any gases that are different in thermal conductivity to the carrier gas. TCD detectors consist of several filaments in a Wheatstone bridge arrangement as depicted in Figure 2.18. The column effluent and reference gas enter cells containing analytical filaments, R_3 and R_4. The other filaments that make up the bridge (R_1 and R_2) have fixed resistances therefore the change in voltage across the bridge is proportional to the change in resistance when a constant current is applied. The resistance of the analytical filament varies depending on the temperature, which is influenced by the thermal conduction of the gas being detected. The voltage across the bridge is measured and the signal is amplified to provide the GC response signal. Electrically heated tungsten-rhenium or platinum wires are typically employed for the analytical filaments [52, 53]. The filaments often have a non-linear response and therefore require individual calibration for each type of gas being analysed.

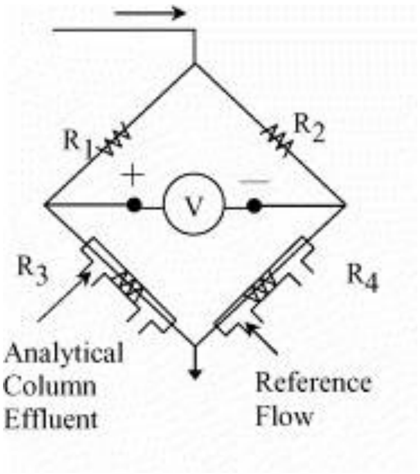

Figure 2.18: Schematic diagram of a typical thermal conductivity detector (taken from [54]).

2.12.3 Flame Ionisation Detection

Flame ionisation detectors (FIDs) are the most commonly used GC detectors for organic gases due to their high detection limits. In FID, the effluent gas from the column is mixed with H_2 and passed through a jet into a chamber, where it is mixed with air and ignited to produce a continuous flame. As different gases are eluted from the column, they pass into the flame and undergo combustion. A very small proportion (0.001 %) of the organic sample is ionised during combustion. The carbon ions are collected onto a polarised electrode, creating an electrical signal that is amplified to provide the GC response signal. A major limitation of this method is the inability to detect H_2 gas [52].

2.13 Fourier-Transform Infra-Red Spectroscopy

Fourier-transform infra-red (FTIR) spectroscopy is a universal technique that can be applied to the analysis of solids, liquids or gases. In this thesis, it has been used for the analysis of high concentrations of CH_4 and CO_2 (30 – 70 %) during the experiments carried out at AIST, Japan as detailed in Chapter 4. A short gas cell of 50 mm (Pike Technologies) was used to avoid signal saturation associated with high gas concentrations.

When IR radiation is incident on a gas sample, absorption will occur if the IR wavelength is resonant with the vibrational frequency of the molecule. The vibrational frequency remains the same but the amplitude changes as a result of the absorbed energy. The vibrational mode may correspond to stretching, rocking, wagging, scissoring or twisting motions of the functional groups [55]. The absorption of IR radiation for each type of chemical bond occurs at a characteristic wavenumber creating a “fingerprint” IR spectrum for each type of molecule. In order for absorptions to be IR active, there must be an interaction between IR radiation and a changing dipole moment. Homonuclear diatomic molecules such as H_2, N_2 and O_2 have no changing dipole moment as the molecule vibrates and are therefore IR inactive [56]. Polyatomic molecules have several fundamental modes of vibration that can give complex absorption spectra. For a molecule with N atoms, the total number of coordinates required to specify the position of all atoms is 3N and they are said to have 3N *degrees of freedom*. Since three coordinates are required to specify the centre of mass of the molecule, three degrees of freedom can be subtracted for translation of the whole molecule in space, three more degrees of freedom can express the rotation of the molecule about its axes, leaving 3N-6 vibrational modes for non-linear molecules. Linear molecules can rotate about only two axes and therefore have two rotational modes leaving 3N-5 vibrational modes.

The intensity of the signal on the IR spectrum is proportional to the concentration of that species, making FTIR spectroscopy suitable for both qualitative and quantitative analyses.

2.13.1 Vibrational Modes of CO_2

Carbon dioxide is a linear molecule and has 3(3) – 5 = 4 vibrational modes, two of which are degenerate resulting in the three modes shown in Figure 2.19. The symmetric stretch is IR inactive due to a lack of changing dipole moment, whilst the antisymmetric stretch and bending modes are IR active. The bending vibration has a degenerate mode that is perpendicular to the motion shown in Figure 2.17 (c). The IR spectrum of CO_2 will therefore contain two fundamental vibrational bands at 2349 cm^{-1} and 667 cm^{-1} [57]. These vibrational transitions are superimposed with rotational lines caused by the simultaneous vibration and rotation of the molecules; this gives rise to the fine structure of the IR vibration bands. In polyatomic molecules such as CO_2, it may happen that two vibrational levels belonging to different vibrations (or combinations thereof) may be accidently degenerate. This can lead to weak absorption bands at energies nearly equal to the addition of the energies corresponding to those vibrational modes, this is known as *Fermi resonance* [57]. During the work in Chapter 4 of this thesis, a calibrated rotational-vibrational transition at 3730 cm^{-1} was used to quantify the CO_2 concentrations in the gas mixtures. This is a Fermi resonant band caused by the perturbation of vibrational modes $v_1 + v_3$ [58]. Considerable care was taken not to confuse this absorption with potential interference from the fundamental absorption bands of water vapour in the same region.

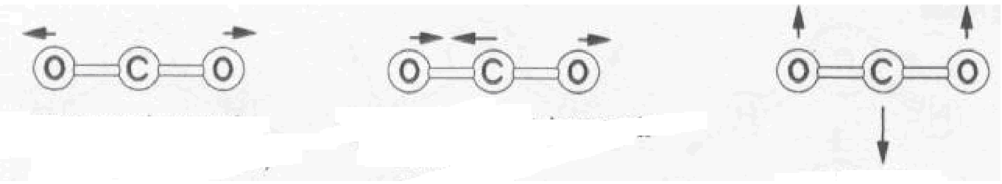

a) Symmetric stretch, $v_1 \approx 1330\ cm^{-1}$

b) Antisymmetric stretch $v_3 \approx 2349\ cm^{-1}$

c) Bend (doubly degenerate) $v_2 \approx 667\ cm^{-1}$

Figure 2.19: Vibrational modes and wavenumbers for the IR absorptions of CO_2 (taken from [59]).

2.13.2 Vibrational Modes of CH_4

Methane is a non-linear molecule and therefore has 3(5) – 6 = 9 modes of vibration. Of these nine modes, there are two triply degenerate modes which result in vibrational bands on the IR spectra at 3020 cm^{-1} and 1306 cm^{-1}, these correspond to v_3 and v_4 as shown on Figure 2.20. The remaining three vibrational modes correspond to symmetric motions and are therefore IR inactive (v_1 and v_2) [57]. During the work carried out in Chapter 4 of this thesis, a rotational-vibrational band at 3158 cm^{-1} was used to determine the CH_4 concentrations in the experimental gas mixtures.

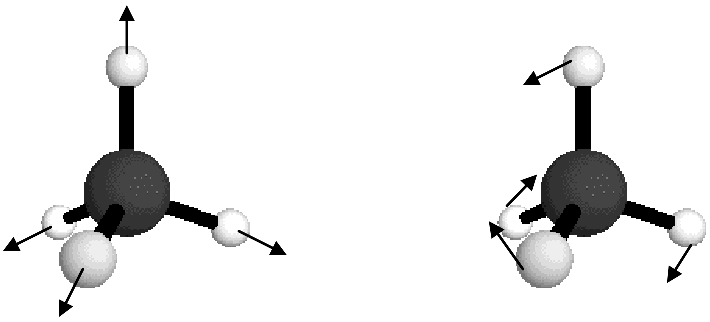

a) Symmetric stretch, $v_1 \approx 2914\ cm^{-1}$

b) Symmetric deformation (doubly degenerate), $v_2 \approx 1526\ cm^{-1}$.

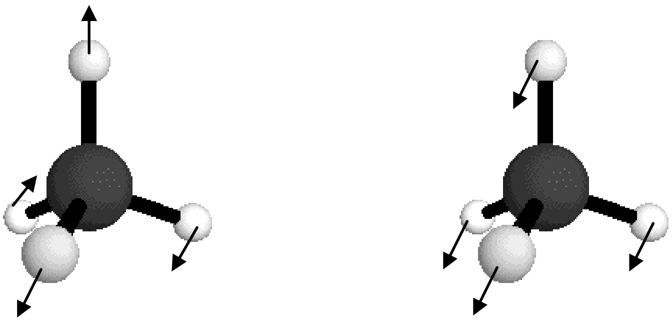

c) Asymmetric stretch (triply degenerate), $v_3 \approx 3020\ cm^{-1}$.

d) Asymmetric deformation (triply degenerate), $v_4 \approx 1306\ cm^{-1}$.

Figure 2.20: Vibrational modes and wavenumbers for the IR absorptions of CH_4 [57].

2.14 X-Ray Diffraction

X-Ray diffraction (XRD) is a technique used to characterise crystal structures at the atomic level. Under the influence of an electromagnetic field, the electrons in a crystal structure will oscillate at the incoming frequency. Destructive interference between the incident X-rays and electron oscillatory motion will occur in almost all directions. In a few characteristic directions, the waves will be in-phase and constructive interference will occur, resulting in X-ray reflection from the specimen surface at an angle θ (equal to the angle of incoming radiation) [60]. This is illustrated in Figure 2.21. The intensities of the reflected X-rays are dependent on the electron densities around the atoms. The types of atom and interatomic distances are specific to each crystal structure, resulting in a characteristic XRD pattern.

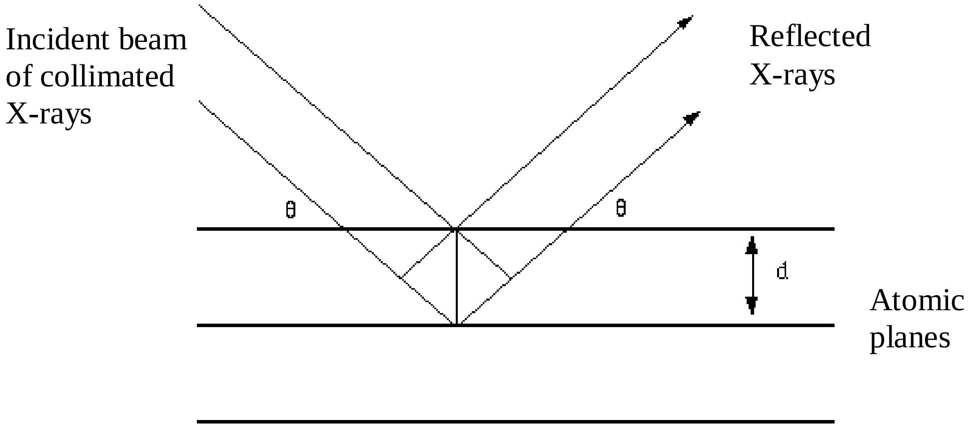

Figure 2.21: Reflection of X-rays at an angle (θ) from two planes of atoms with separation distance (d) in a crystalline solid.

To obtain an XRD pattern, a collimated beam of monochromatic X-rays is directed at a crystal surface. The X-ray source and a detector are automatically rotated about the sample surface to obtain the desired range of angles for the incoming and reflected radiation. For X-ray powder diffraction, the samples are prepared by grinding the solid into a fine homogeneous powder, which is pressed into a sample holder and smoothed. This produces a sample where the crystallites are distributed at random orientations. Only crystallites with atomic planes that are parallel with the smoothed surface will contribute to the reflected intensities.

The instrument used for XRD analysis in this work was a Philips X’Pert diffractometer with multi-channel detector and X’Pert Data Collector software.

The machine was set to detect 2θ in the range 5 – 100 °. XRD was performed at room temperature with a scanning speed of 0.042 ° min^{-1}. The source of radiation for the XRD came from a copper anode, which emits radiation at a wavelength of 1.45060 Å. X'Pert Highscore Plus Database was utilised for comparison of experimental XRD patterns with those of known species.

2.15 Scanning Electron Microscopy

Scanning electron microscopy (SEM) has been used in this thesis to produce high resolution images of catalyst surfaces for the work in Chapters 5 and 6. SEM uses an accelerated beam of electrons ($\lambda \approx 0.12$ Å) as the illuminating source for producing images of surface structures. Resolution of structures as small as 10 nm can be resolved by SEM [61].

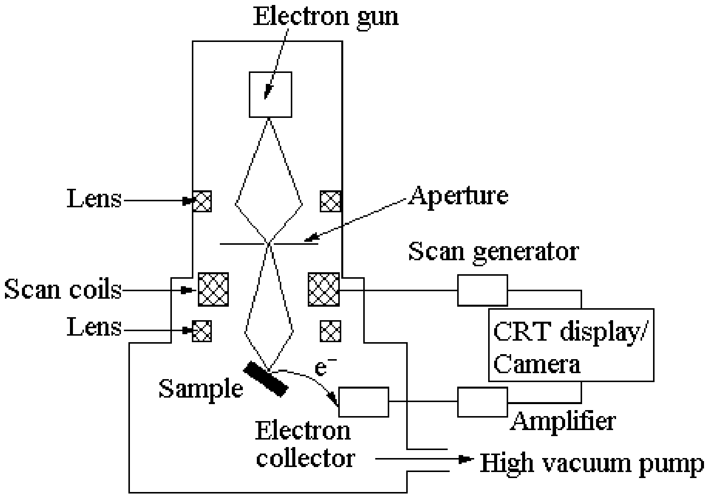

Figure 2.22: Schematic of a scanning electron microscope (taken from [61]).

Figure 2.22 shows a typical environmental scanning electron microscope (ESEM). The electron source is a thermionic tungsten filament that emits high energy electrons (1 – 30 keV) when a voltage is applied. Magnetic lenses focus electrons through an aperture to produce an intense electron beam. The scanning coils deflect the beam causing it to sweep a rectangular area of the sample in a grid fashion at a set speed. When the beam strikes the sample, high energy backscattered electrons are emitted as well as relatively low energy secondary electrons. These signals are detected, amplified and fed to a cathode ray tube to produce an image of the surface structure [62]. The instrument used for imaging in these experiments was an FEI Quanta 200 ESEM and was operated at a pressure of 0.60 Torr. The high vacuum conditions prevent collisions between electrons and atmospheric gas molecules that would interfere with the imaging.

2.16 Elemental Analysis

Elemental analysis of both liquid and powder samples has been performed using a Carlo Erba EA 1108 elemental analyser. A micro-sample (milligram quantities) is introduced into a combustion chamber in a flow of helium carrier gas. Complete combustion of the sample in high purity O_2 converts carbon into CO_2, hydrogen into H_2O, nitrogen into N_2 and NO_x and sulphur into SO_2. Subsequently the combustion products are passed over a removable bed of copper, in the second part of a two tier furnace as shown in Figure 2.23. The purpose of the copper is to remove the remaining O_2 and convert any NO_x combustion products into N_2. The remaining gases are then passed through a GC column and identified quantitatively using thermal conductivity detection [63].

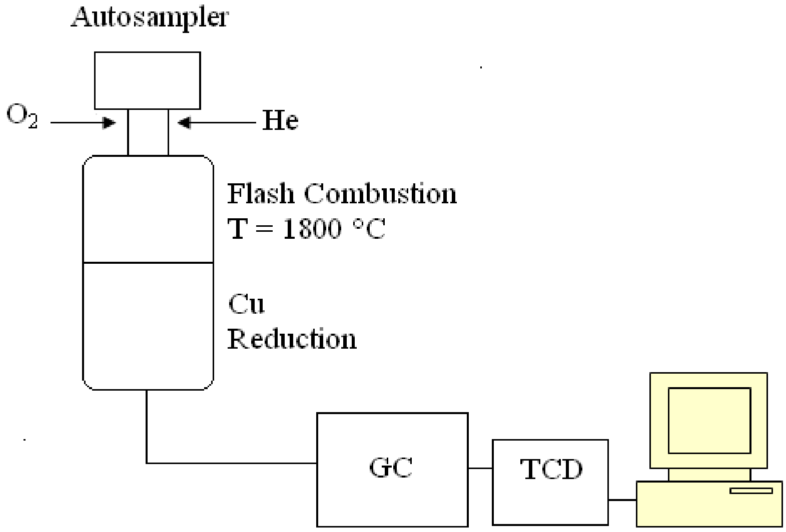

Figure 2.23: Schematic diagram of a CHNS elemental analyser.

2.17 References

1. Conrads, H.and Schmidt, M., *Plasma Generation and Plasma Sources.* Plasma Sources Sci. T., 2000. **9**(4): p. 441-454.
2. Graham, B., *Technological Plasmas.* Phys. World, 2001. **14**(3): p. 31-36.
3. Fridman, A., *Plasma Chemistry*. 2008, New York: Cambridge University Press.
4. Eliasson, B.and Kogelschatz, U., *Nonequilibrium Volume Plasma Chemical-Processing.* IEEE T. Plasma Sci., 1991. **19**(6): p. 1063-1077.
5. Tonks, L., *Birth of Plasma.* Am. J. Phys., 1967. **35**(9): p. 857-&.
6. Kawai, Y., Ikegami, H., Sato, N., Matsuda, A., Uchino, K., Kuzuya, M.and Mizuno, A., eds. *Industrial Plasma Technology. Applications from Environmental to Energy Technologies.* 2010, Wiley-VCH: Weinheim.
7. Kogelschatz, U., Eliasson, B.and Egli, W., *From Ozone Generators to Flat Television Screens: History and Future Potential of Dielectric-Barrier Discharges.* Pure Appl. Chem., 1999. **71**(10): p. 1819-1828.
8. Hippler, R., Pfau, S., Schmidt, M.and Schoenbach, K.H., *Low Temperature Plasma Physics*. 2001, Berlin: Wiley-VCH.
9. Fridman, A.and Kennedy, L.A., *Plasma Physics and Engineering*. 2004, New York: Taylor & Francis.
10. Chang, J.S., Lawless, P.A.and Yamamoto, T., *Corona Discharge Processes.* IEEE T. Plasma Sci., 1991. **19**(6): p. 1152-66.
11. Lieberman, M.A.and Lichtenberg, A.J., *Principles of Plasma Discharges and Materials Processing*. 2nd ed. 2005, Hoboken, New Jersey: John Wiley & Sons, Inc.
12. Liu, G.H., Li, Y.L., Chu, W., Shi, X.Y., Dai, X.Y.and Yin, Y.X., *Plasma-Assisted Preparation of Ni/SiO_2 Catalyst Using Atmospheric High Frequency Cold Plasma Jet.* Catal. Commun., 2008. **9**(6): p. 1087-1091.
13. Kogelschatz, U., *Filamentary, Patterned, and Diffuse Barrier Discharges.* IEEE T. Plasma Sci., 2002. **30**(4): p. 1400-1408.
14. Manley, T.C., *The Electric Characteristics of the Ozonator Discharge.* Trans. Electrochem. Soc., 1943. **84**: p. 83-96.
15. McAdams, R., *Prospects for Non-Thermal Atmospheric Plasmas for Pollution Abatement.* J. Phys. D Appl. Phys., 2001. **34**(18): p. 2810-2821.
16. Zhou, L.M., Xue, B., Kogelschatz, U.and Eliasson, B., *Nonequilibrium Plasma Reforming of Greenhouse Gases to Synthesis Gas.* Energ. Fuel., 1998. **12**: p. 1191-1199.
17. Huang, A., Xia, G., Wang, J., Suib, S.L., Hayashi, Y.and Matsumoto, H., *CO_2 Reforming of CH_4 by Atmospheric Pressure AC Discharge Plasmas.* J. Catal., 1999. **189**: p. 349-359.
18. Liu, C.J., Xue, B.Z., Eliasson, B., He, F., Li, Y.and Xu, G.H., *Methane Conversion to Higher Hydrocarbons in the Presence of Carbon Dioxide Using Dielectric-Barrier Discharge Plasmas.* Plasma Chem. Plasma P., 2001. **21**(3): p. 301-310.
19. Zhang, A.-J., Zhu, A.-M., Guo, J., Xu, Y.and Shi, C., *Conversion of Greenhouse Gases into Syngas via Combined Effects of Discharge Activation and Catalysis.* Chem Eng. J., 2009. **156**: p. 601-606.
20. Futamura, S.and Annadurai, G., *Effects of Temperature, Voltage Properties, and Initial Gas Composition on the Plasma Reforming of*

Aliphatic Hydrocarbons with CO_2. IEEE T. Ind. Appl., 2008. **44**(1): p. 53-60.

21. Brock, S.L., Shimojo, T., Suib, S.L., Hayashi, Y.and Matsumoto, H., *Application of Non-Thermal Atmospheric Pressure AC Plasmas to the Carbon Dioxide Reforming of Methane.* Res. Chem. Intermediat., 2002. **28**(1): p. 13-24.
22. Sarmiento, B., Brey, J.J., Viera, I.G., Gonzalez-Elipe, A.R., Cotrino, J.and Rico, V.J., *Hydrogen Production by Reforming of Hydrocarbons and Alcohols in a Dielectric Barrier Discharge.* J. Power Sources, 2007. **169**(1): p. 140-143.
23. Li, X., Bai, M.-G., Tao, X.-M., Shang, S.-Y., Yin, Y.-X.and Dai, X.-Y., *Carbon Dioxide Reforming of Methane to Synthesis Gas by an Atmospheric Pressure Plasma Jet.* Journal of Fuel Chemistry and Technology, 2010. **38**(2): p. 195-200.
24. Ghorbanzadeh, A.M.and Modarresi, H., *Carbon Dioxide Reforming of Methane by Pulsed Glow Discharge at Atmospheric Pressure: The Effect of Pulse Compression.* J. Appl. Phys., 2007. **101**(12).
25. Chen, Q., Dai, W., Tao, X.M., Yu, H., Dai, X.Y.and Yin, Y.X., *CO_2 Reforming of CH_4 by Atmospheric Pressure Abnormal Glow Plasma.* Plasma Sci. Technol., 2006. **8**(2): p. 181-184.
26. Rueangjitt, N., Akarawitoo, C., Sreethawong, T.and Chavadej, S., *Reforming of CO_2-Containing Natural Gas Using an AC Gliding Arc System: Effect of Gas Components in Natural Gas.* Plasma Chem. Plasma P., 2007. **27**(5): p. 559-576.
27. Bo, Z., Yan, J.H., Li, X.D., Chi, Y.and Cen, K.F., *Plasma Assisted Dry Methane Reforming Using Gliding Arc Gas Discharge: Effect of Feed Gases Proportion.* Int. J. Hydrogen Energ., 2008. **33**(20): p. 5545-5553.
28. Li, M.W., Tian, Y.L.and Xu, G.H., *Characteristics of Carbon Dioxide Reforming of Methane via Alternating Current (AC) Corona Plasma Reactions.* Energ. Fuel., 2007. **21**(4): p. 2335-2339.
29. Mutaf-Yardimci, O., Saveliev, A.V., Fridman, A.A.and Kennedy, L.A., *Employing Plasma as Catalyst in Hydrogen Production.* Int. J. Hydrogen Energ., 1998. **23**(12): p. 1109-1111.
30. Yao, S.L., Okumoto, M., Nakayama, A.and Suzuki, E., *Plasma Reforming and Coupling of Methane with Carbon Dioxide.* Energ. Fuel., 2001. **15**: p. 1295-1299.
31. Zhang, J.Q., Zhang, J.S., Yang, Y.J.and Liu, Q., *Oxidative Coupling and Reforming of Methane with Carbon Dioxide Using a Pulsed Microwave Plasma Under Atmospheric Pressure.* Energ. Fuel., 2003. **17**(1): p. 54-59.
32. Goujard, V., Tatibouet, J.M.and Batiot-Dupeyrat, C., *Use of a Non-Thermal Plasma for the Production of Synthesis Gas from Biogas.* Appl. Catal. A Gen., 2009. **353**(2): p. 228-235.
33. Chen, H.L., Lee, H.M., Chen, S.H., Chang, M.B., Yu, S.J.and Li, S.N., *Removal of Volatile Organic Compounds by Single-Stage and Two-Stage Plasma Catalysis Systems: A Review of the Performance Enhancement Mechanisms, Current Status, and Suitable Applications.* Environ. Sci. Technol., 2009. **43**(7): p. 2216-2227.
34. Kim, H.-H., Prieto, G., Takashima, K., Katsura, S.and Mizuno, A., *Performance Evaluation of Discharge Plasma Process for Gaseous Pollutant Removal.* J. Electrostat., 2002. **55**: p. 25-41.

35. Van Durme, J., Dewulf, J., Leys, C.and Van Langenhove, H., *Combining Non-Thermal Plasma with Heterogeneous Catalysis in Waste Gas Treatment: A Review.* Appl. Catal. B Environ., 2008. **78**(3-4): p. 324-333.
36. Whitehead, J.C., *Plasma Catalysis: A Solution for Environmental Problems.* Pure Appl. Chem., 2010. **82**(6): p. 1329-1336.
37. Mizuno, A., *Industrial Applications of Atmospheric Non-Thermal Plasma in Environmental Remediation.* Plasma Phys. Control Fusion, 2007. **49**: p. A1-A15.
38. Wang, Q., Yan, B.-H., Jin, Y.and Cheng, Y., *Dry Reforming of Methane in a Dielectric Barrier Discharge Reactor with* Ni/Al_2O_3 *Catalyst: Interaction of Catalyst and Plasma.* Energy & Fuels, 2009. **23**(8): p. 4196-4201.
39. Chen, H.L., Lee, H.M., Chen, S.H., Chao, Y.and Chang, M.B., *Review of Plasma Catalysis on Hydrocarbon Reforming for Hydrogen Production-Interaction, Integration and Prospects.* Appl. Catal. B Environ, 2008. **85**: p. 1-9.
40. Nicole, J., Tsiplakides, D., Wodiunig, S.and Comninellis, C., *Activation of Catalyst for Gas-Phase Combustion by Electrochemical Pretreatment.* J. Electrochem. Soc., 1997. **144**(12): p. L312-L314.
41. Poppe, J., Volkening, S., Schaak, A., Schutz, E., Janek, J.and Imbihl, R., *Electrochemical Promotion of Catalytic CO Oxidation on Pt/YSZ Catalysts Under Low Pressure Conditions.* Phys. Chem. Chem. Phys., 1999. **1**(22): p. 5241-5249.
42. Nozaki, T., Hiroyuki, T.and Okazaki, K., *Hydrogen Enrichment of Low-Calorific Fuels Using Barrier Discharge Enhanced* $Ni/\gamma\text{-}Al_2O_3$ *Bed Reactor: Thermal and Nonthermal Effect of Nonequilibrium Plasma.* Energ. Fuel., 2006. **20**(1): p. 339-345.
43. Eliasson, B., Kogelschatz, U., Xue, B.and Zhou, L.-M., *Hydrogenation of Carbon Dioxide to Methanol with a Discharge-Activated Catalyst.* Ind. Eng. Chem. Res., 1998. **37**: p. 3350-3357.
44. Futamura, S., Einaga, H., HKabashima, H.and Hwan, L.Y., *Synergistic Effect of Silent Discharge Plasma and Catalysts on Benzene Decomposition.* Catal. Today, 2004: p. 89-95.
45. Futamura, S.and Gurusamy, A., *Synergy of Nonthermal Plasma and Catalysts in the Decomposition of Fluorinated Hydrocarbons.* J. Electrostat., 2005. **63**: p. 949-954.
46. Wallis, A.E., *Plasma-Catalysis for the Removal of Gaseous Pollutants*, in *School of Chemistry*. 2005, University of Manchester.
47. Gorry, P., *Power Measurement in a DBD Plasma Reactor*. 2009, The University of Manchester (can be found in Appendix A).
48. Feng, R., Castle, G.S.P.and Jayaram, S., *Automated System for Power Measurement in the Silent Discharge.* IEEE T. Ind. Appl., 1998. **34**(3): p. 563-570.
49. Falkenstein, Z.and Coogan, J.C., *Microdischarge Behaviour in the Silent Discharge of Nitrogen-Oxygen and Water-Air Mixtures.* J. Phys. D Appl. Phys., 1997. **30**: p. 817-825.
50. Valdivia-Barrientos, R., Pacheco-Sotelo, J., Pacheco-Pacheco, M., Benitez-Read, J.S.and Lopez-Callejas, R., *Analysis and Electrical Modelling of a Cylindrical DBD Configuration at Different Operating Frequencies.* Plasma Sources Sci. T., 2006. **15**: p. 237-245.

51. Wagner, H.-E., Brandenburg, R., Kozlov, K.V., Sonnenfeld, A., Michel, P.and Behnke, J.F., *The Barrier Discharge: Basic Properties and Applications to Surface Treatment.* Vacuum, 2003. **71**: p. 417-436.
52. Baugh, P.J., *Gas Chromatography A Practical Approach*. The Practical Approach Series, ed. D. Rickwood and B.D. Hames. 1993, Oxford: Oxford University Press.
53. Stock, R.and Rice, C.B.F., *Chromatographic Methods*. 2 ed. 1967, London: Chapman and Hall Ltd.
54. Cruz, D., Chang, J.P., Showalter, S.K., Gelbard, F., Manginell, R.P.and Blain, M.G., *Microfabricated Thermal Conductivity Detector for the Micro-ChemLab(TM).* Sensors and Actuators B: Chemical, 2007. **121**(2): p. 414-422.
55. Higson, S.P.J., *Analytical Chemistry*. 2004, New York: Oxford University Press Inc.
56. George, B.and McIntyre, P., *Infrared Spectroscopy*. Analytical Chemistry by Open Learning, ed. D.J. Mowthorpe. 1987, London: John Wiley and Sons.
57. Herzberg, G., *Infrared and Raman Spectra of Polyatomic Molecules*. Vol. 2. 1945, New York: D.Van Nostrand Company, Inc.
58. Joly, L., Parvitte, B., Zeninari, V.and Durry, G., *Development of a Compact CO_2 Sensor Open to the Atmosphere and Based on Near-Infrared Laser Technology at 2.68 μm.* Appl. Phys. B Lasers O., 2007. **86**(4): p. 743-748.
59. Banwell, C.and McCash, E., *Fundamentals of Molecular Spectroscopy*. 4th ed. 1994: McGraw-Hill International Ltd.
60. Hammond, C., *The Basics of Crystallography and Diffraction*. 2009, New York: Oxford University Press.
61. Leeds, S.M., *Characterisation of the Gas-Phase Environment in a Microwave Plasma Enhanced Diamond Chemical Vapour Deposition Reactor using Molecular Beam Mass Spectrometry*. 1999, University of Bristol.
62. Goodhew, P.J., Humphreys, J.and Beanland, R., *Electron Microscopy and Analysis*. 3rd ed. 2001, London: Taylor and Francis.
63. Thompson, M., *CHNS Elemental Analysers.* Royal Society of Chemistry AMC Technical Briefs, 2008. **29**.

3. Dry Reforming of Methane: Effect of Packing Materials in a DBD Reactor

3.1 Introduction

When introducing a catalyst into a plasma discharge, the influence that the dielectric properties of the catalyst have on plasma generation must be considered for dry reforming of CH_4, in addition to other operating parameters such as specific input energy (SIE), CH_4/CO_2 molar ratio, gas temperature, operating pressure and DBD configuration. Catalysts that have been investigated in coaxial DBD reactors for dry reforming of methane include nickel/alumina [1, 2], various zeolites [3-6], metal-coated monoliths [7] and ceramic foams [8]. Table 3.0 summarises some of the conditions used and the results of these previous studies. The use of a Ni/Al_2O_3 catalyst by Song et al. [1] has been shown to enhance reactant conversions. However, the selectivity towards H_2 decreased compared to the reaction with plasma and Al_2O_3 (without the 'active' metal). The use of zeolites has been shown by several authors to be effective for enhancing selectivities towards light hydrocarbon products, particularly C_2 – C_4 species. Zeolites are known for their adsorbent properties, these are beneficial to plasma reactions because it allows species to be adsorbed onto the zeolite surface or inside the pore structure, which can increase the residence time of the reactant species in the plasma discharge. This can lead to an increased probability of successful collisions with active plasma species. Interestingly, the selectivity towards higher hydrocarbons (C_5+) was reduced and the formation of plasma polymerised films was inhibited by the use of zeolites with a small pore size (0.42 nm). The authors suggested that this was due to shape-selectivity, where long chain hydrocarbon formation is limited by a lack of available space in the zeolite pores [4].

This chapter investigates the effects of different reactor packing materials on both the chemical and physical properties of plasma-assisted dry reforming of methane in a coaxial DBD reactor. The materials studied include quartz wool, alumina beads (γ-Al_2O_3), barium titanate beads ($BaTiO_3$), zeolite 3A beads and titanium dioxide beads (TiO_2), as well as the reaction in the absence of any packing material. Zeolite 3A is a potassium exchanged zeolite with a molecular composition of $Na_{35.4}K_{60.0}Al_{95.4}Si_{96.6}O_{384}\cdot 160\ H_2O$ [9]. It consists of a three-dimensional cage structure with pores running perpendicular in the x, y and z planes, which are 0.3 nm in diameter. Negative charges that exist inside the zeolite pore structure are neutralised by freely moving protons. These constitute acidic sites that under thermal conditions can catalyse the isomerisation and cracking of hydrocarbons. Consequently, zeolites have important industrial uses as cracking catalysts in oil refining [10]. The other materials studied in this chapter do not exhibit catalytic activity in the traditional sense; however, they do have different dielectric constants and morphologies which can influence the plasma discharge, as well as different adsorbent properties which will affect the residence time of gas molecules in the plasma discharge. A second DBD reactor configuration, known as a packed-bed DBD reactor containing $BaTiO_3$ beads as the dielectric material, has also been investigated. Comparisons have been made between the performances of the dry reforming of methane reaction using the two different reactor configurations.

The analysis of plasma electrical signals has been carried out for the characterisation of discharge modes when quartz wool and zeolite 3A are present in the plasma discharge, as well as for no packing material. In addition, images of plasma generation on several different surfaces have been taken using a microscope-intensified charge coupled device (ICCD) camera to demonstrate the observable effects of reactor packing materials on plasma generation.

Catalyst	**Power Range (W)**	**Temp. (°C)**	**SIE[a] (kJ L^{-1})**	**CH_4 Conversion (%)**	**CO_2 Conversion (%)**	**H_2 Selectivity (%)**	**CO Selectivity (%)**	**H_2/CO**	**Other Identified Products**	**Ref.**
2 – 10 wt. % Ni/γ-Al_2O_3	130	-	260	55.2 – 55.7	32.6 – 33.5	51.9 – 53.5	60.6 – 63.9	1.0 – 1.1	C_2 – C_4 hydrocarbons	[1]
Zeolite A	100 – 500	150	30 – 150	6.0 – 63.6	2.0 – 39.4	23 – 50[a]	43 – 50[b]	0.7 – 1.6	C_2 – C_5+ hydrocarbons	[3]
Zeolite HY	100 – 500	150	30 – 150	12.5 – 63.0	2.6 – 37.0	-	41.8 – 46.1	0.9 – 1.0	C_2 – C_5+ hydrocarbons	[4]
Zeolite NaX	500	150	37.5 – 200	60 – 22 [b]	50 – 18[b]	-	40.1 – 44.9	-	C_2 – C_5+ hydrocarbons	[5]
Zeolite NaY	500	150	150	66.6	39.9	38.6[a]	42.7	-	C_2 – C_5+ hydrocarbons	[6]
Quartz fleece	500	150	150	68.4	39.7	36.4[a]	46.0	-		
Perovskite ($LaNiO_3$)-coated monolith	12	RT	32	19.2	13.3	-	40.5	1.1	C_2 – C_5+ hydrocarbons, methanol, ethanol, acetone	[7]

Table 3.0: Comparison of plasma-catalytic performances for dry reforming of CH_4 in coaxial DBD reactors (CH_4/CO_2 = 1, pressure = 1 bar), [a] indicates where data has been calculated and [b] indicates where data has been taken from graphs, RT = room temperature.

3.2 Experimental Section

Figure 3.0 shows a schematic representation of the experimental set-up used in this investigation.

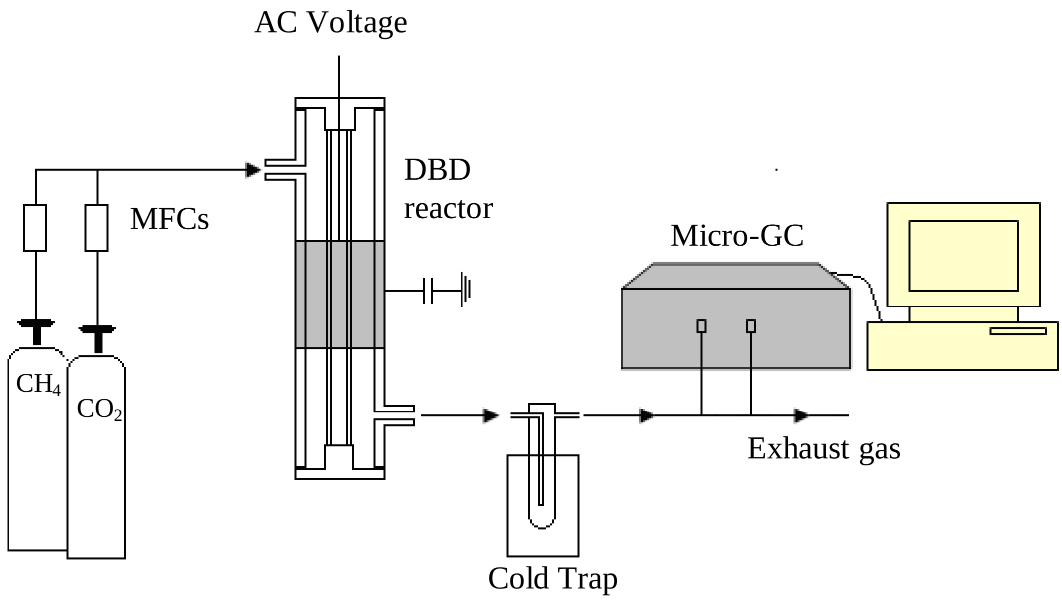

Figure 3.0: Schematic diagram of the experimental set-up used for plasma-assisted dry reforming of methane (MFCs = mass flow controllers).

CH_4 and CO_2 (BOC Gases, 99.9 %) were fed into the reactor at a pressure of 1 bar and a total flow rate of 50 ml min^{-1}. All experiments were conducted at a mixing ratio of CH_4/CO_2 = 1. Gas flow rates were controlled by previously calibrated mass flow controllers (MKS Instruments) and gas mixtures were stabilised before the plasma was turned on. The experiments have been carried out in a coaxial DBD reactor (Figure 3.1) with a double dielectric barrier to prevent any contribution from the metal electrodes on the reaction performance. The reactor consisted of two coaxial quartz tubes with stainless steel (SS) mesh electrodes of 5.7 cm length, which are positioned on the inside of the inner tube and outside of the outer tube. Polytetrafluoroethylene (PTFE) plugs with rubber o-rings were used to seal the reactor at each end. When assembled, the reactor had a discharge gap of 4.5 mm. The materials investigated were packed inside the discharge gap and held in place with quartz wool as shown in Figure 3.1 (b), so that the quartz wool was positioned outside of the discharge region. The materials investigated in this chapter are quartz wool (Fisher Scientific), γ-Al_2O_3 beads (4 mm diameter), zeolite 3A beads (2 mm diameter, Fisher Scientific), $BaTiO_3$ beads (4 mm diameter) and TiO_2 pellets (5 mm, Alfa Aesar). Each of the reactor packing materials (except quartz wool) was baked at 600 °C for 3 hours prior to use, to remove any adsorbed gas species. During the experiments, the material was packed into the reactor so that it filled the entire discharge volume of 16.5 cm^3.

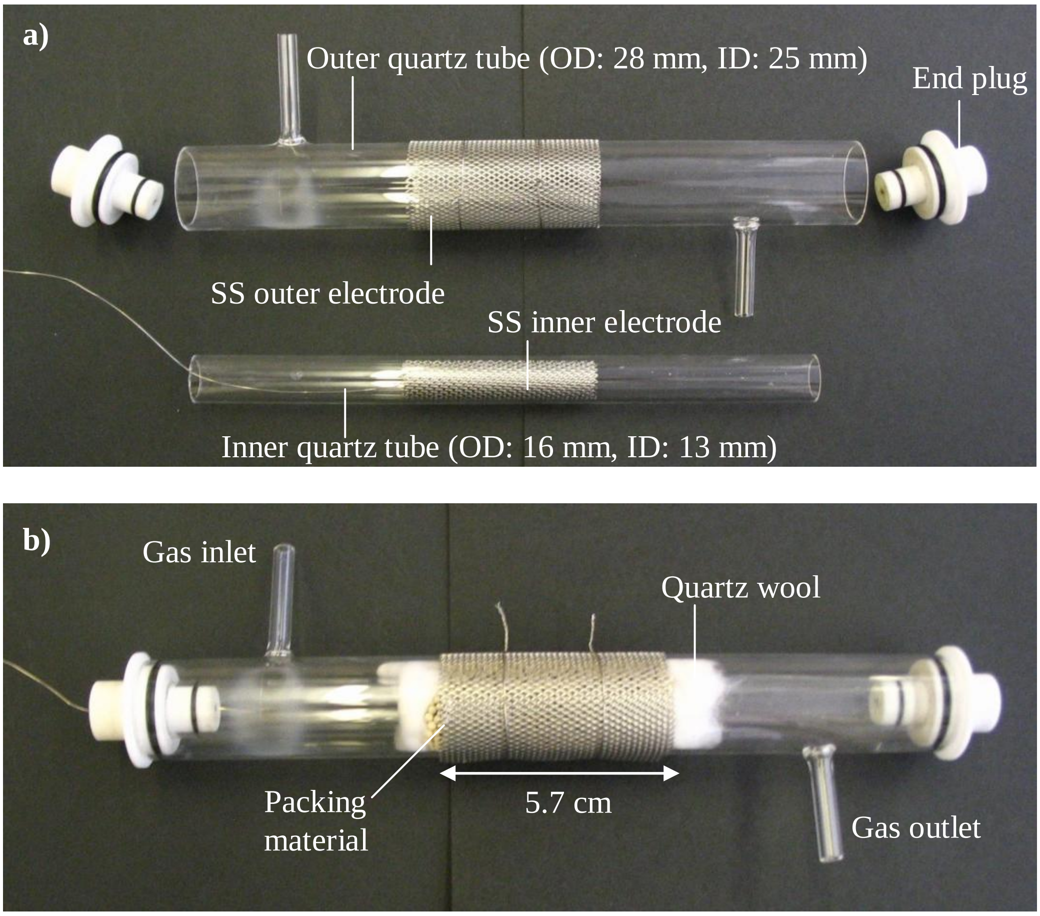

Figure 3.1: Coaxial DBD reactor a) dissembled and b) assembled with packing material in the discharge gap held in place by quartz wool.

The second reactor configuration investigated was a $BaTiO_3$ packed-bed DBD reactor, consisting of two parallel plate stainless steel electrodes positioned 4.2 cm apart, inside a quartz tube as shown in Figure 3.2. The area between the electrodes was packed with $BaTiO_3$ beads (4 mm) that were baked at 600 °C prior to each experiment to remove any adsorbed species.

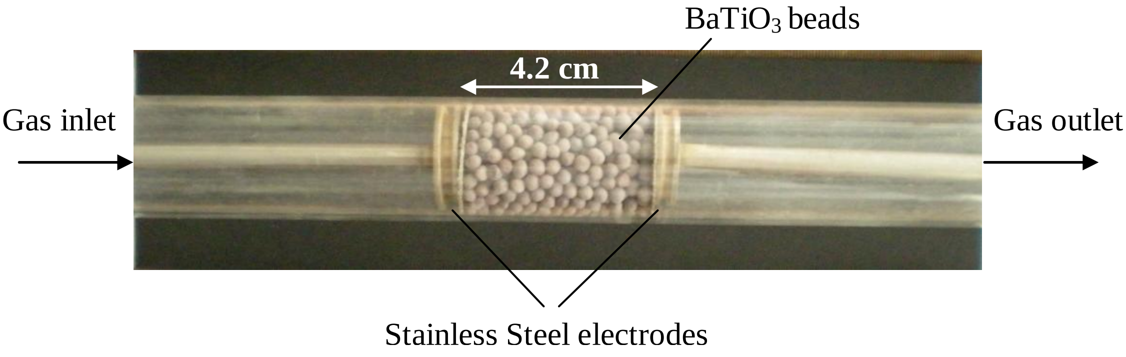

Figure 3.2: $BaTiO_3$ packed-bed DBD reactor.

A custom built high voltage power supply consisting of an audio amplifier, a signal generator and a high voltage transformer was used to apply a variable voltage of < 22 $kV_{pk\text{-}pk}$ across the discharge gap. The AC sine wave frequency of 31 – 39 kHz was optimised for each experiment and remained constant throughout. The optimised frequency varied depending on the packing material. A LabVIEW system was utilised for the measurement of the plasma power by the area calculation of Lissajous figures [11]. The LabVIEW system is based on a 2-channel analogue to digital conversion (ADC) sampling method using Picoscope hardware (ADC – 200); this was used to record the waveforms for the high voltage AC sine wave (via a 1000:1 reducing probe) and the voltage across a capacitor (typically 22 nF). Details of the method for power calculation and functions of the LabVIEW system can be found in Appendix A. After a change in the electrical input, the plasma was allowed to stabilise before analysis of the gas mixture was carried out. Gases exiting the reactor were analysed using a micro-GC (described in section 2.12.1). A cold trap consisting of a glass thimble surrounded by solid CO_2 was placed downstream of the reactor in order to condense any liquid products that were formed in the plasma reaction. Calculations of reactant conversions, product selectivities, H_2 yields and carbon balances in the gas stream are defined as shown in equations 3.0 – 3.4. The quantities in square brackets represent the molar % of the total gas volume and ‘n’ represents the carbon number of the product gas.

$$\text{Conversion} = \{[\text{reactant}]_{\text{converted}} / ([CH_4]_{\text{initial}} + [CO_2]_{\text{initial}})\} \times 100\ \% \qquad (3.0)$$

$$\text{Selectivity } (C_n) = \{n \times [\text{product}] / ([CH_4]_{\text{converted}} + [CO_2]_{\text{converted}})\} \times 100\ \% \qquad (3.1)$$

$$\text{Selectivity } (H_2) = \{[H_2] / (2 \times [CH_4]_{\text{converted}})]\} \times 100\ \% \qquad (3.2)$$

$$H_2 \text{ Yield} = (CH_4 \text{ Conversion} \times H_2 \text{ selectivity}) / 100\ \% \qquad (3.3)$$

$$\text{Carbon Balance} = [CH_4] + [CO_2] + [CO] + (2 \times [C_2]) + (3 \times [C_3])\ \% \qquad (3.4)$$

The uncertainty in the measurement of the gas concentrations to one standard deviation is < 2 %. The associated uncertainty in conversion, selectivity and yield data to one standard deviation is typically < 3 %.

3.3 Results

3.3.1 Dry Reforming of CH_4 in a Coaxial DBD with No Packing Material

Dry reforming of CH_4 has been carried out initially with no packing material inside the discharge gap. The results are shown in Figures 3.3 – 3.6.

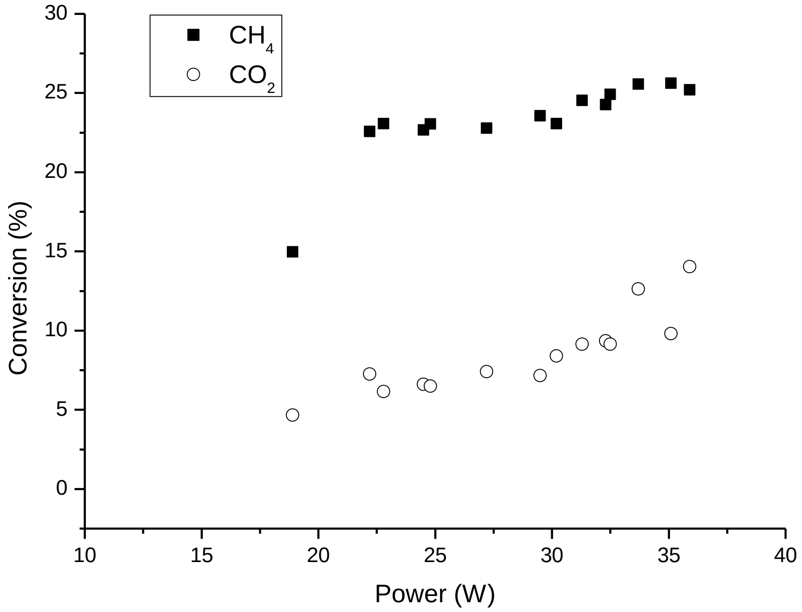

Figure 3.3: Conversions of CH_4 and CO_2 in plasma-assisted dry reforming of methane in the absence of a packing material.

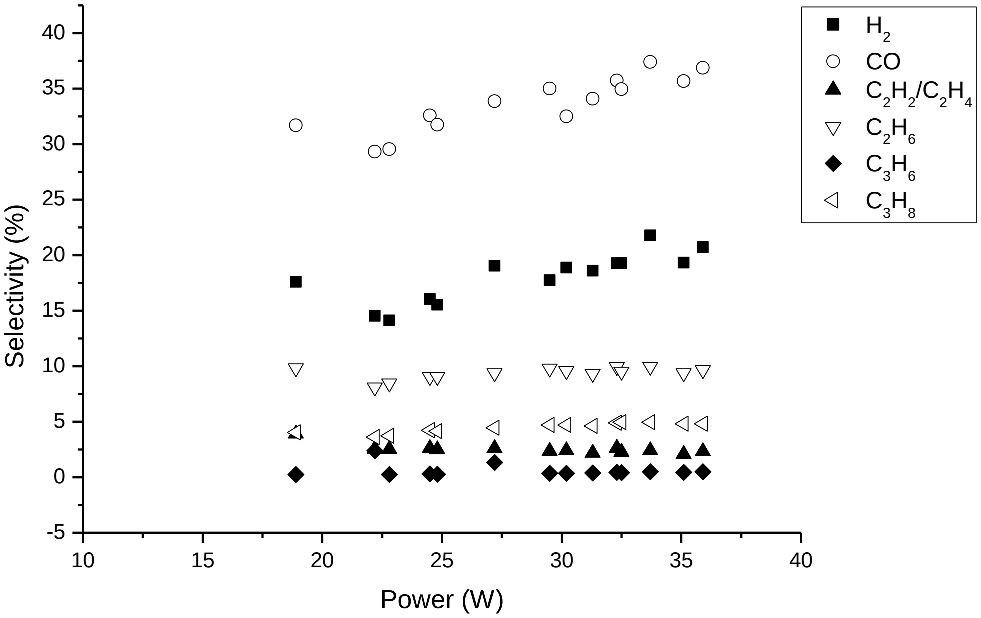

Figure 3.4: Product selectivities in plasma-assisted dry reforming of CH_4 in the absence of a packing material.

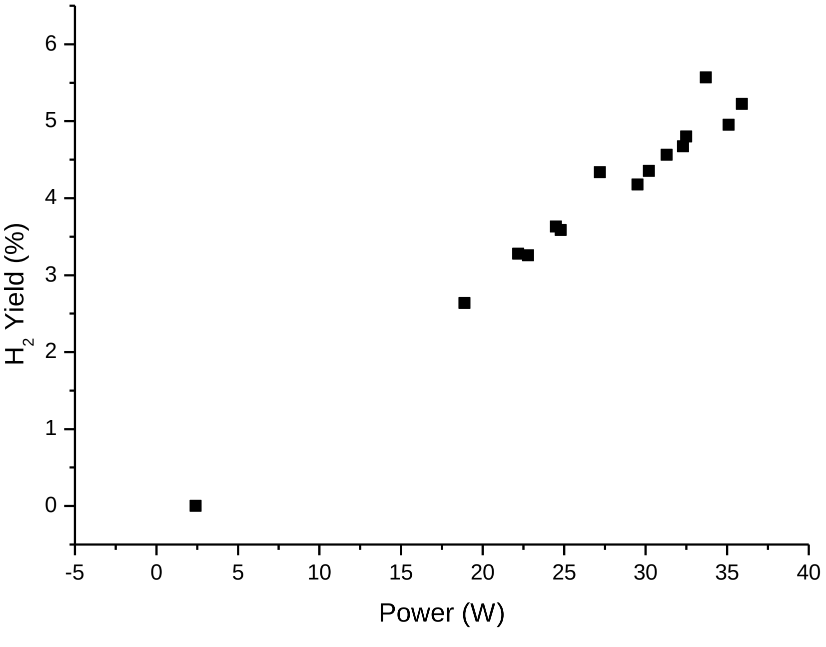

Figure 3.5: H_2 yields in plasma-assisted dry reforming of methane in the absence of a packing material.

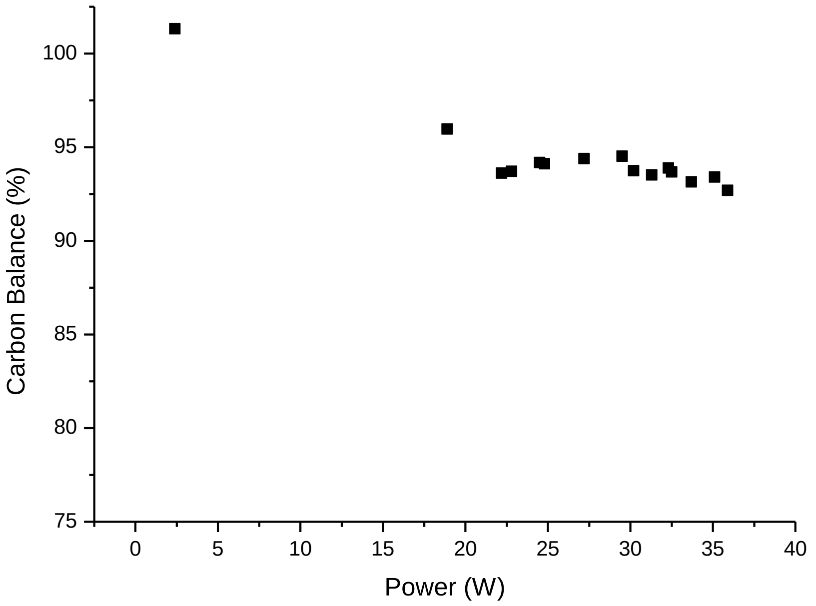

Figure 3.6: Gas stream carbon balance in plasma-assisted dry reforming of methane in the absence of a packing material.

Conversions of both CH_4 and CO_2 increased with increasing applied power up to 25.2 % and 14.0 % respectively, at a discharge power of 35.9 W. This is a commonly reported effect of increased input power [1, 3-7, 12-14]. High discharge power leads to the generation of more highly energetic electrons and ultimately a higher degree of ionisation in the plasma discharge than for a discharge operating at a lower power. This will increase the collision frequency between active plasma species, leading to higher conversion efficiencies. From the stoichiometry of the dry reforming of CH_4 reaction (3.5), equal conversions of CH_4 and CO_2 would be expected. However, this is not the case for dry reforming of CH_4 in non-equilibrium plasma conditions, where CH_4 conversions were 1.8 to 3.4 times greater than CO_2 conversions over the range of discharge powers tested. This is in agreement with results obtained by Song et al. [1] for the same reaction where CH_4 conversions were twice as large as CO_2 conversions under DBD conditions. This difference in conversion efficiencies between CH_4 and CO_2 may be attributed to the higher dissociation energy and ionisation energy of CO_2 compared with CH_4 (equations 3.6 – 3.9), making CO_2 more resistant to the formation of active species in the plasma discharge [13]. Another possible explanation is that additional product channels exist for dissociated CH_4 species in methyl coupling reactions and that recombination of radicals back to CO_2 is more likely than recombination in the case of CH_4. These mechanisms are discussed in detail in Chapter 4 of this thesis.

$CH_4 + CO_2 \rightarrow 2\ H_2 + 2\ CO$ (3.5)

Bond dissociation energy (C–H) = 4.55 eV (3.6)

Bond dissociation energy (C=O) = 5.52 eV (3.7)

Ionisation energy ($CH_4 \rightarrow CH_4^+ + e^-$) = 12.9 eV (3.8)

Ionisation energy ($CO_2 \rightarrow CO_2^+ + e^-$) = 13.8 eV (3.9)

Figure 3.4 shows that CO and H_2 were the main reaction products with selectivities of 36.9 % and 20.7 % respectively at a discharge power of 35.9 W. Higher hydrocarbons were also observed in lower concentrations. C_2 species were formed with greater selectivity than C_3 species and saturated hydrocarbons C_2H_6 and C_3H_8 were formed with higher selectivities than the unsaturated species of the same carbon number, C_2H_2/C_2H_4 and C_3H_6 respectively. No detectable amounts of C_4 hydrocarbons were produced under these conditions. Although some variation in product selectivities with increasing input power can be observed in Figure 3.4, the effect is small and the relative selectivities of all products do not change significantly as the power is increased. The syngas molar ratio of H_2/CO varied slightly in the range from 0.73 to 0.86. The yields of H_2 are shown in Figure 3.5, since CH_4 conversion increased with applied power and the selectivity did not change significantly, the H_2 yield also increased as the power was increased, reaching 5.5 % at 35.9 W. Figure 3.6 shows the carbon balance in the gas stream. Initially, the addition of carbon-containing species before the plasma was turned on, gave a total of 101.9 %. This error is associated with the calibration of the bulk gases CH_4 and CO_2 and can be considered negligible. As the power was increased, the carbon balance decreased. The sum of the selectivities of the carbon-containing products at 35.9

W is equal to 54.2 %, indicating that 45.8 % of the carbon converted went into the production of liquid products or solid carbonaceous deposits that were not detected by micro-GC. This corresponds to 9.2 % of the total carbon in the reaction mixture. Deposited solid carbon could be found on the walls of the reactor in the form of soot and as traces of a yellow-orange film close to the discharge area. A similar product has been described by Liu et al. [12] who operated the same reaction at a higher input power of 500 W. IR analysis of this solid product identified a highly branched hydrocarbon structure containing many oxygenated groups. The deposition of this polymerised product could create problems for prolonged run times, should the dielectric barrier become coated. The authors also reported that the formation of the polymerised product could be inhibited by the addition of zeolite to the discharge gap [5]. In addition, a small amount of colourless liquid was collected in the cold trap during this investigation. The liquid sample was analysed and the results are shown in section 3.3.2.

3.3.2 Comparison of Dry Reforming of CH_4 with Different Reactor Packing Materials

The results for plasma-assisted dry reforming of methane with different materials inside the discharge gap are shown in Figures 3.7 to 3.11. In comparison to the reaction with no packing material, the conversions of CH_4 shown in Figure 3.7 were enhanced by the addition of quartz wool to the plasma discharge but there was no significant change to CO_2 conversions (Figure 3.8). The addition of Al_2O_3 decreased the conversions of both CH_4 and CO_2 slightly at low discharge powers, whilst $BaTiO_3$, zeolite 3A and TiO_2, caused a significant decrease in the conversions when they were used inside the discharge gap, in comparison to the reaction with no packing material. Carbon dioxide conversions were consistently lower than methane conversions for each packing material. In the cases of Al_2O_3, zeolite 3A and TiO_2, the CO_2 conversions were slightly negative at low applied powers, indicating that the CO_2 concentrations had actually increased when the plasma discharge was switched on. This may be caused by residual adsorbed CO_2 which has become desorbed under plasma conditions or alternatively a reaction between CH_4 and other adsorbed species such as O_2 or H_2O. Negative CO_2 conversions were not observed in the cases of no packing, quartz wool and $BaTiO_3$, which have negligible adsorption properties in contrast to Al_2O_3, zeolites and TiO_2, which are known for their adsorbent properties.

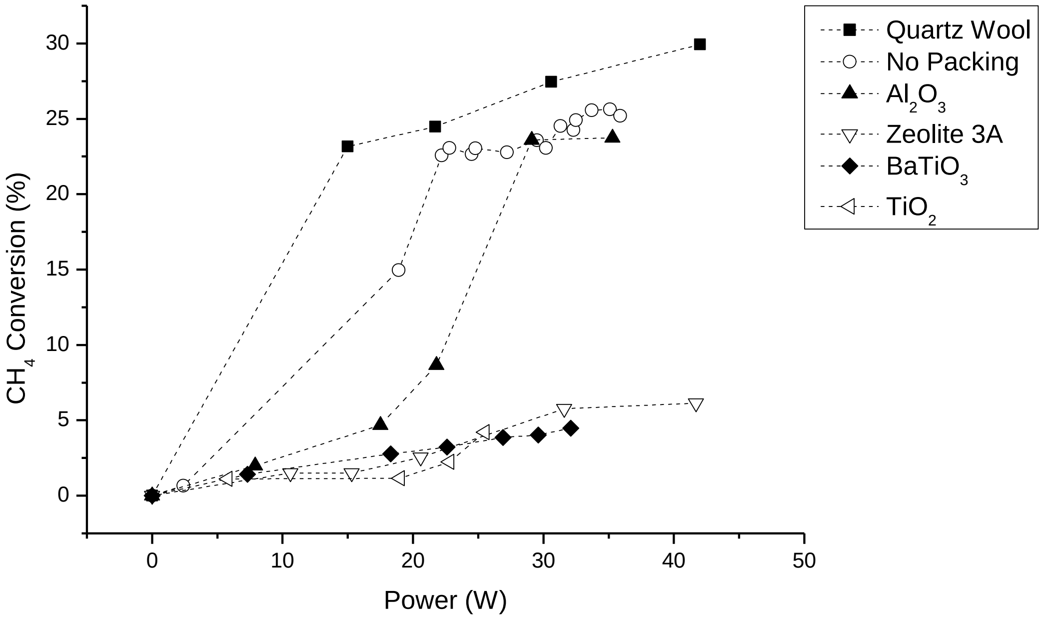

Figure 3.7: CH_4 conversions during plasma-assisted dry reforming of methane with different reactor packing materials.

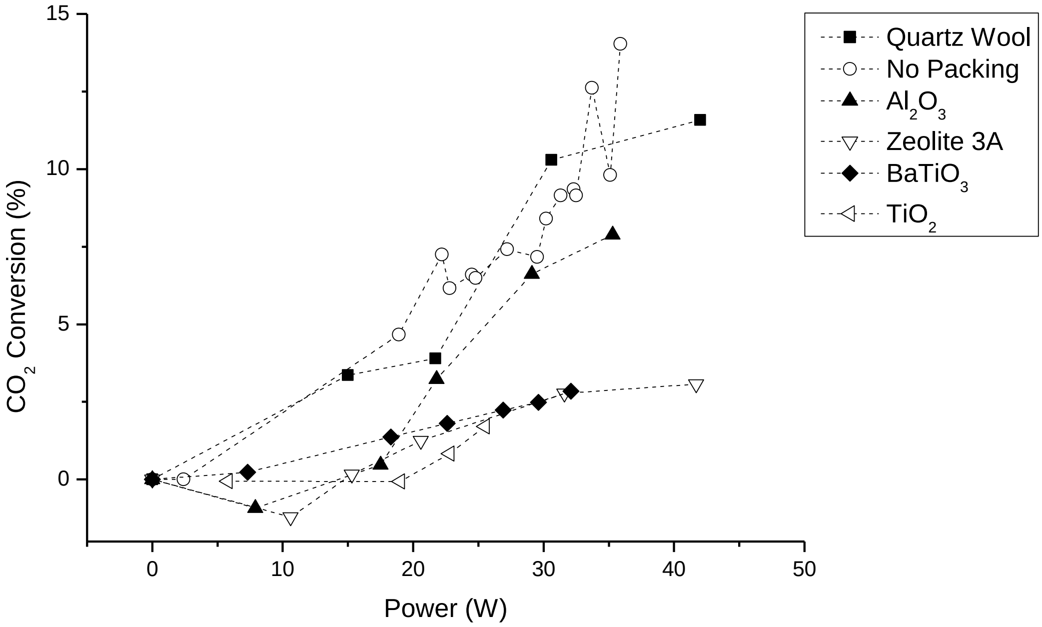

Figure 3.8: CO$_2$ conversions during plasma-assisted dry reforming of methane with different reactor packing materials.

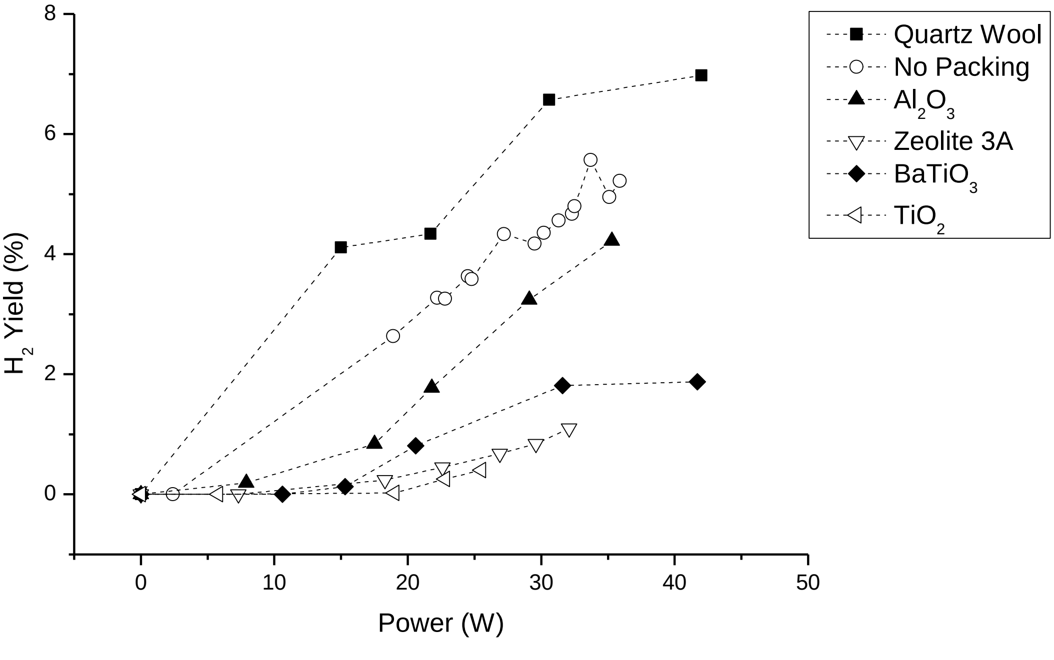

Figure 3.9: H$_2$ yields during plasma-assisted dry reforming of methane with different reactor packing materials.

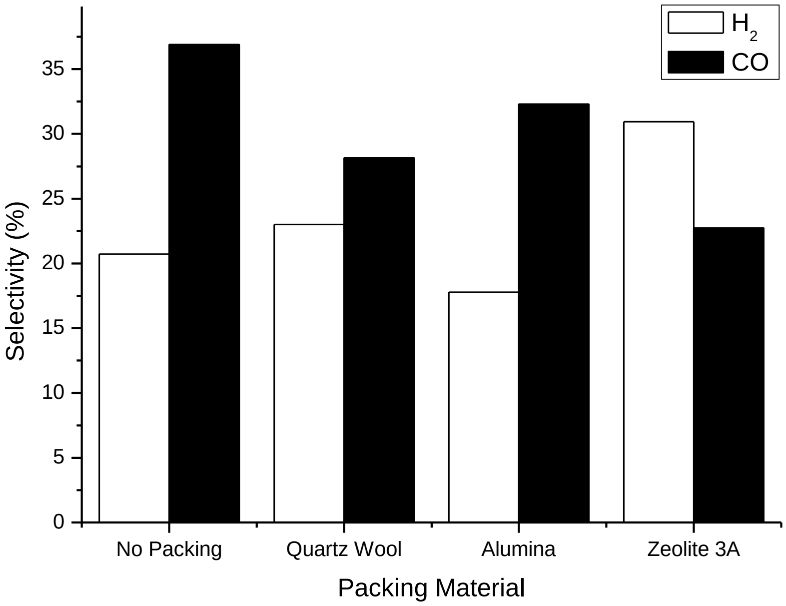

Figure 3.10: Selectivities of H_2 and CO during plasma-assisted dry reforming of methane with different reactor packing materials (discharge power = 35 W).

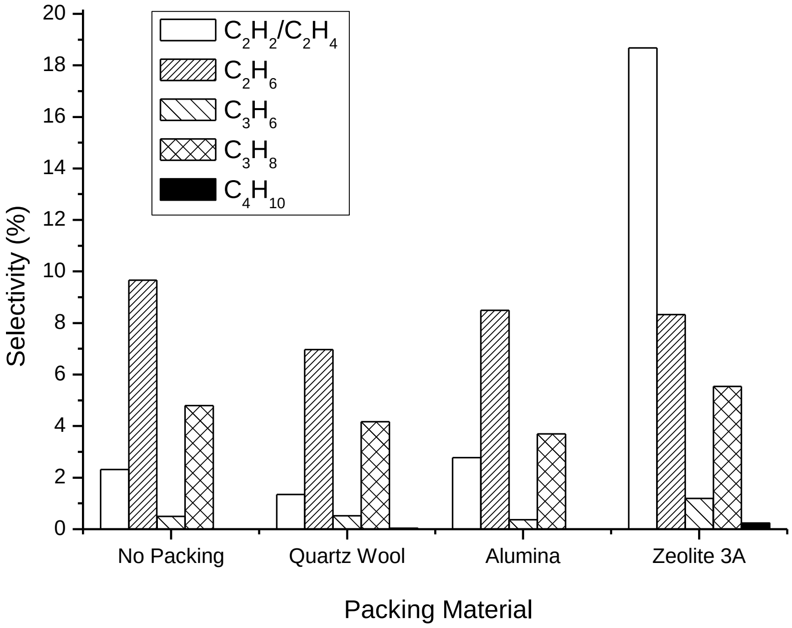

Figure 3.11: Selectivities of higher hydrocarbons during plasma-assisted dry reforming of methane with different reactor packing materials (discharge power = 35 W).

Figure 3.9 shows the yields of H_2 for each of the packing materials. It can be seen that the relative H_2 yields reflect the conversions of CH_4. Quartz wool enhanced the H_2 yield in comparison to no packing material, whilst the other materials resulted in decreased H_2 yields. The selectivities towards H_2 and CO at a discharge power of 35 W are shown for comparison in Figure 3.10. The carbon selectivities towards CO varied between 23.1 % for zeolite 3A and 36.9 % when no packing material was present. Hydrogen selectivities varied between 17.8 % for Al_2O_3 and 26.4 % for zeolite 3A. Results for the use of zeolite A in plasma dry reforming of CH_4 by Jiang et al. [3] also showed a decrease in CO selectivity compared with no packing material, but a comparison was not made for the H_2 selectivities. The selectivities towards hydrocarbon products are shown in Figure 3.11. For no packing, quartz wool and Al_2O_3, the selectivities towards the light hydrocarbon products varied only slightly. However, for zeolite 3A a significant enhancement in the selectivity towards the unsaturated C_2 species, acetylene and ethylene was observed. Selectivities towards other hydrocarbon species were also equal to or slightly greater for the use of zeolite 3A, than observed for the other materials. A small amount of butane was also formed, which was only observed for the use of zeolite and quartz wool and not for the use of the other packing materials. In contrast, Jiang et al. [3] observed an unspecified C_4 species as the main hydrocarbon product for the use of zeolite A with a DBD. One possible accountable difference is the smaller pore diameter of the zeolite used in this study (0.3 nm as opposed to 0.42 nm). In line with suggestions made by Zhang et al. [4], the smaller pore size could lead to the inhibition of long-chain species and as a consequence, the formation of the short-chain C_2 species are enhanced. This is also supported by the observation that C_2H_2/C_2H_4 were formed with a higher selectivity than C_2H_6, as the unsaturated hydrocarbons are shorter in length than the saturated species due to the presence of double and triple bonds.

	No Packing	Quartz Wool	Alumina	Zeolite 3A
% wt. C and H in liquid product	C = 3.2 H = 10.7	C = 2.3 H = 11.2	C = 2.7 H = 11.1	C = 0.7 H = 12.4

Table 3.1: Carbon and hydrogen compositions of liquid products obtained during plasma-assisted dry reforming of methane with different reactor packing materials (discharge power = 35 W).

The elemental analyses of the colourless liquid products that were collected in the cold trap are shown in Table 3.1. The relative concentrations of carbon and hydrogen in the liquid samples suggest that they contain mostly H_2O, assuming that the only other element present in the samples was oxygen. However, some carbon-containing compounds are present, and the concentrations of these were decreased slightly when quartz wool or alumina was used as a packing material. When zeolite 3A was used, the carbon content of the liquid sample decreased significantly from 3.2 % (for no packing) to 0.7 %. This indicates that the selectivity towards liquid hydrocarbons (C_5+) or oxygenated species was significantly reduced by the use of zeolite 3A in the discharge gap. This is in contrast to the results of Eliasson et al. [5], who reported the GC analysis of the organic compounds in a yellow liquid sample obtained during dry reforming of methane in DBD packed with zeolite NaX. The analysed sample was found to contain > 200 different species of branched hydrocarbons ranging from C_5 to C_{11}. They did not report the identification of H_2O as a reaction product. This indicates that the properties of the different zeolites influences the formation of reaction products significantly, this could be a result of different framework structures, pore sizes and acid/base properties.

3.3.3 Dry Reforming of CH_4 in a $BaTiO_3$ Packed-Bed DBD Reactor

The results for plasma-assisted dry reforming of methane in a packed-bed DBD configuration are shown in Figures 3.12 to 3.15.

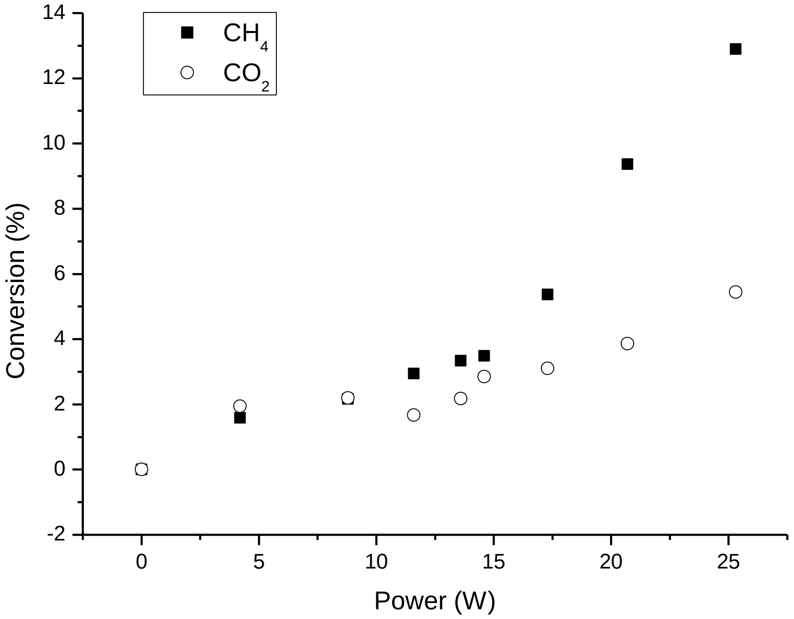

Figure 3.12: Conversions of CH_4 and CO_2 in plasma-assisted dry reforming of methane in a $BaTiO_3$ packed-bed DBD reactor.

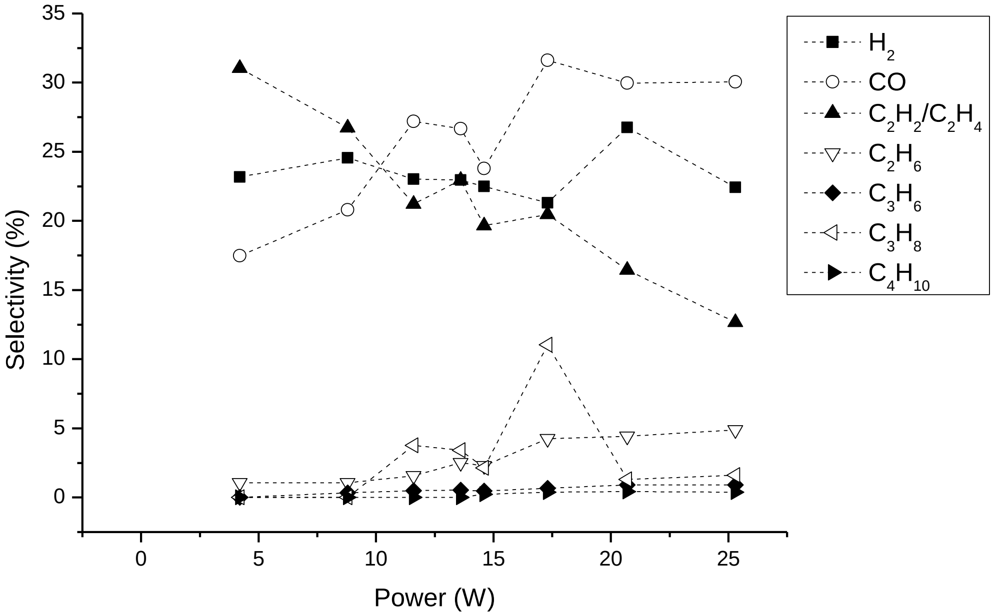

Figure 3.13: Product selectivities in plasma-assisted dry reforming of methane in a $BaTiO_3$ packed-bed DBD reactor.

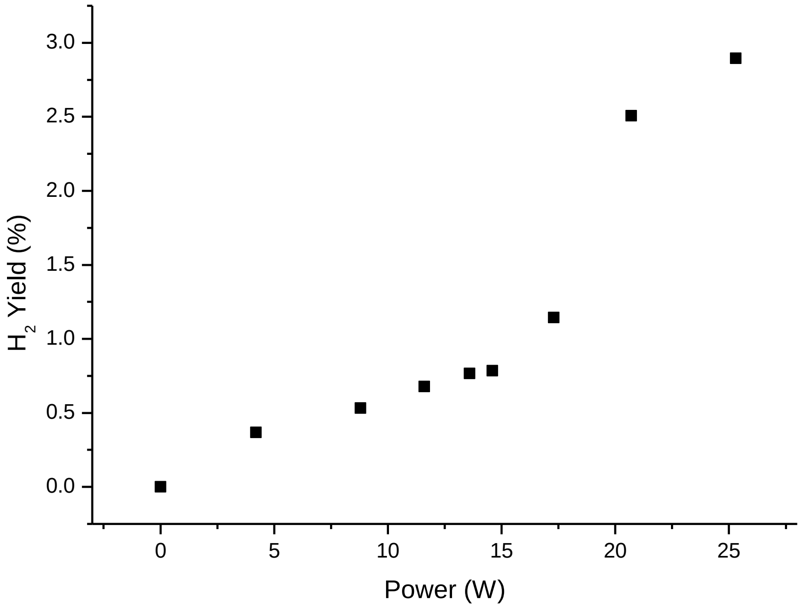

Figure 3.14: H_2 yields in plasma-assisted dry reforming of methane in a $BaTiO_3$ packed-bed DBD reactor.

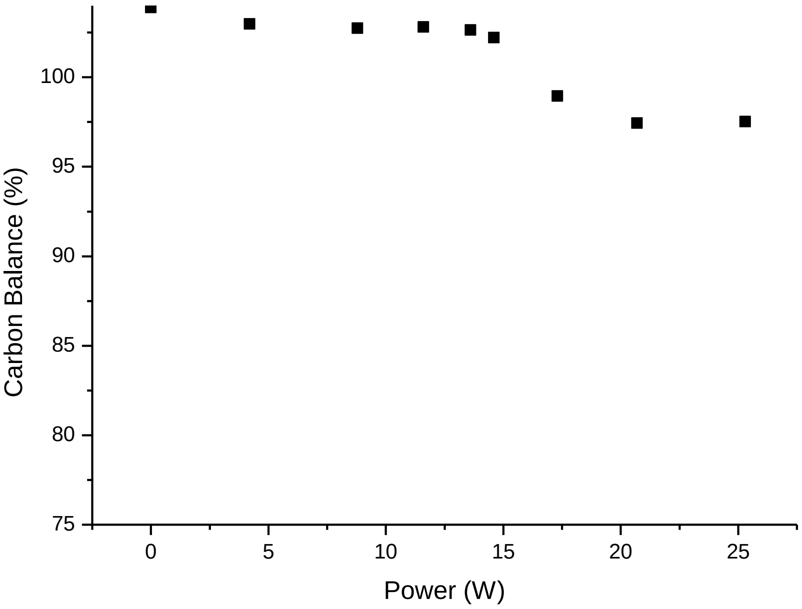

Figure 3.15: Gas stream carbon balance for the plasma-assisted dry reforming of methane in a $BaTiO_3$ packed-bed DBD reactor.

At comparable discharge powers the conversions of CH_4 and CO_2 were lower in the $BaTiO_3$ packed-bed reactor (Figure 3.12) than in the coaxial DBD reactor. This indicates that the input of energy in the coaxial reactor is likely to be more efficient for production of highly energetic electrons and other plasma active species. Figure 3.13 shows the product selectivities in the packed-bed reactor. These differ from the results obtained for the coaxial reactor configuration in that CO selectivity is slightly lower, whilst H_2 selectivity is slightly greater. Selectivity towards C_2H_2/C_2H_4 is greater in the packed-bed configuration at low power. However, it decreases significantly with increased input power. Figure 3.13 also shows that a small amount of butane was formed in addition to the C_2 and C_3 species, which was not observed in the coaxial configuration except when zeolite or quartz wool were used as the packing materials. Despite selectivities towards H_2 being higher in the packed-bed reactor, the H_2 yields shown in Figure 3.14 are lower than in the case of the coaxial DBD due to lower conversions of methane. Figure 3.15 shows the carbon balance in the gas stream which decreases with input power, due to the formation of liquid carbon-containing species and/or the deposition of solid carbon products. The carbon loss from the gas stream was greater in the case of the coaxial DBD reactor (with no packing) compared to the packed-bed DBD reactor at comparable discharge powers. This can be attributed to lower reactant conversions in the packed-bed DBD system, meaning that the difference in carbon balance is due to unconverted CH_4 and CO_2, rather than a reduced selectivity towards the formation of solid or liquid carbon products. Examination of the $BaTiO_3$ beads after the plasma reaction revealed some deposition of carbon black in small spots that corresponded to the contact points between the beads where plasma formation was most intense. However, no polymerised film could be seen on the walls of the quartz tube in the packed-bed DBD reactor configuration. These results indicate that overall the coaxial DBD reactor offers greater potential for H_2 production from dry reforming of methane than the packed-bed DBD configuration.

3.4 Calculations of the Thermodynamic Equilibrium Composition for Dry Reforming of Methane

The thermodynamic equilibrium compositions for dry reforming of methane at temperatures ranging from 100 – 1100 °C have been calculated using HSC Chemistry Software (Ver. 5.0). The assumed equilibrium products were H_2, CO, H_2O and C_2 hydrocarbons. The results are shown in Figure 3.16. Temperatures of > 400 °C are required for the conversion of both CH_4 and CO_2 under equilibrium conditions in the absence of a catalyst. The concentrations of CH_4 and CO_2 decrease with increasing temperature up to ~ 800 °C, although CO_2 conversion is ~ 10 % greater than CH_4 conversion at a given temperature. At temperatures > 800 °C, there is close to complete conversion of both reactants to produce syngas. A small amount of H_2O production is predicted which peaks at ~ 600 °C.

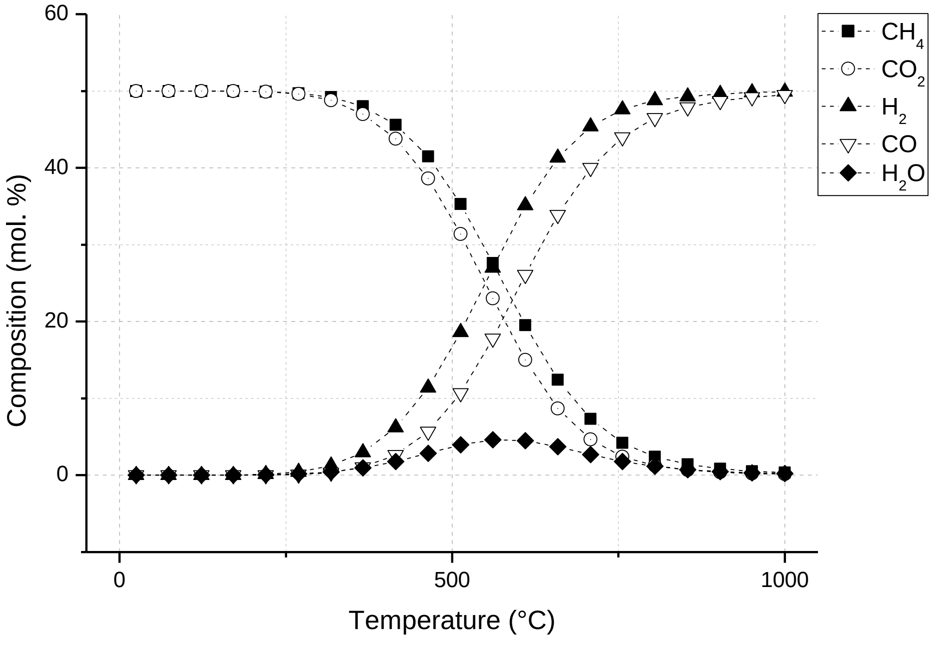

Figure 3.16: Thermodynamic equilibrium gas compositions for dry reforming of CH_4 at elevated temperatures in the absence of a catalyst (CH_4/CO_2 = 1, pressure = 1 atm).

There are several key differences between the thermodynamic equilibrium compositions in dry reforming of methane and the compositions that have been experimentally observed under plasma conditions, where equilibrium conditions are not met. During the plasma experiments in the coaxial DBD reactor, the maximum observed temperature (measured using a thermocouple on the outer electrode) was 275 °C, this is significantly lower than the temperatures required for conversions under thermal conditions. This low temperature chemical activity in plasma results from collisions with highly energetic electrons and other active plasma species such as excited molecules and free radicals. The relative conversions of CH_4 and CO_2 are also distinctly different. Under thermal conditions, CO_2 conversion is greater than CH_4 conversion, whilst the opposite is true of plasma-assisted dry reforming of methane. Another noticeable difference is the formation of higher hydrocarbons with the use of plasma that are not produced during the thermal reaction.

3.5 Effect of Packing Materials on the Electrical Characteristics of DBDs

The waveforms for the discharge current and applied voltage have been measured using an oscilloscope (Textronix TPS 2014), for the comparison of electrical characteristics during plasma generation on quartz wool, zeolite 3A and in the absence of a packing material. In addition, the voltage across a capacitor has been measured and used to calculate the gas voltage. Details of the calculation method can be found in Appendix B.

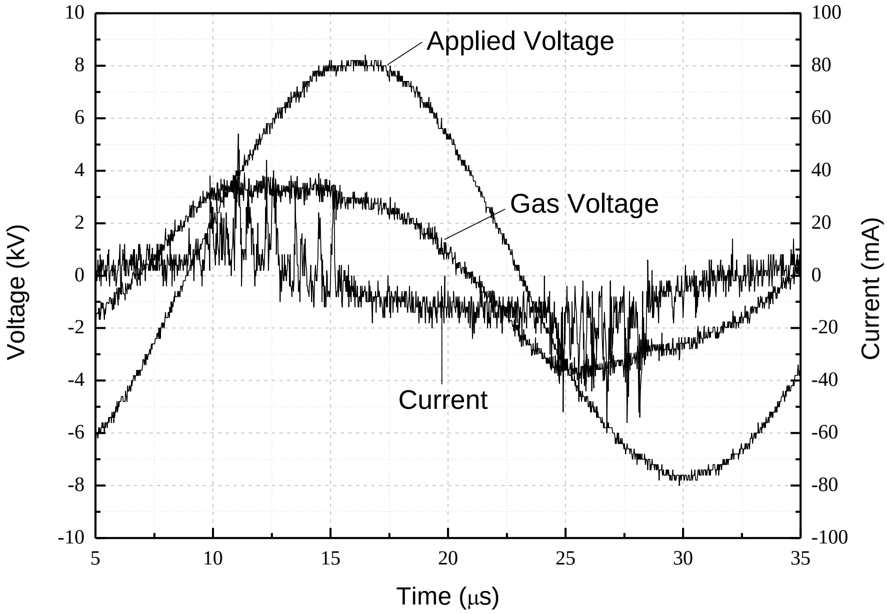

Figure 3.17: Electrical waveforms for the plasma-assisted dry reforming of methane with no packing in the discharge gap (discharge power = 30 W).

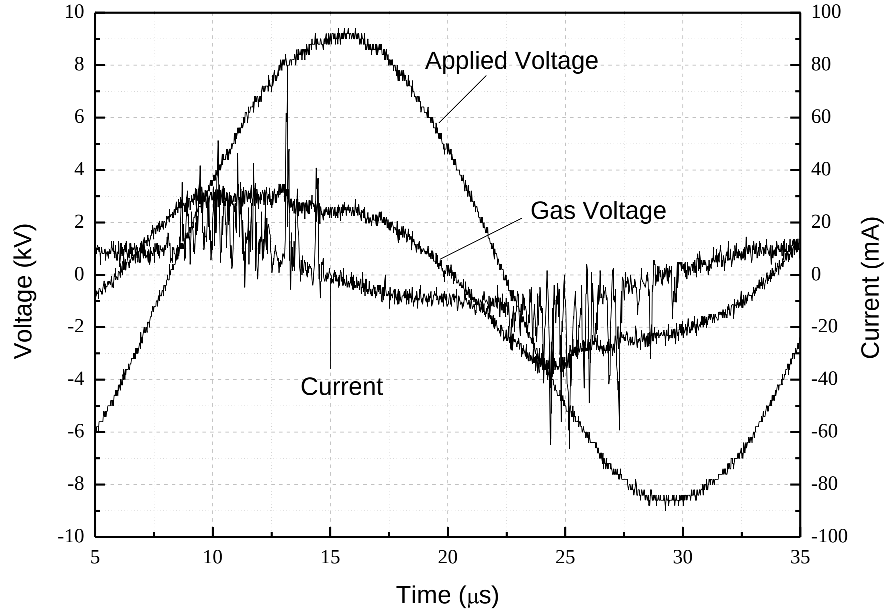

Figure 3.18: Electrical waveforms for the plasma-assisted dry reforming of methane with quartz wool in the discharge gap (discharge power = 30 W).

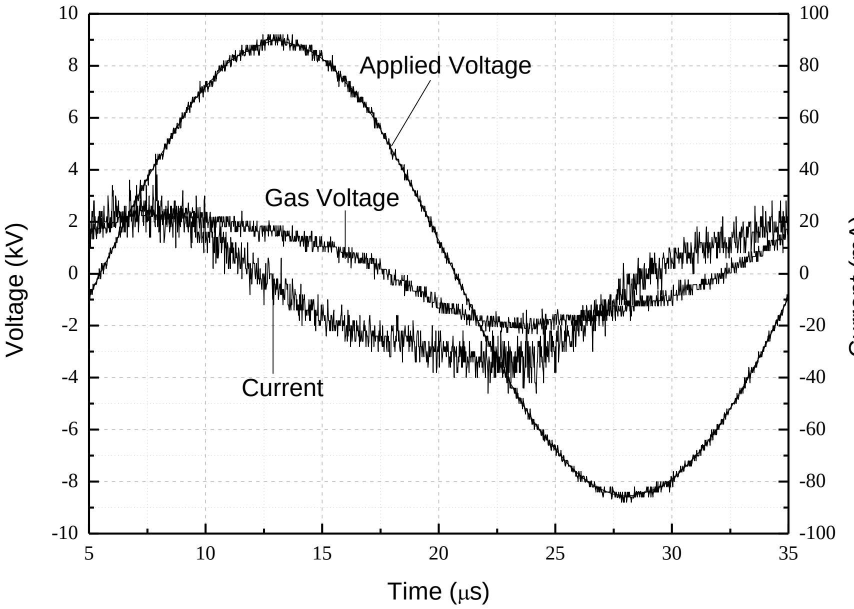

Figure 3.19: Electrical waveforms for the plasma-assisted dry reforming of methane with zeolite 3A beads in the discharge gap (discharge power = 30 W).

In Figure 3.17, which shows the current signal in the absence of a packing material, the waveform is quasi-sinusoidal with numerous superimposed current spikes per half-cycle. These current pulses correspond to filamentary microdischarges. In appearance, they are randomly distributed in time and space over the dielectric surface and extend across the entire discharge gap. The typical radii of these current filaments have been reported as in the range of 100 – 200 μm [15]. The duration of a single filamentary microdischarge in this case is ~ 40 ns. When quartz wool is packed into the discharge gap, the characteristic spikes of the filamentary microdischarges can be observed on the current waveform as shown in Figure 3.18. The amplitude of several spikes is large in comparison with the case of no packing material, showing that the strength of current pulses has been enhanced. In addition to the filamentary mode, the quartz fibres provide a surface along which a surface discharge can propagate. Therefore, it is likely that both filamentary and surface discharges operate when quartz wool is present in the discharge gap. The introduction of zeolite 3A to the discharge region causes both the amplitude and the number of current pulses to decrease significantly (Figure 3.19). When zeolite beads were packed into the discharge gap, the available discharge volume was greatly reduced, effectively limiting the distance over which filamentary microdischarges can form. However, weak filaments can be generated in the void between particle-particle and particle-quartz barrier. The relative contributions of filamentary and surface discharges is therefore dependent on the particle size and hence volume fraction of the packed material [16].

The Lissajous figures for no packing, quartz wool and zeolite 3A are shown in Figure 3.20 for a constant discharge power of 30 W. The shape of the Lissajous figure for no packing material and quartz wool are almost identical and can barely be distinguished on the same plot. However, the Lissajous shape changed when zeolite beads were used as a reactor packing material. This further indicates that physical changes to the discharge mode have taken place.

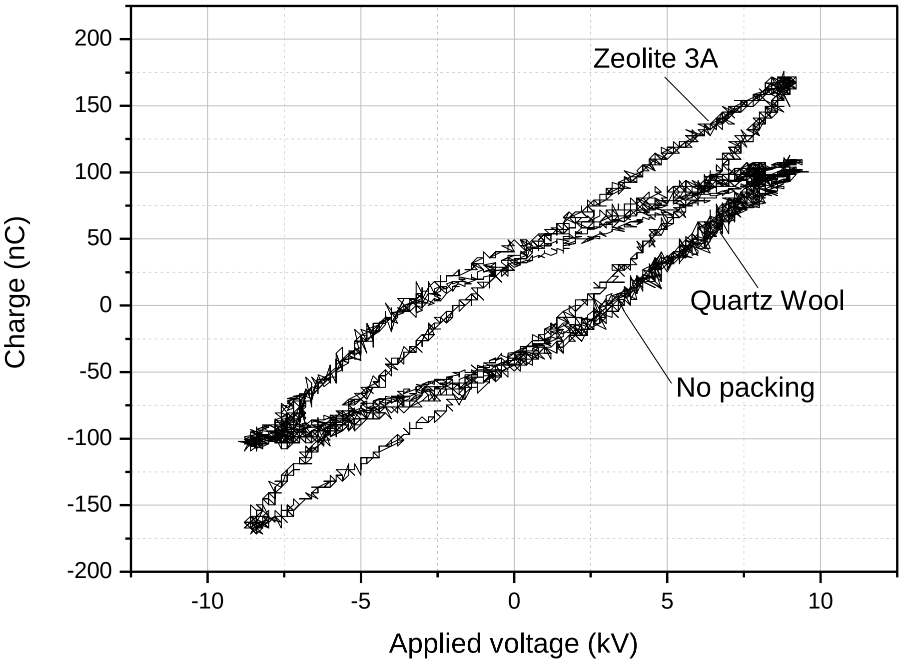

Figure 3.20: Lissajous figures of a $CH_4/CO_2 = 1$ DBD with the discharge gap packed with quartz wool, zeolite 3A and in the absence of a packing material, at a fixed discharge power of 30 W.

The angles in the Lissajous figures represent different electrical parameters of the discharge. These have been calculated for the plasma discharges and are shown quantitatively in Table 3.2. Methods for the calculation of these parameters have been derived from several publications on electrical properties of DBDs [17-19] and are detailed in Appendix B.

Gas Type	Packing Material	Applied Voltage pk-pk (kV)	Breakdown Voltage (kV)	Charge pk-pk (nC)	Charge Discharged (nC)	Transferred Charge per Half Cycle (nC)	Total Capacitance (pF)
CH_4/CO_2	No Packing	16.4	2.19	202	122	81	7.7
CH_4/CO_2	Quartz Wool	18.2	1.59	211	103	70	7.5
CH_4/CO_2	Zeolite 3A	19.0	0.66	343	177	77	15.8

Table 3.2: Electrical parameters of a DBD at constant power (30 W) in the absence of a packing material and when quartz wool and zeolite 3A are packed into the discharge gap. Methods for the calculation of these parameters have been derived from several publications on electrical properties of DBDs [11, 17-19] and are detailed in Appendix B.

The results in Table 3.2 show that despite the constant dissipated power in the plasma discharge, the applied voltage increases from 16.4 kV_{pk-pk}, in the case of no packing to 18.2 kV_{pk-pk} and 19.0 kV_{pk-pk} in the cases of quartz wool and the zeolite respectively. Given that the discharge power is the same in each case, the current must be smaller in the quartz wool and zeolite packed plasma discharges. This is due to the increased resistance of the packing materials in comparison with the gas gap, which will limit the current flow. The breakdown voltage (V_b) decreases significantly with the addition of packing materials from 2.19 kV to 1.59 kV for quartz wool and 0.66 kV for zeolite. This can be attributed to a change in discharge mode in going from purely filamentary discharge to a combination of filamentary and surface discharges with quartz wool and predominantly surface discharge when zeolite is used. The breakdown of gas in the formation of surface discharge is likely to require a lower breakdown voltage due to the accumulation of charges that occur on the surface of the packing material. This is demonstrated in the data for peak to peak charge shown in Table 3.2 where the charge is greater for quartz wool (211 nC) and zeolite (343 nC) discharges compared with the discharge when no packing material is present (202 nC). Especially in the case of zeolite packing, the peak to peak charge is large, which suggests that the zeolite has an enhanced ability to store electrical charge on the surface. This is demonstrated by a larger capacitance value of 15.8 pF, more than twice the magnitude of the capacitance for no packing and for quartz wool (7.7 pF and 7.5 pF respectively).

3.6 Images of Plasma Generation on Packing Materials (work carried out at AIST, Japan)

Images have been taken of plasma generation during dry reforming of CH_4 in the absence of a packing material and with different materials packed inside the discharge gap. A schematic diagram of the optical observation system used to take these images is shown in Figure 3.21. The system consists of a parallel-plate DBD reactor, an AC power supply (Neon transformer), an XY stage, an optical microscope (Hamamatsu Photonics, A7976), an image-intensified charge coupled device (ICCD) camera and a PC installed with HiPic software

(Ver. 8.1). The ICCD consisted of an image-intensifier (Hamamatsu Photonics, C9016-03) and a digital CCD camera (Hamamatsu Photonics, C8484-05G). This microscopic observation system offers a rough-but-rapid evaluation of materials for plasma-catalytic processes [20].

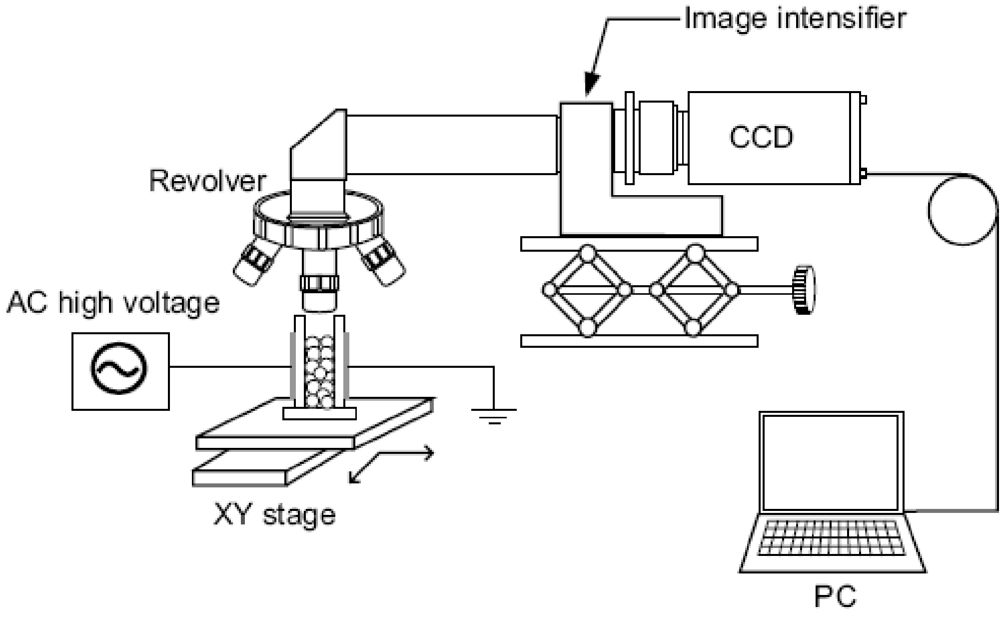

Figure 3.21: Schematic diagram of the optical microscopic observation system for plasma generation on different surfaces. Taken from [20].

The gas mixture of CH_4 and CO_2 ($CH_4/CO_2 = 1$) was controlled using mass flow controllers at a total flow rate of 100 ml min^{-1} at a pressure of 1 bar. The revolver was positioned to use a lens of 2 × magnification. The lens was focused onto the packing material using the XY stage. A 45 kV potential difference was applied across the discharge gap and the plasma was allowed to stabilise before the images were taken. The exposure time of the ICCD camera was set to 100 ms, which corresponds to ~ 5 cycles of the AC applied voltage (50 Hz). The DBD reactor consists of a closed glass cell with a 6 mm discharge gap. Aluminium tape electrodes (10 mm × 28 mm) were attached to the outer sides of the two glass dielectrics (Figure 3.22 a). The upper face of the cell was a quartz plate, through which the images were taken (Figure 3.22 b).

Imaging of plasma generation on different materials or catalysts can yield valuable information about the influence of that material on the discharge formation. Challenges associated with imaging of CH_4 and CO_2 discharges include a relatively low light intensity and the need for a closed cell to contain the gas mixture. The use of a closed gas cell inevitably leads to some reflection of light that can interfere with the quality of the images.

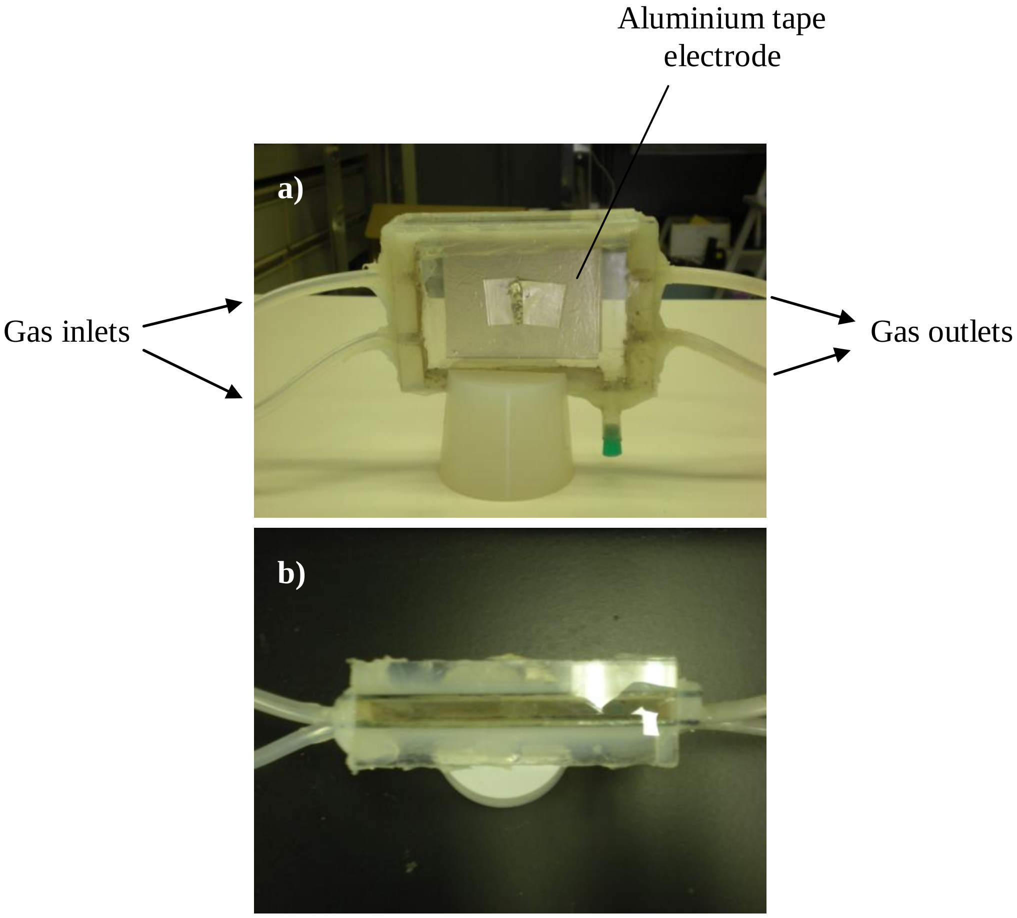

Figure 3.22: DBD reactor used to take images of plasma generation on different surfaces during dry reforming of CH_4 a) DBD cell (side-view), b) quartz upper plate of DBD cell with a 6 mm discharge gap.

3.6.1 Plasma Generation in the Absence of a Packing Material

In the absence of a packing material, the plasma was of a relatively high intensity at one electrode but it was not uniform across the discharge gap as shown in Figure 3.23. Formation of a few individual plasma filaments could be observed extending across the discharge gap.

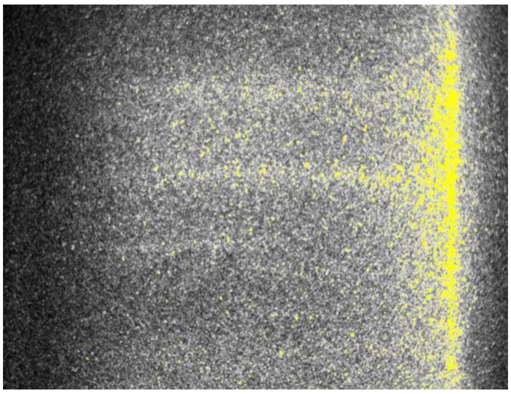

Figure 3.23: Microscope-ICCD image of plasma generation in the absence of a reactor packing material.

3.6.2 Quartz Wool

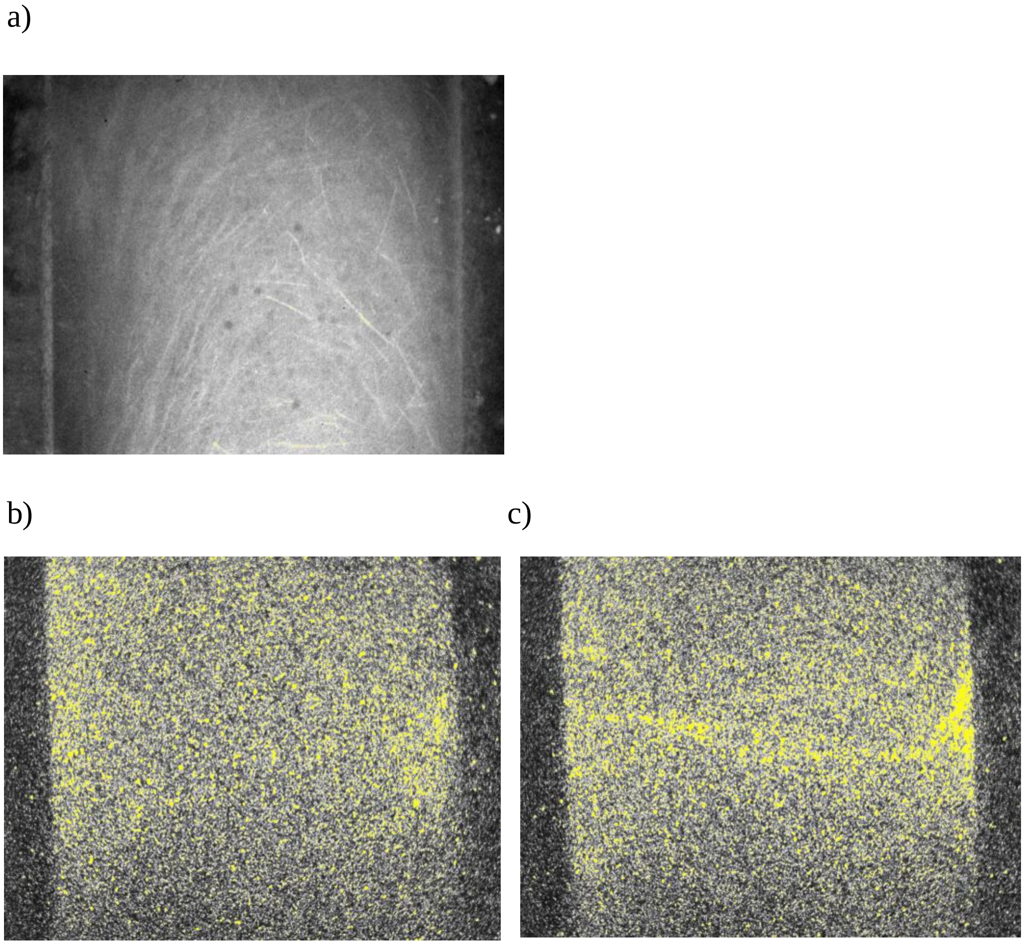

Figure 3.24: Microscope-ICCD images of a) quartz wool, b) uniform plasma discharge observed on the surface of quartz wool c) streamer formation on the quartz wool surface.

The addition of quartz wool to the discharge gap enhanced the intensity and uniformity of the plasma generation. Figure 3.24 (a) shows the discharge gap when it was packed with quartz wool, before the plasma was switched on. When the plasma discharge was turned on, plasma filaments could be seen extending across the entire discharge gap between the two electrodes, as shown in Figure 3.24 (b and c).

3.6.3 γ-Al_2O_3

The use of Al_2O_3 beads in the discharge gap appeared to give a relatively low intensity of observable plasma, as shown in Figure 3.25. Weak surface discharges could be observed on the beads, as well as slightly more intense microdischarges between the beads where the electric field strength is likely to be greater.

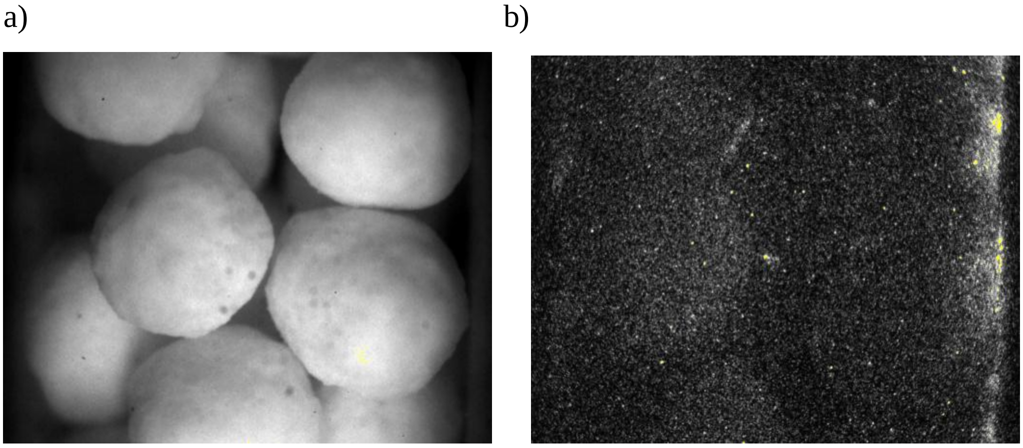

Figure 3.25: Microscope-ICCD images of a) γ-Al_2O_3 beads and b) plasma generation on γ-Al_2O_3 beads.

3.6.4 $BaTiO_3$ Beads

Plasma generation in the presence of $BaTiO_3$ beads is shown in Figure 3.26. In Figure 3.26 (b), three spots of intense plasma can be observed that correspond to the contact points between the beads. This is due to an enhanced electric field strength at these contact points. In addition, the formation of a single plasma filament was observed, that extended across the surface of the upper-most bead

(Figure 3.26 c). Kim et al. [21] have obtained similar images of plasma generation with the presence of zeolite in the discharge gap, they found that plasma generation could be extended more homogeneously across the surface of the beads when the zeolite beads were coated with silver nanoparticles.

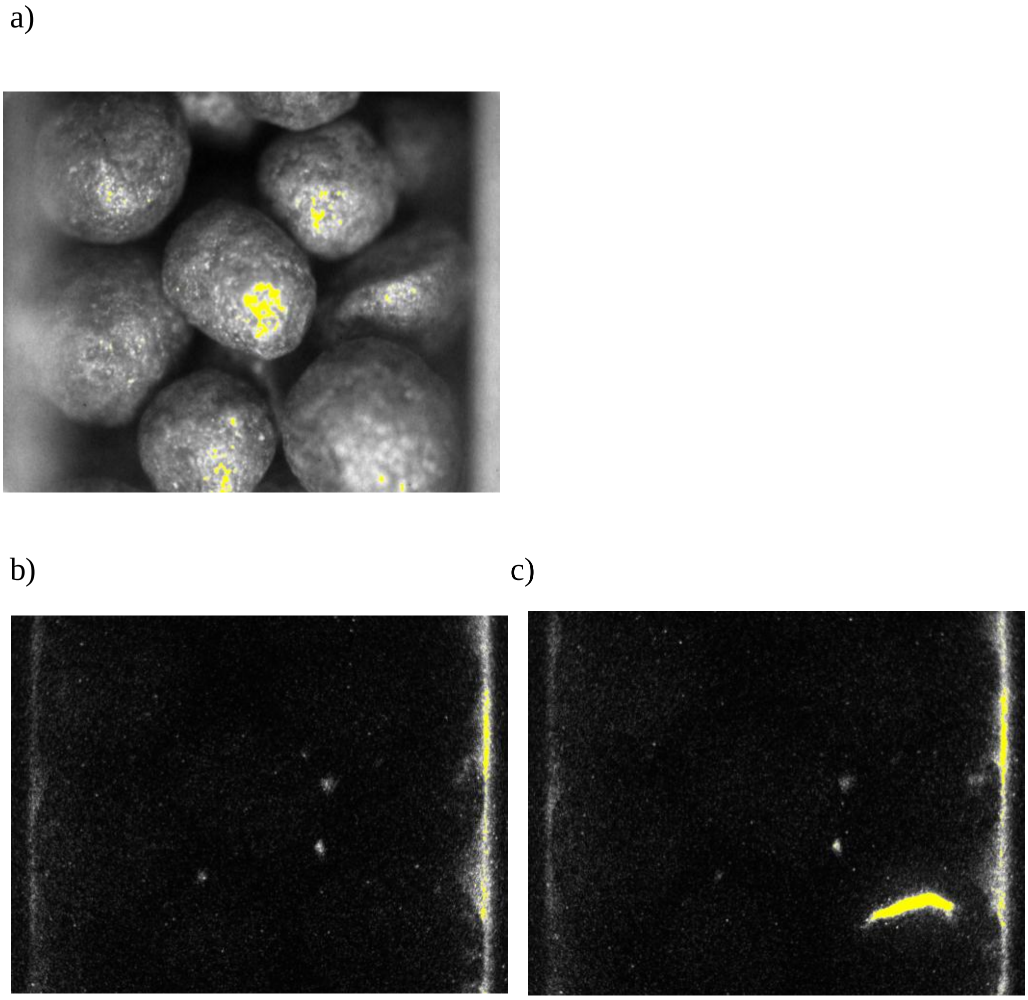

Figure 3.26: Microscope-ICCD images of a) $BaTiO_3$ beads, b) spots of plasma generation at contact points between $BaTiO_3$ beads and c) streamer extending over the surface of a $BaTiO_3$ bead.

3.7 Discussion

The observed changes in both conversion efficiencies and product selectivities, when different materials were present in the discharge gap suggest that these materials may have had catalytic effects on dry reforming of methane. However, the role of a catalyst in plasma systems may be substantially different to that of catalysts in conventional thermal reactions. In conventional catalysis, the role of the catalyst is in the adsorption and dissociation of gas molecules. There are two generally accepted models for heterogeneous catalysis: 1) the *Langmuir-Hinshelwood* mechanism, where gas molecules are adsorbed onto the catalyst surface and reactions occur between adsorbents and 2) the *Eley-Rideal* mechanism where adsorbed molecules react upon collision with species still in the gas phase [22]. The plasma may assist in these processes by providing radicals and vibrationally excited species (formed in the plasma volume) that could be more susceptible to adsorption and also more reactive. The chemisorption and desorption processes are likely to differ significantly in a plasma where substantial charges exist on the surface of materials packed in the discharge gap [23]. In addition, new stable molecules will be formed in the plasma volume, for example in a CH_4 and CO_2 discharge, higher hydrocarbons C_2 and C_3 are formed. These hydrocarbons may also be adsorbed onto a catalyst and undergo conversion into new species. This provides alternate reaction pathways in plasma systems that do not exist by conventional thermal catalysis. These processes may help to explain why some materials that do not possess any thermal catalytic activity can have catalytic effects in plasma systems.

The addition of packing materials into a discharge gap can affect the type of discharge formed as shown by the observed changes to the current waveforms for the use of different packing materials. The change in discharge mode between filamentary and surface discharges or a combination of both may induce a shift in the energy distribution of the accelerated electrons, which in turn will influence the production of active plasma species such as free radicals and excited states and ultimately lead to the formation of different end products [24]. Materials that can enhance the plasma intensity such as quartz wool are effective in improving conversions of CH_4 and CO_2. Other materials such as zeolite are effective in changing the product selectivities towards different end products such as H_2 and also C_2 – C_4 hydrocarbons (in the case of zeolite 3A).

The dielectric constants of the packing materials studied in this chapter vary greatly as shown by the data in Table 3.3. Assuming that the dielectric properties of the gas in the discharge gap is negligible, one might expect that the differences in plasma generation and hence, chemical activity for the different packing materials could be attributed to a trend in dielectric constants, however this is not the case. This suggests that the dielectric properties of the packing material may not be as significant as other factors such as the size, shape and porosity of the material.

Material	Dielectric Constant (k)	Reference
Quartz	4	[25]
Al_2O_3	9	[26]
Zeolite	1 – 3	[25]
$BaTiO_3$	6000 – 10000	[27]
TiO_2	114	[28]

Table 3.3: Dielectric constants of the packing materials at 1 MHz (at ~ 300 K).

Packing materials can also enhance the ability to form a stable plasma discharge at a given voltage. For example, the range of input powers that could be achieved when no packing material was present in the coaxial reactor was quite narrow (~ 18 W – 37 W), whereas with packing materials present there was an ability to form stable discharges at a wider range of input powers for the same range of applied voltages.

3.8 Conclusions

The comparison of a coaxial DBD reactor and a $BaTiO_3$ packed-bed DBD reactor has shown that the coaxial configuration is more effective for converting CH_4 and CO_2 and resulted in higher yields of H_2. In addition, the coaxial configuration provides a greater potential for modification of reaction products by the addition of catalysts to the discharge gap. The use of different packing materials in the coaxial reactor revealed changes to the reactant conversions and product selectivities for the use of different packing materials. The activity was found to decrease in the order: quartz wool > no packing > Al_2O_3 > zeolite 3A > $BaTiO_3$ > TiO_2. Zeolite 3A was found to improve selectivities towards H_2 as well as light hydrocarbons (C_2 – C_4), which is thought to be due to shape selectivity, determined by the pore size of the zeolite.

Analysis of the electrical waveforms showed that changes to the discharge mode occurred when different packing materials were used in the discharge gap. Intense filamentary discharges were formed when quartz wool was packed into the discharge gap. Whereas the addition of zeolite 3A can inhibit filamentary discharges but allows the formation of a weak surface discharge. Microscope-ICCD images of these packing materials show that enhanced plasma generation is visible on quartz wool in comparison with other packing materials. The evaluation of the plasma activity with different packing materials in the discharge gap can provide an insight into the appropriateness of these materials for use as catalyst supports. This could aid the development of supported catalysts specifically for plasma processes.

3.9 References

1. Song, H.K., et al., *Synthesis Gas Production via Dielectric Barrier Discharge over Ni/γ-Al_2O_3 Catalyst.* Catal. Today, 2004. **89**: p. 27-33.
2. Wang, Q., et al., *Dry Reforming of Methane in a Dielectric Barrier Discharge Reactor with Ni/Al_2O_3 Catalyst: Interaction of Catalyst and Plasma.* Energy & Fuels, 2009. **23**(8): p. 4196-4201.
3. Jiang, T., et al., *Plasma Methane Conversion Using Dielectric-Barrier Discharges with Zeolite A.* Catal. Today, 2002. **72**: p. 229-235.
4. Zhang, K., B. Eliasson, and U. Kogelschatz, *Direct Conversion of Greenhouse Gases to Synthesis Gas and C_4 Hydrocarbons over Zeolite HY Promoted by a Dielectric-Barrier Discharge.* Ind. Eng. Chem. Res., 2002. **41**(6): p. 1462-1468.
5. Eliasson, B., C.J. Liu, and U. Kogelschatz, *Direct Conversion of Methane and Carbon Dioxide to Higher Hydrocarbons Using Catalytic Dielectric-Barrier Discharges with Zeolites.* Ind. Eng. Chem. Res., 2000. **39**(5): p. 1221-1227.
6. Zhang, K., U. Kogelschatz, and B. Eliasson, *Conversion of Greenhouse Gases to Synthesis Gas and Higher Hydrocarbons.* Energ. Fuel., 2001. **15**(2): p. 395-402.
7. Goujard, V., J.M. Tatibouet, and C. Batiot-Dupeyrat, *Use of a Non-Thermal Plasma for the Production of Synthesis Gas from Biogas.* Appl. Catal. A Gen., 2009. **353**(2): p. 228-235.
8. Kraus, M., et al., *CO_2 Reforming of Methane by the Combination of Dielectric-Barrier Discharges and Catalysis.* Phys. Chem. Chem. Phys., 2001. **3**(3): p. 294-300.

9. Adams, J.M. and D.A. Haselden, *The Structure of Dehydrated Zeolite 3A (Si/Al = 1.01) by Neutron Profile Refinement.* J. Solid State Chem., 1983. **47**(2): p. 123-131.
10. Smit, B. and T.L.M. Maeson, *Towards a Molecular Understanding of Shape Selectivity.* Nature, 2008. **451**(7): p. 671-678.
11. Manley, T.C., *The Electric Characteristics of the Ozonator Discharge.* Trans. Electrochem. Soc., 1943. **84**: p. 83-96.
12. Liu, C.J., et al., *Methane Conversion to Higher Hydrocarbons in the Presence of Carbon Dioxide Using Dielectric-Barrier Discharge Plasmas.* Plasma Chem. Plasma P., 2001. **21**(3): p. 301-310.
13. Rico, V.J., et al., *Evaluation of Different Dielectric Barrier Discharge Plasma Configurations as an Alternative Technology for Green C_1 Chemistry in the Carbon Dioxide Reforming of Methane and the Direct Decomposition of Methanol.* J. Phys. Chem. A, 2010. **114**(11): p. 4009-4016.
14. Zhang, A.-J., et al., *Conversion of Greenhouse Gases into Syngas via Combined Effects of Discharge Activation and Catalysis.* Chem Eng. J., 2009. **156**: p. 601-606.
15. Massines, F., et al., *Recent Advances in the Understanding of Homogeneous Dielectric Barrier Discharges.* Eur. Phys. J. Appl. Phys., 2009. **47**(2): p. 10.
16. Tu, X., H.J. Gallon, and J.C. Whitehead. *Electrical and Spectroscopic Diagnostics of Atmospheric Nitrogen Dielectric Barrier Discharge: Effect of Packing Catalysts*. in *Hakone XII*. 2010. Trenčianske Teplice, Slovakia.
17. Falkenstein, Z. and J.C. Coogan, *Microdischarge Behaviour in the Silent Discharge of Nitrogen-Oxygen and Water-Air Mixtures.* J. Phys. D Appl. Phys., 1997. **30**: p. 817-825.
18. Valdivia-Barrientos, R., et al., *Analysis and Electrical Modelling of a Cylindrical DBD Configuration at Different Operating Frequencies.* Plasma Sources Sci. T., 2006. **15**: p. 237-245.
19. Wagner, H.-E., et al., *The Barrier Discharge: Basic Properties and Applications to Surface Treatment.* Vacuum, 2003. **71**: p. 417-436.
20. Kim, H.H., J.H. Kim, and A. Ogata, *Microscopic Observation of Discharge Plasma on the Surface of Zeolites Supported Metal Nanoparticles.* J. Phys. D Appl. Phys., 2009. **42**(13): p. 10.
21. Kim, H.-H., J.-H. Kim, and A. Ogata. *Adsorption and Oxygen Plasma-Driven Catalysis for Total Oxiadtion of VOCs*. in *The 6th International Symposium on Non-Thermal Plasma Technology for Pollution Control and Sustainable Energy Development*. 2008. Wan-Li, Taipei, Taiwan.
22. Bond, G.C., *Heterogeneous Catalysis: Principles and Applications*. 2nd ed. 1987, New York: Oxford Science Publications.
23. Istadi, N.A.S.A., *Co-generation of Synthesis Gas and C_2+ Hydrocarbons from Methane and Carbon Dioxide in a Hybrid Catalytic-Plasma Reactor.* Fuel, 2006. **85**: p. 577-592.
24. Van Durme, J., et al., *Combining Non-Thermal Plasma with Heterogeneous Catalysis in Waste Gas Treatment: A Review.* Appl. Catal. B Environ., 2008. **78**(3-4): p. 324-333.
25. Sun, M., et al., *Dielectric Constant Measurement of Zeolite Powders by Time-Domain Reflectometry.* Micropor. Mesopor. Mat., 2009. **123**(1-3): p. 10-14.

26. Accuratus. *Aluminium Oxide, Al_2O_3 [online] (http://accuratus.com/alumox.html)*. [cited 14/10/2010].
27. Wang, H.-L., *Structure and Dielectric Properties of Perovskite - Barium Titanate ($BaTiO_3$)*. 2002, San Jose State University.
28. *The Physics Hypertextbook [online]*. http://physics.info/dielectrics/. [cited 14/10/2010].

4. Dry Reforming of Methane in a Coaxial DBD Reactor: Variation of CH_4/CO_2 Ratio and Introduction of a NiO/Al_2O_3 Catalyst

4.1 Introduction

The work in this chapter has been carried out whilst a fellow at the National Institute for Advanced Industrial Science and Technology (AIST) in Tsukuba, Japan. This fellowship has formed part of an ongoing collaboration with the Excited State Chemistry Group of these national laboratories. Consequently, the experimental set-up and DBD reactor used in this study is slightly different to that used in the rest of this thesis.

The present understanding of the reactions of CH_4 and CO_2 in plasma-assisted dry reforming of methane is limited, making it difficult to optimise reaction conditions or predict end-products theoretically. In a review by Istadi [1] the discharge power, discharge gap, voltage and CH_4/CO_2 molar ratio are identified as having the most significant effects on the reaction performance. The reforming of CH_4-only and CO_2-only in DBDs has received little attention in the literature; however, the behaviour of these species in a plasma discharge has fundamental implications for plasma-assisted dry reforming of methane. The reforming of undiluted CH_4 in DBD with a ceramic foam packing material has been investigated by Kraus et al. [2], who identified the reaction products as H_2, ethane, ethylene and propane. Paulussen et al. [3] have investigated undiluted CO_2 reforming in a DBD reactor for the formation of CO and O_2. Variation of CH_4/CO_2 mixing ratio for dry reforming of methane in DBDs has been studied over various zeolites [4, 5], Ni and Rh-coated ceramic foams [6], perovskite $LaNiO_3$ [7] and in the absence of a catalyst [8-10]. In general, it is agreed that increasing the discharge power or the inlet gas temperature leads to increased reactant conversions but the effects of mixing ratio and reactor geometries on dry reforming of methane is more ambiguous, particularly concerning the relative selectivities of products.

This chapter investigates the effect of the variation in feed gas ratios (CH_4/CO_2) in the absence of a catalyst, including the reforming of 100 % CH_4 and 100 % CO_2 in a DBD reactor. The effect of the addition of a NiO/Al_2O_3 catalyst to the discharge gap is also examined for different feed gas ratios. The catalyst used in these experiments is a commercial steam methane reforming catalyst. In the latter part of this chapter, results for the calculated thermodynamic equilibrium gas compositions for dry reforming of methane are presented for different feed gas ratios and comparisons are made with the reaction in non-equilibrium plasma.

4.2 Experimental Section

The experimental set-up used for this investigation was similar to that used at The University of Manchester except for the addition of a valve with gas sampling point downstream of the DBD reactor and the use of FTIR spectroscopy in place of the micro-GC, as shown in Figure 4.0.

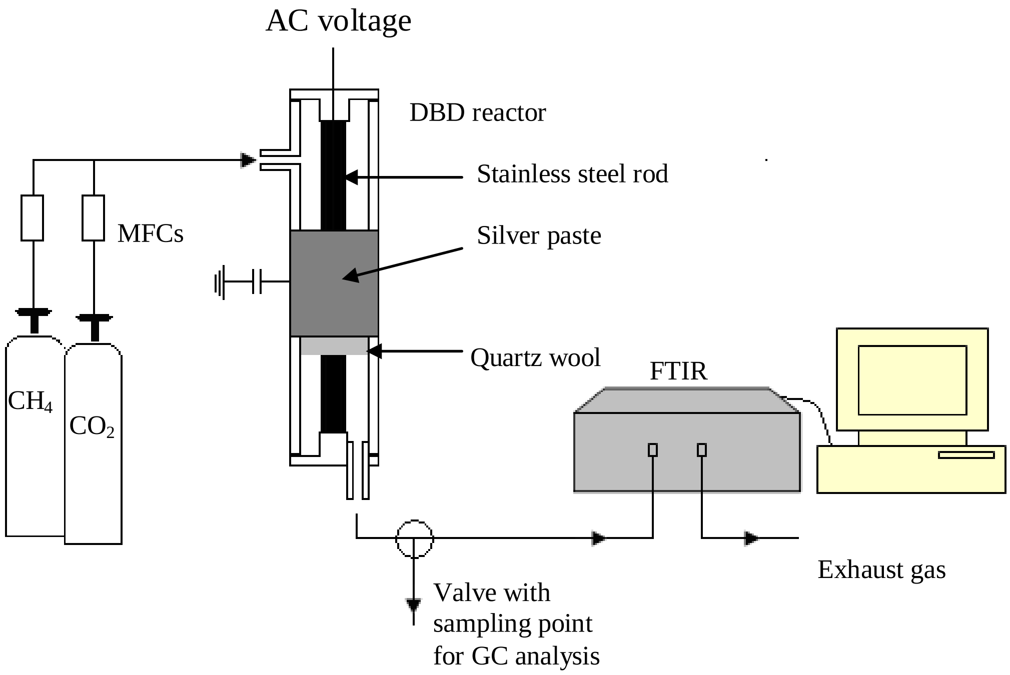

Figure 4.0: Schematic diagram of the experimental set-up and coaxial DBD reactor used for dry reforming of methane experiments (carried out at AIST, Tsukuba).

Methane and carbon dioxide (Takachiho, 99.99% and 99.95 % respectively) gas flows (50 – 100 ml min^{-1}) were controlled by previously calibrated mass flow controllers (Kofloc) and fed into the reactor at a pressure of 1 bar. Concentrations of CH_4 and CO_2 were measured using FTIR spectroscopy (Perkin Elmer, Spectrum One) with a 50 mm length gas cell (Pike Technologies) to avoid signal saturation caused by high concentrations of these reactant gases. The humidity of the laboratory air was controlled throughout and the area immediately surrounding the gas cell was continuously purged with N_2 to avoid any interference from atmospheric H_2O vapour and CO_2. Concentrations of product gases (H_2, CO and C_2 – C_3 hydrocarbons) were measured using three GC instruments with a sampling and injection technique (H_2 – Shimadzu GC-8A with TCD, hydrocarbons – Shimadzu GC-14A with FID, CO – Shimadzu GC-14B with TCD).

Figure 4.0 also shows the coaxial DBD reactor that was used in these experiments. It consisted of a single quartz tube (OD: 24 mm, ID: 20.5 mm) which acted as the dielectric barrier, as well as containing the gas flow. A concentrically positioned stainless steel rod (OD: 12.5 mm) served as the inner electrode and a silver paste (Nilaco) that was uniformly painted to the outside of the quartz tube (5 cm length) served as the outer electrode. The volume of the discharge region was 10.4 cm^3. The reactor was housed in a furnace, which was switched off after pre-treatment of the catalyst.

During plasma-catalytic experiments, a 33 wt. % NiO/Al_2O_3 catalyst (Johnson Matthey) was introduced to the discharge gap. Prior to use, the catalyst was crushed and sieved to give particle sizes of 1 – 1.2 mm and was heated to 300 °C in a N_2 atmosphere to remove any adsorbed species. During the experiments, the catalyst filled the entire discharge gap and was supported by quartz wool, which was positioned just below the discharge region (Fig. 4.0). Approximately 12 g of catalyst were used for each experiment. Between experiments an O_2 plasma was used to oxidise any carbonaceous deposits on the reactor walls; a technique which has been described by Kim et al. [11].

A high voltage power supply (Dawonsys) was used to apply a variable AC voltage of < 28 $kV_{pk\text{-}pk}$ at a fixed sine wave frequency of ~ 1 kHz. The voltage-current waveforms were measured using an oscilloscope (Tektronix TDS-3034B) and the plasma power was calculated using the Lissajous method by software that was developed in-house at AIST (V-Q Lissajous Program Ver. 1.71). During these experiments, the power in the reactor was increased between each measurement up to a maximum of ~ 30 W. In order to achieve a higher specific input energy (SIE), the total flow rate was varied between 50 and 100 ml min^{-1}. The SIE is defined as shown by equation 4.0. The short lifetimes of active species and the rapid reactions in a plasma discharge means that the gas flow rates (and residence times) are not a limiting factor in plasma reactions and therefore do not directly influence the reaction performance. However, the specific input energy is an important variable that directly influences the reaction and this parameter does change with flow rate and/or residence time. The experiments that are reported in Chapter 3 were carried out at a constant flow rate; therefore it was not necessary to convert the conditions to units of SIE (kJ L^{-1}). For comparison, the experiments in this chapter were performed in the range 5 – 25 kJ L^{-1} and the experiments in Chapter 3 were performed in the range 23 – 43 kJ L^{-1}.

$$\text{Specific Input Energy (kJ L}^{-1}\text{)} = [\text{Power (W)} / \text{Flow rate (L s}^{-1}\text{)}] / 1000 \qquad (4.0)$$

Calculations of conversions, selectivities, H_2 yields and carbon balances were performed as described in Chapter 3 (equations 3.0 – 3.4).

4.3 Results

In order to optimise reaction conditions for dry reforming of methane, it is important to gain an understanding of the fundamental reactions taking place in both CH_4-only and CO_2-only plasmas in the absence of a catalyst.

4.3.1 CH_4 Reforming

The results for reforming of CH_4 in a DBD are shown in Figures 4.1 – 4.3. The conversions of CH_4 increase from 0.8 – 2.5 % with increasing SIE in the range 4.7 – 10.9 kJ L^{-1} (Fig. 4.1). The low conversions reflect the high stability of the CH_4 molecule. Figure 4.2 shows that the relative selectivities of the products of CH_4 reforming decrease in the order: $C_2H_2 > H_2 \approx C_3H_8 > C_2H_4 \approx C_2H_6 \approx C_3H_6$.

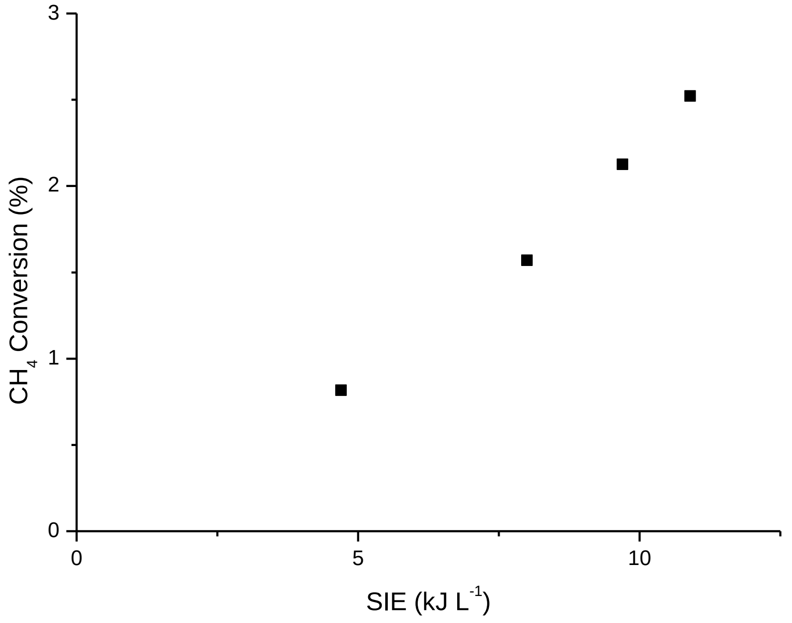

Figure 4.1: Conversions of CH_4 in a DBD reactor (feed gas 100 % CH_4).

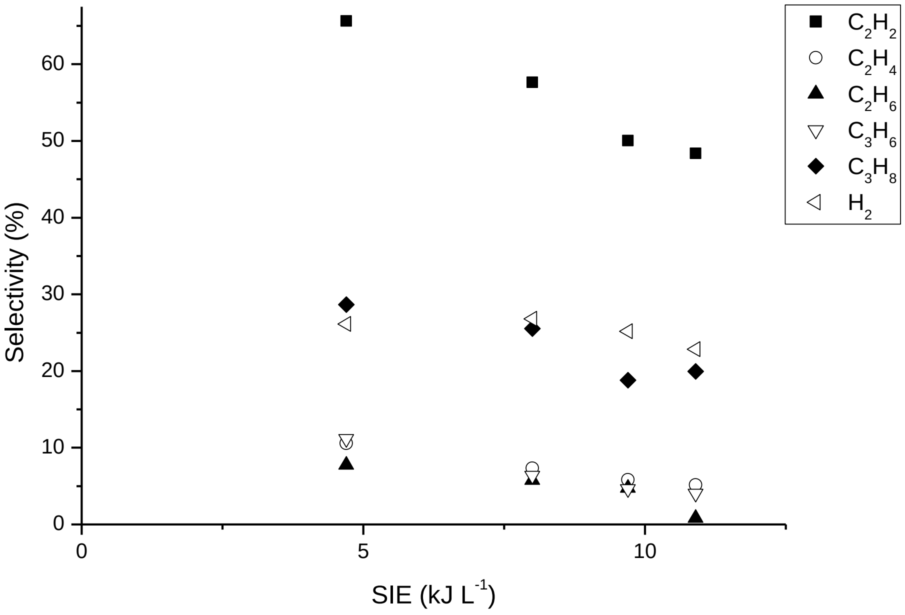

Figure 4.2: Product selectivities during the reforming of CH_4 in a DBD reactor (feed gas 100 % CH_4).

The decrease in product selectivities with increasing SIE (Fig. 4.2) is not considered to be significant in this case due to an association of larger measurement uncertainties for very small gas concentrations (< 0.5 % of the total gas concentration) using GC. Kraus et al. [6] performed CH_4 reforming in a DBD reactor containing a ceramic foam. The detected hydrocarbon products were C_2H_6/C_2H_4 (unseparated) and C_3H_8 in a 3/1 ratio. Brock et al. [2] carried out reforming of 1.13 % CH_4 diluted in helium using a DBD, they reported ethane and propane to be the main reaction products. These studies are in contrast to this investigation where acetylene (C_2H_2) was observed in the highest concentration amongst the reaction products.

In a plasma discharge, the formation of higher hydrocarbons proceeds via reactions involving ions, radicals and electronically excited species. Radical reactions where the rate-determining step is the formation of methyl radicals ($CH_3^{\cdot}$) are likely to be the most important processes in plasma mechanisms [12]. Reactions also proceed via $CH_2^{\cdot}$ and $CH^{\cdot}$ radicals but the rate of formation of these species is lower than for methyl radicals and therefore is considered less significant, as implied by the rate constants for the electron impact processes shown in equations 4.0 and 4.1. Table 4.0 lists the main radical reactions responsible for the formation of H_2 and light hydrocarbons, and demonstrates the complexity of the possible reaction mechanisms occurring within the plasma volume. Competing reactions include the recombination of radicals to form CH_4 and the electron impact dissociations of the higher hydrocarbons to give lighter hydrocarbon products, as well as the reactions of excited state species. There are generally two routes to C_2 hydrocarbons: reactions involving *primary radicals* ($CH_3^{\cdot}$, $CH_2^{\cdot}$, $CH^{\cdot}$ and $H^{\cdot}$) and those involving *secondary radicals* ($C_2H_3^{\cdot}$, $C_2H_5^{\cdot}$, $C_2H_7^{\cdot}$ etc.). It could be expected that C_3+ hydrocarbons would be less abundant as they can only be formed through reactions of secondary radicals. However, in this investigation C_3H_8 was more abundant than C_2H_6 and C_2H_4 in the reforming products.

Eq.	Reaction	Rate constant / cm^3 molecule^{-1} s^{-1}	Temperature Range / K
	Primary Processes		
4.0	$CH_4 + e^- \rightarrow CH_3^{\cdot} + H^{\cdot} + e^-$	3.46×10^{-10}	400
4.1	$CH_4 + e^- \rightarrow CH_2^{\cdot} + H_2 + e^-$	3.13×10^{-10}	400
4.2	$CH_4 + e^- \rightarrow CH^{\cdot} + H_2 + H^{\cdot} + e^-$		
4.3	$CH_4 + e^- \rightarrow C + H_2 + H_2 + e^-$		
	Hydrogen Formation		
4.4	$H^{\cdot} + H^{\cdot} \rightarrow H_2$	8.0×10^{-14}	400
	Ethane Formation		
4.5	$CH_3^{\cdot} + CH_3^{\cdot} \rightarrow C_2H_6$	1.19×10^{-7}	400
4.6	$CH_4 + CH_2^{\cdot} \rightarrow C_2H_6$	4.3×10^{-1}	298
4.7	$C_2H_6 + e^- \rightarrow C_2H_5^{\cdot} + H^{\cdot} + e^-$		
4.8	$C_2H_5^{\cdot} + C_2H_5^{\cdot} \rightarrow C_2H_4 + C_2H_6$	2.51×10^{-11}	323 – 488
	Ethylene Formation		
4.9	$CH_3^{\cdot} + CH_3^{\cdot} \rightarrow C_2H_4 + H_2$		
4.10	$CH_2^{\cdot} + CH_2^{\cdot} \rightarrow C_2H_4$		
4.11	$CH_3^{\cdot} + CH_2^{\cdot} \rightarrow C_2H_4 + H^{\cdot}$	7.01×10^{-11}	300 – 3000
4.12	$C_2H_5 + CH_3^{\cdot} \rightarrow C_2H_4 + CH_4$	9.13×10^{-12}	351 – 521
4.13	$C_2H_5^{\cdot} + CH_2^{\cdot} \rightarrow C_2H_4 + CH_3^{\cdot}$	3.01×10^{-11}	300 – 2500
4.8	$C_2H_5^{\cdot} + C_2H_5^{\cdot} \rightarrow C_2H_4 + C_2H_6$	2.51×10^{-11}	323 – 488
4.14	$C_2H_5^{\cdot} + H^{\cdot} \rightarrow C_2H_4 + H_2$	2.82×10^{-12}	503 – 753
4.15	$C_2H_5^{\cdot} \rightarrow C_2H_4 + H^{\cdot}$	3.04×10^{-8}	400
	Acetylene Formation		
4.16	$CH_2^{\cdot} + CH_2^{\cdot} \rightarrow C_2H_2 + H_2$	5.3×10^{-11}	298
4.17	$CH^{\cdot} + CH^{\cdot} \rightarrow C_2H_2$	1.99×10^{-10}	298
4.18	$CH_2^{\cdot} + CH^{\cdot} \rightarrow C_2H_2 + H^{\cdot}$		
4.19	$C_2H_4 + H^{\cdot} \rightarrow C_2H_3^{\cdot} + H_2$	2.84×10^{-11}	300 – 1500

4.20	$C_2H_4 + e^- \rightarrow C_2H_3^{\cdot} + H^{\cdot} + e^-$		
4.21	$C_2H_3^{\cdot} + H^{\cdot} \rightarrow C_2H_2 + H_2$	2.02×10^{-10}	200 – 2000
4.22	$C_2H_3^{\cdot} \rightarrow C_2H_2 + H^{\cdot}$	4.98×10^{-9}	500 – 2500
	Propane Formation		
4.23	$C_2H_6 + CH_3^{\cdot} \rightarrow C_3H_8 + H^{\cdot}$	4.7×10^{-11}	300 – 800
4.24	$C_2H_5^{\cdot} + CH_3^{\cdot} \rightarrow C_3H_8$	4.06×10^{-11}	400
4.25	$C_2H_6 + CH_2^{\cdot} \rightarrow C_3H_8$	4.8×10^{-12}	304
4.26	$C_2H_5^{\cdot} + CH_4 \rightarrow C_3H_8 + H_2$		
4.27	$C_2H_5^{\cdot} + C_2H_4 \rightarrow C_3H_8 + CH^{\cdot}$		
4.28	$C_2H_5^{\cdot} + C_2H_5^{\cdot} \rightarrow C_3H_8 + CH_2^{\cdot}$		
	Propene Formation		
4.29	$C_2H_3^{\cdot} + CH_3^{\cdot} \rightarrow C_3H_6$	1.2×10^{-10}	298
4.30	$C_2H_4 + CH_3^{\cdot} \rightarrow C_3H_6 + H^{\cdot}$		
4.31	$C_2H_5^{\cdot} + CH_3^{\cdot} \rightarrow C_3H_6 + H_2$		
4.32	$C_2H_4 + CH_2^{\cdot} \rightarrow C_3H_6$		
4.33	$C_2H_5^{\cdot} + CH_2^{\cdot} \rightarrow C_3H_6 + H^{\cdot}$		
4.34	$C_2H_6 + CH_2^{\cdot} \rightarrow C_3H_6 + H_2$		
4.35	$C_2H_6 + CH^{\cdot} \rightarrow C_3H_6 + H^{\cdot}$	3.0×10^{-11}	298
4.36	$C_3H_8 + e^- \rightarrow C_3H_7^{\cdot} + H^{\cdot} + e^-$		
4.37	$C_3H_7^{\cdot} \rightarrow C_3H_6 + H^{\cdot}$		

Table 4.0: Radical reactions and kinetic data (where available at low temperatures) for the reforming of CH_4 in a plasma discharge (rate data taken from NIST online database [13]).

Figure 4.3 shows that the carbon balance in the gas stream decreases with increasing SIE. The selectivity towards coking can be obtained by subtracting the selectivities of carbon-containing products from 100 %, using Figure 4.2 (assuming that formation of other unidentified carbonaceous products is negligible). Using this method, the selectivity towards solid carbon at 10.9 kJ L^{-1} is ~ 22 %. This accounts for a loss of ~ 0.6 % of the total carbon from the gas mixture. However, a larger loss of ~ 2 % carbon is apparent from the carbon balance. The discrepancy between these values is within the uncertainty of 3 % associated with the measurements. Brock et al. observed a very large selectivity towards coking of 89.0 % (with 6.8 % CH_4 conversion) in a DBD reactor [2]. However, in this case the CH_4 reactant was diluted in helium which may have had a detrimental effect on the relative product selectivities. In the study of undiluted CH_4 reforming by Kraus [14], carbon deposits were observed on the ceramic foam that was used to pack a DBD reactor, but the deposition was not quantified.

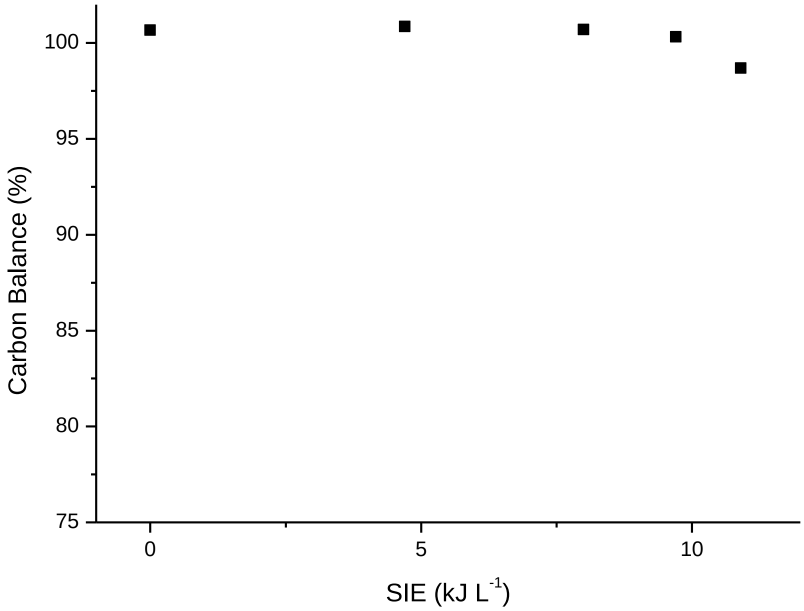

Figure 4.3: Gas stream carbon balance during the reforming of CH_4 in a DBD reactor.

4.3.2 CO_2 Reforming

$$CO_2 \rightarrow CO + \tfrac{1}{2} O_2 \qquad \Delta H^o = 283\ kJ\ mol^{-1} \qquad (4.38)$$

The plasma reforming of CO_2 is much more straightforward than plasma reforming of CH_4, owing to the formation of only two gaseous products as shown by equation 4.38. The conversions of CO_2 increased with increasing SIE from 3.1 – 5.3 % at specific input energies of 6.1 – 13.6 kJ L^{-1} (Figure 4.4). For the same SIE, the conversions of CO_2 are approximately twice as large as the conversions of CH_4. This is thought to be due to a lower threshold energy for the electron impact dissociations of CO_2 (~ 6.4 eV) compared with that of CH_4 (~7.5 eV), as discussed in section 4.4.

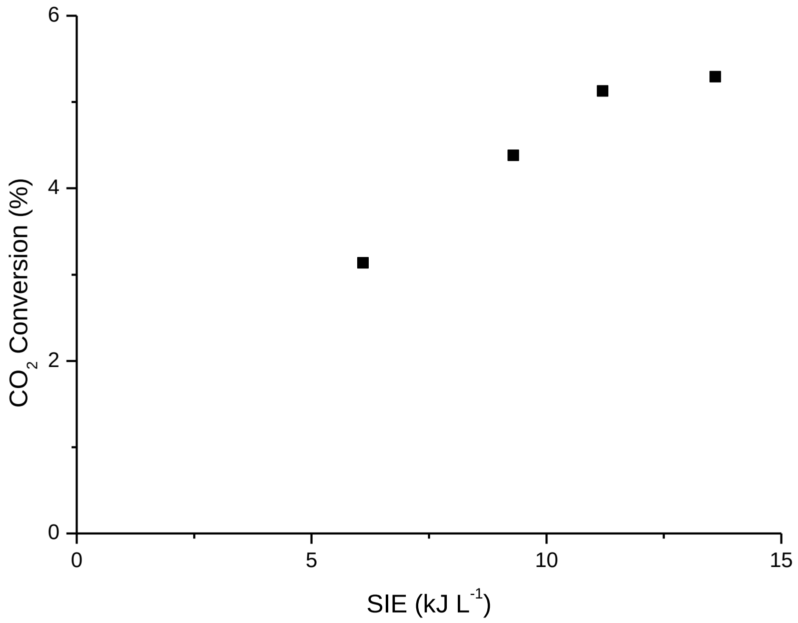

Figure 4.4: CO_2 conversion in a DBD reactor (feed gas 100 % CO_2).

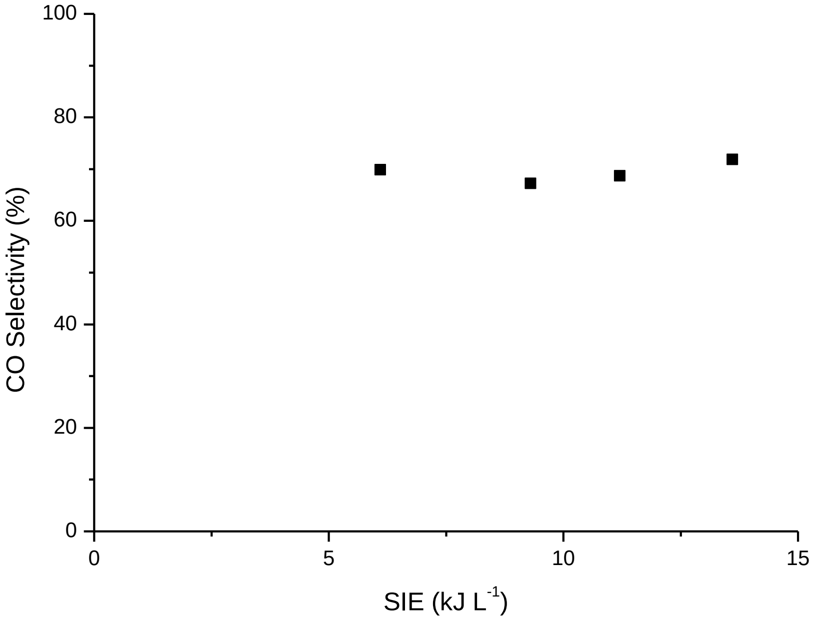

Figure 4.5: CO selectivity during the reforming of CO_2 in a DBD reactor (feed gas 100 % CO_2).

The selectivity towards CO is largely independent of the SIE. Under the range of conditions tested, the CO selectivity varied between 67.3 % and 71.9 %. Similar results were obtained by Paulussen et al. [3], who reported that the CO yield was weakly dependent on the discharge power, varying between 3.5 % and 6 % for a variation of wall power in the range 100 – 200 W. The primary and secondary radical processes showing the formation of CO and O_2 are shown in Table 4.1. The dissociation of CO_2 is responsible for the formation of carbon monoxide and oxygen radicals (4.39) or solid carbon and O_2 (4.40). O_2 can be formed during the coupling of oxygen radicals (4.41). In addition, CO can undergo a dissociation that is responsible for the deposition of solid carbon (4.42).

Eq.	Reaction	Rate constant / cm^3 $molecule^{-1}$ s^{-1}	Temperature Range / K
	Primary Processes		
4.39	$CO_2 + e^- \rightarrow CO + O^{\cdot} + e^-$	1.29×10^{-9}	400
4.40	$CO_2 + e^- \rightarrow C + O_2 + e^-$		
	Secondary Processes		
4.41	$O^{\cdot} + O^{\cdot} \rightarrow O_2$	1.39×10^{-9}	400
4.42	$CO + e^- \rightarrow C + O^{\cdot} + e^-$		

Table 4.1: Radical reactions and kinetic data (where available at low temperatures) for reforming of CO_2 in a plasma discharge (rate data taken from NIST online database [13]).

The carbon balance in the gas stream during the plasma-assisted reforming of CO_2 is shown in Figure 4.6. The carbon balance decreases slightly with increasing SIE. At 13.6 kJ L^{-1}, the selectivity towards solid carbon is 28.1 %, accounting for a loss of ~ 1.5 % of the total carbon from the gas mixture. In a similar investigation, Kraus et al [6] observed carbon in the reactor after dry reforming of CH_4, but they were unable to quantify this carbon deposition.

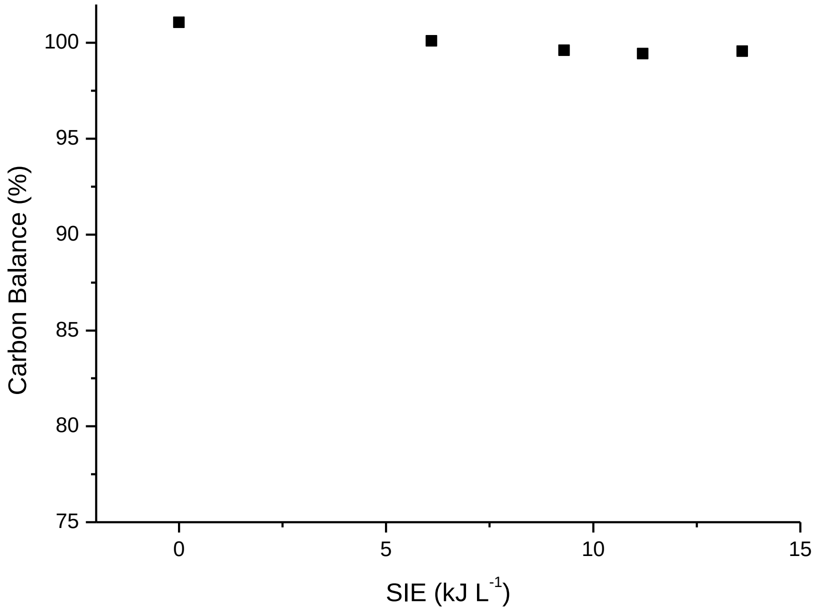

Figure 4.6: Gas stream carbon balance during the reforming of CO_2 in a DBD reactor.

4.3.3 Variation of CH_4/CO_2 Ratio

Methane conversions are strongly influenced by the presence of CO_2. The conversions of CH_4 increased significantly with increasing CO_2 concentration in the feed gas. This is shown in Figure 4.7 in the results for dry reforming of CH_4 at three different CH_4/CO_2 ratios. The conversions of CO_2 increased only slightly with increasing CO_2 in the feed gas, as shown in Figure 4.8. In agreement with these observations, Goujard et al. [7] reported increased conversions of both reactants with a decreasing CH_4/CO_2 feed gas ratio. Conversions of CH_4 are promoted by the presence of excited oxygen species in a plasma discharge containing CO_2 [1]. The reactive oxygen may assist by the removal of H atoms from CH_4 to generate hydroxyl radicals (4.43) [7]. In turn, hydroxyl radicals could have a similar role in the reaction chemistry by removing an H atom from CH_4 to form H_2O (4.44).

$CH_4 + O^{\cdot} \rightarrow CH_3^{\cdot} + {}^{\cdot}OH$ (4.43)

$CH_4 + {}^{\cdot}OH \rightarrow CH_3^{\cdot} + H_2O$ (4.44)

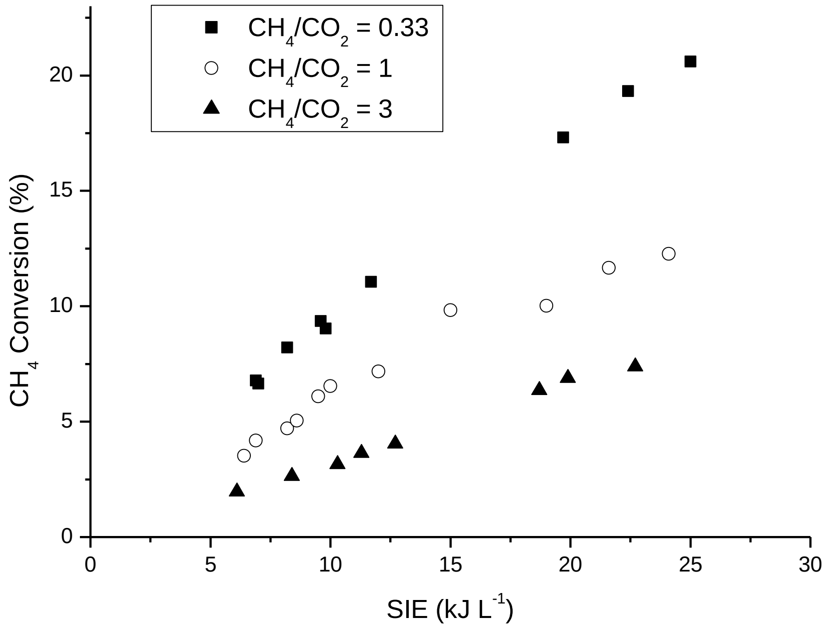

Figure 4.7: Effect of CH_4/CO_2 ratio on CH_4 conversions in plasma-assisted dry reforming of methane in a DBD reactor.

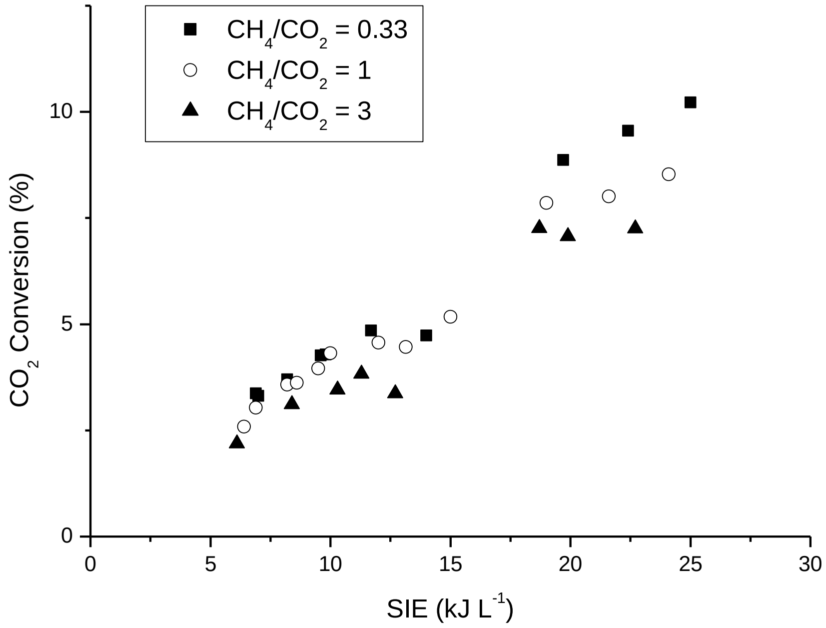

Figure 4.8: Effect of CH_4/CO_2 ratio on CO_2 conversions in plasma-assisted dry reforming of methane in a DBD reactor.

During plasma-assisted dry reforming of methane, the conversions of CH_4 are greater than the conversions of CO_2. This is in agreement with the results obtained in Chapter 3. However, these results are surprising, considering the results for reforming of CH_4-only and CO_2-only, where the CO_2 conversions were greater than those of CH_4. It has been suggested by Yao et al. [15] that CO_2 conversions during dry reforming of methane are hindered by a competing reaction between CO and $^{\cdot}OH$ radicals (4.45); a process that is not possible during CO_2 reforming alone.

$$CO + {}^{\cdot}OH \rightarrow CO_2 + H^{\cdot} \qquad (4.45)$$

The relative product selectivities for each of the three CH_4/CO_2 feed gas ratios are shown in Figures 4.9 – 4.11. It is clear that for higher CH_4/CO_2 ratios, higher selectivities towards C_2 and C_3 hydrocarbons are obtained. The highest selectivity of hydrocarbons was observed for a pure methane feed; however, the conversion of CH_4 was lower in the absence of CO_2. The selectivity towards H_2 was found to increase slightly for increasing the CH_4/CO_2 ratio. It follows that selectivity towards CO is strongly dependent on the feed gas ratio, with greater selectivities when there is a higher CO_2 content in the feed. These results are in agreement with those obtained in similar studies [7, 10, 16].

Figure 4.12 shows the H_2 yields for three different CH_4/CO_2 feed gas ratios. H_2 yields were greater when the CH_4 concentration in the feed was low due to enhanced conversions of CH_4. The H_2/CO ratio in the product gas is shown in Figure 4.13, where higher CH_4/CO_2 ratios lead to a lower syngas ratio.

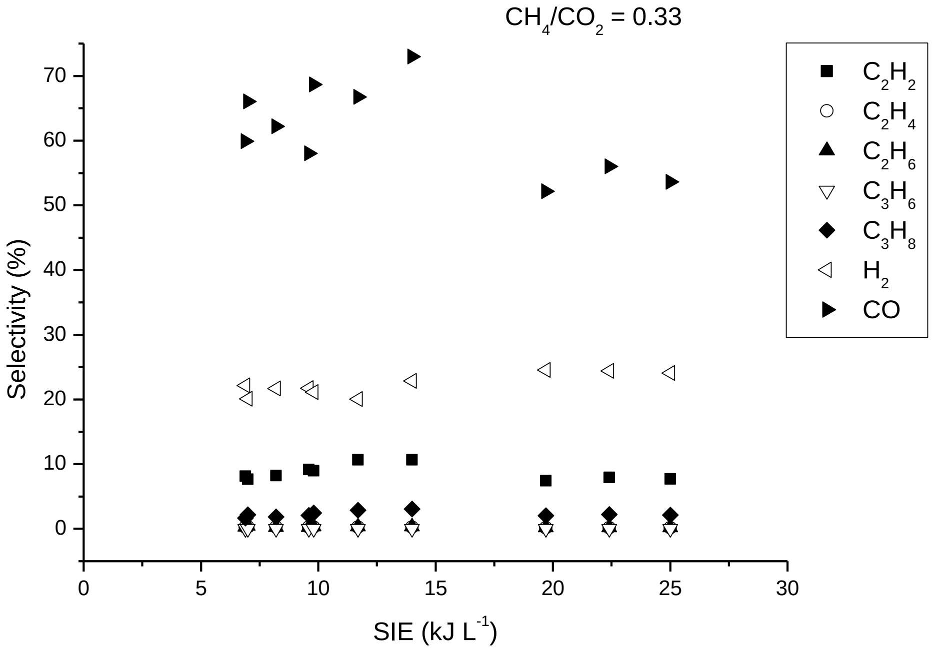

Figure 4.9: Product selectivities during the plasma-assisted dry reforming of CH_4, where CH_4/CO_2 = 0.33.

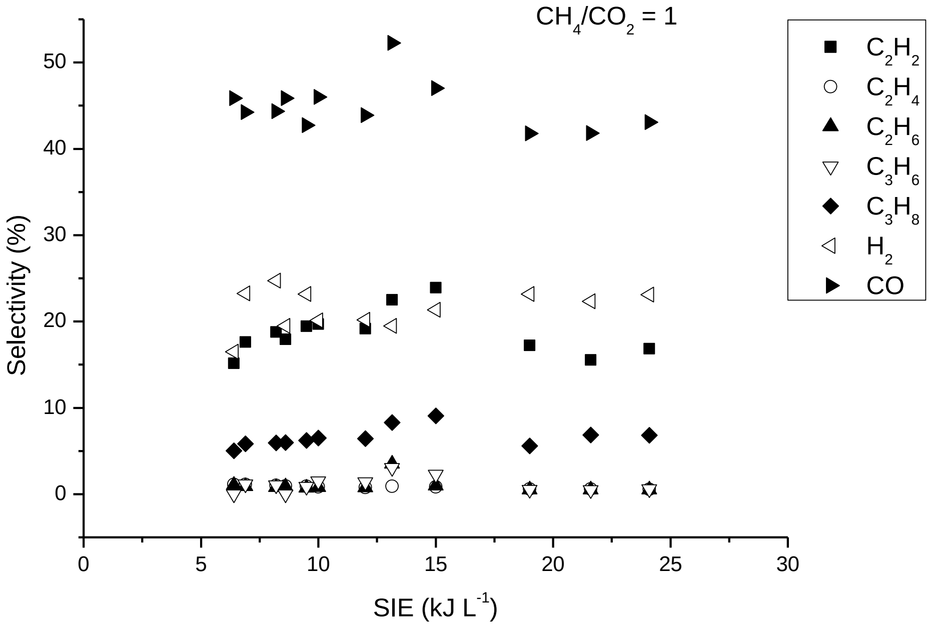

Figure 4.10: Product selectivities during the plasma-assisted dry reforming of CH_4, where CH_4/CO_2 = 1.

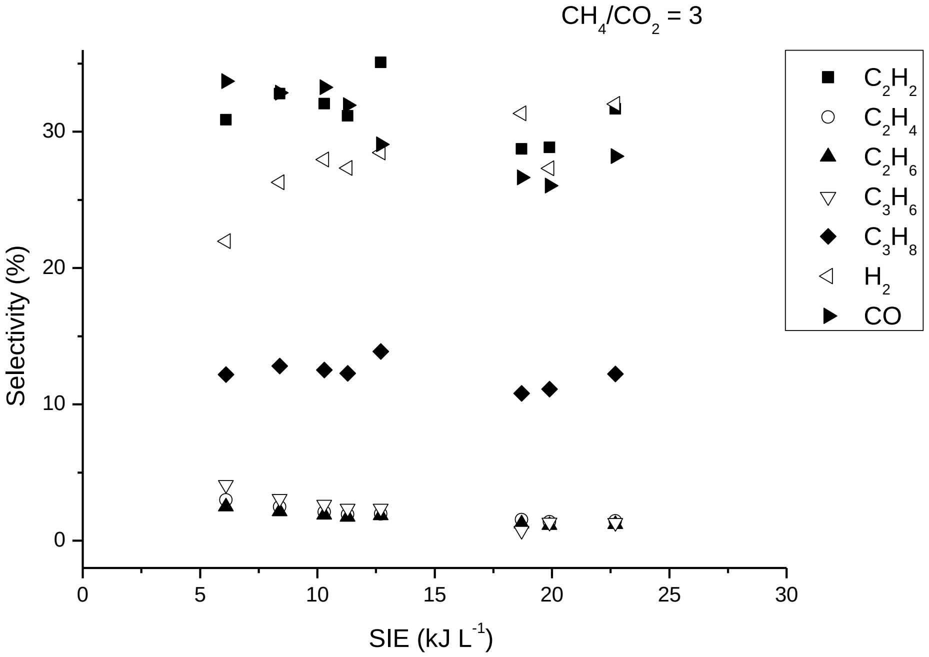

Figure 4.11: Product selectivities during the plasma-assisted dry reforming of CH_4, where $CH_4/CO_2 = 3$.

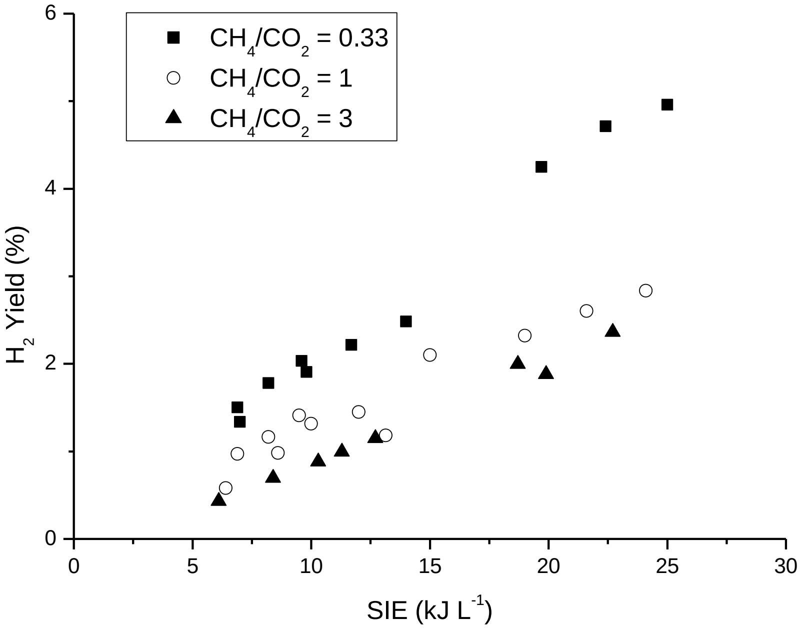

Figure 4.12: Effect of CH_4/CO_2 ratio on H_2 yield in plasma-assisted dry reforming of methane in a DBD reactor.

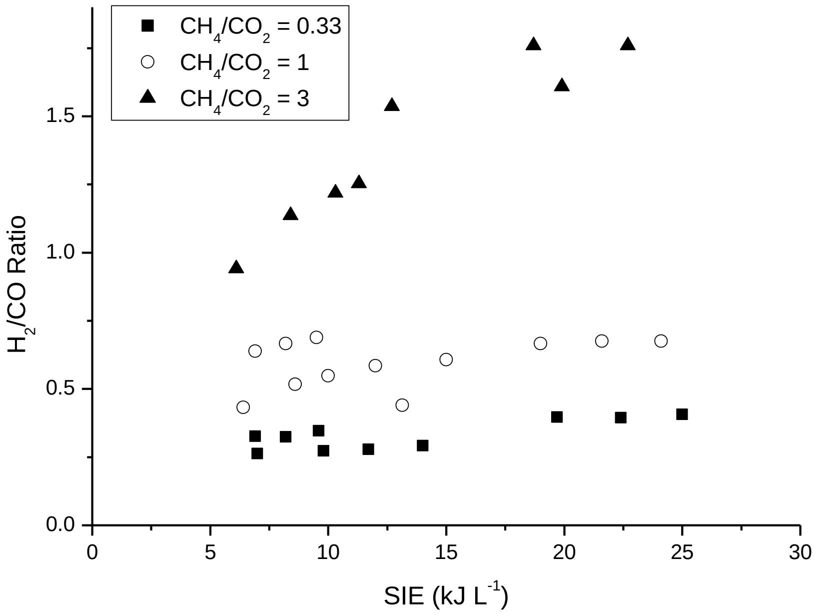

Figure 4.13: Effect of CH_4/CO_2 ratio on the H_2/CO ratio in plasma-assisted dry reforming of methane in a DBD reactor.

The generation of $O^{\cdot}$ and $^{\cdot}OH$ radicals in dry reforming of CH_4 can create additional product channels leading to the formation of oxygenated species. The formation of H_2O, methanol (CH_3OH), dimethyl ether (CH_3OCH_3) and formaldehyde (CH_2O) have been reported as minor reaction products [10, 17] as well as heavier oxygenates including C_7 – C_{12} species [7]. Many different reactions are possible in a CH_4/CO_2 mixture, these have been listed by Nair et al. [18] showing the formation of many higher oxygenated compounds. In this investigation, a small amount of methanol was detected using a colourimetric methanol detection tube; however, quantification was not possible using this method. The most probable route to methanol formation is through the coupling of methyl and hydroxyl radicals (4.46).

$$CH_3^{\cdot} + {}^{\cdot}OH \rightarrow CH_3OH \qquad (4.46)$$

The results for the gas stream carbon balance show that deposition of carbon was more severe for mixing ratios with a lower CH_4/CO_2 ratio. However, this is due to the higher conversions of CH_4 and CO_2 in this case and no significant difference in the selectivities towards solid carbon could be derived from the experimental results. This is due to errors associated with the measurement of very small hydrocarbon concentrations giving a relatively large fluctuation in the calculated selectivities for the hydrocarbon species. Across each of the feed gas ratios, the selectivities towards solid carbon (or other unidentified carbonaceous products) fluctuated in the range 10 – 38 %. Goujard et al. [7] described the same observation as 'missing carbon' and it has been quantified as 34.2 – 43.1 %. However, in this case the missing carbon clearly increased with increasing CO_2 content in the feed gas. They suggested that the selectivity towards oxygenated species was higher in CO_2-rich mixtures. In contrast, Huang et al. [16] reported the opposite trend of increased 'missing carbon' for CH_4-rich mixtures, which they suggested was a result of CH_4 decomposition to give H_2 and solid carbon.

4.3.4 Variation of CH_4/CO_2 Ratio Using a NiO/Al_2O_3 Catalyst

The presence of a catalyst in a plasma discharge can affect the plasma reactions in a number of different ways, as previously discussed. It has been shown in Chapter 3 that introducing different packing materials into the discharge gap can affect the performance of plasma-assisted dry reforming of methane, despite an absence of active catalytic sites. This has been discussed in terms of the dielectric properties of the material, as well as the importance of particle size, shape and porosity, all of which are important considerations when selecting a reforming catalyst for use in a plasma system. Following on from this work, the effect of introducing an unreduced NiO/Al_2O_3 catalyst to the discharge gap has been investigated using three different CH_4/CO_2 feed gas ratios for comparison with previous results. In conventional catalytic reactions, this material does not show any catalytic activity in the oxidised form (it is active in the reduced Ni/Al_2O_3 form). The catalyst was not reduced in-situ during the plasma reaction in this study because the temperature of the plasma remained close to room temperature throughout. The use of Al_2O_3 as a packing material has been shown to decrease the reactant conversions during methane reforming compared to the reaction with no packing material at the same power. However, the presence of

33 wt. % NiO supported on Al_2O_3 may lower the dielectric constant and change the reaction performance, resulting in a possible catalytic effect.

The results for dry reforming of methane with an unreduced NiO/Al_2O_3 packed into the discharge gap of the DBD reactor are shown in Figures 4.14 – 4.20. The conversions of CH_4 (Figures 4.14) are not significantly changed in the presence of the catalyst compared with the plasma-only reaction. The conversions of CO_2 are increased in the presence of the NiO catalyst (Figure 4.15). One tentative explanation is that CO_2 is adsorbed more strongly onto alumina, resulting in a longer residence time for CO_2 molecules in the plasma and an increased probability of a dissociative reaction.

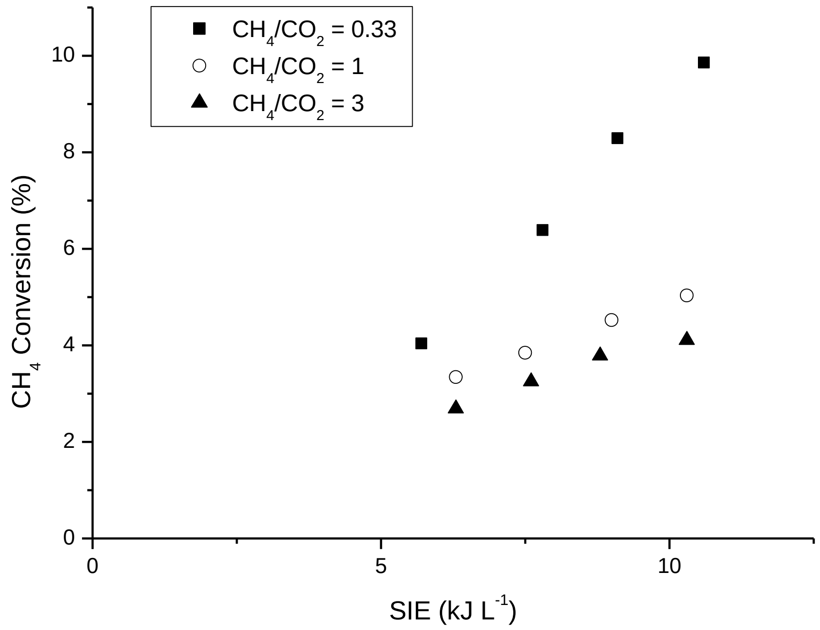

Figure 4.14: Effect of CH_4/CO_2 ratio on CH_4 conversions in plasma-assisted dry reforming of methane with unreduced NiO/Al_2O_3 in the DBD reactor.

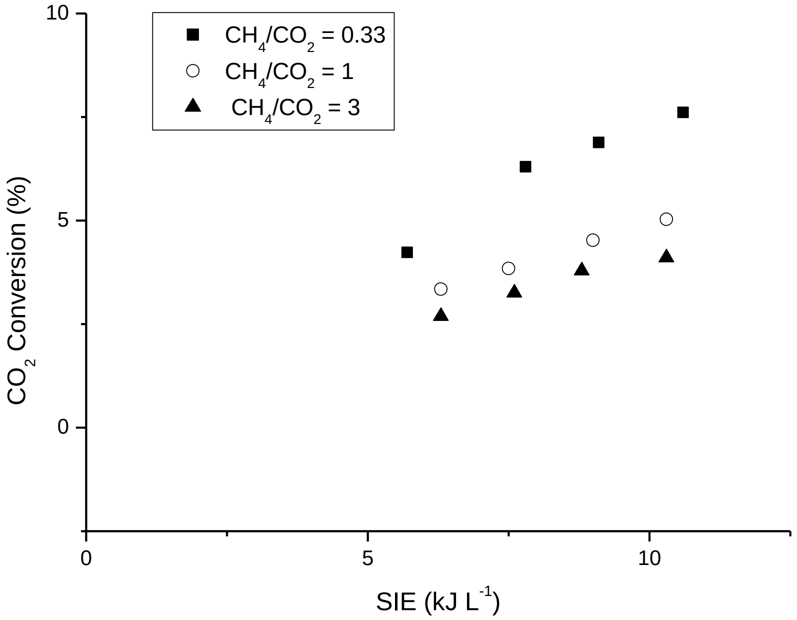

Figure 4.15: Effect of CH_4/CO_2 ratio on CO_2 conversions in plasma-assisted dry reforming of methane with unreduced NiO/Al_2O_3 in the DBD reactor.

The relative product selectivities for each of the three CH_4/CO_2 ratios tested are shown in Figures 4.16 – 4.18. The same general trends in product selectivities with different CH_4/CO_2 mixing ratios have been obtained in the presence and absence of the catalyst, although the product selectivities are not exactly the same in all cases. No significant differences in the product selectivities with and without the catalyst can be conclusively determined from the results. The H_2 yield at ~ 10 kJ L^{-1} varies between 0.6 – 1.6 % with the catalyst (Figure 4.19), compared with 0.9 – 1.9 % in the absence of the catalyst. The H_2/CO ratios in the presence of the catalyst are shown in Figure 4.20, these are comparable to the H_2/CO ratios during dry reforming of methane when no catalyst was present (Fig. 4.13). Overall, it can be deduced that the reaction performance has not been significantly improved by the presence of the unreduced NiO/Al_2O_3.

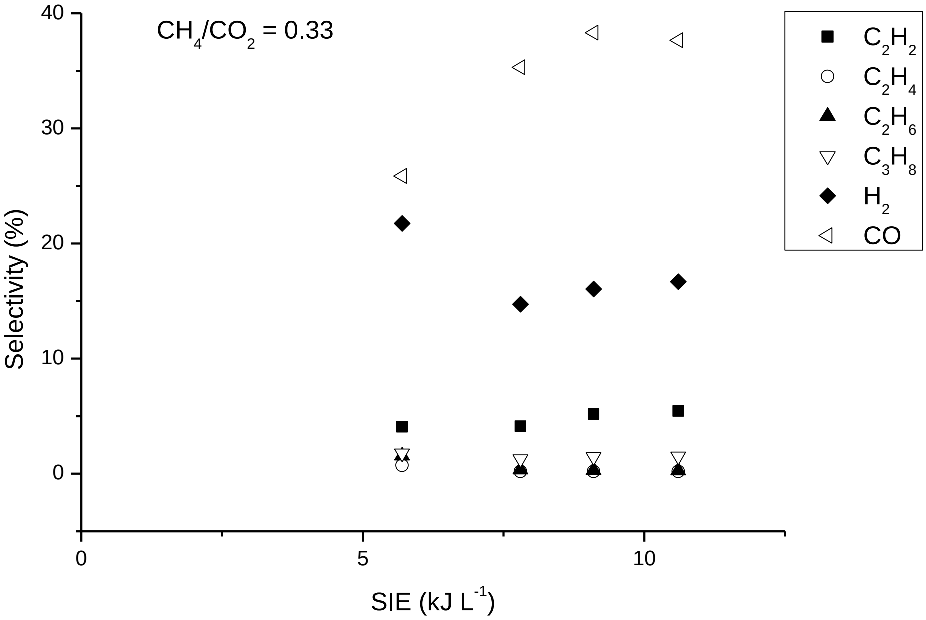

Figure 4.16: Product selectivities during the plasma-assisted dry reforming of CH_4 with unreduced NiO/Al_2O_3, where CH_4/CO_2 = 0.33.

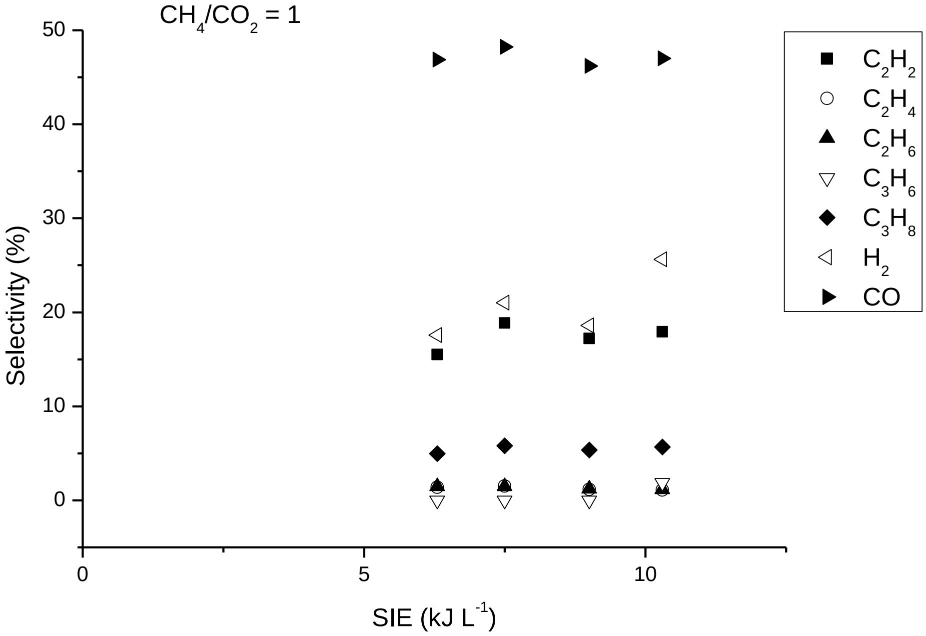

Figure 4.17: Product selectivities during the plasma-assisted dry reforming of CH_4 with unreduced NiO/Al_2O_3, where CH_4/CO_2 = 1.

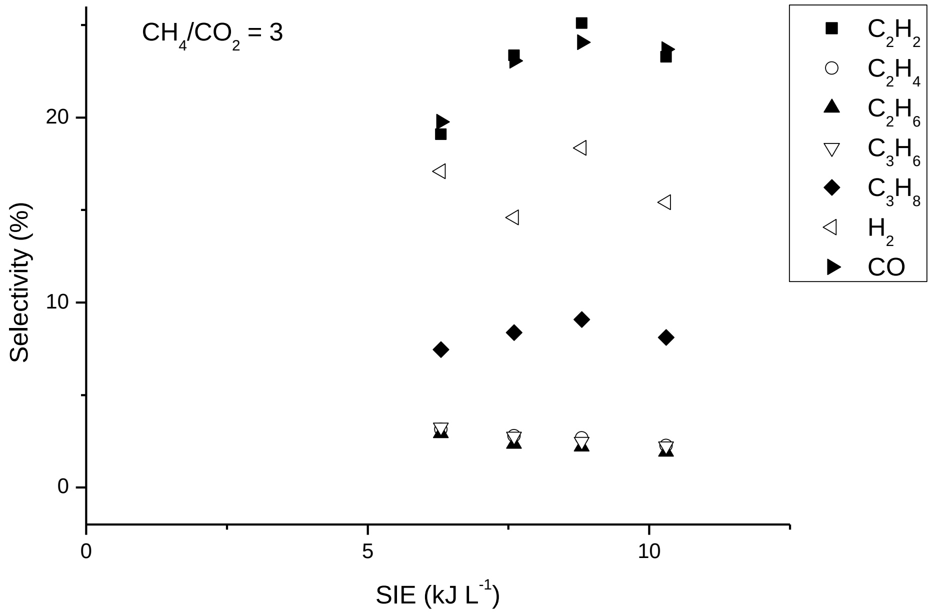

Figure 4.18: Product selectivities during the plasma-assisted dry reforming of CH_4 with unreduced NiO/Al_2O_3, where $CH_4/CO_2 = 3$.

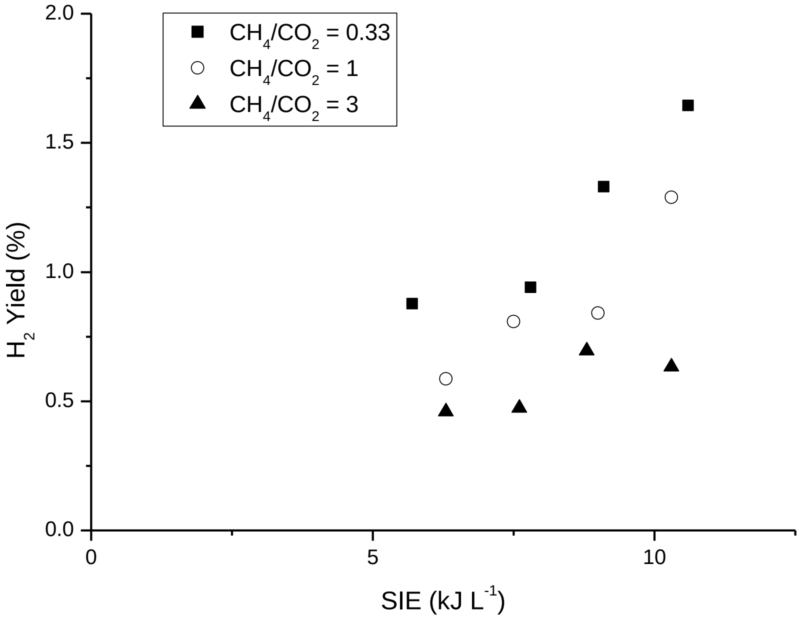

Figure 4.19: Effect of CH_4/CO_2 ratio on H_2 yields in plasma-assisted dry reforming of CH_4 with unreduced NiO/Al_2O_3 in a DBD reactor.

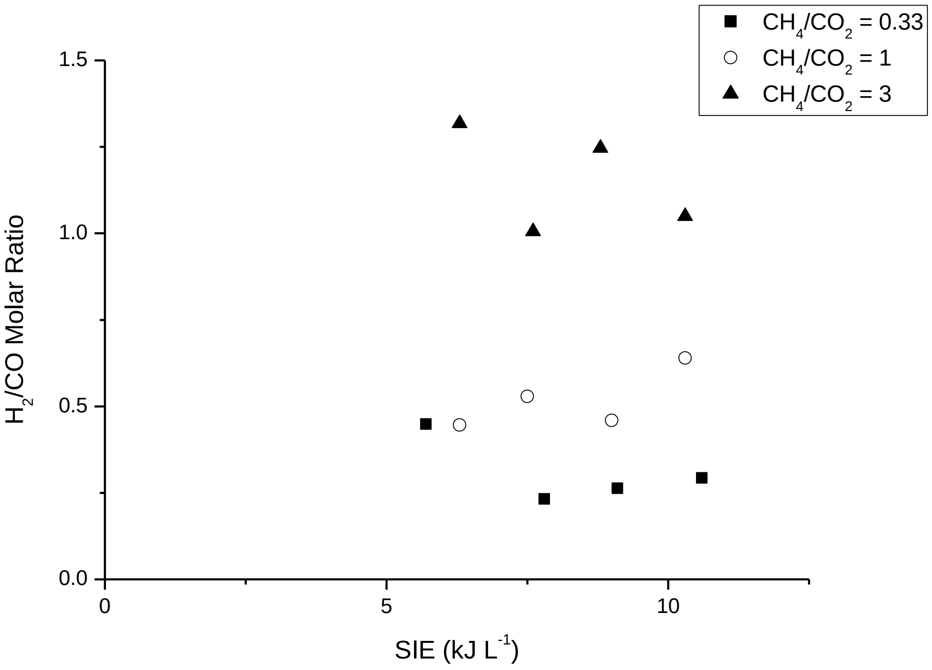

Figure 4.20: Effect of CH_4/CO_2 ratio on the H_2/CO ratio in plasma-assisted dry reforming of CH_4 with unreduced CH_4/CO_2 in a DBD reactor.

4.4 Cross Sections for the Electron Impact Dissociations of CH_4 and CO_2

$$CH_4 + e^- \rightarrow CH_3^{\cdot} + H^{\cdot} + e^- \qquad (4.0)$$

$$CO_2 + e^- \rightarrow CO^{\cdot} + O^{\cdot} + e^- \qquad (4.39)$$

The cross sections depicted in Figure 4.21 represent the probability of a dissociative reaction during a gas molecule collision with a free electron, as a function of the electron energy. The activation energy (E_a) for the electron impact dissociation of methane (4.0) is reported to be ~ 7.5 eV [19] and an increasing probability of dissociation exists at higher electron energies. Carbon dioxide has a lower activation energy of ~ 6.4 eV for electron impact dissociation (4.39) [20]. The CO_2 cross section peaks at ~ 6.9 eV and then drops to almost zero at 9 eV. This means that collisions between CO_2 and energetic electrons will result in a dissociation when the electron energy is within a fairly narrow range (6.4 < eV < 9).

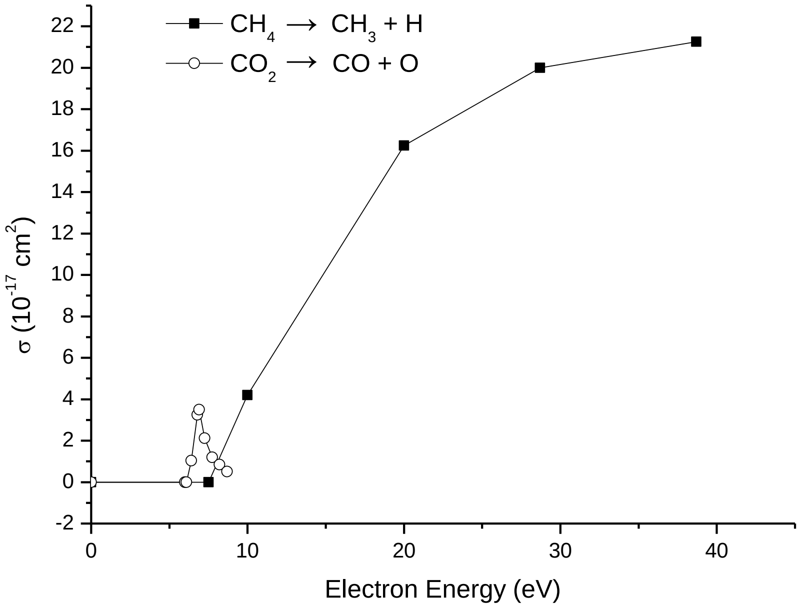

Figure 4.21: Cross sections for the low energy electron impact dissociations of CH_4 and CO_2 (data taken from [19] and [20]).

A solution of the Boltzmann equation has been performed for determination of the electron energy distribution function (EEDF) in a CH_4 and CO_2 plasma discharge. This has been achieved using the ELENDIF computer code [21] developed to solve Boltzmann's equation for partially ionised plasmas using the electron-molecule cross sections for CH_4 and CO_2, from the works of Erwin and Kunc [19] and Phelps [20]. The output EEDF is shown in Figure 4.22. The ELENDIF computer code has also been used to calculate the mean electron energy of this electron distribution, which is indicated on the EEDF at 4.4 eV. By comparison of the cross sections and EEDF, it is clear that the mean electron energy is below the threshold energy for electron impact dissociation of both CH_4 and CO_2. Only the higher energy electrons in the tail of the EEDF have sufficient energy to induce a reaction during collisions.

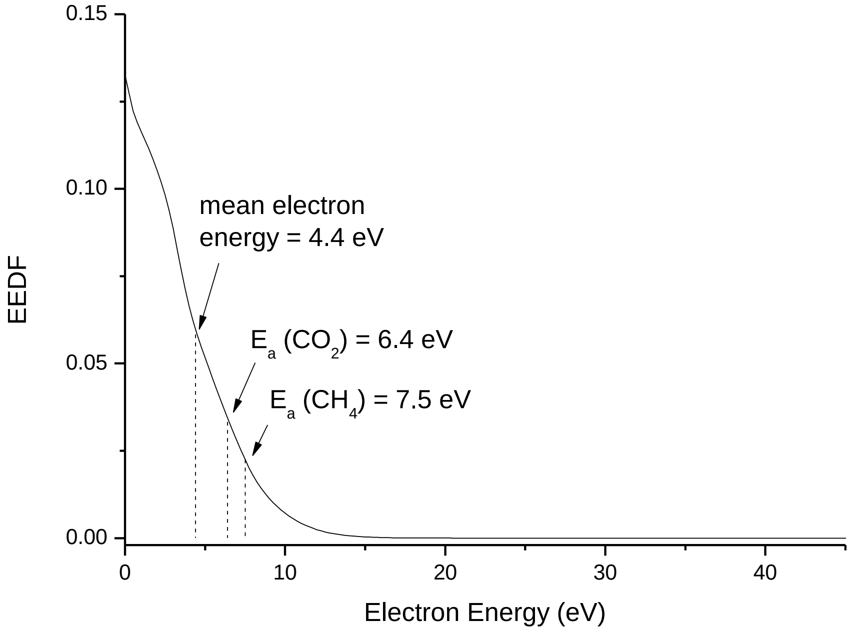

Figure 4.22: Electron energy distribution function for a CH_4 and CO_2 plasma. Calculated using ELENDIF computer code for conditions of $CH_4/CO_2 = 1$ at 1 atm and 127 °C.

Figures 4.23 and 4.24 show the EEDF for a 100 % CH_4 plasma and a 100 % CO_2 plasma, respectively. The mean electron energy in a CH_4 plasma is 4.6 eV, whereas the mean electron energy in a CO_2 plasma is 4.3 eV, as indicated on the EEDFs. The mean electron energy is lower in a CO_2 plasma because there are more successful electron impact collisions with CO_2 (4.39) than in the case of CH_4. During reactive collisions some of the electron energy is transferred to the dissociation products, therefore the mean electron energy is decreased. During electron impact collisions with CH_4 (4.0), a higher proportion of collisions are unsuccessful, in which case the electrons would retain more energy, on average. In a mixture of CH_4 and CO_2 as shown in Figure 4.22, the mean electron energy (4.4 eV) is between that of CH_4-only and CO_2-only plasmas, as would be expected.

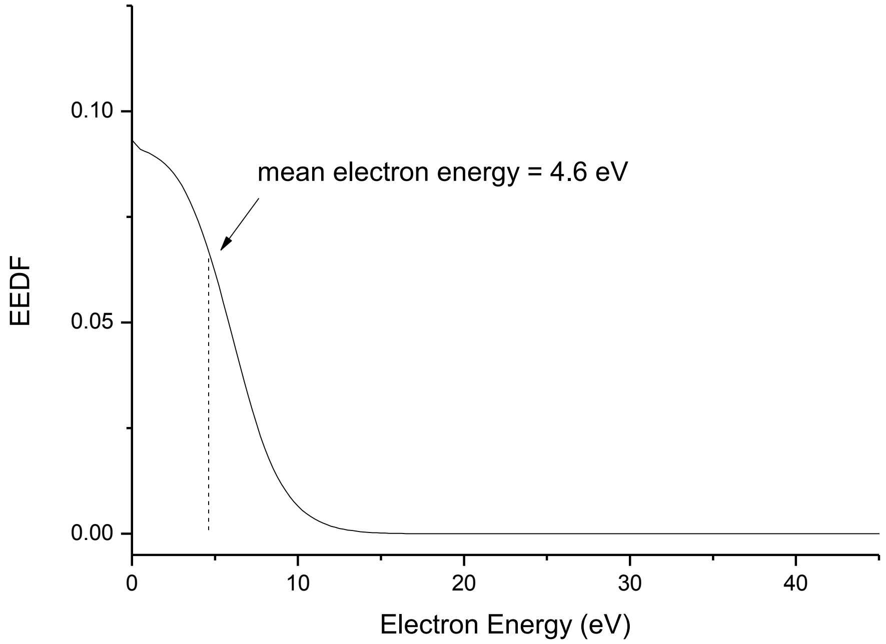

Figure 4.23: Electron energy distribution function for a 100 % CH_4 plasma. Calculated using ELENDIF computer code for conditions of 1 atm and 127 °C.

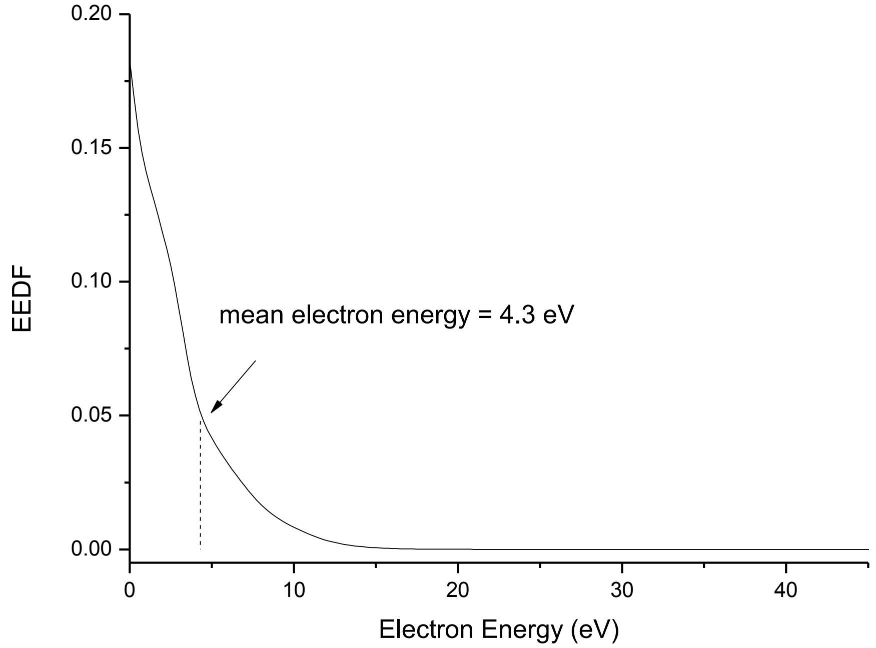

Figure 4.24: Electron energy distribution function for a 100 % CO_2 plasma. Calculated using ELENDIF computer code for conditions of 1 atm and 127 °C.

Considering the relative proportion of electrons above the threshold energies for each species, it is expected that the electron impact dissociation of CO_2 should be greater than the electron impact dissociation of CH_4 during dry reforming of methane. This supports the results obtained for reforming of CO_2-only and CH_4-only where CO_2 conversions are greater than CH_4 conversions under equivalent reaction conditions. However, during dry reforming of CH_4, the conversions of CH_4 are greater than those of CO_2, suggesting that another process may be important for breakdown of CH_4 molecules during dry reforming. As previously suggested (in section 4.3.3), it is probable that reactive oxygen radicals and hydroxyl radicals play a major role in enhancing the dissociation of CH_4 in a plasma discharge.

4.5 Calculation of Thermodynamic Equilibrium Compositions with Variation in CH_4/CO_2 Ratio

HSC Chemistry Software (Ver. 5.0) has been used to calculate the thermodynamic equilibrium gas compositions for CH_4 reforming, CO_2 reforming and dry reforming of CH_4 at various CH_4/CO_2 mixing ratios and elevated temperatures. The assumed equilibrium products were H_2, CO, O_2 and C_2 hydrocarbons. Reforming of CH_4 requires temperatures > 500 °C but higher temperatures are needed to achieve significant conversions (Figure 4.25). At temperatures > 1500 °C, close to complete conversion of CH_4 can be obtained. Methane is predominantly decomposed to form H_2 and solid carbon; although a significant amount of C_2 hydrocarbons are formed at temperatures >1000 °C. Ethylene is the most abundant hydrocarbon product at high temperatures, acetylene production is low (< 6.4 % of the total gas mixture) and peaks at 955 °C and a smaller amount of ethane (< 0.05 % of the total gas mixture) is also produced, which peaks at 1150 °C.

The temperature of the DBD reactor during the experiments in this investigation remained close to room temperature as a result of the use of low applied power and low AC frequency (in contrast to the DBD reactor used in the other chapters of this thesis, where significant gas heating resulted from the use of high applied power and high AC frequency). In the experimental results for plasma-reforming of CH_4 (section 4.3.1), a 2.5 % conversion of CH_4 was obtained. By comparison, a temperature of ~ 700 °C would be necessary to achieve this small conversion in the absence of the plasma. The relative product selectivities differ greatly between the plasma experimental results and the thermodynamic equilibrium compositions. In the plasma reaction, acetylene was the most abundant product, followed by H_2 and propane. The thermodynamic equilibrium composition does not contain C_3 hydrocarbons at temperatures < 2000 °C. Carbon deposition is severe in both cases; however, it is greater in the thermal reaction where H_2 is the main product, in comparison to plasma CH_4 reforming where higher hydrocarbon formation is more significant.

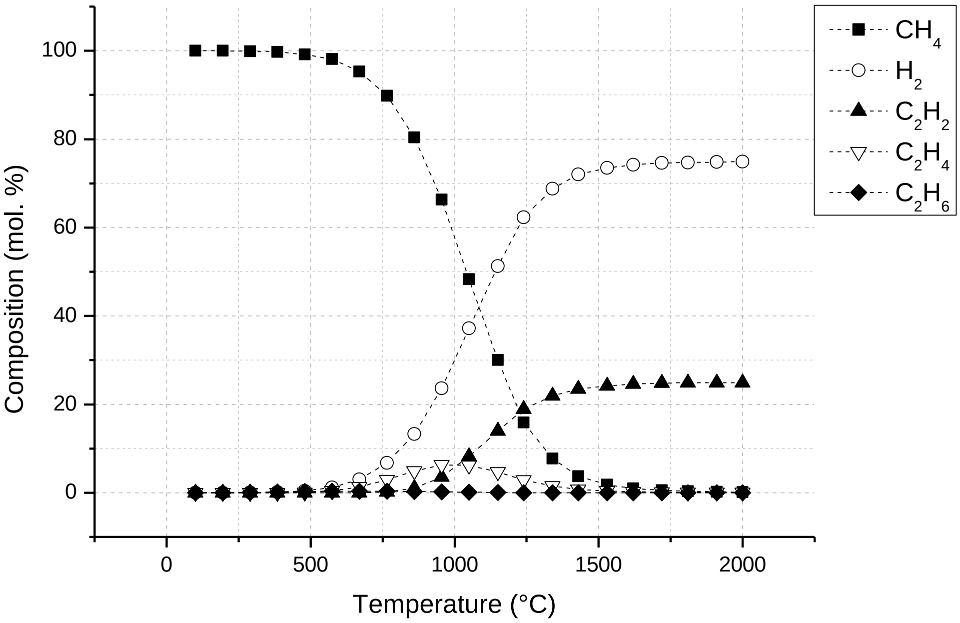

Figure 4.25: Thermodynamic equilibrium gas compositions for CH_4 reforming at elevated temperatures in the absence of a catalyst (pressure = 1 atm).

The thermodynamic equilibrium composition for CO_2 reforming at elevated temperatures is shown in Figure 4.26. CO_2 is converted to CO and O_2 at temperatures > 2000 °C. Complete CO_2 conversion requires temperatures of ~4000 °C. Carbon dioxide is more difficult to destroy than methane by thermal methods due to a higher bond dissociation energy for a C=O bond (5.52 eV) compared to a C-H bond (4.55 eV) [9]. The experimental results for plasma reforming of CO_2 gave conversions of 5.3 %. In the absence of a non-thermal plasma, a temperature of ~1840 °C would result in the same conversion.

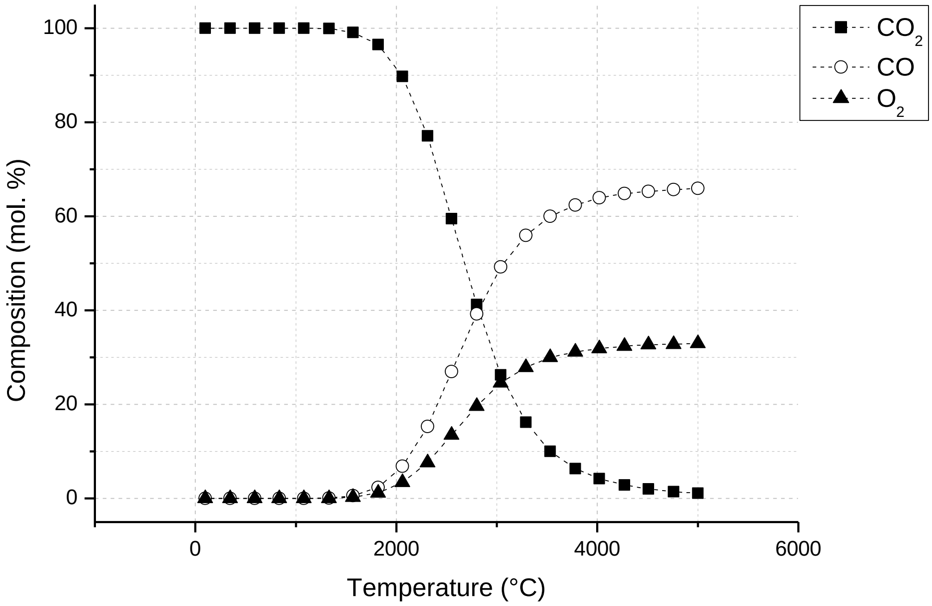

Figure 4.26: Thermodynamic equilibrium gas compositions for CO_2 reforming at elevated temperatures in the absence of a catalyst (pressure = 1 atm).

Figures 4.27 and 4.28 show the conversions of CH_4 and CO_2 calculated from the thermodynamic equilibrium compositions at various mixing ratios. Conversions of both gases start at ~ 400 °C and increase with increasing temperature. A lower CH_4/CO_2 ratio gives higher CH_4 conversions at the same temperatures and a higher CH_4/CO_2 gives higher CO_2 conversions at the same temperatures. This is in contrast to plasma-assisted dry reforming of CH_4 where both CH_4 and CO_2 conversions are increased when the CH_4/CO_2 ratio is lower.

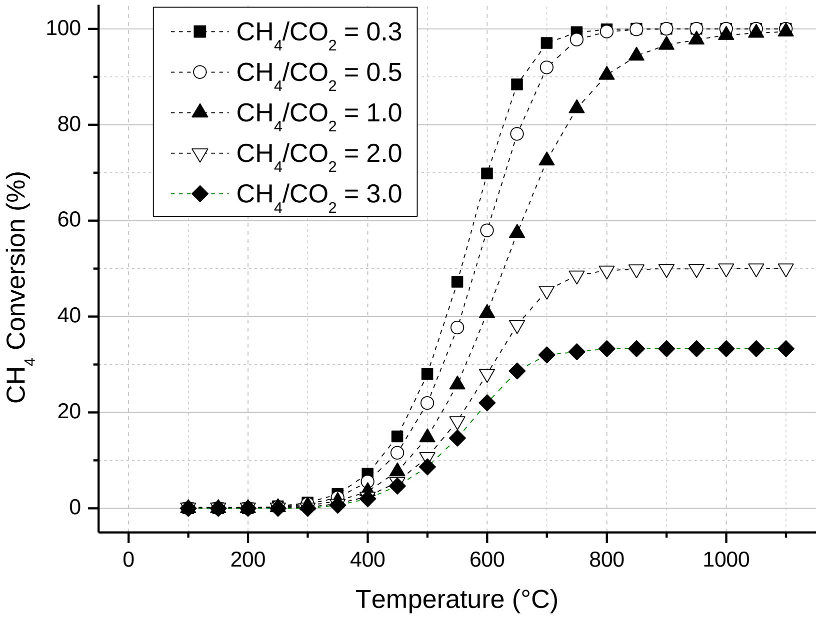

Figure 4.27: CH_4 conversions calculated from thermodynamic equilibrium compositions for dry reforming of methane with different feed gas ratios (pressure = 1 atm).

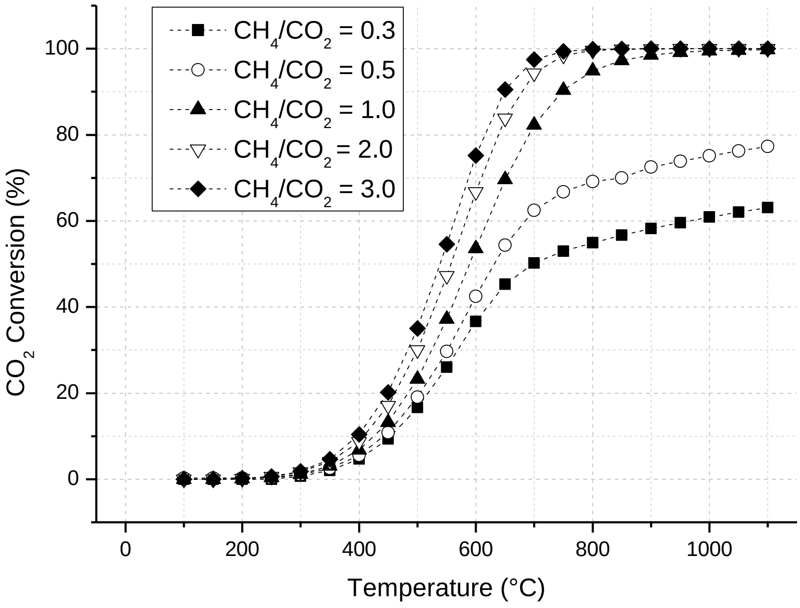

Figure 4.28 CO_2 conversions calculated from thermodynamic equilibrium compositions for dry reforming of methane with different feed gas ratios (pressure = 1 atm).

The observed differences between the thermodynamic equilibrium compositions for dry reforming of methane and the experimental results in a DBD show that methane and carbon dioxide conversions proceed via different reaction mechanisms for these two types of reactions. The reactions of radicals and excited species are important in the plasma mechanism, whereas pyrolysis of gas molecules (mostly in the ground state) dominates thermal reaction mechanisms. The formation of C_3+ hydrocarbons and methanol are not thermodynamically feasible under equilibrium conditions; however, under non-equilibrium plasma conditions these products were observed.

4.6 Discussion

4.6.1 Comparison of Dry Reforming of CH_4 with Different DBD Reactor Systems

Two different coaxial DBD reactor systems have been used to obtain results for dry reforming of methane. The results obtained in Chapter 3 used a DBD reactor with two dielectric barriers, whereas the results obtained in this investigation used a DBD reactor with a single dielectric barrier, where the stainless steel electrode was in contact with the plasma. The discharge gap and electrical parameters also differed between these two reactors. Each of these factors could affect the reaction chemistry. In both reactors, CH_4 conversions were significantly higher than CO_2 conversions and the same gaseous reaction products were identified. In general, hydrocarbons with a lower carbon number (C_2 species) are produced with a higher selectivity than products with higher carbon numbers (C_3+ species); this has also been consistently observed by other researchers [4, 7, 8, 10, 16, 22]. However, the relative selectivities of reaction products, particularly the C_2 species were substantially different between the two different DBD systems investigated. In this study (using a single dielectric), dry reforming of methane consistently yielded acetylene (C_2H_2) as the main hydrocarbon product. In contrast, the results for the reactor with a double dielectric (section 3.3.1) show that ethane (C_2H_6) was the most abundant hydrocarbon product. Other researchers have reported the formation of saturated hydrocarbons with a higher selectivity than unsaturated species in DBD [4, 7, 8, 10, 16, 22]; this is in contrast to the results of this study. Interestingly, researchers that have investigated dry reforming of methane with alternative types of plasma have also produced acetylene with a higher selectivity than ethylene and ethane, these methods have all included pulsed DC discharges such as point-to-point reactors [15, 23], microwave plasma [24], corona [25], and a glow discharge [26]. It is not clear why these differences in C_2 product selectivities are observed.

It should also be considered that the contact between the plasma and the stainless steel electrode could affect the reaction chemistry. Li et al. [27] have investigated dry reforming of methane in DBD with different electrode materials (aluminium, copper, steel and titanium) and they found the choice of electrode to have little influence over the reaction chemistry. However, a direct comparison between DBD reactors with double dielectric and single dielectric has not been made.

4.6.2 Introduction of an Unreduced NiO/Al_2O_3 Catalyst

The results of this investigation have shown that dry reforming of methane is not catalysed by the presence of NiO/Al_2O_3. It has been shown in Chapter 3 that the addition of Al_2O_3 to the plasma discharge resulted in decreased conversions of both CH_4 and CO_2, which was accompanied by a change in discharge type from filamentary mode to surface discharge. The dielectric properties of the catalyst will be altered by the presence of 33 % wt. NiO but this has not had a detrimental effect on the reaction performance indicating that if used in the ‘active’ reduced form (Ni/Al_2O_3), this catalyst may be beneficial to the reaction mechanism.

4.7 Conclusions

Comparison of the results for plasma-assisted reforming of CH_4-only and CO_2-only in a DBD reactor has shown that the CO_2 conversions are approximately double the conversions of CH_4 under the range of conditions tested. This can be explained in terms of the cross sections for electron impact dissociations of CH_4 and CO_2, which are expected to be the most significant processes for the breakdown of these gases in a non-thermal plasma discharge. However, for a mixture of CH_4 and CO_2 the conversions of CH_4 are higher than those of CO_2, indicating that another process is important in the breakdown of CH_4. It has been suggested that CH_4 reacts with active oxygen and hydroxyl radicals to form methyl species; these can combine with a number of different species during coupling reactions to form the reaction products observed in this study. Possible reactions for each of the investigated reforming processes have been given together with the rate data for these processes (where available). This data may help to indicate the relative importance of each of these processes.

The presence of an unreduced NiO/Al_2O_3 catalyst to the discharge gap during dry reforming of CH_4 made no significant improvements to the reaction performance. However, it did not hinder the reaction significantly either indicating that it may be a suitable catalyst for plasma-assisted dry reforming of methane in the reduced form, which is known to be active for conventional catalytic methane reforming.

4.8 References

1. Istadi, N.A.S.A., *Co-generation of Synthesis Gas and C_2+ Hydrocarbons from Methane and Carbon Dioxide in a Hybrid Catalytic-Plasma Reactor.* Fuel, 2006. **85**: p. 577-592.
2. Brock, S.L., et al., *Application of Non-Thermal Atmospheric Pressure AC Plasmas to the Carbon Dioxide Reforming of Methane.* Res. Chem. Intermediat., 2002. **28**(1): p. 13-24.
3. Paulussen, S., et al., *Conversion of Carbon Dioxide to Value-Added Chemicals in Atmospheric Pressure Dielectric Barrier Discharges.* Plasma Sources Sci. Technol., 2010. **19**: p. 1-6.
4. Eliasson, B., C.J. Liu, and U. Kogelschatz, *Direct Conversion of Methane and Carbon Dioxide to Higher Hydrocarbons Using Catalytic Dielectric-Barrier Discharges with Zeolites.* Ind. Eng. Chem. Res., 2000. **39**(5): p. 1221-1227.
5. Zhang, K., U. Kogelschatz, and B. Eliasson, *Conversion of Greenhouse Gases to Synthesis Gas and Higher Hydrocarbons.* Energ. Fuel., 2001. **15**(2): p. 395-402.
6. Kraus, M., et al., *CO_2 Reforming of Methane by the Combination of Dielectric-Barrier Discharges and Catalysis.* Phys. Chem. Chem. Phys., 2001. **3**(3): p. 294-300.
7. Goujard, V., J.M. Tatibouet, and C. Batiot-Dupeyrat, *Use of a Non-Thermal Plasma for the Production of Synthesis Gas from Biogas.* Appl. Catal. A Gen., 2009. **353**(2): p. 228-235.

8. Li, Y., et al., *Synthesis of Oxygenates and Higher Hydrocarbons Directly from Methane and Carbon Dioxide Using Dielectric-Barrier Discharges: Product Distribution*. Energ. Fuel., 2002. **16**: p. 864-870.
9. Rico, V.J., et al., *Evaluation of Different Dielectric Barrier Discharge Plasma Configurations as an Alternative Technology for Green C_1 Chemistry in the Carbon Dioxide Reforming of Methane and the Direct Decomposition of Methanol*. J. Phys. Chem. A, 2010. **114**(11): p. 4009-4016.
10. Liu, C.J., et al., *Methane Conversion to Higher Hydrocarbons in the Presence of Carbon Dioxide Using Dielectric-Barrier Discharge Plasmas*. Plasma Chem. Plasma P., 2001. **21**(3): p. 301-310.
11. Kim, H.-H., et al., *Decomposition of Gas-Phase Benzene Using Plasma-Driven Catalyst Reactor: Complete Oxidation of Adsorbed Benzene Using Oxygen Plasma*. J. Adv. Technol. , 2005. **8**(2): p. 226-233.
12. Liu, C.-J., R. Mallinson, and L. Lobban, *Nonoxidative Methane Conversion to Acetylene over Zeolite in a Low Temperature Plasma*. J. Catal., 1998. **179**(1): p. 326-334.
13. *National Institute of Standards and Technology (NIST), Kinetics Database[online]*. http://kinetics.nist.gov/kinetics/KineticsSearchForm.jsp.
14. Kraus, M., *Catalytic CO_2 Reforming of Methane in a Dielectric-Barrier Discharge* 2001, Swiss Federal Institute of Technology: Zurich.
15. Yao, S.L., et al., *Plasma Reforming and Coupling of Methane with Carbon Dioxide*. Energ. Fuel., 2001. **15**: p. 1295-1299.
16. Huang, A., et al., *CO_2 Reforming of CH_4 by Atmospheric Pressure AC Discharge Plasmas*. J. Catal., 1999. **189**: p. 349-359.
17. Liu, C.-J., et al., *Production of Acetic Acid Directly from Methane and Carbon Dioxide Using Dielectric-Barrier Discharges*. Chem. Lett., 2001: p. 1304-1305.
18. Nair, S.A., T. Nozaki, and K. Okazaki, *Methane oxidative conversion pathways in a dielectric barrier discharge reactor - Investigation of gas phase mechanism*. Chemical Engineering Journal, 2007. **132**(1-3): p. 85-95.
19. Erwin, D.A. and J.A. Kunc, *Dissociation and Ionisation of the Methane Molecule by Nonrelativistic Electrons Including the Near Threshold Region*. J. Appl. Phys., 2008. **103**.
20. Phelps, A.V. *Compilation of Electron Cross Sections Used [online]* http://jila.colorado.edu/~avp/collision_data/electronneutral/ELECTRON.TXT. [cited 10/12/2010].
21. Morgan, W.L. and B.M. Penetrante, *ELENDIF - A Time-Dependent Boltzmann Solver for Partially Ionized Plasmas*. Comput. Phys. Commun., 1990. **58**(1-2): p. 127-152.
22. Song, H.K., et al., *Synthesis Gas Production via Dielectric Barrier Discharge over Ni/γ-Al_2O_3 Catalyst*. Catal. Today, 2004. **89**: p. 27-33.
23. Kado, S., Y. Sekine, and K. Fujimoto, *Direct Synthesis of Acetylene from Methane by Direct Current Pulse Discharge*. Chem. Commun., 1999(24): p. 2485-2486.
24. Zhang, J.Q., et al., *Oxidative Coupling and Reforming of Methane with Carbon Dioxide Using a Pulsed Microwave Plasma Under Atmospheric Pressure*. Energ. Fuel., 2003. **17**(1): p. 54-59.

25. Zhang, X., et al., *The Simultaneous Activation of Methane and Carbon Dioxide to C_2 Hydrocarbons Under Pulse Corona Plasma.* Catal. Today, 2002. **72**: p. 223-227.
26. Ghorbanzadeh, A.M. and H. Modarresi, *Carbon Dioxide Reforming of Methane by Pulsed Glow Discharge at Atmospheric Pressure: The Effect of Pulse Compression.* J. Appl. Phys., 2007. **101**(12).
27. Li, Y., et al., *Co-generation of Syngas and Higher Hydrocarbons from CO_2 and CH_4 Using Dielectric-Barrier Discharge: Effect of Electrode Materials.* Energ. Fuel., 2001. **15**(2): p. 299-302.

5. Plasma-Reduction of a NiO/Al_2O_3 Catalyst in a Coaxial DBD Reactor

5.1 Introduction

NiO/Al_2O_3 catalysts are used commercially for large-scale production of hydrogen via steam methane reforming (SMR), prior to which they are reduced to Ni/Al_2O_3 by hydrogen-containing gases or natural gas-steam mixtures at elevated temperatures [1]. The reduction generates active Ni sites, which are effective for hydrogen production from methane. The use of non-thermal, atmospheric pressure plasma for reduction of supported metal catalysts has been investigated by several researchers as a potential alternative to thermal reduction processes (Table 5.0). Plasma-reduction methods have been reported to have several advantages including short treatment time, the use of inexpensive and non-hazardous reducing agents and enhanced physical and chemical properties of the prepared catalyst.

Liu et al. [2, 3] have reported the use of a H_2/N_2 atmospheric pressure, glow discharge plasma jet for calcination and reduction of $NiO/\gamma\text{-}Al_2O_3$ and NiO/SiO_2 catalysts. A short plasma treatment time of ten minutes resulted in improved dispersion and reduced Ni particle size, in comparison with a sample reduced thermally over 2 hours. The plasma-reduced samples had a higher specific surface area due to a reduction in sintering, which is known to be a major drawback of thermal reduction methods. Noble metal catalysts including Rh, Ir, Pd, Pt, Ag and Au supported on various materials, have been successfully reduced in an argon glow discharge by Cheng et al. [4]. The reducing capability of argon plasma is surprising due to the inert nature of argon gas. The authors suggested that free high energy electrons in the plasma act as the reducing species and that this is independent of the type of plasma-forming gas. Wang et al. [5] proposed that an indirect plasma-reduction mechanism may exist where adsorbed H_2O on the catalyst surface may dissociate under discharge conditions producing $H^{\cdot}$ radicals and hydrated electrons e_{aq}^{-}, which are both strong reducing species [6]. In support of this hypothesis they were able to reduce Pd/HZSM-5 in an O_2 glow discharge [7]. However, they were unable to reduce

$Ni(NO_3)_2$, $Fe(NO_3)_3$ and $Co(NO_3)_2$ catalysts in an argon glow discharge; in these cases only decomposition to the oxide forms was observed [4, 8]. IR imaging of the glow discharge reactor shows that the catalyst bed was close to room temperature (< 30 °C) under the discharge conditions [9].

Plasma-reduction in DBD is limited to Pt- and Co-based catalysts in a H_2/N_2 discharge [10]. However, the catalyst temperature under discharge conditions was not ascertained during these experiments and therefore it is difficult to deduce the reduction mechanisms involved. Further investigations in this area are required in order to define the reaction mechanisms for plasma-reduction of metal catalysts. In particular, whether plasma-reduction of metal catalysts is a consequence of plasma active species (eg. high energy electrons) or whether the reduction is an effect of elevated temperature under discharge conditions.

Reduction of a 33 wt. % NiO/Al_2O_3 catalyst by 100 % CH_4 and 20 % H_2/Ar DBD is presented in this chapter. Analyses of gas compositions exiting the reactor provides information about the reactions occurring both in the plasma volume and on the catalyst surface. Characterisation of these catalysts has been carried out using X-ray diffraction (XRD) and scanning electron microscopy (SEM). Temperature programmed reduction (TPR) has been performed on the NiO/Al_2O_3 catalyst in both CH_4/He and H_2/He in order to determine the reducing temperature required under these gas streams in the absence of a non-thermal plasma. In addition, the effect of metal reduction on the electrical properties of the plasma has been investigated.

Catalyst (Reduced Form)	Plasma Type & Reactor Conditions	Gas Type	Method	Additional Information	Reference
Ni/SiO_2 $Ni/\alpha\text{-}Al_2O_3$	- Glow - 1 atm - 25 ml min^{-1} - 527 °C	20 % H_2/N_2	$Ni(NO_3)_2/SiO_2$ and $Ni(NO_3)_2/Al_2O_3$ were calcined and reduced by cold plasma jet for 10 minutes.		Yin & co-workers [2] [3]
$Pd/\gamma\text{-}Al_2O_3$ Pt/TiO_2 Ag/TiO_2 Au/TiO_2 Pd/HZSM-5 $Pt/\gamma\text{-}Al_2O_3$ $Ir/\gamma\text{-}Al_2O_3$ $Rh/\gamma\text{-}Al_2O_3$ Pt/C Pd/SBA-15 Pt/SBA-15 Ag/SBA-15 Au/SBA-15	- Glow - 50-200 Pa - 900 V - Room temperature	Ar	The following catalyst precursors were treated in plasma for 10 minutes, stirred and repeated 5 or 6 times. Followed by calcinations thermally if required. $PdCl_2/\gamma\text{-}Al_2O_3$, H_2PtCl_6/TiO_2, $AgNO_3/TiO_2$, $HAuCl_4/TiO_2$, $PdCl_2$/HZSM-5, $H_2PtCl_6/\ \gamma\text{-}Al_2O_3$, $H_2IrCl_6/\ \gamma\text{-}Al_2O_3$, $RhCl_3/\ \gamma\text{-}Al_2O_3$, H_2PtCl_6/C, $PdCl_2$/SBA-15, H_2PtCl_6/SBA-15, $HAuCl_4$/SBA-15, $AgNO_3$/SBA-15 and $PdCl_2$/HZSM-5	$Ni(NO_3)_2/Al_2O_3$, $Ni(NO_3)_2/ZrO_2$, $Fe(NO_3)_3$ and $Co(NO_3)_2$ could not be reduced by this method.	Liu & co-workers [4] [11] [12] [13] [14] [5]

Pd/HZSM-5	• Glow • 50-200 Pa • 900 V Room temperature	O_2			[7]
$Pt/\gamma\text{-}Al_2O_3$ $Co/\ \gamma\text{-}Al_2O_3$	• DBD • 1 atm • 3 kV • 37-39 W • 10 ml min^{-1} • Temp not given.	20 % H_2/N_2	$H_2PtCl_6/\ \gamma\text{-}Al_2O_3$ and $Co(NO_3)_2$ were treated by plasma for 120 minutes.	TPR was performed on each catalyst. Results show that the Pt catalyst reduced rapidly between 200-250 °C and reduction of the Co catalyst started at 120 °C and continued to reduce various Co species up to 680 °C.	Kim & co-workers [10]
Ag/TiO_2 Au/TiO_2 Pd/TiO_2 Pt/TiO_2	• Glow • 24 Pa • 10 W • Temp not given.	H_2	Ions of Ag, Au, Pd and Pt incorporated into ultra-thin films of TiO_2 were treated by a H_2 plasma etcher.		Kunitake & co-workers [15]

Table 5.0: Plasma-reduction of supported metal catalysts.

5.2 Experimental Section

The experimental set-up used for this investigation is described in section 3.2, with the only modification being the substitution of reactant gases. Reduction of a 33 wt. % NiO/Al_2O_3 catalyst (Johnson Matthey) has been accomplished using methane (BOC Gases, 99.9 %) and a mixture of 20 % hydrogen (BOC Gases, 99.995 %) in argon (BOC Gases, 99.9 %) as the plasma-forming gases. In addition, the behaviour of the catalyst in an argon discharge has been investigated. This commercial catalyst may contain other unspecified components such as carbonates. The total gas flow rates were 50 ml min^{-1} in CH_4 experiments and 100 ml min^{-1} in H_2/Ar and Ar-only experiments.

NiO/Al_2O_3 catalyst pellets were crushed to give particles of non-uniform dimensions (0.85 mm – 5 mm). The catalyst was heated to 300 °C for 3 hours immediately before each experiment to remove moisture. The catalyst was packed into the discharge gap and held in place by quartz wool (Figure 3.1 b). Preliminary experiments were carried out using a uniform catalyst particle size of 0.5 – 0.8 mm. Plasma generation was weak under these conditions and subsequently the use of non-uniform particles showed a marked improvement in plasma generation, possibly due to an enhanced transfer of electrical charge in the voids between catalyst particles.

Prior to each experiment, the system was purged to remove air and stabilise the gas mixtures. The plasma was turned on at $t = 0$ and gases exiting the reactor were analysed by micro-GC at regular intervals. Experiments were carried out under approximately constant applied voltage and optimised frequency. The optimised frequency varied depending on the gas type. The conditions for each experiment are shown in Table 5.1. In an attempt to gain an approximation of the minimum bulk gas temperature, a thermocouple (CVT Heater Controller) was used to measure the temperature of the outer electrode of the reactor. No external heating was applied to the reactor.

Gas Type	Applied Voltage (kV_{pk-pk})	Frequency (kHz)
100 % CH_4	21.2	33.1
20 % H_2/Ar	18.3	31.2
100 % Ar	18.1	31.9

Table 5.1: Experimental conditions used for plasma-reduction of NiO/Al_2O_3.

5.3 Results

5.3.1 Reduction of NiO/Al_2O_3 in a CH_4 Plasma

Plasma reduction of a NiO/Al_2O_3 catalyst has been carried out in 100 % CH_4 in a coaxial DBD reactor. The results for the gaseous analysis are shown in Figures 5.0 – 5.2. Product gases CO_2, CO, H_2, C_2H_2/C_2H_4, C_2H_6, C_3H_6 and C_3H_8 were observed. The discharge power and temperature are shown in Figure 5.3.

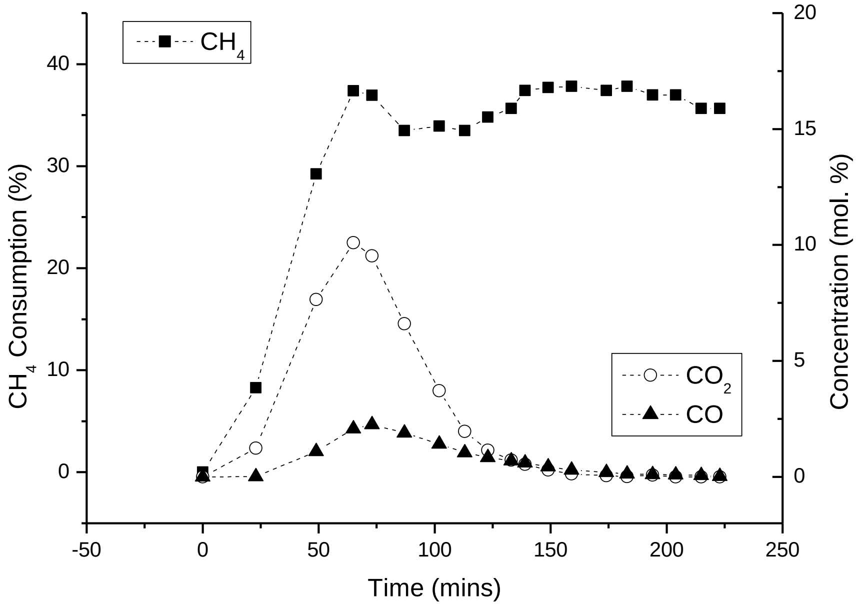

Figure 5.0: CH_4 consumption and concentration of reduction products during reduction of NiO/Al_2O_3 in a 100 % CH_4 DBD.

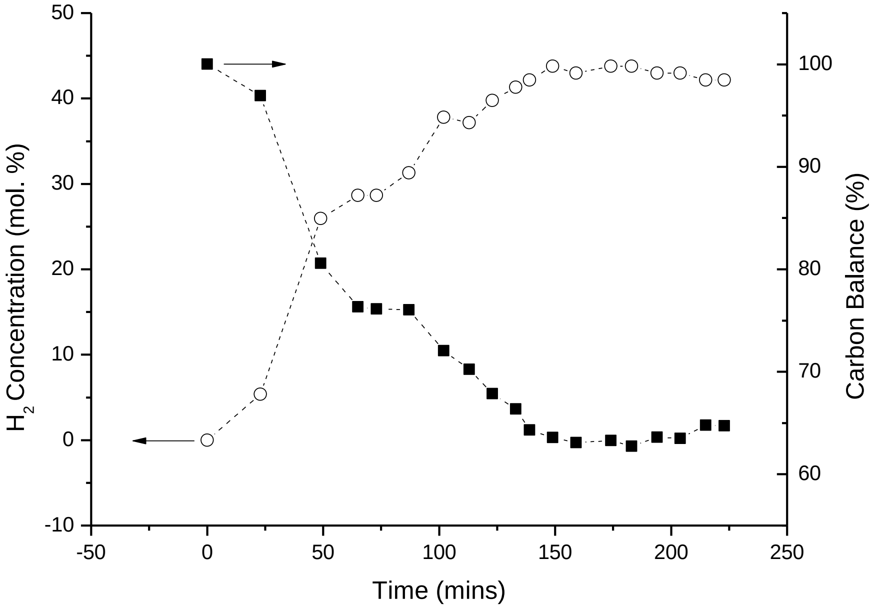

Figure 5.1: H_2 production and carbon balance in the gas stream during reduction of NiO/Al_2O_3 in a 100 % CH_4 DBD.

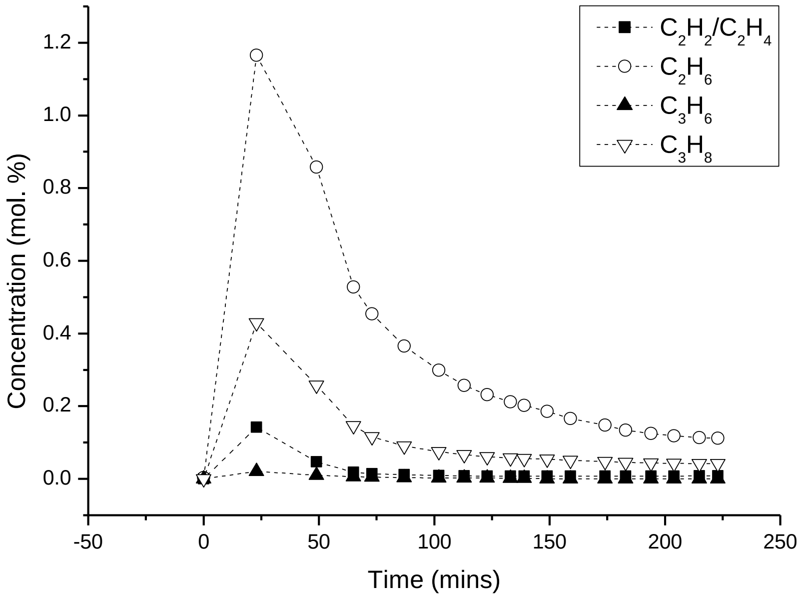

Figure 5.2: Production of higher hydrocarbons during reduction of NiO/Al_2O_3 in a 100 % CH_4 DBD.

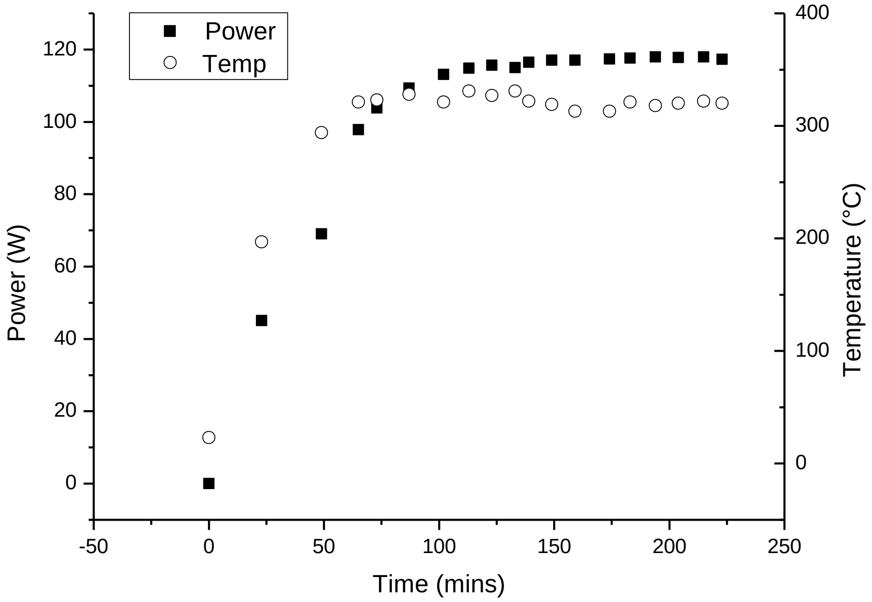

Figure 5.3: Power and temperature profiles for reduction of NiO/Al_2O_3 in a 100 % CH_4 DBD.

Figure 5.0 shows the consumption of the reducing gas CH_4, which increases initially as the discharge power and temperature increase and then remains constant after ~ 150 minutes on stream. The overall reduction proceeds as shown by equation 5.0, generating CO_2 and H_2O. The production of CO is likely to be a result of partial oxidation of CH_4 by NiO (5.1) and/or the water-gas shift reaction (5.2). Concentrations of both CO_2 and CO peaked at ~ 60 minutes, before decreasing, as the rate of NiO reduction slows down. The evolution of CO_2 and CO terminates when reduction of NiO is complete at ~ 150 minutes.

$$4\ NiO\ (s) + CH_4\ (g) \rightarrow 4\ Ni\ (s) + CO_2\ (g) + 2\ H_2O\ (l) \qquad (5.0)$$

$$NiO\ (s) + CH_4\ (g) \rightarrow Ni\ (s) + 2\ H_2\ (g) + CO \qquad (5.1)$$

$$CO\ (g) + H_2O\ (l) \leftrightarrow H_2\ (g) + CO_2\ (g) \qquad (5.2)$$

$$CH_4\ (g) \rightarrow C\ (s) + 2\ H_2\ (g) \qquad (5.3)$$

$$2\ CO\ (g) \leftrightarrow C\ (s) + CO_2\ (g) \qquad (5.4)$$

H_2 concentration and carbon balance in the gas stream are shown in Figure 5.1, it can be seen clearly that the data points mirror each other. This suggests that methane decomposition (5.3) catalysed by metallic Ni is responsible for generation of H_2 and solid carbon. As the reduction proceeds, Ni sites are generated and the rate of methane decomposition increases. When reduction of NiO is complete and all Ni sites are generated, the rate of the catalytic reaction 5.3 becomes constant. As a result, CH_4 consumption plateaus as does the H_2 concentration and the carbon balance.

A second reaction that is possible for carbon deposition in this experiment due to the presence of carbon monoxide is the Boudouard reaction (5.4). However, the shape of the H_2 and carbon balance profiles in Figure 5.1 indicate that catalytic CH_4 decomposition is significant and therefore, reaction 5.4 can be considered less important in this case.

Higher hydrocarbons ethylene/acetylene, ethane, propene and propane were detected and are shown in Figure 5.2. These products are likely to be generated in the plasma volume by radical coupling reactions, as discussed in section 4.3.1, where these products were observed in a CH_4 DBD in the absence of a catalyst. Higher concentrations of hydrocarbon products are observed in the early stages of the experiment before NiO reduction has taken place. As the catalyst is reduced the concentration of hydrocarbons decreased to close to zero. This indicates that in the presence of active Ni sites, CH_4 consumption in surface reactions 5.0, 5.1 and 5.3 may successfully compete with radical coupling reactions in the plasma volume and therefore production of higher hydrocarbons is negligible in the presence of the catalyst.

In addition to the gaseous products, a colourless liquid was collected in the cold trap during the experiment. The masses of the reduced catalyst and liquid product are shown in Table 5.2, together with the carbon and hydrogen contents that have been determined by elemental analysis.

	Before Reduction	After Reduction
Mass of catalyst (g)	19.53	20.06
Mass of liquid product (g)	-	0.78
% wt. C and H in the catalyst	C = 3.3 H = 1.3	C = 16.7 H = 0.0
% wt. C and H in the liquid product	-	C = 0.5 H = 11.3

Table 5.2: Mass and elemental analysis of NiO/Al_2O_3 catalyst and liquid product before and after reduction in a 100 % CH_4 DBD.

Table 5.2 shows that the mass of the catalyst increased by 0.53 g after the reduction. The expected mass of the catalyst after reduction was 18.15 g due to loss of oxygen from the sample, assuming that the NiO was completely reduced to Ni. The observed mass increase is due to deposition of solid carbon on the catalyst (1.91 g). The elemental analysis shows that a 5-fold increase in the carbon content of the catalyst was observed after reduction. Using the observed mass increase of the catalyst to calculate the carbon loss from the gas stream, predicts a carbon loss of 34 % and therefore 66 % of the carbon remaining in the gas stream. This is in excellent agreement with the results shown in Figure 5.2, in which the carbon balance is ~ 66 % of the original value. After the reduction, a colour change from grey to black was observed in the catalyst, further indicative of the presence of carbon in the reduced catalyst.

The relative concentrations of carbon to hydrogen in the liquid product reveals that it contained mostly H_2O, with trace amounts of higher hydrocarbon (C_5+) (assuming that the only other element present in the liquid is oxygen). This is in agreement with the reaction for NiO reduction (5.0) in which H_2O is a reaction product. The calculated mass of H_2O expected for the reduction of NiO/Al_2O_3 is 0.820 g, a difference of 4.7 %. However, the calculation does not account for any H_2O that might be consumed in the water-gas shift reaction (5.2).

5.3.2 Reduction of NiO/Al_2O_3 in a 20 % H_2/Ar Plasma

Reduction of NiO/Al_2O_3 by 20 % H_2 in an argon carrier gas has been carried out in a coaxial DBD reactor. The consumption of H_2 during the reduction is shown in Figure 5.4. Although H_2O is the only product of NiO reduction by H_2 (5.5), the presence of small amounts of carbon-containing gases CO_2, CO and CH_4 have been detected and are shown in Figures 5.5 and 5.6. The discharge power and temperature of the reactor are shown in Figure 5.7.

$$NiO + H_2 \rightarrow Ni + H_2O \qquad (5.5)$$

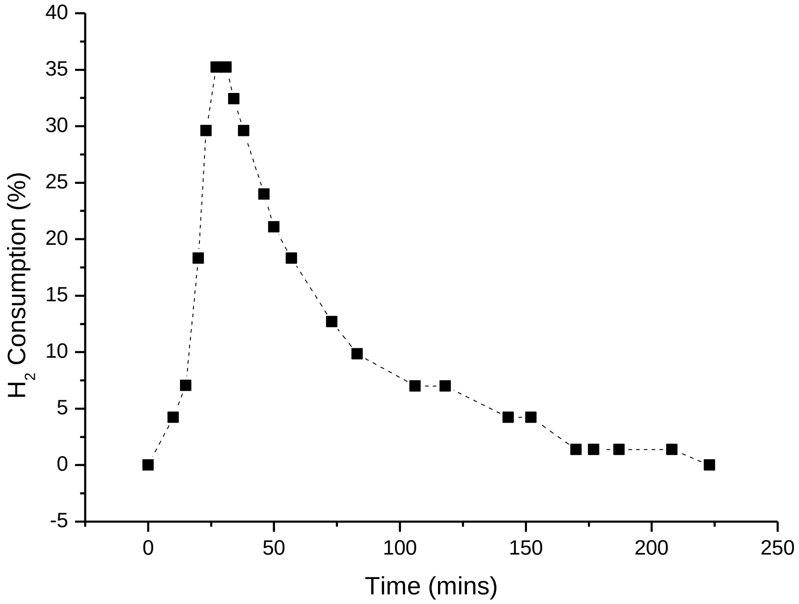

Figure 5.4: H_2 consumption during reduction of NiO/Al_2O_3 in a 20 % H_2/Ar DBD.

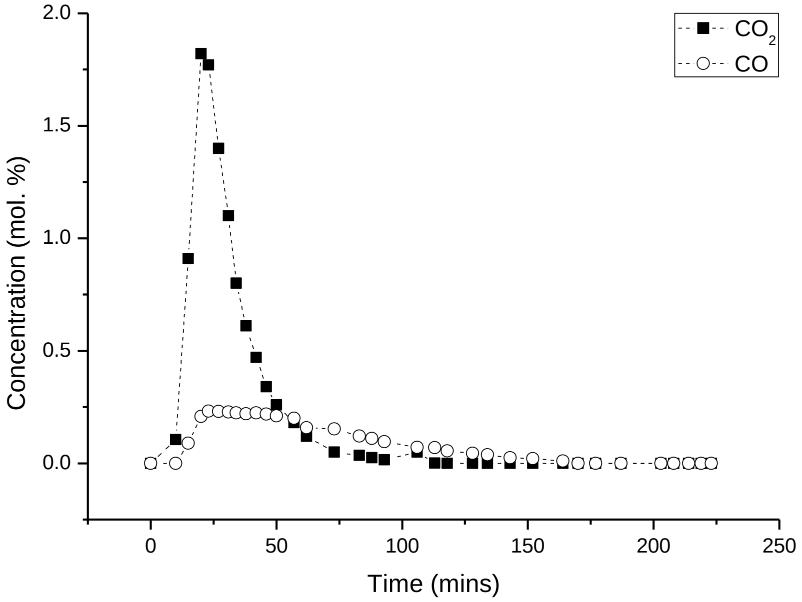

Figure 5.5: CO_2 and CO concentrations during reduction of NiO/Al_2O_3 in a 20 % H_2/Ar DBD.

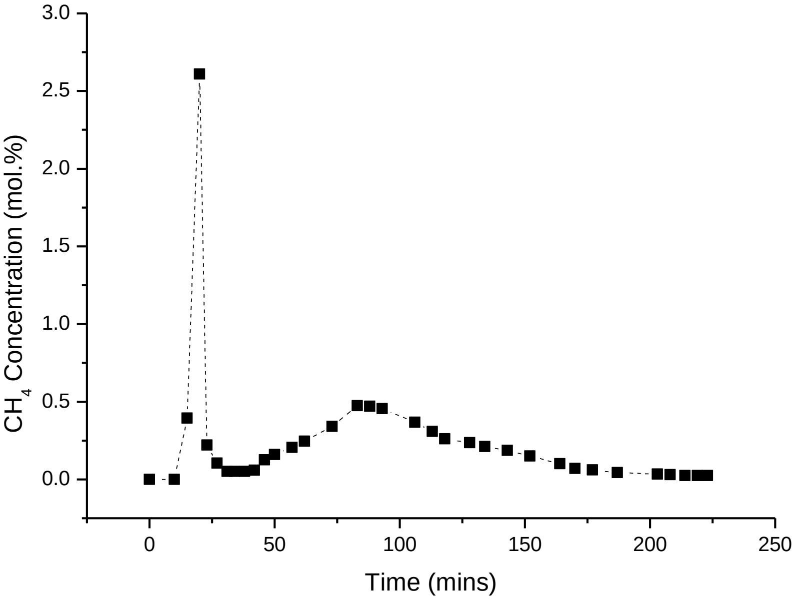

Figure 5.6: CH_4 concentration during reduction of NiO/Al_2O_3 in a 20 % H_2/Ar DBD.

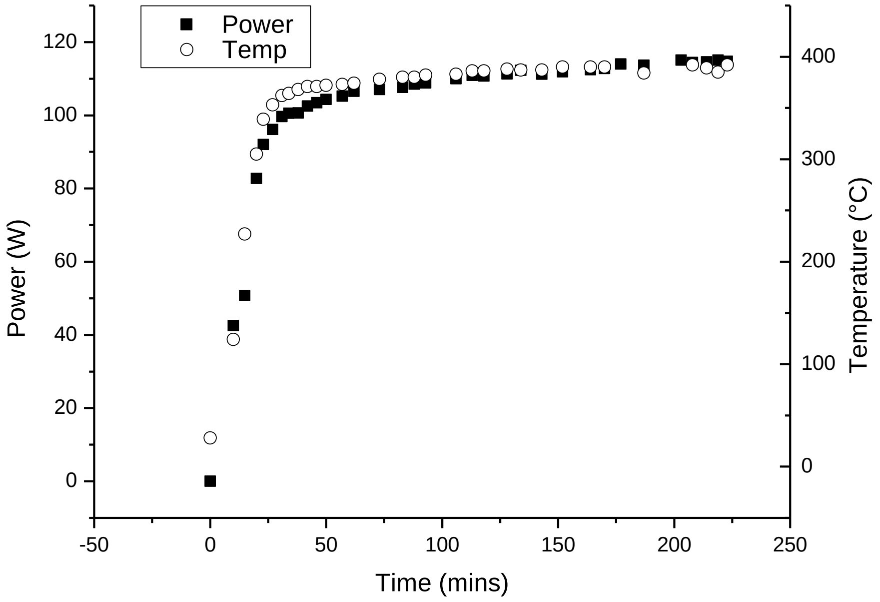

Figure 5.7: Power and temperature profiles during reduction of NiO/Al_2O_3 in a 20 % H_2/Ar DBD.

Figure 5.4 shows that H_2 consumption peaked at ~ 30 minutes and then gradually returned to its initial concentration indicating that reduction of NiO had gone to completion. Similar profiles for H_2 consumption have been obtained for plasma-reduction of Pt and Co-based catalysts by Kim et al [10]. The evolution of carbon-containing products is due to the plasma action causing reactions to occur with carbonates that are present in the catalyst. Consequently, the concentrations of CO_2 and CO are significantly lower than in the case of plasma-reduction with CH_4, where CO_2 and CO are products of the reduction. Concentrations of CO_2 and CO peaked at ~ 20 minutes as shown in Figure 5.5, the presence of these species with H_2 and H_2O make the water-gas shift reaction possible (5.2). The production of CH_4, shown in Figure 5.6 is a result of a reaction between H_2 and carbonates in the catalyst. The concentration of CH_4 peaked initially at 20 minutes and then decreased. This is possibly due to CH_4 consumption in reduction of NiO, producing CO_2 and CO as shown in reactions 5.0 and 5.1 respectively. A second peak in CH_4 production at a lower concentration is observed at ~ 75 minutes, when the rate of NiO reduction is slower and therefore CH_4 may be less readily consumed in NiO reduction. All carbon–containing product gases decreased to zero as the surface carbonate source in the catalyst became used up.

	Before Reduction	After Reduction
Mass of catalyst (g)	7.39	6.32
Mass of liquid product (g)	-	0.61
% wt. C and H in the catalyst	C = 3.3 H = 1.3	C = 2.3 H = 0.0
% wt. C and H in the liquid product	-	C = 0.5 H = 11.8

Table 5.3: Mass and elemental analysis of NiO/Al_2O_3 catalyst and liquid product before and after reduction in a 20 % H_2/Ar DBD.

The carbon and hydrogen contents of the NiO/Al_2O_3 catalyst before and after reduction are shown in Table 5.3. The carbon content of the reduced Ni/Al_2O_3 catalyst decreased by 30 %, in accordance with the production of carbon-containing gases CH_4, CO_2 and CO. It is possible that only surface carbonates reacted whilst carbonates in the bulk of the catalyst remained present in the sample. In contrast to the catalyst reduced in CH_4, there was no colour change observed for the reduction of NiO/Al_2O_3 in H_2. The liquid product analysis showed that it is predominantly H_2O with trace amounts of higher hydrocarbons. The calculated mass of H_2O expected from the reduction by H_2 is 0.59 g, close to the observed mass of 0.61 g.

When the sample was removed from the reactor, a pyrophoric reaction was observed by a rapid temperature increase to 93 °C, this energy is released as a result of a highly exothermic oxidation of Ni to form an amorphous NiO film on the surface of the catalyst. This is in contrast to the reduction of NiO in a CH_4 plasma, where no exothermic reaction was observed on removing the catalyst from the reactor. In the case of the CH_4 plasma-reduction, carbon deposition prevented the re-oxidation by forming a protective physical barrier.

5.3.3 Treatment of NiO/Al_2O_3 Catalyst with an Argon Plasma

The treatment of NiO/Al_2O_3 with an argon plasma has been carried out, in order to determine whether NiO can be reduced by high energy electrons at a temperature significantly higher (up to 320 °C) than previously investigated by other researchers in this field. Previous research on treatment of NiO/Al_2O_3 in an argon plasma was conducted in a discharge that was close to room temperature where NiO reduction was not observed; despite the ability to reduce other metals under the same conditions (Table 5.0). The results of the gaseous analysis and profiles for power and temperature are shown in Figures 5.8 and 5.9 respectively.

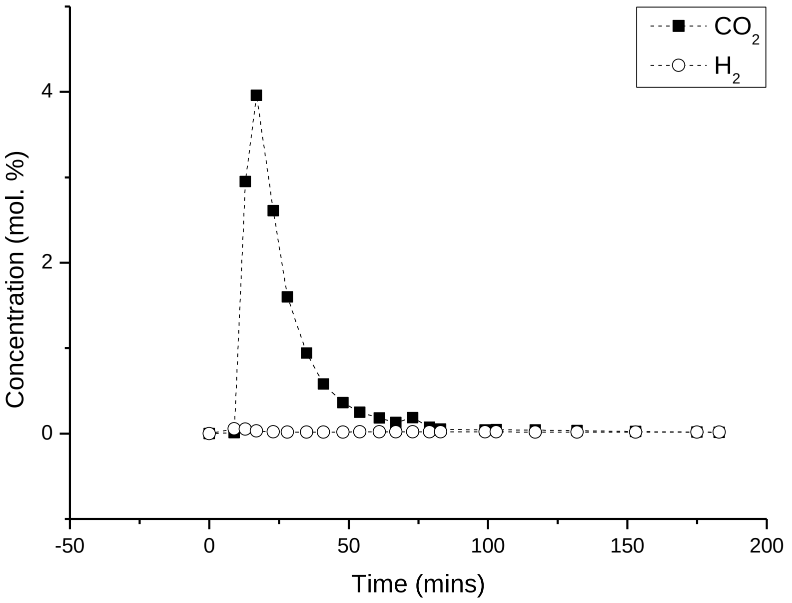

Figure 5.8: Concentration of gaseous products CO_2 and H_2 during the treatment of a NiO/Al_2O_3 catalyst in an Ar DBD.

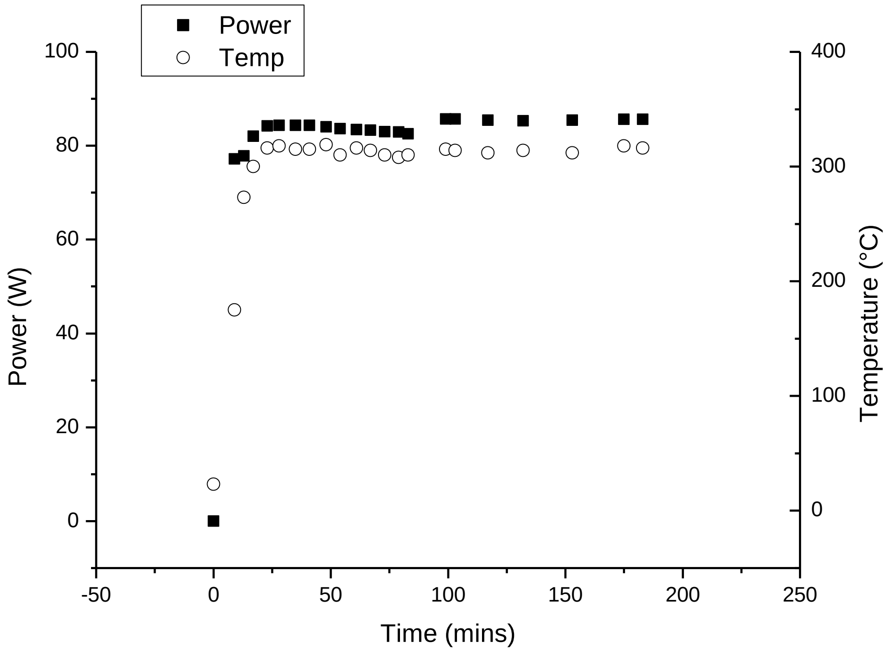

Figure 5.9: Power and temperature profiles for the treatment of a NiO/Al_2O_3 catalyst in an Ar DBD.

The products detected by micro-GC were CO_2 and H_2, as shown in Figure 5.8. The concentration of CO_2 peaked at ~ 10 – 20 minutes. The source of CO_2 in this experiment is considered to be solely from the carbonates present in the catalyst. As the NiO catalyst was found not to be reduced, there cannot be any involvement of CO_2 with a NiO reduction mechanism or water-gas shift reaction (5.2), as in the case of H_2 and CH_4 plasmas. A small amount of H_2 was detected which peaked at the same time as CO_2. Similarly, this is a result of the plasma action releasing species from the catalyst, although the concentration of H_2 was negligible at < 0.06 % throughout the experiment. There was no observed evolution of CO, as was seen in experiments where CH_4 or H_2 were present. This indicates that CO production is a result of the NiO reduction and water-gas shift mechanisms (in the case of CH_4 and H_2 plasma-reductions) and that CO is not released directly from the plasma action on carbonates that may be present in the catalyst.

	Before Reduction	After Reduction
Mass of catalyst (g)	18.57	17.70
Mass of liquid product (g)	-	0.40
% wt. C and H in the catalyst	C = 3.8 H = 1.6	C = 3.4 H = 0.3
% wt. C and H in the liquid product	-	C = 0.4 H = 12.2

Table 5.4: Mass and elemental analysis of NiO/Al_2O_3 catalyst and liquid product before and after treatment in an Ar DBD.

Table 5.4 shows the mass of the catalyst and liquid product, as well as the elemental analyses of these samples for the carbon and hydrogen content. The mass loss observed in the catalyst is possibly due to a loss of residual adsorbed H_2O from the catalyst surface. As in previous cases, the liquid product was mostly H_2O with trace amounts of carbon. The mass of H_2O collected during this experiment is unexpectedly high in comparison with previous results for CH_4 and H_2 plasmas, given that reduction of NiO did not occur in this experiment. The water collected could be either from H_2O adsorbed on the catalyst surface which has been desorbed under plasma conditions and/or a result of reactions between OH groups which are abundant on the alumina support. In CH_4 and H_2 plasma-reduction experiments, the mass of H_2O collected was 0.78 g and 0.61 g respectively, however, it is possible that a water-gas shift (5.2) has reduced the concentration of H_2O during these experiments (NiO/Al_2O_3 is known to be an effective catalyst for water-gas shift [16]). In addition, it is possible that a reaction between OH groups on the catalyst support, which could result in H_2O formation, would be suppressed by a competing reaction that involves OH groups in the reduction of NiO when CH_4 or H_2 are present.

In agreement with previous work by Cheng et al. [4, 8], where NiO reduction did not occur in a room temperature glow discharge, the results of this experiment show that NiO reduction does not occur in an argon DBD at elevated temperature. Cheng et al. [4] made the observation that ion pairs (M^{n+}/M) with positive standard electrode potentials are reducible in an argon plasma and those with negative standard electrode potentials (i.e. Ni^{2+}/Ni) are not reducible under these conditions. The results of this study are in agreement with this hypothesis. Metal reduction by argon plasma may be feasible in accordance with the electrochemical properties of the metal and if the electrochemical properties are such that the catalyst is not reducible under these conditions, the temperature of the system will have no effect.

5.3.4 Reduction of NiO/Al_2O_3 coated $BaTiO_3$ by 20 % H_2/Ar in a Packed-Bed DBD Reactor

A powdered coating of 33 wt. % NiO/Al_2O_3 has been applied to $BaTiO_3$ beads (4 mm diameter). Reduction of the NiO/Al_2O_3 coated $BaTiO_3$ by 20 % H_2/Ar has been carried out in a packed-bed DBD reactor (this reactor has been previously described in section 3.2). The NiO reduced rapidly under these conditions and an orange arc-like discharge was observed, after which the experiment was immediately terminated. A colour change from grey to black was observed in some of the beads used in this experiment. The black beads were found to be highly conductive, showing a resistance of 10 Ω when 1 kV was applied (measured using a Kyoritsu mega ohm meter). Due to the highly conductive coating, a large electric current was able to flow directly through the packed-bed where there are many contact points between the beads, giving arcing rather than a stable plasma discharge. In contrast, the grey beads still had insulating properties (∞ Ω), which is essential for the formation of a DBD. Although several studies have been carried out previously in which $BaTiO_3$ beads have been combined with catalysts in the reactor [17-19], this is the first study to coat the catalyst directly onto the beads and thereby modify the dielectric properties of the beads.

5.4 Catalyst Characterisation

5.4.1 XRD

The bulk structures of all the catalysts were investigated by X-ray powder diffraction. The XRD pattern of a fresh sample of NiO/Al_2O_3 (as supplied) was also analysed for comparison, the results are presented in Figure 5.10.

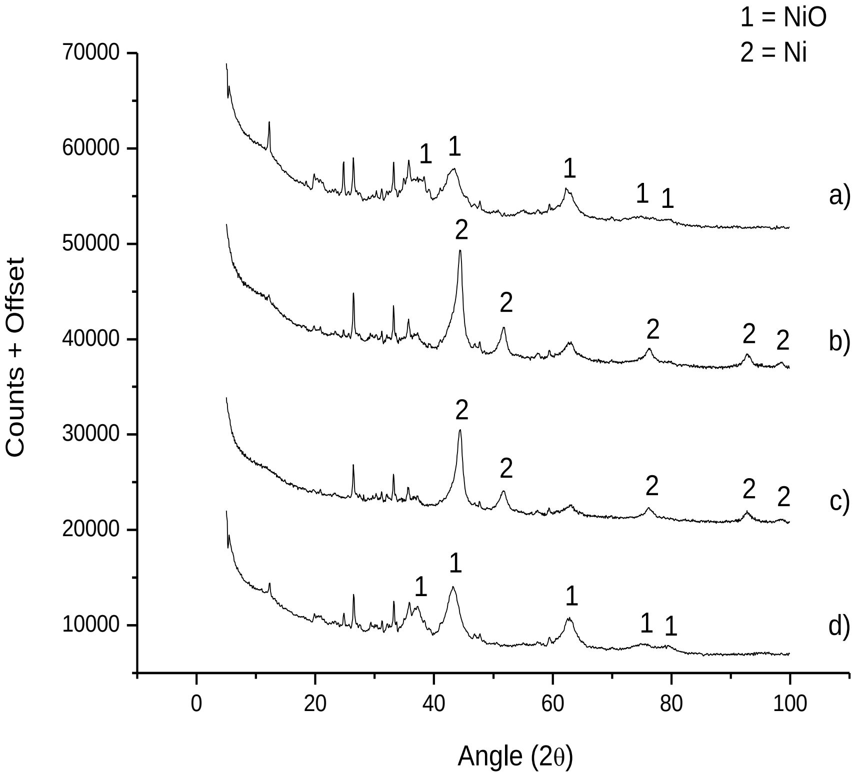

Figure 5.10: XRD patterns of NiO/Al_2O_3 catalysts after a) no treatment, b) CH_4 plasma-reduction, c) H_2 plasma-reduction, d) treatment in an Ar plasma. NiO peaks at 2θ = 37.2°, 43.2°, 62.9°, 75.4° and 79.4°. Ni peaks at 2θ = 44.4°, 51.6°, 76.1°, 92.1° and 98.1° [20].

The fresh NiO/Al_2O_3 shown in Figure 5.10 (a) shows broad NiO peaks at 2θ = 37.2°, 43.2°, 62.9°, 75.4° and 79.4°, as well as some sharp unidentified peaks at 2θ < 37°. Peaks for Al_2O_3 have been looked for and cannot be found, indicating that the support is amorphous and therefore is not detectable by XRD. It can be seen from Figure 5.10 (d) that the sample treated with argon plasma is similar to the fresh sample, confirming that the NiO crystal structure remained unchanged during treatment with an Ar DBD. Figure 5.10 (b and c) show the appearance of peaks corresponding to metallic Ni at 2θ = 44.4°, 51.6°, 76.1°, 92.1° and 98.1°. These peaks indicate that metal reduction has taken place in both CH_4 and H_2/Ar plasma. The NiO peaks at 2θ = 62.9° and peak shoulders at 2θ ≈ 44° on the XRD patterns of the reduced catalysts, indicate that the bulk of the catalyst may not have been fully reduced. There is a peak at 2θ = 24.8° on the fresh catalyst, which matches the reference pattern for nickel silicate hydrate (3 NiO·2 SiO_2·2 H_2O) [20]; this species is also reduced in both CH_4 and H_2/Ar plasma as indicated by the disappearance of this peak on Figure 5.10 (b and c).

Crystallite sizes (Table 5.5) have been calculated using the well-known Scherrer equation (5.6), where d is the average volume diameter of the crystallite, λ is the wavelength of the incident X-rays from a Cu source, θ the X-ray incidence angle with respect to the sample surface, β is the peak width at half peak height (in radians) and β_0 is the instrumental line broadening [21].

$$d = \frac{0.89\lambda}{(\beta - \beta o)\cos\theta} \qquad (5.6)$$

Sample	Crystallite Size (nm)
a) Fresh NiO/Al_2O_3	6
b) CH_4 plasma reduced Ni/Al_2O_3	6
c) H_2/Ar plasma reduced Ni/Al_2O_3	7
d) NiO/Al_2O_3 after Ar plasma	6

Table 5.5: Estimation of the crystallite size of a NiO/Al_2O_3 catalyst after plasma treatments. Uncertainty in the measurement to one standard deviation is ± 1 nm.

Table 5.5 shows that the crystallite size was not affected by the plasma treatment. The small crystallite size (6 nm) of NiO in the fresh catalyst and Ni in the plasma-reduced samples indicates that no sintering of Ni particles has occurred under plasma conditions. These findings are in agreement with results obtained in previous work [10, 11], where direct comparisons of Pt/Al_2O_3

catalysts before and after plasma-reductions have shown that crystallite sizes in the nm range have not been changed significantly by plasma treatment.

5.4.2 SEM

SEM images of samples of each catalyst are shown in Figures 5.11 to 5.14 at various magnifications. The images show an amorphous Al_2O_3 phase with highly dispersed nanoparticles of Ni/NiO.

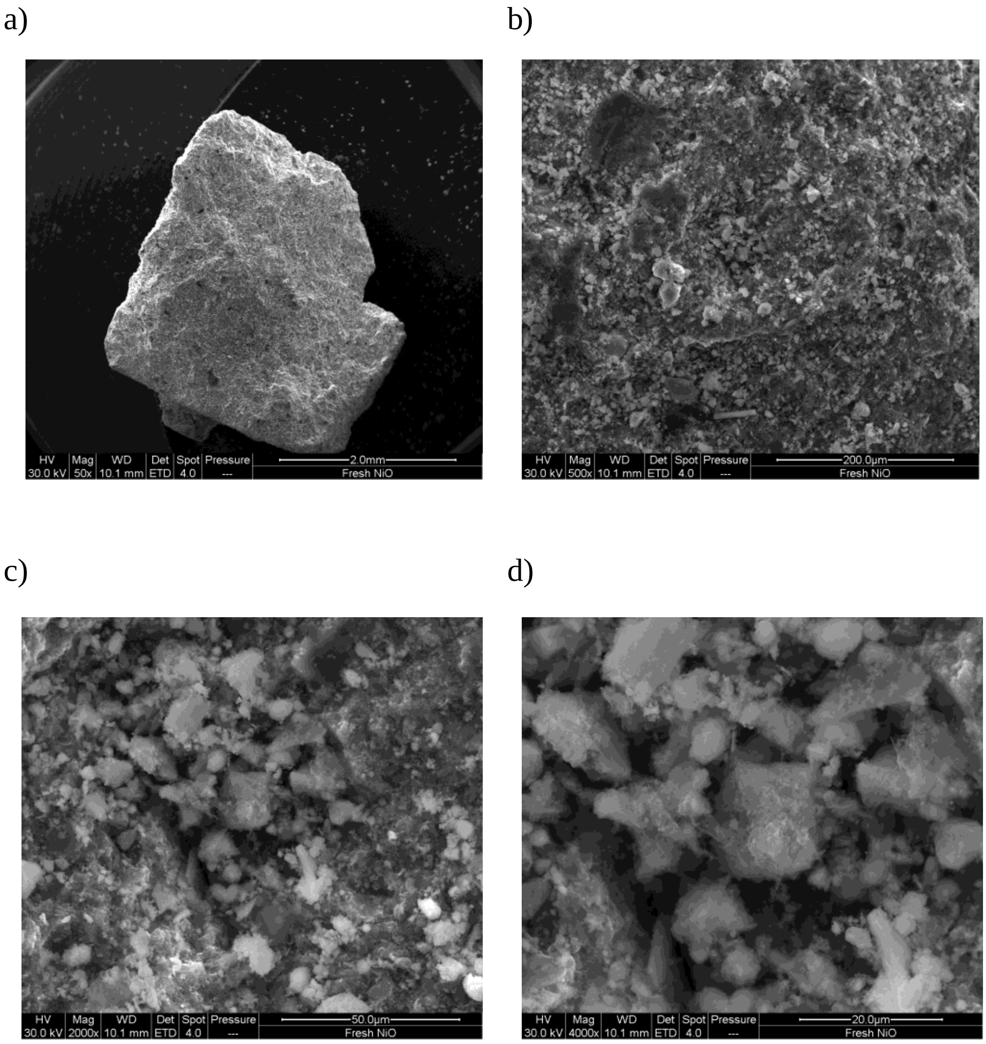

Figure 5.11: SEM images of the NiO/Al_2O_3 catalyst as supplied a) mag. 50 × b) mag. 500 × c) mag. 1000 × d) mag. 4000 ×.

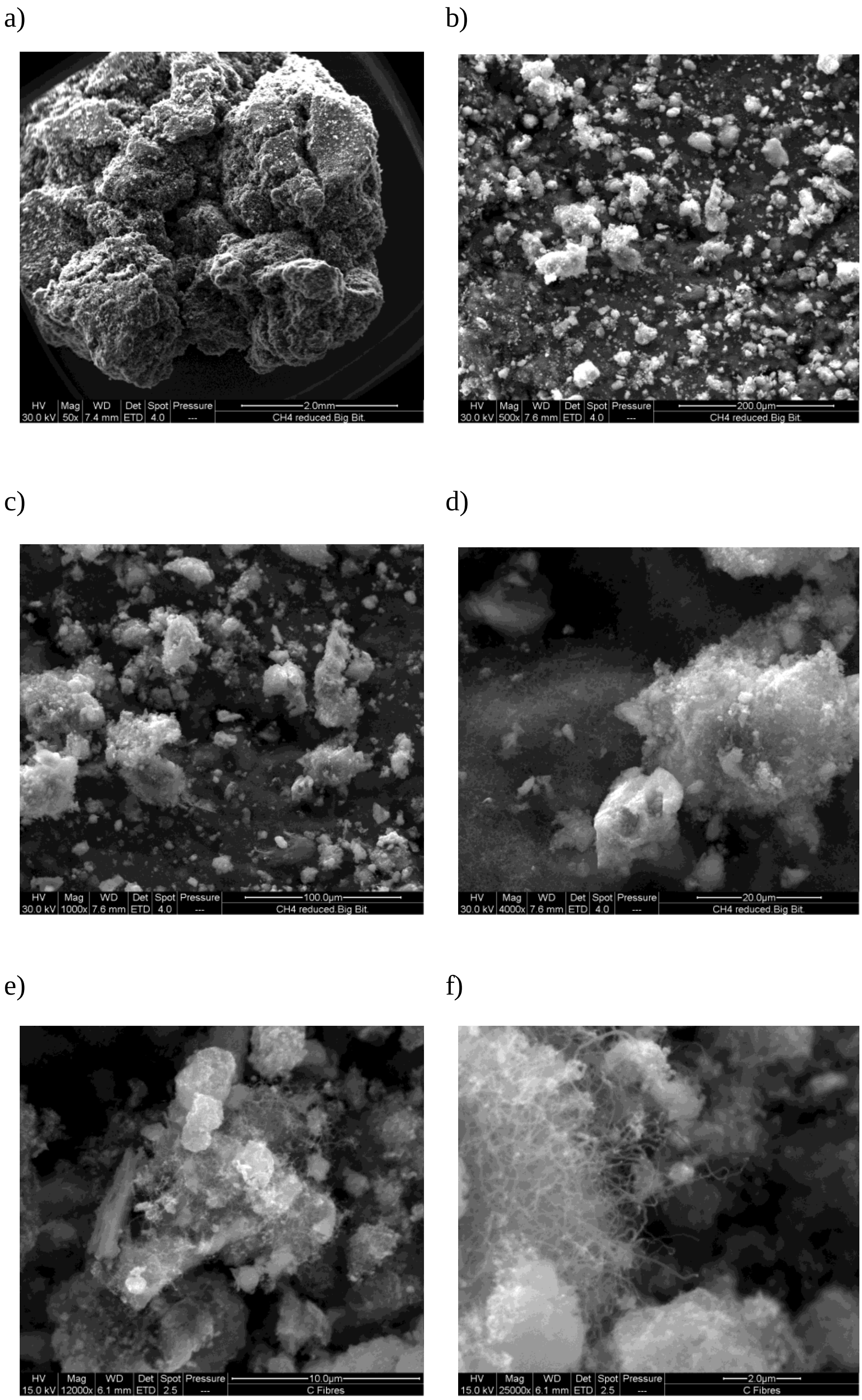

Figure 5.12: SEM images of the NiO/Al_2O_3 catalyst reduced in CH_4 plasma a) mag. 50 × b) mag. 500 × c) mag. 1000 × d) mag. 4000 × e) mag. 12000 × f) mag. 25000 ×.

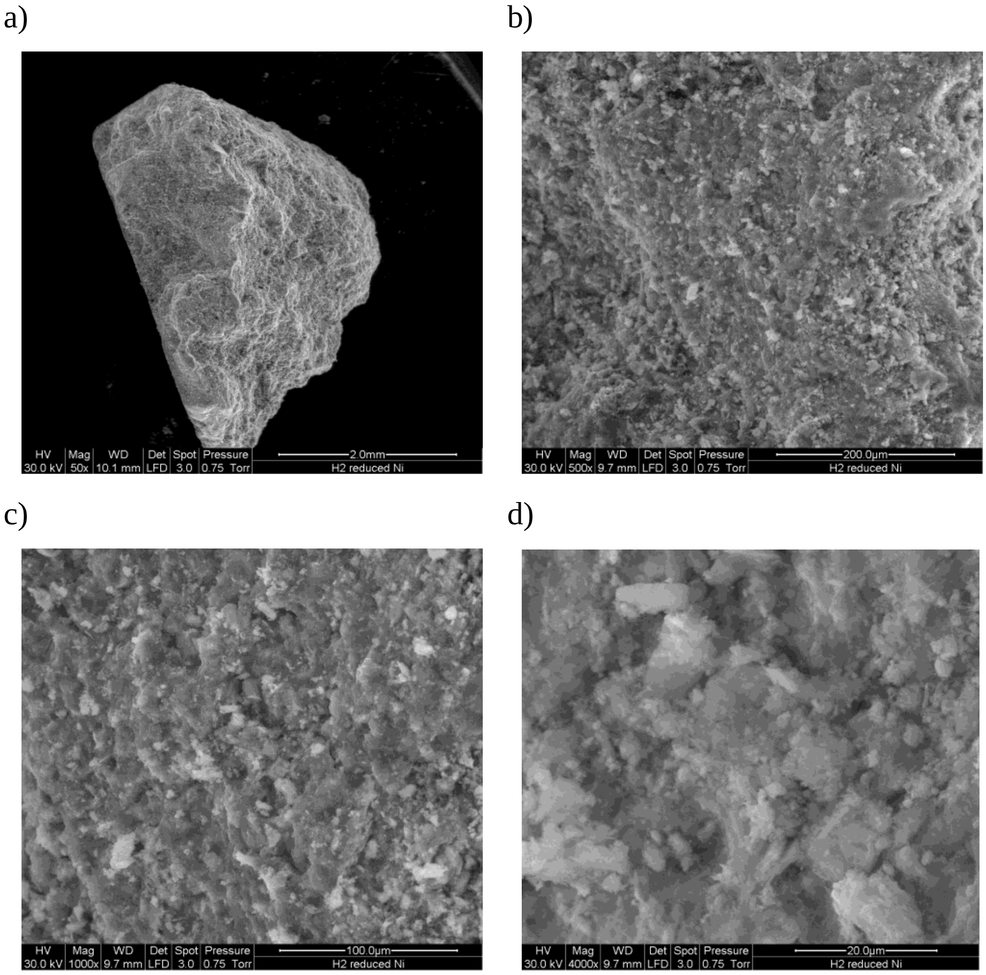

Figure 5.13: SEM images of the NiO/Al_2O_3 catalyst reduced in H_2/Ar plasma a) mag. 50 × b) mag. 500 × c) mag. 1000 × d) mag. 4000 ×.

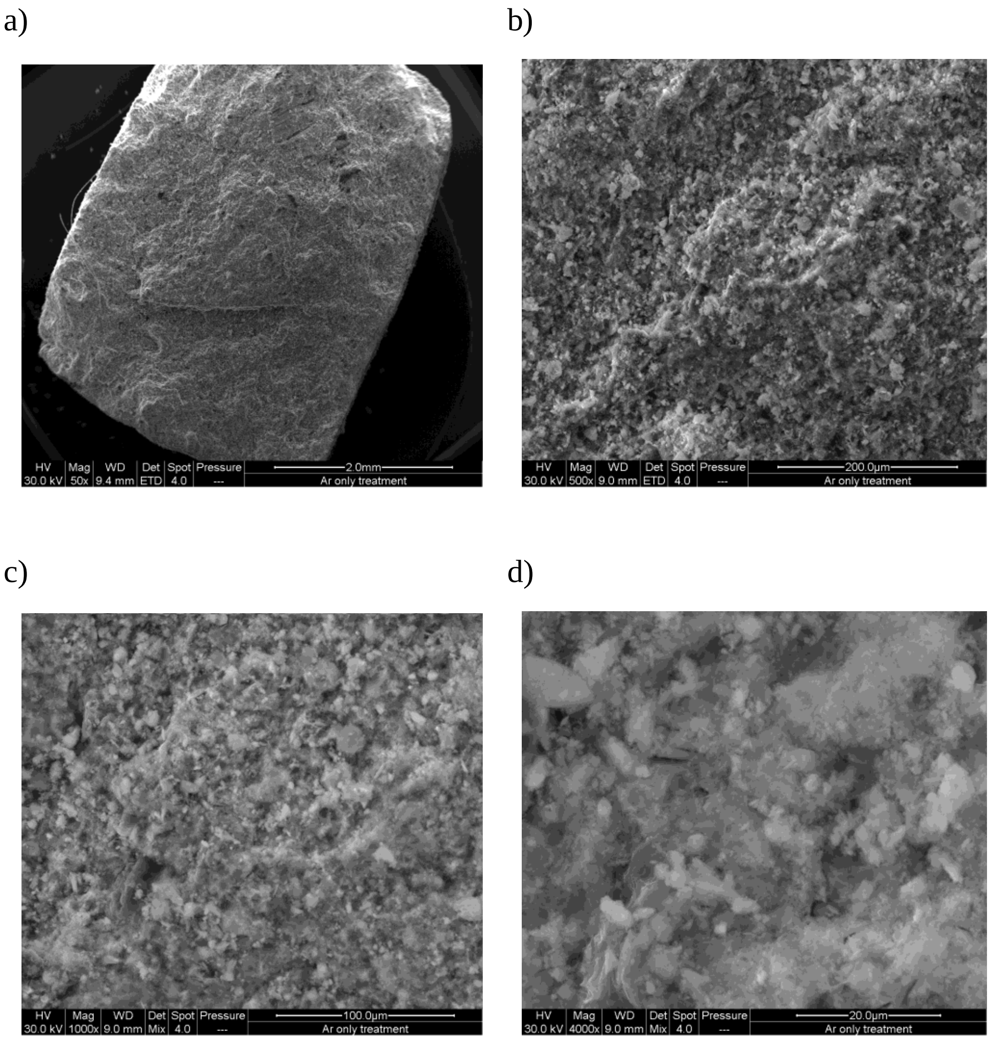

Figure 5.14: SEM images of the NiO/Al_2O_3 catalyst after treatment with Ar plasma a) mag. 50 × b) mag. 500 × c) mag. 1000 × d) mag. 4000 ×.

The catalyst that has been reduced by a CH_4 plasma (Figure 5.12) is different in appearance to the other three samples. This can be seen by the naked eye due to a colour change from grey to black, as well as the adherence of individual particles to form large solid blocks (Figure 5.12 a). The cotton wool-like structures that can be seen in Figure 5.12 (b – d) are fibrous carbon structures; these can be seen clearly in Figure 5.12 (e and f) in which individual carbon nanofibres are visible. SEM software allowed the measurement of these carbon fibres, which revealed a mean outer diameter of 55 nm, ranging from 28 – 80 nm. The presence of carbon fibres on the surface of the catalyst provides a protective barrier that prevents re-oxidation of Ni on exposure to air. For this reason, the pyrophoric oxidation observed with the H_2 plasma-reduced sample was not observed for the CH_4 plasma-reduced sample.

Plasma production of carbon nanostructures has been extensively reviewed [22-25], due to the great potential of these materials for a wide range of applications including as a hydrogen storage media [26] and a reinforcing agent in polymers and metals [22]. The use of thermal arc-jet plasma for continuous carbon nanotubes (CNT) synthesis from CH_4, catalysed by Ni-Y powders has been reported by Choi et al. [27], the produced CNTs had an outer diameter of 10 – 50 nm. It would be interesting to further investigate the structure of the carbon deposited in this study by the use of transmission electron microscopy (TEM).

5.5. Electrical Properties of the Plasma when Packed with NiO/Al_2O_3

The voltage and current signals for CH_4 discharges in the empty DBD reactor and in the presence of a NiO/Al_2O_3 catalyst packed into the discharge gap are presented in Figures 5.15 and 5.16, at a fixed discharge power of 30 W. Filamentary discharges which correspond to the numerous current spikes that can be seen in Figure 5.15 are less easily formed in the presence of a catalyst due to a decrease in the effective discharge gap. The catalyst surface allows for the formation of a homogeneous surface discharge which is shown by a decrease in the number and amplitude of current spikes seen in Figure 5.16. The same effect was observed in a previous investigation when the reactor was packed with zeolite as described in section 3.5.

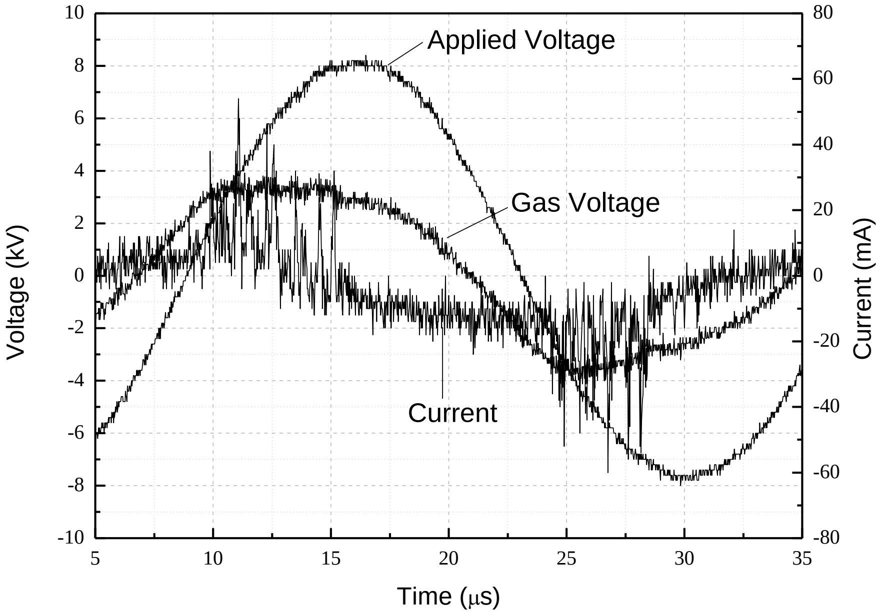

Figure 5.15: Electrical waveforms for the applied voltage, gas voltage and current in a 100 % CH_4 DBD in the absence of a catalyst (CH_4 flow rate = 100 ml min^{-1}, discharge power = 30 W).

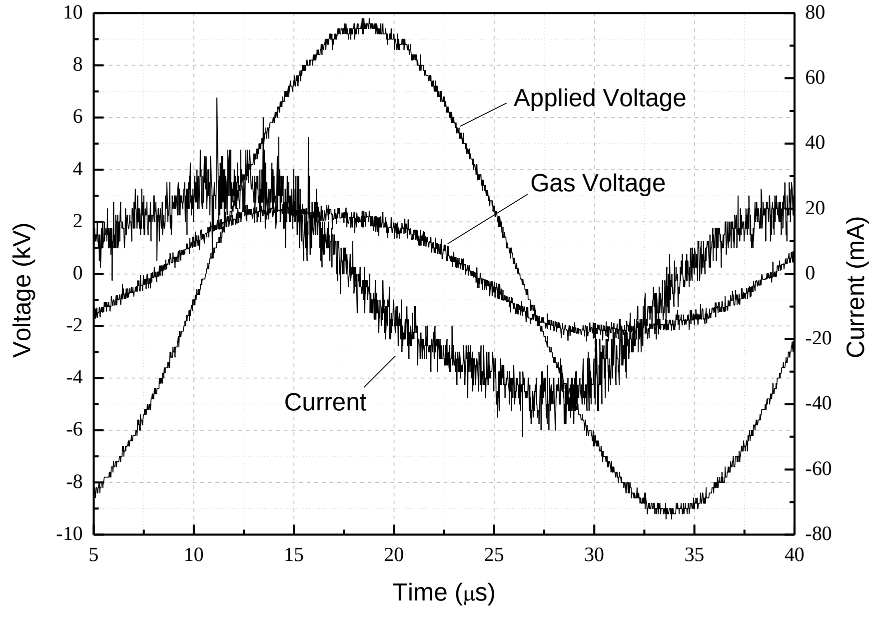

Figure 5.16: Electrical waveforms for the applied voltage, gas voltage and current in a 100 % CH_4 DBD packed with NiO/Al_2O_3 catalyst (CH_4 flow rate = 50 ml min^{-1}, discharge power = 30 W).

5.5.1. Effect of NiO Reduction on Electrical Parameters

Reduction of NiO to Ni may result in changes to the dielectric properties of the catalyst and hence, the plasma discharge. Table 5.6 shows some of the plasma electrical properties for 100 % CH_4 and 20 % H_2/Ar plasma discharges, packed with both NiO/Al_2O_3 and Ni/Al_2O_3 (before and after the plasma-reductions).

Gas Type	Packing Material	Applied Voltage pk-pk (kV)	Breakdown Voltage (kV)	Charge pk-pk (nC)	Charge Discharged (nC)	Transferred Charge per Half Cycle (nC)	Total Capacitance (pF)
CH_4	$NiO/\gamma Al_2O_3$	18.9	0.75	377	207	76	15.6
CH_4	$Ni/\gamma\text{-}Al_2O_3$	15.6	0.64	434	281	129	20.6
Ar/H_2	$NiO/\gamma\text{-}Al_2O_3$	17.7	0.88	408	227	88	17.8
Ar/H_2	$Ni/\gamma\text{-}Al_2O_3$	13.9	1.07	360	220	119	17.8

0

Table 5.6: Electrical parameters of DBD at constant power (30 W) when unreduced NiO/Al_2O_3 and reduced Ni/Al_2O_3 are packed into the discharge gap. Methods for the calculation of these parameters have been derived from several publications on electrical properties of DBDs [28-31] and are detailed in Appendix B.

Table 5.6 and Figure 5.17 show that the applied voltage required to sustain a discharge power of 30 W in CH_4 is lower for the more conductive Ni phase. At a maximum, the applied voltage for the discharge packed with NiO/Al_2O_3 was 18.9 $kV_{pk\text{-}pk}$ and when packed with Ni/Al_2O_3 it was reduced to 15.6 $kV_{pk\text{-}pk}$. The same effect can be seen in the H_2/Ar discharge with a reduction in applied voltage from 17.7 $kV_{pk\text{-}pk}$ to 13.9 $kV_{pk\text{-}pk}$.

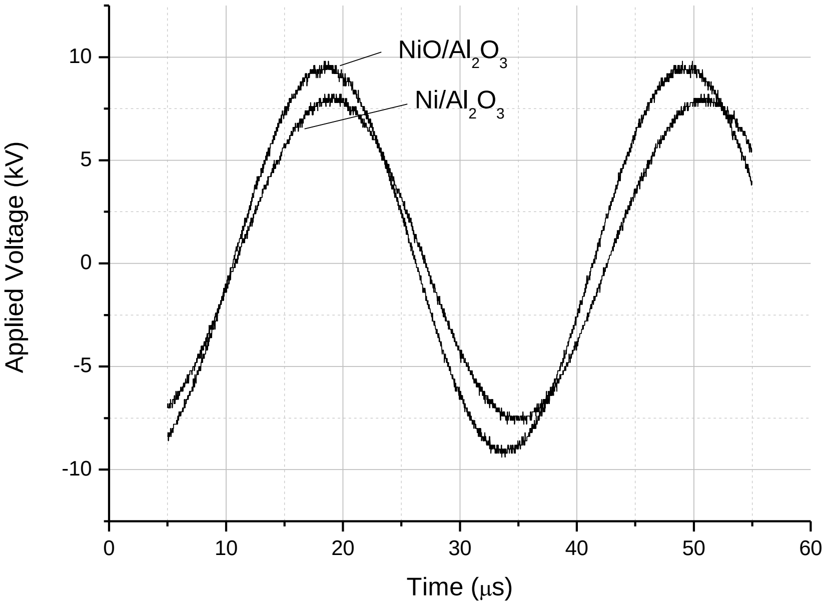

Figure 5.17: The applied voltage waveforms of a 100 % CH_4 DBD packed with the unreduced NiO/Al_2O_3 catalyst and the reduced Ni/Al_2O_3 catalyst.

The breakdown voltage (V_b) increases in going from NiO to Ni for a H_2/Ar discharge from 0.88 kV to 1.07 kV respectively. This can be explained by the increase in transferred charge per half cycle from 88 nC to 109 nC, resulting in a reduced charge remaining in the discharge region at the end of each half cycle. Consequently, an increased voltage is required to breakdown the gas. However, the observation was different in the CH_4 discharge, where a slight decrease in V_b was observed in going from NiO to Ni (0.75 kV to 0.64 kV respectively); in this case, there is thought to be significant contribution from a change in gas composition when Ni is present.

Lissajous figures for the CH_4 and H_2/Ar discharges are shown in Figures 5.18 and 5.19 respectively. The data was recorded at a fixed discharge power of 30 W before and after the reduction of NiO/Al_2O_3. The total capacitance of the

DBD system can be calculated from the Lissajous figure and is shown in Table 5.6. In a CH_4 discharge, the capacitance increases in going from a NiO/Al_2O_3 packing to a Ni/Al_2O_3 packing, from 15.6 pF to 20.55 pF respectively. However, the metal reduction is coupled with a change in the gas composition to include a significant concentration of H_2. This could also affect the capacitance of the system. It can be seen from Figure 5.19 that in a H_2/Ar discharge (where gas compositions are similar for both NiO/Al_2O_3 and Ni/Al_2O_3) the reduction of NiO in the catalyst had little effect on the Lissajous figure and correspondingly, the capacitance remained constant (17.77 – 17.78 pF). These results suggest that the gas composition has a major contribution to the total capacitance which is more significant than the change in the material from NiO/Al_2O_3 to Ni/Al_2O_3.

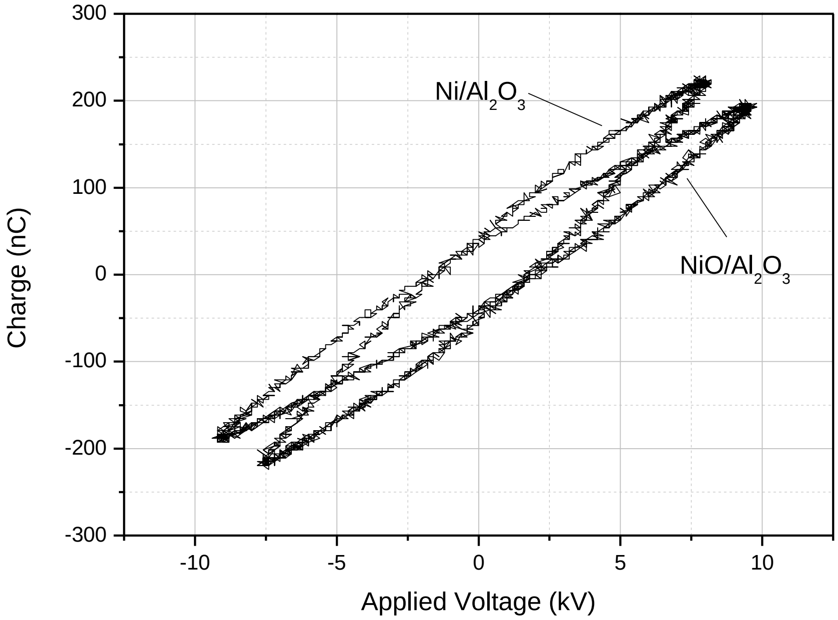

Figure 5.18: Lissajous figures for a CH_4 DBD packed with NiO/Al_2O_3 and CH_4 plasma-reduced Ni/Al_2O_3 at a fixed discharge power of 30 W (CH_4 flow rate = 50 ml min^{-1}).

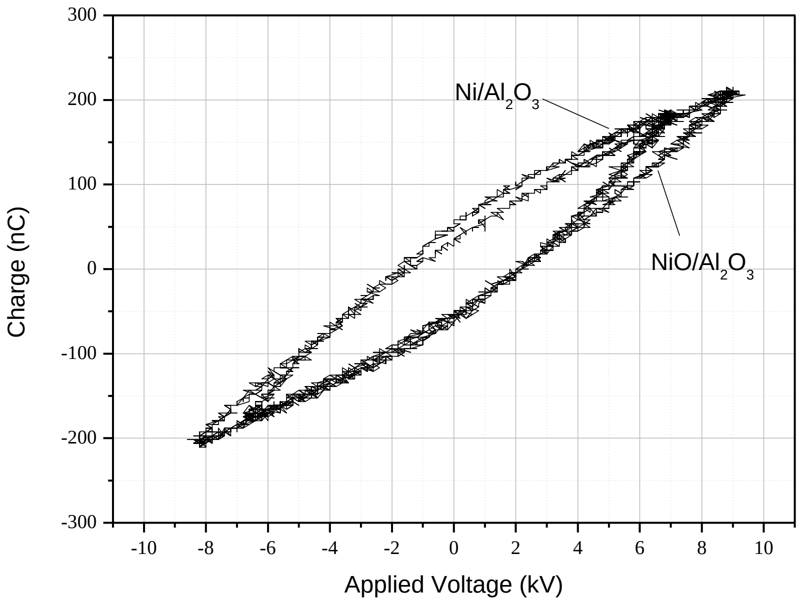

Figure 5.19: Lissajous figures for a 20 % H_2/Ar DBD packed with NiO/Al_2O_3 and H_2/Ar plasma-reduced Ni/Al_2O_3 at a fixed discharge power of 30 W (total flow rate = 100 ml min^{-1}).

5.6 Temperature Programmed Reduction of NiO/Al_2O_3

TPR of the NiO/Al_2O_3 catalyst has been carried out with CH_4 and H_2 in helium diluents, in order to compare both the temperature and products of these processes with the plasma-reduction processes. The experiments were performed at a pressure of 1 bar in a fully automated CATLAB microreactor (Hiden Analytical) at Newcastle University. The microreactor outlet fed into a soft ionisation quadrupole mass spectrometer (QIC-20) via a heated capillary line for continuous online analysis. An internal K-type thermocouple in an inert alumina sleeve was inserted into the microreactor catalyst bed for both control and measurement of the temperature.

5.6.1 Thermal Reduction of NiO/Al_2O_3 by CH_4

The results for TPR of NiO/Al_2O_3 with 10 % CH_4 in helium are shown in Figure 5.20. The onset of reduction occurred rapidly at 440 °C, as can be seen by a sharp decrease in CH_4 concentration and simultaneous increase in H_2, H_2O, CO_2 and CO. The molar consumption and production of each gaseous species have been calculated and are shown in Table 5.7.

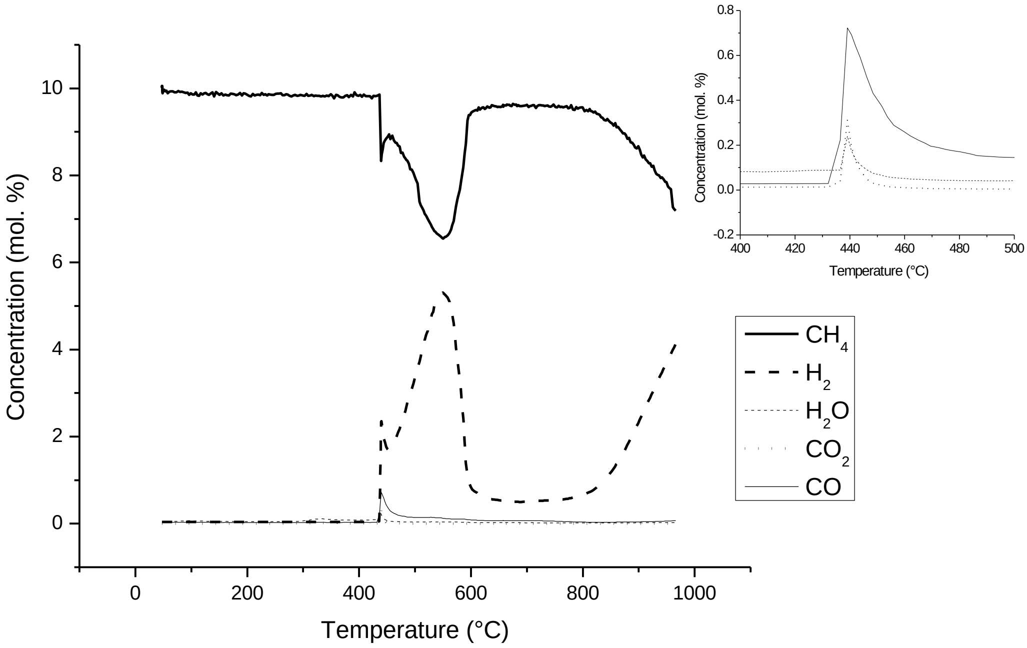

Figure 5.20: TPR profile for the reduction of NiO/Al_2O_3 by 10 % CH_4/He (mass of catalyst = 25.0 mg, flow rate = 100 ml min^{-1}, temperature ramp = 10 °C min^{-1}). The inset shows the profiles of H_2O, CO_2 and CO in the temperature range 400 – 500 °C.

Species	Total μmol
NiO	111
CH_4 consumption	3509
H_2 produced	4654
H_2O produced	197
CO_2 produced	31
CO produced	287

Table 5.7: Total μmol of each species consumed or produced during the TPR of NiO/Al_2O_3 by CH_4 (mass of catalyst = 25.0 mg, flow rate = 100 ml min^{-1}, temperature ramp = 10 °C min^{-1}).

In the temperature range 440 – 500 °C (Figure 5.20, inset), the reduction of NiO by CH_4 is observed by the presence of reduction products CO_2, CO and H_2O (5.0 – 5.2). Simultaneously, a rapid catalytic conversion of CH_4 to H_2 and solid carbon (5.3) takes place between 440 °C and 600 °C, for this reason, the molar quantities for CH_4 consumption and H_2 production far exceed the stoichiometry of the NiO reduction. At temperatures > 600 °C, catalytic CH_4 conversion has ceased due to heavy carbon deposition and subsequent deactivation of the catalyst. Pyrolysis of CH_4 to form H_2 and solid carbon (5.3) is observed at temperatures > 800 °C; however, this is in the gas phase and is distinct from the catalytic process observed at lower temperatures. This is in agreement with results obtained by Qin et al. [32] where CH_4 was heated to 800 °C at atmospheric pressure in the absence of a catalyst and pyrolysis of CH_4 was observed to form coke and H_2.

$$4\ NiO\ (s) + CH_4\ (g) \rightarrow 4\ Ni\ (s) + CO_2\ (g) + 2\ H_2O\ (l) \qquad (5.0)$$

$$NiO\ (s) + CH_4\ (g) \rightarrow Ni\ (s) + 2\ H_2\ (g) + CO \qquad (5.1)$$

$$CO\ (g) + H_2O\ (l) \leftrightarrow H_2\ (g) + CO_2\ (g) \qquad (5.2)$$

$$CH_4\ (g) \rightarrow C\ (s) + 2\ H_2\ (g) \qquad (5.3)$$

After TPR had been carried out, a 16.1 mg increase in the mass of the catalyst was observed. Elemental analysis revealed that the reduced catalyst contained 42.5 wt. % carbon as a result of heavy carbon deposition from both the catalytic and pyrolytic decomposition of CH_4. The onset temperature of 440 °C for NiO reduction by CH_4 is significantly lower than reduction temperatures that have been previously presented in the literature, with most studies investigating reduction of NiO by CH_4 at temperatures $\geq$ 600 °C [33-35]. Chernavskii et al. [36] reported a reduction temperature of 550 °C for TPR studies of 2 - 6 wt. % NiO/Al_2O_3. They reported no change in reduction temperature for this range of metal loading; however, studies of NiO/ZrO_2 in the same publication show that increased Ni loading decreased the reduction temperature. The NiO loading in this study is significantly greater than in other studies, therefore it can be deduced that the low reduction temperature is a result of a relatively high Ni loading on the catalyst.

The molar quantities listed in Table 5.7 show that the amount of CO far exceeds the amount of NiO in the sample, which is unexpected if NiO is considered to be the main source of oxygen in the gaseous products. This observation was also observed in TPR studies by Chernavskii et al. [36] and led them to suggest that CO is released as a result of an interaction between adsorbed carbon (C_{ad}) formed in the decomposition of CH_4 and surface hydroxyl groups (OH) on the catalyst support (5.7). NiO can be reduced by hydrogen generated in the same reaction (5.8).

$$C_{ad} + OH \rightarrow CO\,(g) + H \qquad (5.7)$$

$$NiO + H \rightarrow Ni + OH \qquad (5.8)$$

5.6.2 Thermal Reduction of NiO/Al_2O_3 by H_2

The results for TPR of NiO/Al_2O_3 by 5 % H_2 in helium are shown in Figure 5.21 and Table 5.8. The onset of NiO reduction in H_2 occurred at the lower temperature of 280 °C producing H_2O as the only product (5.5).

$$NiO + H_2 \rightarrow Ni + H_2O \qquad (5.5)$$

The observed reduction temperature is similar to results obtained by Richardson et al. where the onset of NiO/Al_2O_3 reduction was found to occur at 300 °C in H_2 [1] or at the lower temperature of 275 °C when a NiO/Al_2O_3 catalyst was promoted with Ca [37]. A small amount of CH_4 was also observed during the TPR experiment; however, this is likely to be a reaction between H_2 and carbonates already present in the catalyst, as seen previously in H_2 plasma-reduction of this catalyst (section 5.3.2). A model for the reduction of NiO/Al_2O_3 has been proposed by Richardson et al. [1]. The authors suggested that H_2 is dissociated firstly on NiO and then more rapidly on Ni sites as they become available. The hydrogen atoms rupture the Ni-O bonds, producing Ni^0 atoms and H_2O. The reduced Ni atoms will then diffuse away from the centre of reduction and nucleate to form metal clusters of a similar size to the original NiO crystallites [37].

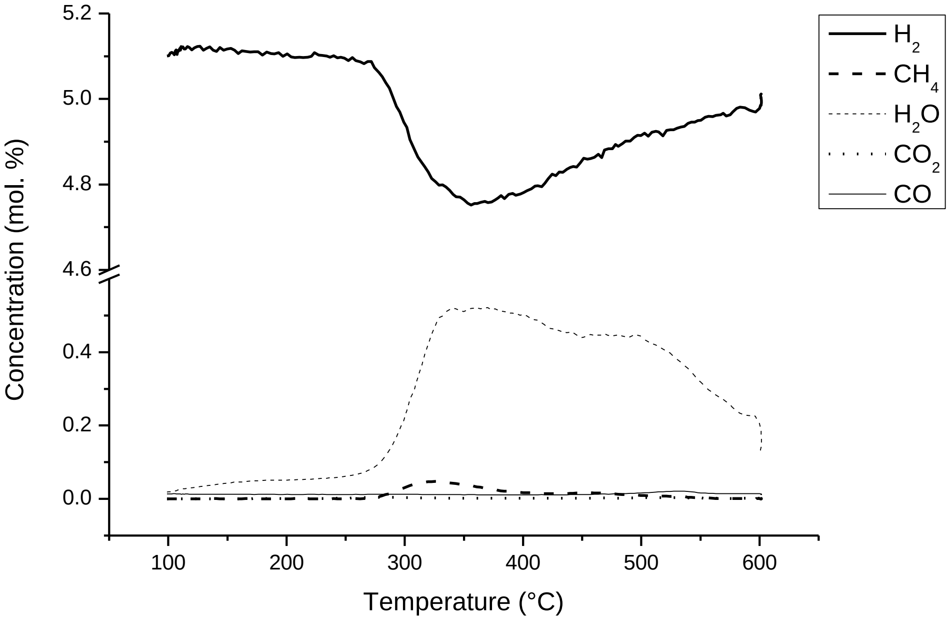

Figure 5.21: TPR profile for the reduction of NiO/Al_2O_3 by 5 % H_2/He (mass of catalyst = 50.5 mg, flow rate = 100 ml min^{-1}, temperature ramp = 10 °C min^{-1}).

Species	Total µmol
NiO	223
H_2 consumption	388
H_2O produced	597

Table 5.8: Total µmol of each species consumed or produced during the TPR of NiO/Al_2O_3 by H_2 (mass of catalyst = 50.5 mg, flow rate = 100 ml min^{-1}, temperature ramp = 10 °C min^{-1}).

5.6.3. Characterisation of Thermally Reduced Ni/Al_2O_3 Catalysts

XRD patterns of the thermally reduced samples of Ni/Al_2O_3 are shown in Figure 5.22. An estimation of crystallite size for these samples has been calculated using the Scherrer equation and is shown in Table 5.9. The XRD pattern for the CH_4 TPR sample (Fig. 5.22 b) shows that complete reduction of NiO to Ni has occurred. The sharp Ni peaks indicate that the sample has a large crystallite size, which has been calculated as 22 nm. In this experiment, the temperature was raised to 1000 °C resulting in sintering of the Ni particles. In addition, the high temperatures have caused graphitisation of the deposited carbon, which can be observed by the peak at 2θ = 26.3°. The broad peaks in Figure 5.22 (c) show that a small crystallite size of 6 nm was retained in the H_2 reduced sample; however the temperature was raised only to 600 °C during this experiment.

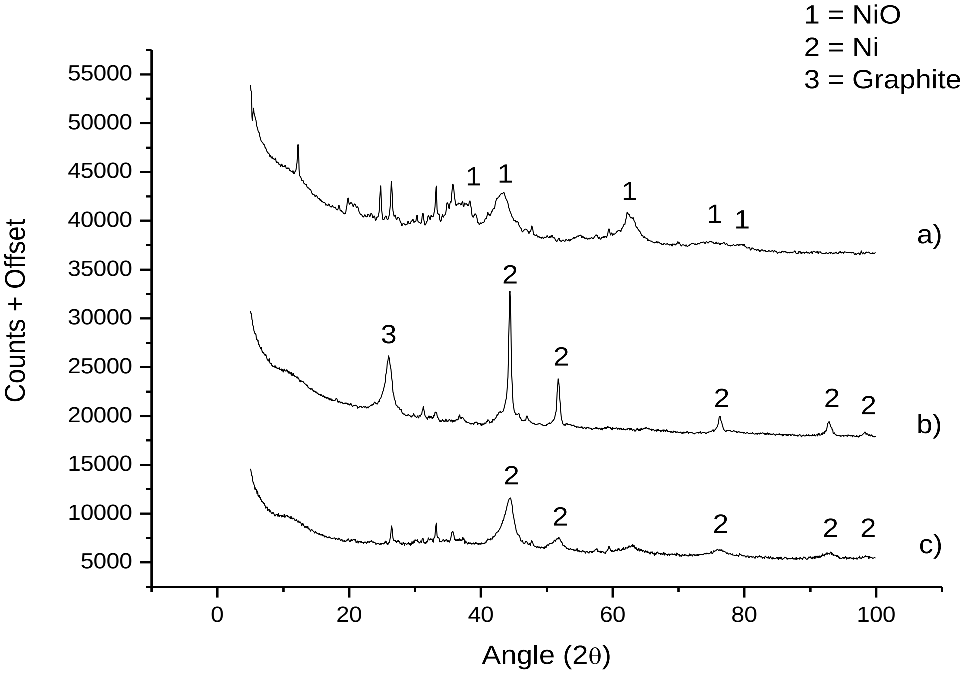

Figure 5.22: XRD patterns of the NiO/Al_2O_3 catalysts after a) no treatment, b) CH_4 TPR and c) H_2 TPR. NiO peaks at 2θ = 37.2°, 43.2°, 62.9°, 75.4° and 79.4°. Ni peaks at 2θ = 44.4°, 51.6°, 76.1°, 92.1° and 98.1°, Graphite peak at 26.3° [20].

Sample	Crystallite Size (nm)
a) Fresh NiO/Al_2O_3	6
b) Ni/Al_2O_3 – TPR in CH_4	22
c) Ni/Al_2O_3 – TPR in H_2	6

Table 5.9: Estimation of the crystallite size of $Ni/NiO-Al_2O_3$ after TPR. Uncertainty in the measurement to one standard deviation is ± 1.2 nm.

SEM images of the catalysts that were reduced thermally in CH_4 and H_2 are shown in Figures 5.23 and 5.24 respectively.

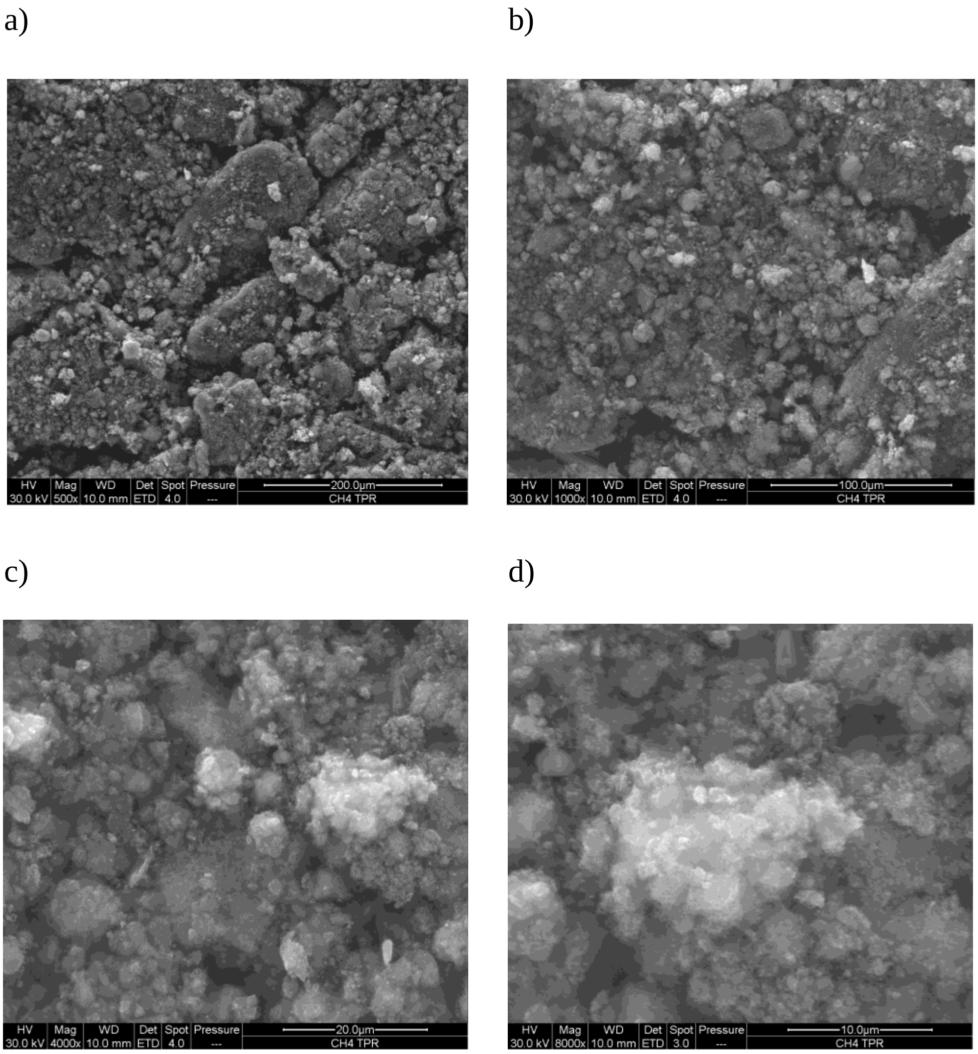

Figure 5.23: SEM images of Ni/Al_2O_3 which has been reduced thermally in CH_4 TPR a) mag. 500 × b) mag. 1000 × c) mag. 4000 × d) mag. 8000 ×.

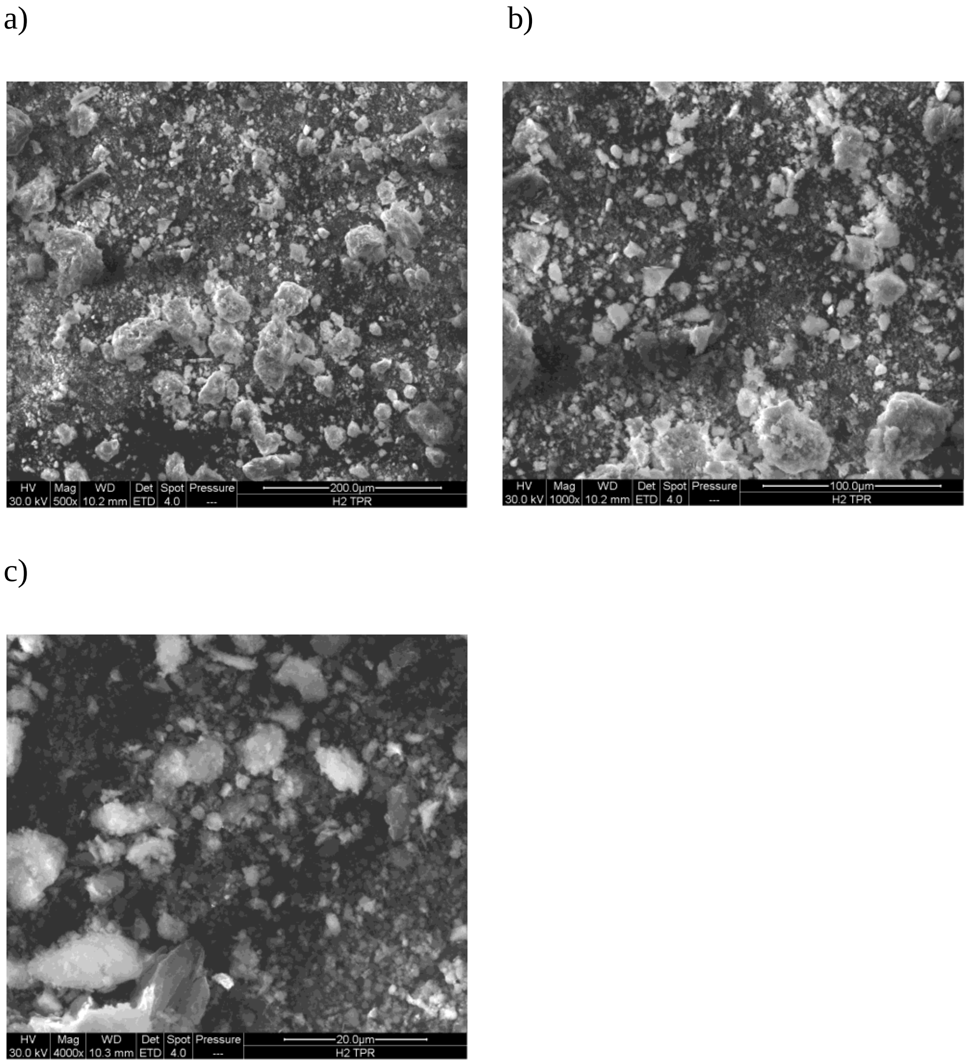

Figure 5.24: SEM images of Ni/Al_2O_3 which has been reduced thermally in H_2 TPR a) mag. 500 × b) mag. 1000 × c) mag. 4000 ×.

Carbon fibres were formed on the CH_4 thermally reduced sample as can be seen by the cotton wool-like structures in Figure 5.23 (c and d). From XRD and SEM analyses, the catalyst has been found to contain both amorphous carbon and crystalline graphitic carbon as a result of exposure to high temperatures (600 – 1000 °C). Mechanisms for carbon formation from CH_4 on Ni catalysts at elevated temperatures have been reviewed [38, 39]. Carbon deposition is generally regarded as a negative effect, which can lead to a loss of catalytic activity caused by blockage of the Ni sites or pore mouths and/or a physical breakdown of the catalyst support. Rostrup-Nielsen and Trimm [38] characterised carbon deposition into 4 distinct morphologies: 1) well-ordered graphitic deposits, 2) carbon whiskers, 3) non-orientated deposits and 4) various carbides. The Ni/Al_2O_3 sample that was thermally reduced in H_2 (Figure 5.24) is similar in appearance to the H_2 plasma-reduced sample shown previously in Figure 5.13. There are no carbon structures on either of the H_2 reduced catalysts.

5.7 Discussion

5.7.1 Comparison of Reduction Temperatures for NiO/Al_2O_3

The temperatures of the reactor during each of the plasma-reduction experiments have been recorded and are shown in Figures 5.3 and 5.7. In the case of a CH_4 discharge the recorded temperature was ~ 320 °C and for a H_2/Ar discharge it was ~ 390 °C, at similar discharge powers of ~ 117 W and ~ 115 W respectively. These temperatures were measured from the electrode on the outside of the reactor and can be regarded as a lower limit for the temperature of the bulk gas. The temperature of the DBD system is proportional to the applied power, since there is no external temperature control or insulation of the reactor to prevent heat loss. Significant energy loss through gas flow cooling and radiation is able to prevent excessive temperature rise. Plasma processes are allothermal; the energy input is independent of the reactions occurring within the plasma reactor. For this reason, differences in reactor temperature exist between different experiments even when the discharge powers are similar; this is a result of the differing thermodynamics of the reactions taking place. A possible explanation for the lower temperature in CH_4 plasma compared with the H_2/Ar plasma is the significant rate of an endothermic CH_4 decomposition (5.3) that will remove energy in the form of heat from the system.

$$CH_4\ (g) \rightarrow C\ (s) + 2\ H_2\ (g) \qquad \Delta H^o = 75.6\ kJ\ mol^{-1} \qquad (5.3)$$

Reduction of 33 % NiO/Al_2O_3 by CH_4 in the absence of a plasma discharge requires 440 °C as shown by the TPR results (Fig. 5.20). During the CH_4 plasma reduction, the temperature of the outer electrode was recorded as 320 °C. This is a lower limit for the temperature of the bulk gas. It is feasible that a 120 °C difference may exist between the centre of the discharge and the outer wall of the reactor. However, the catalyst packing will give reasonable thermal conduction between the plasma and the outer electrode.

In TPR of NiO/Al_2O_3 with CH_4, carbon monoxide production was far greater than carbon dioxide production. However, the relative concentrations of these products were different for the plasma-reduction in CH_4 where CO_2 production was ~ 5 times greater than CO. The complexity of the possible reactions occurring in CH_4 reduction makes it difficult to draw conclusions about mechanistic differences from this study. CO and CO_2 concentrations may be dependent on not just the CH_4 reduction mechanism but also the rate of reduction by CO and H_2, the water-gas shift, the Boudouard reaction and potentially dry reforming of CH_4.

Reduction of 33 % NiO/Al_2O_3 by H_2 requires 280 °C as shown by the TPR results in Figure 5.21. This is significantly lower than the temperature recorded for the H_2/Ar discharge at 390 °C. Therefore a thermal reduction would have taken place in the DBD reactor. However, these processes were not optimised and therefore it is possible that the reduction could take place at a lower discharge power and hence lower temperature. The product CH_4 was observed in both the plasma-reduction and thermal reduction in H_2. However, the production of CO_2 and CO was observed only in the plasma-reduction, indicating that the plasma is responsible for the formation of these products from the catalyst.

In an argon discharge, which did not have reducing capability for NiO/Al_2O_3, the reactor reached a steady temperature of 315 °C at 85 W (Fig. 5.9). Similarly, in studies by Cheng et al. [4], NiO could not be reduced by an Ar glow discharge at room temperature despite the ability to reduce noble metal catalysts under the same conditions. Literature values for reduction temperatures of noble metal supported catalysts indicate that noble metals are more easily reduced than transition metals. Tauster et al. [40, 41] reduced Ru, Rh, Pd, Os, Ir, and Pt on various oxide supports at 200 °C in H_2 and in the case of Pd/TiO_2 at 175 °C. Based on these results, there is no evidence that free high energy electrons have a role as a reducing species for NiO/Al_2O_3 as they have been shown to for noble metal catalysts [4, 5, 11-14]. In plasma experiments where CH_4 and H_2 are present, these gases can act as the reducing species at elevated temperature by the same mechanism as that of conventional, thermal reduction of NiO. Although it is possible that the plasma has an enhancing role in metal reduction such as by the dissociation of the reducing gas or activation of the catalyst surface, further studies would be needed with cooling of the reactor in order to determine whether plasma-reduction could occur at lower temperatures.

5.7.2 Mechanism for Plasma-Reduction of NiO/Al_2O_3 with CH_4

By analogy with thermal reduction of NiO/Al_2O_3 by CH_4, the first step in the plasma-reduction is likely to be the decomposition of adsorbed CH_4 to form active adsorbed carbon (C_{ad}) and hydrogen as shown by the following equations [35]:

$CH_4\ (g) \rightarrow CH_4\ (ad)$ (5.9)
$CH_4\ (ad) \rightarrow CH_3\ (ad) + H\ (ad)$ (5.10)
$CH_3\ (ad) \rightarrow CH_2\ (ad) + H\ (ad)$ (5.11)
$CH_2\ (ad) \rightarrow CH\ (ad) + H\ (ad)$ (5.12)
$CH\ (ad) \rightarrow C_{ad} + H\ (ad)$ (5.13)
$2\ [2\ H\ (ad) \rightarrow H_2\ (g)]$ (5.14)
Overall: $CH_4\ (g) \rightarrow C_{ad} + 2\ H_2$ (5.15)

NiO can be reduced by active adsorbed carbon (5.16) to form carbon monoxide. The generated CO can then go on to reduce NiO as shown in equation 5.17, giving the overall reduction shown in equation 5.0.

$C_{ad} + NiO \rightarrow CO + Ni$ (5.16)
$CO + NiO \rightarrow CO_2 + Ni$ (5.17)
$4\ NiO\ (s) + CH_4\ (g) \rightarrow 4\ Ni\ (s) + CO_2\ (g) + 2\ H_2O\ (l)$ (5.0)

Reduction of NiO by hydrogen is also possible (5.5), as H_2 is produced through CH_4 decomposition in the plasma. If this reaction was significant, a greater mass of water would have been expected in the reaction products. However, a water-gas shift could explain the low mass of H_2O observed.

$H_2 + NiO \rightarrow H_2O + Ni$ (5.5)

5.8 Conclusions

Reduction of a 33 wt. % NiO/Al_2O_3 by CH_4 plasma has been carried out in a DBD reactor. The consumption of CH_4 and production of gaseous products have been monitored throughout the reduction process. The evolution of reduction products CO_2 and CO indicate when the plasma-reduction has gone to completion. The gaseous analysis showed that the consumption of CH_4 remained high (~ 37 %) even after catalyst reduction was complete due to the decomposition of CH_4 into H_2 and solid carbon. SEM images revealed the presence of carbon fibres on the catalyst after reduction in CH_4 plasma. The carbon fibres provide a protective barrier, making it possible for a Ni/Al_2O_3 catalyst to be exposed to air without oxidising. Comparison of the reduction temperatures for the plasma and thermal reductions, indicates that the reduction mechanism may be similar in both cases. A mechanism has been proposed for the reduction of a NiO/Al_2O_3 catalyst in a CH_4 plasma. The reduction of a NiO/Al_2O_3 catalyst by a H_2 DBD has been carried out. The consumption of H_2 has been monitored throughout the reduction process. XRD analysis showed that the plasma-reduced Ni crystallites had a similar size before and after the reduction in both CH_4 and H_2/Ar DBD. The reduction of NiO/Al_2O_3 catalysts by CH_4 and H_2 in a DBD reactor is an effective method for catalyst activation for plasma-catalytic reactions such as dry reforming of CH_4 where it provides a convenient and in-situ method for catalyst reduction without the need for additional pre-treatment of the catalyst. Treatment of a NiO/Al_2O_3 catalyst in an argon DBD has been carried out and did not reduce the catalyst or change the morphology of the catalyst significantly in comparison with a freshly supplied sample. A NiO/Al_2O_3 catalyst has been applied as a coating to $BaTiO_3$ beads and used in a packed-bed DBD reactor. In H_2/Ar plasma, the NiO/Al_2O_3 coating was rapidly reduced to Ni/Al_2O_3 leading to significant changes in the dielectric properties of the beads and limiting the formation of a stable plasma.

5.9 References

1. Richardson, J.T., R.M. Scates, and M.V. Twigg, *X-Ray Diffraction Study of the Hydrogen Reduction of* $NiO/\alpha\text{-}Al_2O_3$ *Steam Reforming Catalysts.* Appl. Catal. A Gen., 2004. **267**: p. 35-46.

2. Liu, G.H., et al., *Plasma-Assisted Preparation of Ni/SiO_2 Catalyst Using Atmospheric High Frequency Cold Plasma Jet.* Catal. Commun., 2008. **9**(6): p. 1087-1091.
3. Shang, S.Y., et al., *Research on Ni/γ-Al_2O_3 Catalyst for CO_2 Reforming of CH_4 Prepared by Atmospheric Pressure Glow Discharge Plasma Jet.* Catal. Today, 2009. **148**(3-4): p. 268-274.
4. Cheng, D.G., *Plasma Decomposition and Reduction in Supported Metal Catalyst Preparation.* Catal. Surv. Asia, 2008. **12**(2): p. 145-151.
5. Wang, Z.-J., Y. Xie, and C.-J. Liu, *Synthesis and Characterization of Noble Metal (Pd, Pt, Au, Ag) Nanostructured Materials Confined in the Channels of Mesoporous SBA-15.* J. of Phys. Chem. C, 2008. **112**(50): p. 19818-19824.
6. Belloni, J., *Nucleation, Growth and Properties of Nanoclusters Studied by Radiation Chemistry - Application to Catalysis.* Catal. Today, 2006. **113**(3-4): p. 141-156.
7. Cheng, D.G. and X.L. Zhu, *Reduction of Pd/HZSM-5 Using Oxygen Glow Discharge Plasma for a Highly Durable Catalyst Preparation.* Catal. Lett., 2007. **118**(3-4): p. 260-263.
8. Cheng, D.G., et al., *Carbon Dioxide Reforming of Methane Over Ni/Al_2O_3 Treated with Glow Discharge Plasma.* Catal. Today, 2006. **115**(1-4): p. 205-210.
9. Liu, C.J., et al., *Plasma Application for More Environmentally Friendly Catalyst Preparation.* Pure Appl. Chem., 2006. **78**(6): p. 1227-1238.
10. Kim, S.S., et al., *Plasma-Assisted Reduction of Supported Metal Catalyst Using Atmospheric Dielectric-Barrier Discharge.* Catal. Today, 2004. **89**(1-2): p. 193-200.
11. Zhu, X.L., et al., *Characterization of Argon Glow Discharge Plasma Reduced Pt/Al_2O_3 Catalyst.* Ind. Eng. Chem. Res., 2006. **45**(25): p. 8604-8609.
12. Zhao, Y., et al., *Carbon Dioxide Reforming of Methane Over Glow Discharge Plasma-Reduced Ir/Al_2O_3 Catalyst.* Catal. Commun., 2008. **9**(7): p. 1558-1562.
13. Wang, Z.J., et al., *CO_2 Reforming of Methane Over Argon Plasma Reduced Rh/Al_2O_3 Catalyst: A Case Study of Alternative Catalyst Reduction Via Non-Hydrogen Plasmas.* Green Chem., 2007. **9**(6): p. 554-559.
14. Wang, Z., C.J. Liu, and G.L. Zhang, *Size Control of Carbon Black-Supported Platinum Nanoparticles Via Novel Plasma Reduction.* Catal. Commun., 2009. **10**(6): p. 959-962.
15. He, J.H., et al., *In Situ Synthesis of Noble Metal Nanoparticles in Ultrathin TiO_2-Gel Films by a Combination of Ion-Exchange and Reduction Processes.* Langmuir, 2002. **18**(25): p. 10005-10010.
16. Haryanto, A., et al., *Hydrogen Production through the Water-Gas Shift Reaction: Thermodynamic Equilibrium versus Experimental Results Over Supported Ni Catalysts.* Energ. Fuel., 2009. **23**: p. 3097-3102.
17. Harling, A.M., et al., *Temperature Dependence of Plasma-Catalysis Using a Nonthermal, Atmospheric Pressure Packed Bed; the Destruction of benzene and Toluene.* J. Phys. Chem. C, 2007. **111**: p. 5090-5095.
18. Harling, A.M., et al., *Plasma-Catalysis Destruction of Aromatics for Environmental Clean-up: Effect of Temperature and Configuration.* Appl. Catal. B Environ., 2008. **82**(3-4): p. 180-189.

19. Harling, A.M., A.E. Wallis, and J.C. Whitehead, *The Effect of Temperature on the Removal of DCM Using Non-Thermal, Atmospheric-Pressure Plasma-Assisted Catalysis.* Plasma Process. Polym., 2007. **4**(4): p. 463-470.
20. PANanalytical, B.V., *X'Pert HighScore Plus Software 2.0a*. 2004.
21. Richardson, J.T., R.M. Scates, and M.V. Twigg, *X-ray Diffraction Study of the Hydrogen Reduction of NiO/α-*Al_2O_3 *Steam Reforming Catalysts.* Appl. Catal. A-Gen. , 2004. **267**: p. 35-46.
22. Gonzalez-Aguilar, J., M. Moreno, and L. Fulcheri, *Carbon Nanostructures Production by Gas-Phase Plasma Processes at Atmospheric Pressure.* J. Phys. D Appl. Phys., 2007. **40**: p. 2361-2374.
23. Terrones, M., et al., *Nanotubes: A Revolution in Materials Science and Electronics*, in *Fullerenes and Related Structures*. 1999, Springer-Verlag Berlin: Berlin. p. 189-234.
24. Mariotti, D. and R.M. Sankaran, *Microplasmas for Nanomaterials Synthesis.* J. Phys. D Appl. Phys., 2010. **43**(32): p. 21.
25. Ando, Y., *Carbon Nanotube: The Inside Story.* J. Nanosci. Nanotechno., 2010. **10**(6): p. 3726-3738.
26. Cao, A.Y., et al., *Hydrogen Storage of Dense-Aligned Carbon Nanotubes.* Chem. Phys. Lett., 2001. **342**(5-6): p. 510-514.
27. Choi, S.I., et al., *Continuous Process of Carbon Nanotubes Synthesis by Decomposition of Methane Using an Arc-Jet Plasma.* Thin Solid Films, 2006. **506-507**: p. 244-249.
28. Falkenstein, Z. and J.C. Coogan, *Microdischarge Behaviour in the Silent Discharge of Nitrogen-Oxygen and Water-Air Mixtures.* J. Phys. D Appl. Phys., 1997. **30**: p. 817-825.
29. Valdivia-Barrientos, R., et al., *Analysis and Electrical Modelling of a Cylindrical DBD Configuration at Different Operating Frequencies.* Plasma Sources Sci. T., 2006. **15**: p. 237-245.
30. Wagner, H.-E., et al., *The Barrier Discharge: Basic Properties and Applications to Surface Treatment.* Vacuum, 2003. **71**: p. 417-436.
31. Manley, T.C., *The Electric Characteristics of the Ozonator Discharge.* Trans. Electrochem. Soc., 1943. **84**: p. 83-96.
32. Qin, Z. and W.F. Maier, *Coal Pyrolysis in the Presence of Methane.* Energ. Fuel., 1994. **8**: p. 1033-1038.
33. Iliuta, I., et al., *Chemical-Looping Combustion Process: Kinetics and Mathematical Modeling.* Aiche J., 2010. **56**(4): p. 1063-1079.
34. Knight, E., *Production of Hydrogen by Unmixed Steam Reforming of Methane*. 2009, University of Leeds.
35. Alizadeh, R., E. Jamshidi, and H. Ale-Ebrahim, *Kinetic Study of Nickel Oxide Reduction by Methane.* Chem. Eng. Technol., 2007. **30**(8): p. 1123-1128.
36. Chernavskii, P.A., et al., *A Study of the Reduction of Nickel Oxide by Methane on Various Carriers by the Programmed-Temperature Reaction Method.* Russ. J. Phys. Chem., 2001. **75**(1): p. 55-58.
37. Twigg, M.V. and J.T. Richardson, *Reduction of Nickel Oxide on Alpha Alumina: Coalescence of Nickel to Metallic Crystallites.* Cat Lett, 1993. **20**: p. 299-303.
38. Rostrup-Nielsen, J.R. and D.L. Trimm, *Mechanisms of Carbon Formation on Nickel-Containing Catalysts.* J Catal, 1977. **48**: p. 155-165.

39. Rahman, M.S., E. Croiset, and R.R. Hudgins, *Catalytic Decomposition of Methane for Hydrogen Production.* Top. Catal., 2006. **37**(2-4): p. 137-145.
40. Tauster, S.J. and S.C. Fung, *Strong Metal-Support Interactions - Occurence Among Binary Oxides of Gruops IIA-VB.* J. Catal., 1978. **55**(1): p. 29-35.
41. Tauster, S.J., S.C. Fung, and R.L. Garten, *Strong Metal-Support Interactions. Group 8 Noble Metals Supported on* TiO_2. J. Am. Chem. Soc., 1978. **100**(170-175).

6. Dry Reforming of Methane: Performance of Plasma-Reduced Ni/Al_2O_3 Catalysts in a Coaxial DBD Reactor

6.1 Introduction

Dry reforming of methane using conventional catalytic methods has three main challenges that limit the use of this process on a commercial scale:

1) The intensively endothermic reaction requires temperatures > 700 °C to obtain reasonable yields of H_2 and CO, incurring high energy costs.
2) The high carbon content of the reactant gas mixture leads to severe coke deposition and a subsequent ‘blocking’ of metal sites causing deactivation of the catalysts.
3) The occurrence of the reverse water-gas shift reaction leads to a decrease of the H_2/CO ratio in the product gas to < 1, which is unfavourable for applications in the Fischer-Tropsch synthesis [1].

Each of these factors is determined by the thermodynamic equilibria of the reactions involved. The use of non-thermal plasma for dry reforming of methane can, to some extent, overcome thermodynamic limitations. This has been shown for dry reforming of methane, where products have been formed in DBD that are not thermodynamically favourable such as the production of H_2 at temperatures < 400 °C. However, reactant conversions and desired product selectivities are still low.

The success of NiO/Al_2O_3 catalysts in steam methane reforming has led to an interest in this catalyst for dry reforming of methane in DBD. Wang et al. [2] have investigated the effect of a 10 wt. % NiO/Al_2O_3 catalyst for dry reforming of methane with the dilution of CH_4 and CO_2 in an argon carrier gas. They reported a synergistic effect on the CH_4 and CO_2 conversions above 400 °C. They also compared the use of Ni/Al_2O_3 (pre-reduced in H_2) and the same catalyst in the unreduced NiO/Al_2O_3 state. They found that during dry reforming of methane in DBD, the unreduced catalyst was reduced in-situ (at 300 – 550 °C) and that a high carbon content of 11.45 % wt. was observed on this catalyst, compared to 5.37 % wt. carbon for the use of the pre-reduced Ni/Al_2O_3. Images obtained by transmission electron microscopy (TEM) revealed that mostly graphite was formed on the pre-reduced catalyst. In contrast, the carbon deposited on the catalyst that was reduced in-situ during dry reforming of CH_4 was mostly filamentous in structure. Song et al. [3] investigated dry reforming of CH_4 in DBD using a pre-reduced 5 wt. % γ-Ni/Al_2O_3 in the absence of a diluent gas. The presence of the catalyst had little effect on the CH_4 conversions and on H_2 and hydrocarbon selectivities. However, an increase in CO_2 conversions was obtained from 30.95 % (without catalyst) to 33.48 % (with the catalyst). They investigated various nickel loadings and found no significant difference between the uses of nickel in the 2 – 10 wt. % range. Kraus et al. [4] investigated dry reforming of CH_4 in DBD using a porous Al_2O_3 foam with a 6 wt. % nickel coating. The yields of H_2 and hydrocarbons were unchanged by the presence of the Ni catalyst. However, CO yields were increased by 20 – 40 % compared to the results for an uncoated Al_2O_3 foam. Optical emission spectroscopy was performed during these experiments; in addition to the characteristic bands of CO_2 and CH_4, they identified strong bands for CO, CO_2^+ and weak bands corresponding to OH and C_2 species.

This investigation follows on from the work in the previous chapter where NiO/Al_2O_3 catalysts were reduced in a 100 % CH_4 plasma and in a 20 % H_2/Ar plasma. The plasma-reduced Ni/Al_2O_3 catalysts have been used in plasma-catalytic dry reforming of methane to investigate whether this catalyst is able to enhance the reaction performance in DBD. Characterisation of the used catalysts has been performed using XRD and SEM analyses.

6.2 Experimental Section

The experimental set-up used in this investigation has been described in section 3.2. Non-uniform particles of 33 % wt. NiO/Al_2O_3 catalyst (Johnson Matthey) were packed into the discharge gap (~ 19.5 g, 0.85 mm – 5 mm) and reduced in 100 % CH_4 or 20 % H_2/Ar plasma, as described in Chapter 5. Dry reforming of CH_4 (CH_4/CO_2 = 1) was carried out in DBD using the reduced Ni/Al_2O_3 catalysts in the discharge gap, without removing the catalyst from the reactor after the reduction stage. The total gas flow rate was 50 ml min^{-1} at a pressure of 1 bar. The gas mixtures were allowed to stabilise before the plasma was turned on and after each increase in discharge power, before taking the micro-GC measurements.

6.3 Results

6.3.1 Dry Reforming of CH_4 Using Plasma-Reduced Ni/Al_2O_3 Catalysts

The results for dry reforming of methane in a DBD reactor using Ni/Al_2O_3 catalysts are shown in Figures 6.0 – 6.6. Comparisons are made between the reaction performances of the catalysts reduced by the two plasma-reduction processes (in 100 % CH_4 or in 20 % H_2/Ar). The presence of the catalysts in the discharge gap enabled significantly higher discharge powers to be obtained in comparison to the same reaction in the absence of a packing material (without exceeding the maximum input voltage of 22 $kV_{pk\text{-}pk}$). This is due to an enhanced ability of the catalyst to store electrical charge relative to a discharge gap containing only gas with no packing material. The measured charge in the absence of the catalyst was 202 nC and this increased to 348 nC during dry reforming of methane with the Ni/Al_2O_3 catalysts.

The methane conversions were significantly greater for the catalyst that was reduced in a H_2/Ar plasma compared to the CH_4 plasma-reduced catalyst as shown in Figure 6.0. This may be explained by the high carbon deposition during the CH_4 reduction. The deposited carbon may reduce the accessibility of gas molecules to the active Ni sites. In contrast, the H_2/Ar plasma reduction process did not deposit any carbon on the catalyst and therefore the dissociation of CH_4 on the catalytic Ni sites could not be limited by accessibility. Methane conversions increased with increasing discharge power, as expected. The highest conversion of CH_4 was 24.4 %, this was obtained for the H_2/Ar reduced sample at 80 W. In comparison, the conversion of CH_4 when using the CH_4 plasma-reduced sample was ~ 5 % at the same discharge power.

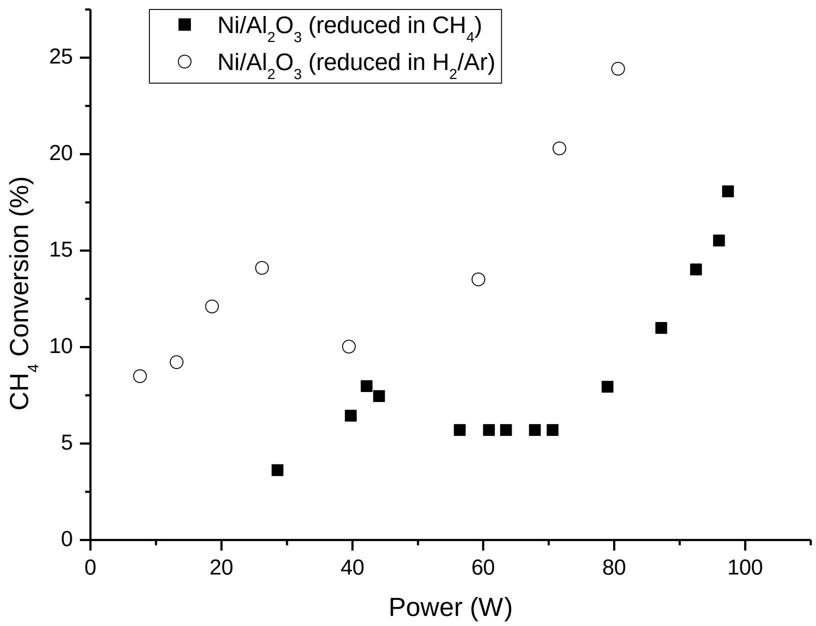

Figure 6.0: CH_4 conversions during dry reforming of methane in DBD with Ni/Al_2O_3 catalysts.

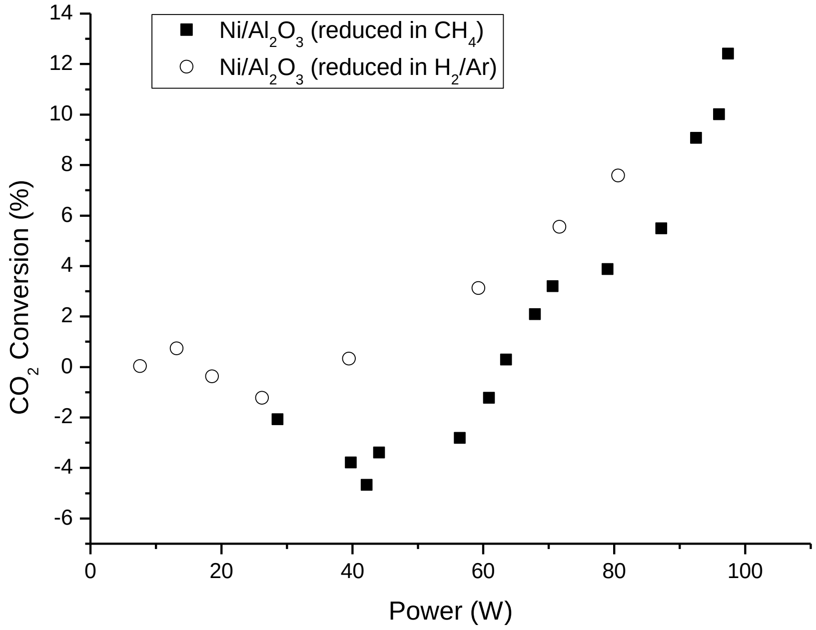

Figure 6.1: CO_2 conversions during dry reforming of methane in DBD with Ni/Al_2O_3 catalysts.

The carbon dioxide conversions are shown in Figure 6.1. For both catalysts, negative CO_2 conversions were obtained at low powers. This may be explained by the cyclical adsorption and desorption of CO_2 at low discharge powers, which is not observed at higher powers as the rate of desorption exceeds that of adsorption. In Chapter 3 (section 3.3.2) negative CO_2 conversions (of -1.2 % at the lowest) were also obtained for the use of low discharge powers when the discharge gap was packed with Al_2O_3, zeolite 3A or TiO_2 and it was suggested that this was due to the desorption of CO_2 under the action of the plasma. The observation that CO_2 conversions were more negative in the case of a CH_4-reduced Ni/Al_2O_3 catalyst (-4.6 %) compared to the H_2/Ar reduced catalyst (-1.2 %) suggests that a reaction of deposited carbon may be responsible for a large part of the CO_2 formation in that instance. The negative CO_2 conversions remained stable over an extended run time of 120 minutes at low power. As the discharge power was increased the CO_2 conversions increased. The catalyst that was reduced in a H_2/Ar plasma gave higher conversions of CO_2, although the difference was less than observed for the CH_4 conversions. At a power of ~ 80 W, a CO_2 conversion of 7.6 % was obtained when using the catalyst reduced in H_2 and a CO_2 conversion of 3.9 % was obtained when using the catalyst reduced in CH_4. As with the CH_4 conversions, the different results for the use of the catalysts may be caused by a reduction in catalytic activity as a result of carbon deposition.

The product selectivities for the use of each catalyst are shown in Figures 6.2 and 6.3. In both cases, H_2 and CO were the most abundant products. Smaller amounts of acetylene/ethylene, ethane and propane were also formed. Propene and butane were not produced during these reactions. The product selectivities at lower discharge powers have been omitted from the graphs due to the negative CO_2 conversions being problematic for the selectivity calculations. The catalyst that was reduced in a CH_4 plasma gave higher selectivities towards H_2 and hydrocarbons compared to the catalyst that was reduced in a H_2/Ar plasma. At discharge powers between 70 W and 100 W, the selectivity towards H_2 increased steadily from 35 % to 45 % (Fig. 6.2). This result is greater than the H_2 selectivities obtained in the absence of the catalyst or any of the investigated packing materials in Chapter 3 (results that were obtained at lower discharge powers). The CO selectivities were in the range 13 – 19 % for discharge powers between 60 and 80 W and were similar for both catalysts. The selectivities towards CO in Figures 6.2 and 6.3 are much lower than those observed in the absence of a catalyst and for the use of other packing materials, which were in the range 24 – 37 % at a discharge power of 35 W (section 3.3.2). These results are in contrast to results obtained by Song et al. [3], who found that the H_2 selectivity decreased slightly and the CO selectivity increased when a Ni/Al_2O_3 catalyst was introduced during dry reforming of methane at a discharge power of 130 W.

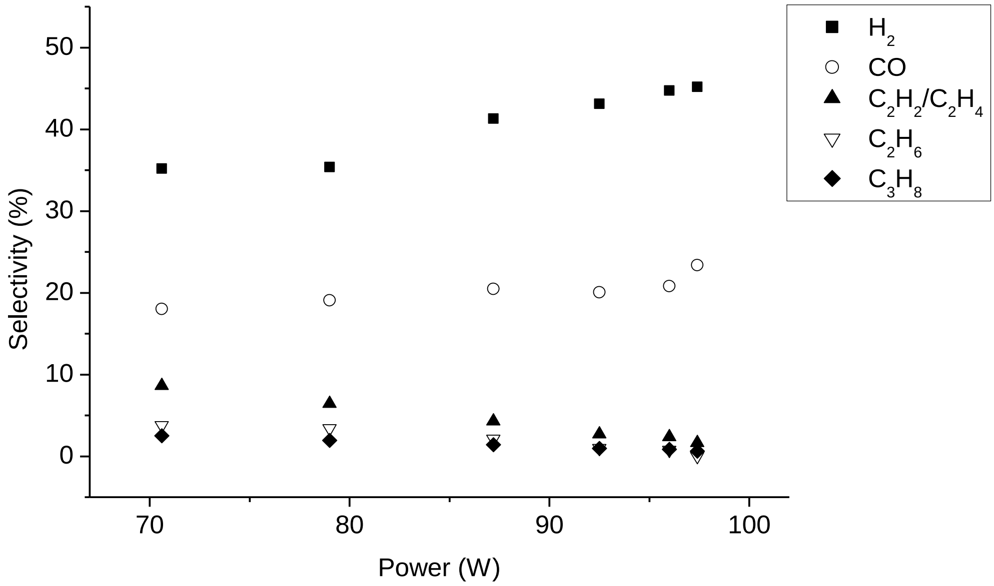

Figure 6.2: Product selectivities during dry reforming of methane using a Ni/Al_2O_3 catalyst (reduced in a 100 % CH_4 plasma).

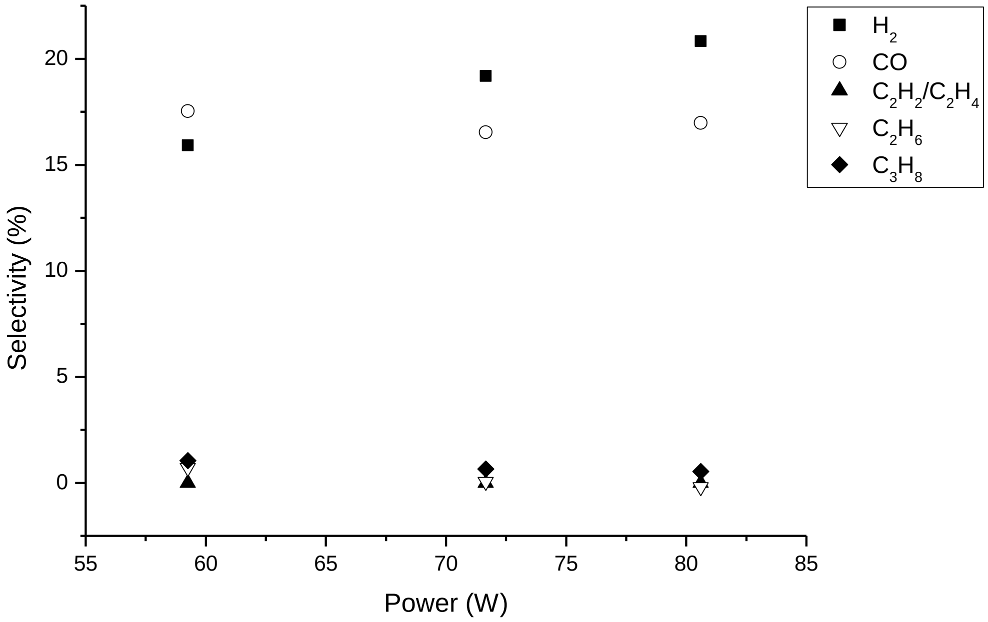

Figure 6.3: Product selectivities during dry reforming of CH_4 using a Ni/Al_2O_3 catalyst (reduced in a 20 % H_2/Ar plasma).

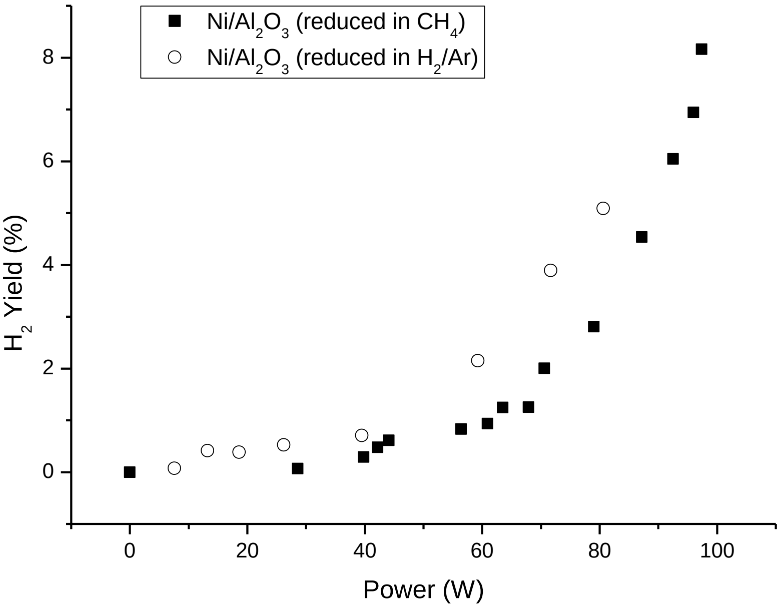

Figure 6.4: H_2 yields during dry reforming of methane in DBD with Ni/Al_2O_3 catalysts.

The yields of H_2 are shown in Figure 6.4. At the same discharge power, the yield of H_2 was slightly greater using the catalyst that was reduced in a H_2/Ar plasma as a result of higher CH_4 conversions. The highest yield of H_2 (8.2 %) was obtained for the CH_4 plasma-reduced catalyst, at a discharge power of 97 W. This is greater than the maximum H_2 yield (5.6 %) that was obtained in the absence of the catalyst (at a lower discharge power).

The carbon balance in the gas stream for the use of both catalysts is shown in Figure 6.5. Higher conversions of CH_4 and CO_2 at higher discharge powers are accompanied by higher carbon deposition. As previously described, carbon deposition could be a result of several reactions including methane decomposition, the Boudouard reaction and/or electron impact dissociations of other gas molecules that might produce solid carbon. The formation of H_2 as a percentage of the total gas mixture resembles a mirror image of the carbon balance as shown in Figure 6.6. Following this observation, it is suggested that methane decomposition to give solid carbon and H_2 is the dominant process that is responsible for carbon deposition during these experiments. At temperatures below 350 °C (the maximum temperature of the bulk gas) this is likely to be a result of electron impact dissociations of methane rather than methane pyrolysis.

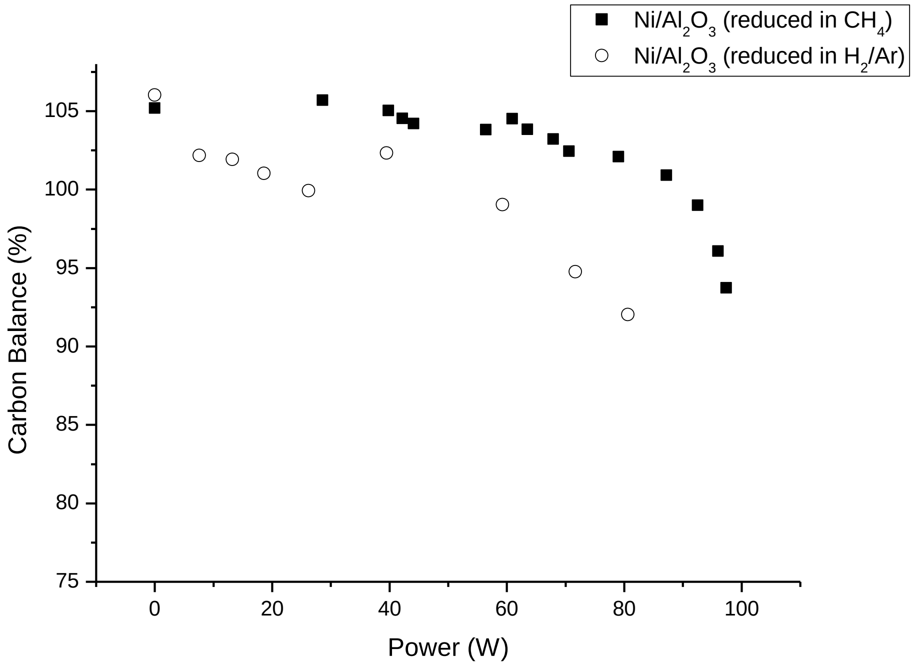

Figure 6.5: Gas stream carbon balance during dry reforming of methane in DBD with Ni/Al_2O_3 catalysts.

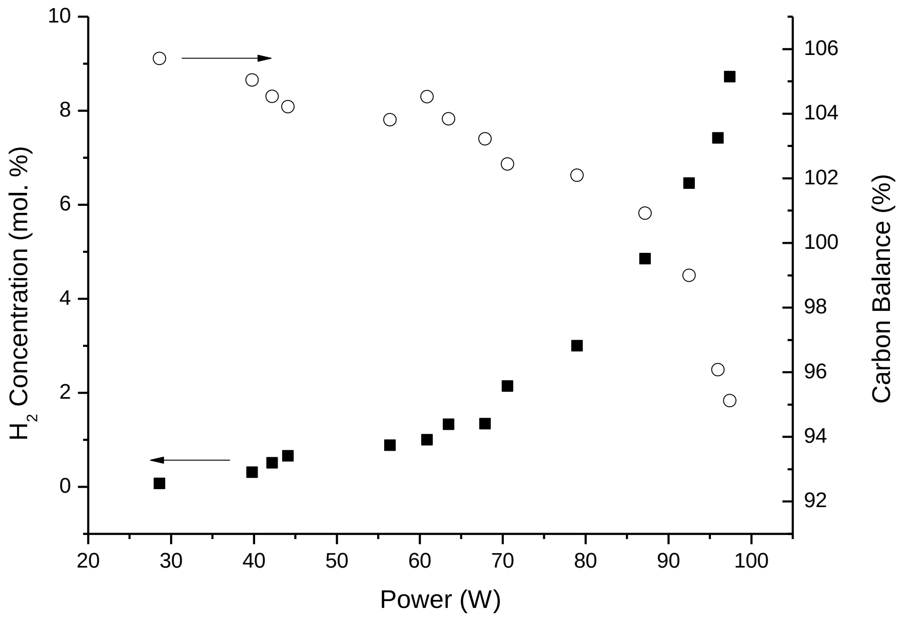

Figure 6.6: H_2 concentration and carbon balance during dry reforming of methane with a Ni/Al_2O_3 catalyst.

6.3.2 Plasma-Assisted Dry Reforming of Methane With and Without a Ni/Al_2O_3 Catalyst at Low Discharge Powers

It can be seen clearly from Table 6.0 that the reaction performance for dry reforming of methane was better in the absence of the catalyst at low discharge powers. The conversions of both CH_4 and CO_2 were significantly greater in the absence of the catalyst. When the Ni/Al_2O_3 catalysts were present the CO_2 conversions were negative or close to zero at a discharge power of 38 W. The H_2 yield was also higher in the absence of the catalyst at 5.2 % compared to <1 % when using a catalyst in the discharge zone. The differences in reaction chemistry may be due to physical differences in the plasma discharge in going from a filamentary discharge in the absence of a catalyst to a surface discharge when the catalyst was present. For example, the electron energy distribution function is likely to differ between these two types of discharge at the same discharge power.

	Conversions (%)		Selectivities (%)		H_2 Yield (%)
	CH_4	CO_2	H_2	CO	
No Catalyst	25.2	14.0	20.7	36.9	5.2
Ni/Al_2O_3 (reduced in a CH_4 plasma)	6.4	-3.8	4.5	9.1	0.3
Ni/Al_2O_3 (reduced in a H_2/Ar plasma)	10.0	0.3	7.1	7.5	0.7

Table 6.0: Comparison of dry reforming of methane in DBD with and without Ni/Al_2O_3 catalysts (~ 38 W).

It was not possible to make a comparison at higher discharge powers because in the absence of the catalyst, the plasma discharge became unstable when the power exceeded ~ 40 W. At low discharge powers the amount of hydrocarbons produced was very low, but their production became more significant at higher discharge powers.

The micro-analytical results for the carbon and hydrogen content in the plasma-reduced catalysts (after dry reforming of methane) and liquid products of dry reforming are shown in Table 6.1.

	% wt. C and H in catalyst	% wt. C and H in liquid product
No Catalyst	-	C = 3.2 H = 10.7
Ni/Al_2O_3 (reduced in a CH_4 plasma)	C = 21.8 H = 0	C = 0.5 H = 12.6
Ni/Al_2O_3 (reduced in a H_2/Ar plasma)	C = 4.0 H = 0	C = 0.5 H = 12.0

Table 6.1: Carbon and hydrogen compositions of the catalysts and liquid products after dry reforming of CH_4.

The high rate of carbon deposition during the reduction stage is likely to be responsible for the majority of the carbon deposited (21.8 wt. %) on the CH_4 reduced sample. The catalyst that was reduced in H_2/Ar plasma contained only ~2 wt. % after the reduction stage and a further 2 wt. % was deposited during dry reforming of CH_4. It can be determined from the low carbon content of the liquid samples that they contained mostly H_2O. The carbon contents of the liquid samples from the plasma-catalytic reactions were significantly lower than the liquid sample produced during the plasma-only reaction. This suggests that the selectivities towards higher hydrocarbon species (C_5+) or oxygenated liquid compounds such as CH_3OH were higher in the absence of the catalyst.

6.4 Catalyst Characterisation

6.4.1 XRD

The XRD patterns for the catalyst samples are shown in Figure 6.7. For comparison, the XRD patterns for a fresh sample of the catalyst (with no pre-treatment) and plasma-reduced Ni/Al_2O_3 catalysts (without dry reforming of CH_4) are also shown. After dry reforming of methane, the catalyst can be characterised as being in the reduced Ni/Al_2O_3 state, as shown by the broad peaks at positions that are characteristic of nickel. The bulk Ni was not oxidised to NiO during the plasma reaction in CH_4 and CO_2.

An estimation of the Ni and NiO crystallite size for each of the catalyst samples, using the Scherrer equation, is shown in Table 6.2. The Ni/NiO particles were calculated as having dimensions of 6 to 8 nm. Within the uncertainty of the measurements (± 1 nm) there is no significant difference between these values.

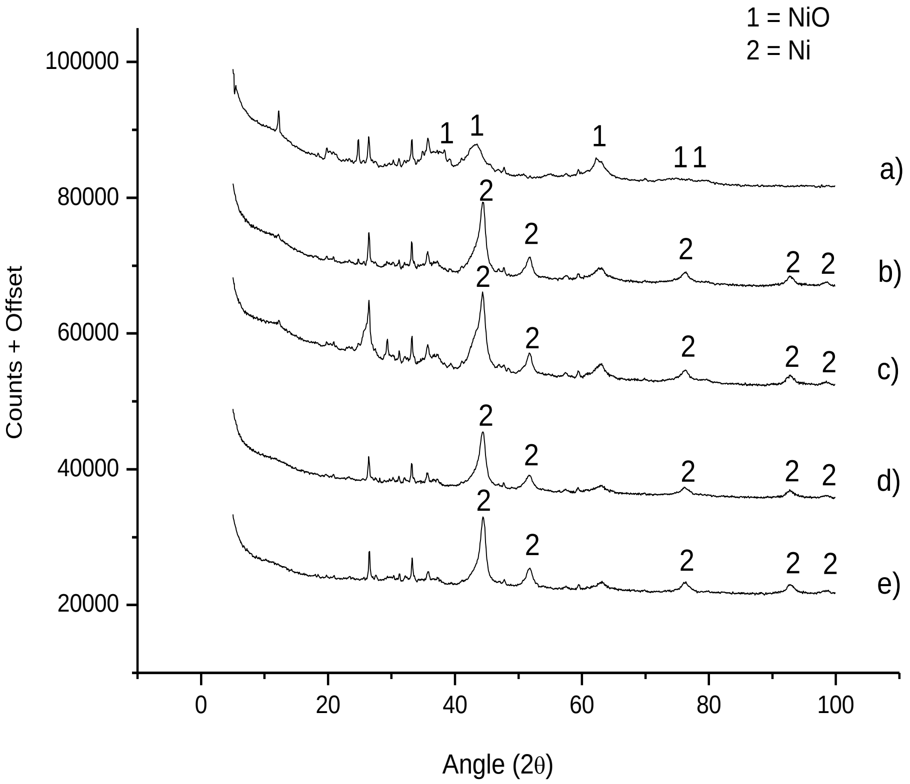

Figure 6.7: XRD patterns of Ni/NiO on Al_2O_3 catalysts a) fresh NiO/Al_2O_3 catalyst b) CH_4 plasma-reduced Ni/Al_2O_3 c) CH_4 plasma-reduced Ni/Al_2O_3 after dry reforming of CH_4 d) H_2/Ar plasma-reduced Ni/Al_2O_3 e) H_2/Ar plasma-reduced Ni/Al_2O_3 after dry reforming of CH_4. NiO peaks at $2\theta = 37.2°$, 43.2°, 62.9°, 75.4° and 79.4°. Ni peaks at $2\theta = 44.4°$, 51.6°, 76.1°, 92.1° and 98.1° [5].

Sample	Crystallite Size (nm)
a) Fresh NiO/Al_2O_3	7
b) CH_4 plasma-reduced Ni/Al_2O_3	6
c) CH_4 plasma-reduced Ni/Al_2O_3 after dry reforming of CH_4	7
d) H_2/Ar plasma-reduced Ni/Al_2O_3	8
e) H_2/Ar plasma-reduced Ni/Al_2O_3 after dry reforming of CH_4	8

Table 6.2: Estimation of crystallite sizes of Ni/NiO-Al_2O_3 after plasma reactions. Uncertainty in the measurement to one standard deviation is ± 1 nm.

6.4.2 SEM

Images have been taken using scanning electron microscopy and are shown in Figures 6.8 and 6.9 for the catalyst samples that were reduced in CH_4 and H_2/Ar plasmas respectively and used during this investigation for dry reforming of methane. It has been shown (in section 5.4.2) that the carbon deposited on the catalyst in a CH_4 plasma has a filamentous structure. These carbon filaments can be viewed on the catalyst after dry reforming of methane as shown in Figure 6.8 (e). The catalyst in Figure 6.9 has been reduced in a H_2/Ar plasma and then used in dry reforming of methane. Carbon filaments could not be observed using SEM on this sample. It is possible that the carbon deposited during dry reforming of methane has a different structure. However, the carbon content was low (4 wt. %) in comparison to the sample reduced in CH_4 (21.8 wt. %), therefore it is possible that with an extended run time for dry reforming of methane, similar carbon filaments would be formed.

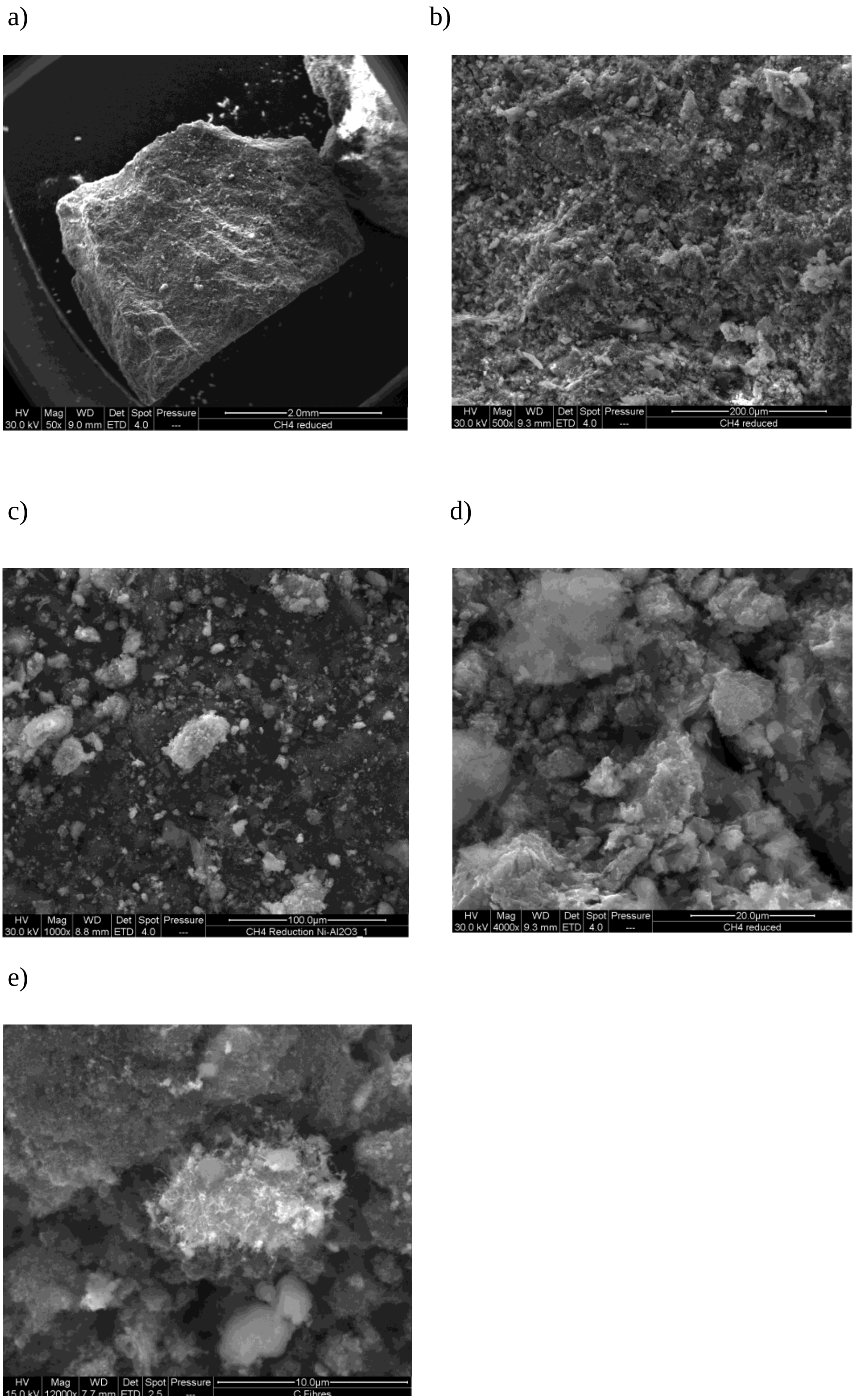

Figure 6.8: SEM images of a Ni/Al_2O_3 (pre-reduced in a 100 % CH_4 plasma) catalyst after dry reforming of methane a) mag. 50 × b) mag. 500 × c) mag. 1000 × d) mag. 4000 × e) 12000 ×.

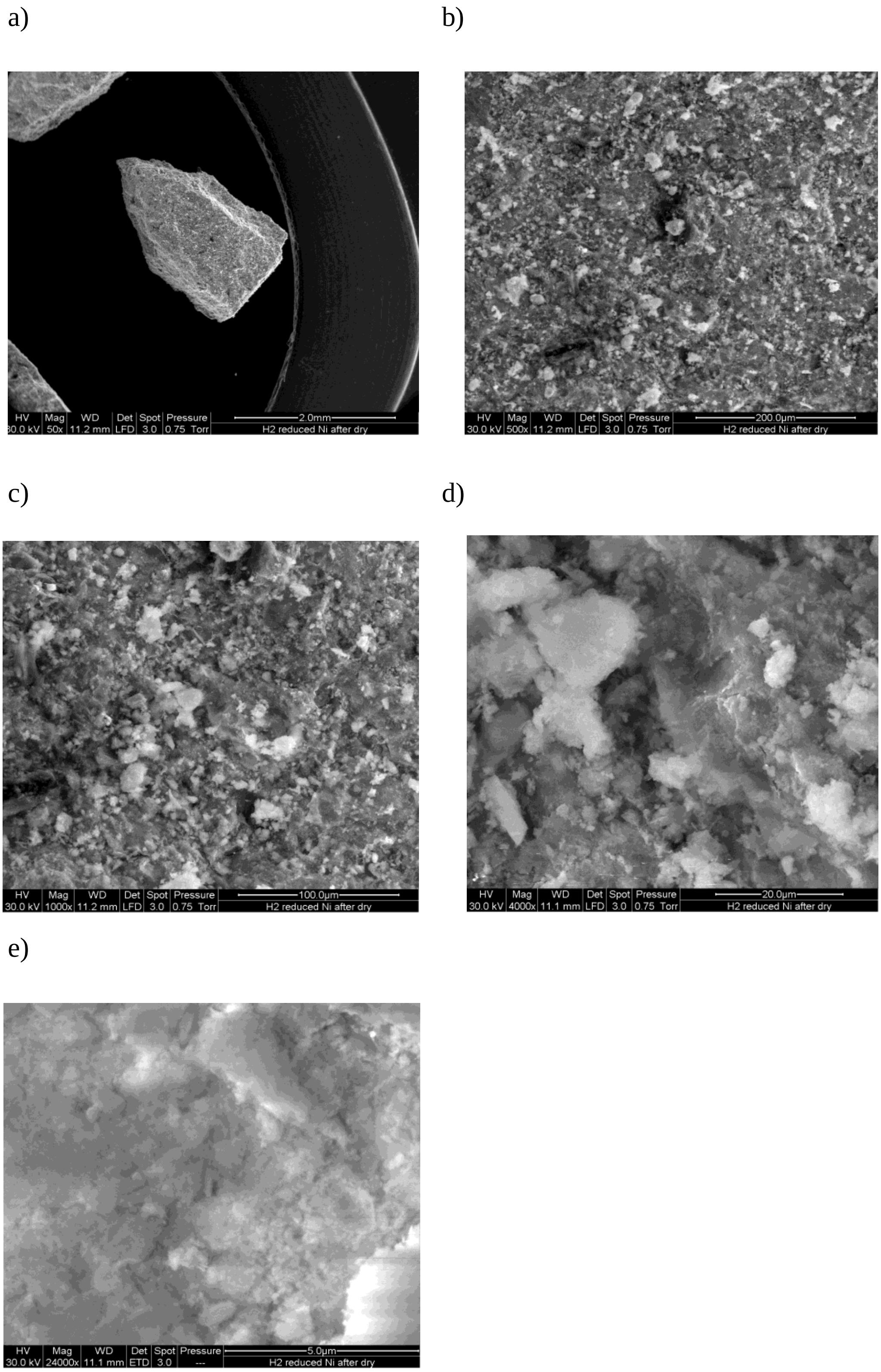

Figure 6.9: SEM images of a Ni/Al_2O_3 (pre-reduced in a 20 % H_2/Ar plasma) catalyst after dry reforming of methane a) mag. 50 × b) mag. 500 × c) mag. 1000 × d) mag. 4000 × e) 24000 ×.

6.5 Discussion

The performance of a Ni/Al_2O_3 catalyst during dry reforming of methane in a DBD is changed by the reduction method of the catalyst. Lower reactant conversions were obtained for the catalyst that was reduced in a CH_4 plasma, which is most likely to be due to a deactivating effect of the deposited carbon. Higher CH_4 and CO_2 conversions were obtained for a catalyst that was reduced in a H_2/Ar plasma, which contained a much lower carbon content after the reduction process. In conventional catalytic dry reforming of methane, the dissociative adsorption of methane is the rate determining step [6]. The observation that reactant conversions were higher in the absence of the catalyst suggests that the rate determining step is different for the plasma-catalytic reaction. Both catalytic surface reactions and electron impact plasma volume processes may be involved in the reaction mechanism. The relative importance of these processes is difficult to ascertain.

It has been confirmed that the carbon deposited on the catalyst in a 100 % CH_4 plasma is filamentous in structure. However, the form of the deposited carbon in the dry reforming of methane reaction could not be determined as there were no observable carbon structures on the catalyst that had been reduced in a H_2/Ar plasma. Graphitic deposits were not observed in either case as witnessed by the XRD results. There is evidence to suggest that the growth mechanism for carbon filaments in plasma processes produces a length of stacked bell-shaped graphene layers with the catalytic metal particle positioned on the protruding end of the filament [7]. In this case, the active metal could still be expected to be involved in catalytic reactions but any possible interactions with the catalytic support would be modified. The selectivity and yield of H_2 was enhanced for the use of the catalyst that was reduced in a CH_4 plasma, therefore it is suggested that this catalyst is more active towards the decomposition of CH_4 into H_2 and solid carbon, rather than for a dry reforming of methane mechanism that involves reactions with CO_2.

6.6 Conclusions

Comparisons of dry reforming of methane with and without the use of a Ni/Al_2O_3 catalyst showed that for the same discharge power, the results were more promising in the absence of the catalyst. However, the higher discharge powers that could be obtained when the catalyst was present led to ultimately higher reactant conversions and yields of H_2. The enhanced conversions are accompanied by increased carbon deposition. It is suggested that electron impact dissociation of methane is the dominant process for the formation of H_2 and solid carbon during these reactions.

The presence of the catalyst made the reactor more effective at coupling power into the plasma discharge. Higher discharge powers could be achieved in the presence of the catalyst (without exceeding the maximum input voltage) due to an increased charge carrying capacity of the catalyst.

6.7 References

1. Fan, M.S., Abdullah, A.Z.and Bhatia, S., *Catalytic Technology for Carbon Dioxide Reforming of Methane to Synthesis Gas.* ChemCatChem, 2009. **1**(2): p. 192-208.
2. Wang, Q., Yan, B.-H., Jin, Y.and Cheng, Y., *Dry Reforming of Methane in a Dielectric Barrier Discharge Reactor with* Ni/Al_2O_3 *Catalyst: Interaction of Catalyst and Plasma.* Energy & Fuels, 2009. **23**(8): p. 4196-4201.
3. Song, H.K., Choi, J.-W., Yue, S.H., Lee, H.and Na, B.-K., *Synthesis Gas Production via Dielectric Barrier Discharge over* $Ni/\gamma\text{-}Al_2O_3$ *Catalyst.* Catal. Today, 2004. **89**: p. 27-33.
4. Kraus, M., Egli, W., Haffner, K., Eliasson, B., Kogelschatz, U.and Wokaun, A., *Investigation of Mechanistic Aspects of the Catalytic* CO_2 *Reforming of Methane in a Dielectric-Barrier Discharge Using Optical Emission Spectroscopy and Kinetic Modeling.* Phys. Chem. Chem. Phys., 2002. **4**(4): p. 668-675.
5. PANanalytical, B.V., *X'Pert HighScore Plus Software 2.0a*. 2004.
6. Kraus, M., Eliasson, B., Kogelschatz, U.and Wokaun, A., CO_2 *Reforming of Methane by the Combination of Dielectric-Barrier Discharges and Catalysis.* Phys. Chem. Chem. Phys., 2001. **3**(3): p. 294-300.
7. Okuno, H., Grivei, E., Fabry, F., Gruenberger, T.M., Gonzalez-Aguilar, J., Palnichenko, A., Fulcheri, L., Probst, N.and Charlier, J.-C., *Synthesis of Carbon Nanotubes and Nano-Necklaces by Thermal Plasma Process.* Carbon, 2004. **42**(12-13): p. 2543-2549.

7.0 Future Work

The main focus for the investigations in this thesis has been the interactions between a plasma discharge and catalysts in a combined system. Following on from this work, there are several promising directions for future research, as detailed in this chapter.

7.1 Plasma-Catalytic Decomposition of Methane

The results in Chapters 5 and 6 have demonstrated that a Ni/Al_2O_3 catalyst can be effective for catalysing CH_4 decomposition in a DBD. When using a plasma of 100 % CH_4, selective production of solid carbon and H_2 can be obtained with minimal formation of higher hydrocarbon by-products. Optimisation of the plasma-catalytic reaction conditions for H_2 production from CH_4 would be an important objective for further investigations.

The solid carbon product is potentially a very interesting material in its own right. Plasma processes have been shown to produce a variety of carbon products including amorphous carbon black, carbon fibres and various fullerenes such as nanotubes and buckyballs [1, 2]. Carbon nanostructures have been dubbed as ‘supermaterials’ due to their unique range of properties including extraordinary strength and hardness and a broad range of optical, thermal and electrical properties depending on the morphology and incorporation of other elements into the carbon structures. Production of these specialist carbon materials is currently achieved using three main methods: thermal arc discharges or laser ablation methods at temperatures of ~ 3730 °C or by chemical vapour deposition (CVD) which usually operates at ~ 1230 °C [1]. Active metal catalysts such as supported nickel are typically employed to catalyse the decomposition of a precursor such as methane, ethylene, CO etc.

In Chapters 5 and 6 of this thesis, SEM images were presented of carbon nanofibres produced on a Ni/Al_2O_3 catalyst in a non-thermal plasma at relatively low temperatures (< 400 °C). Complete characterisation of these structures using Raman spectroscopy and TEM would be an important first step for further investigations. Growth of carbon nanotubes on a substrate is a highly desirable process for a wide range of industries. The extreme temperatures used in current methods for carbon growth would have adverse effects ultimately leading to the destruction of many desirable substrate materials. Consequently, low-temperature processes for growth of carbon nanostructures (that could preserve the substrates) would have promising implications for many industries.

7.2 Development of a Plasma-Membrane Reactor

Hydrogen fuel cell technologies require high purity H_2 in order to avoid catalyst poisoning. In order to access the value of the H_2 produced in plasma reactions it must be separated from the unconverted CH_4 and any other gaseous reaction products. The use of membrane technologies in a plasma-catalytic combined system is a potential solution. A preliminary investigation combining the use of plasma-catalysis and membranes has been reported by Nguyen et al. [3], where the excess heat from the plasma was used to drive the flow of H_2 through a Pd-Ag membrane. The reaction scheme in Figure 7.0 is suggested as a potential method for the production of high purity H_2 with co-production of useful solid carbon products.

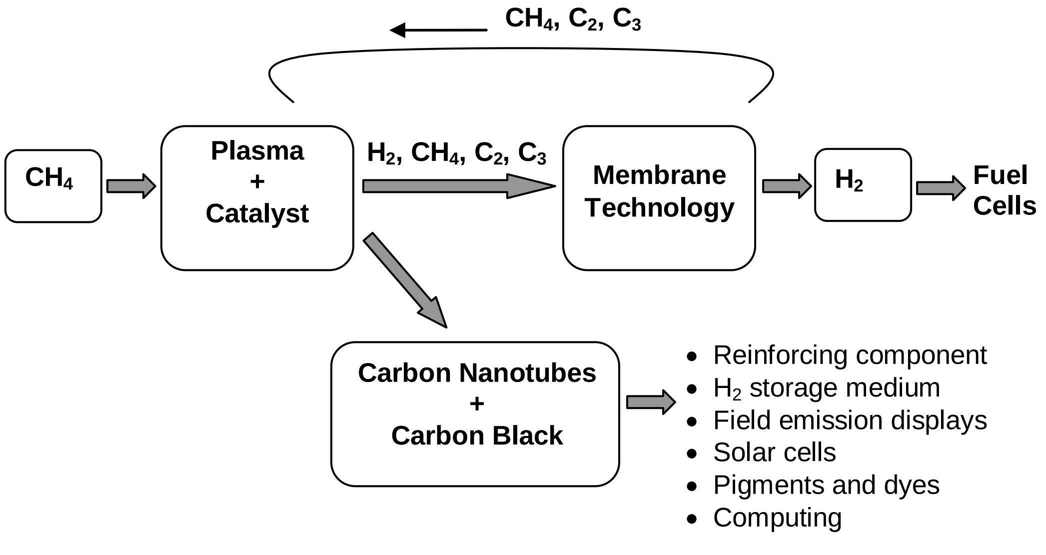

Figure 7.0: A schematic diagram showing the production of H_2 and carbon nanotubes from CH_4 via the use of plasma-catalysis and membrane technologies.

7.3 Development of Specialist Catalysts for Plasma Processes

The development of specialist catalysts for plasma-assisted dry reforming of methane and other plasma processes would be a beneficial area for further investigations. The results in Chapter 3 of this thesis have demonstrated that when different materials are placed in a plasma discharge, the physical properties of the plasma can be modified. This leads to significant changes in the reaction chemistry. It is suggested that the dielectric properties, size, shape and porosity of the material can have a substantial influence. In particular, the incorporation of voids in a catalytic material is considered important for the formation of filamentary discharges in a plasma-catalytic DBD system. For this reason, exploring the use of quartz wool impregnated with Ni particles could be a promising catalyst for plasma-assisted dry reforming of methane. Further studies in this area with careful control of a single variable would allow a better understanding to be gained of the relative importance of each of these factors. In addition to the features mentioned above, there are several important factors that should be deliberated when developing catalysts for any heterogeneous processes, such as:

1) High catalytic activity towards the desired reaction(s).
2) Inhibition of processes that lead to undesired by-products.
3) High surface area of the active species to enhance reaction rates.
4) Interactions of the support material.
5) High stability at elevated temperatures.
6) Costs of preparation and components.

7.4 Development of a Micro-Reactor System for Catalyst Screening

In order to test the performance of potential catalysts quickly and efficiently, screening of small amounts of catalysts for the desired plasma reactions would be required. The DBD reactors used for the investigations in this thesis required relatively large amounts of catalysts in order to completely fill the discharge gap. Consequently the use of these reactors for screening purposes is difficult because the quantities of catalyst required are too large. A solution to this problem would be the development of a micro-reactor system that could accommodate several DBD cells in parallel allowing micrograms of different catalysts to be simultaneously tested for the same reaction. Microreactors can be formed with the same features as typical DBD reactors except on a smaller scale, with discharge gaps typically of ≤ 1 mm [4].

7.5 References

1. Okuno, H., Grivei, E., Fabry, F., Gruenberger, T.M., Gonzalez-Aguilar, J., Palnichenko, A., Fulcheri, L., Probst, N.and Charlier, J.-C., *Synthesis of Carbon Nanotubes and Nano-Necklaces by Thermal Plasma Process.* Carbon, 2004. **42**(12-13): p. 2543-2549.
2. Gonzalez-Aguilar, J., Moreno, M.and Fulcheri, L., *Carbon Nanostructures Production by Gas-Phase Plasma Processes at Atmospheric Pressure.* J. Phys. D Appl. Phys., 2007. **40**: p. 2361-2374.
3. Nguyen, T.H., Mori, S.and Suzuki, M., *Hydrogen Separation from Products of Methane Reforming Reaction Carried out in a Plasma Membrane reactor at Low temperature and Atmospheric Pressure.* J. Chem. Eng. Jpn, 2009. **43**(1): p. 76-81.
4. Kogelschatz, U., *Applications of Microplasmas and Microreactor Technology.* Contrib. Plasm. Phys., 2007. **47**(1-2): p. 80-88.

Appendix A:

Power measurement in a DBD plasma reactor

Peter Gorry

Experimental set up

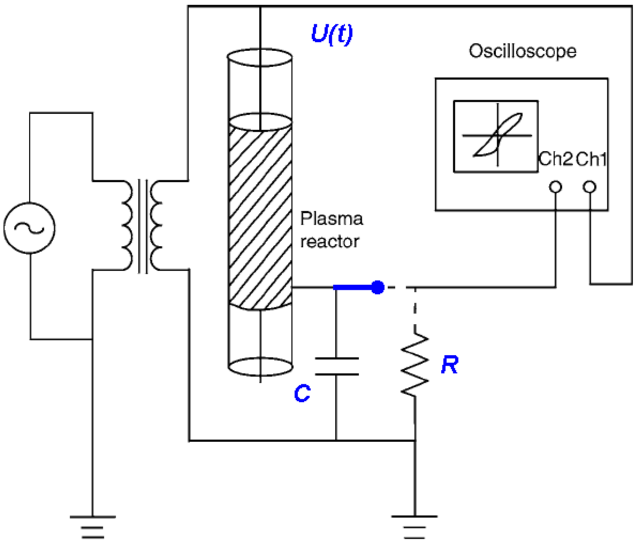

Fig 1 Circuit for measuring the discharge power of a plasma reactor

Figure 1 shows a typical circuit layout [1]. The power can be determined by measuring the high voltage ***U(t)*** and either the current flowing through the resistor ***R*,** or the charge on capacitor ***C***. A switch is used to select which method is used.

Current method

This is the simplest to understand and we follow here the formalism of Feng and Castle [2]. The instantaneous power in the reactor is simply given by

$$p(t) = U(t) \cdot i(t) \tag{1}$$

where $U(t)$ is the high voltage (HV) on the reactor and $i(t)$ is the current flowing through the reactor (and resistor R). The current $i(t)$ is simply found from

$$i(t) = \frac{V_R(t)}{R} \tag{2}$$

where $V_R(t)$ is the voltage across R.

The average power over a single cycle of the high voltage, period T, is given by

$$P = \frac{1}{T}\int_{t_0-T/2}^{t_0+T/2} p\,dt = \frac{1}{T}\int_{t_0-T/2}^{t_0+T/2} U(t)\cdot i(t)\,dt = \frac{1}{T}\int_{t_0-T/2}^{t_0+T/2} \frac{U(t)\cdot V_R(t)}{R}\,dt \qquad (3)$$

where t_0 is the centre of the cycle.

The problem with this method is that the plasma itself is a series of microdischarges of short duration (typically ≤ 2 ns) and the current waveform need to capture this information accurately. This in turn requires a very high bandwidth (and expensive) sampling oscilloscope [3].

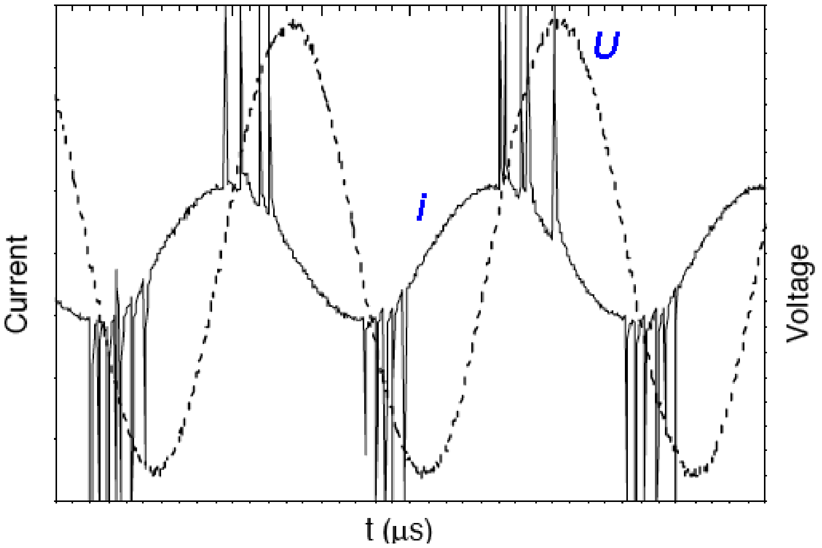

Fig 2 Reactor voltage, $U(t)$, and current $i(t)$.

In practice, even with such an instrument, the overlap of spikes makes the use of Eqn 3 very difficult to perform accurately.

Lissajous method

This method was introduced by Manley [4] in 1943. In the absence of any way of accurately recording the microdischarge current spikes the alternative is to replace the probe resistor ***R*** by a probe capacitor ***C***. The capacitor accumulates a *charge* from the current flowing through the reactor and this can be determined by measuring the voltage on the capacitor V_c.

$$q(t) = C\cdot V_c(t) \qquad (4)$$

The advantage is that the charge is stored in the capacitor and doesn't require a fast transient digitiser to record it. The *energy* per cycle, *W*, can be found from Eqn 3 by multiplying by T.

$$W = \int_{t_0 - T/2}^{t_0 + T/2} U(t) \cdot i(t) dt \tag{5}$$

The current flowing through the measuring capacitor, *C*, is given by

$$i(t) = \frac{dq}{dt} = C \frac{dV_c}{dt} \tag{6}$$

hence we have

$$q(t) = C \cdot V_c(t) \tag{7}$$

and the energy per cycle becomes

$$W = \int_{t_0 - T/2}^{t_0 + T/2} U(t) \cdot C \cdot V_c(t) dt = \int_{t_0 - T/2}^{t_0 + T/2} U(t) \cdot dq(t) \tag{8}$$

If we record U(t) and q(t) as a series of *n* regularly sampled points over one cycle we can approximate Eqn 8 by a summation, using trapezoidal integration, as

$$W \approx \sum_{k=1}^{n} \left(\frac{U_{k+1} + U_k}{2} \right) (q_{k+1} - q_k) \tag{9}$$

We now simply have to multiply by the number of cycles per second to get the power in the reactor. So, if the voltage *U* has a frequency, *f*, where *f* = 1/*T* , we have

$$P = W \cdot f = f \sum_{k=1}^{n} \left(\frac{U_{k+1} + U_k}{2} \right) (q_{k+1} - q_k) \tag{10}$$

The integrals in Eqns 8 and 10 represent the area of a *U*-*q* Lissajous figure.

Equivalent circuit analysis

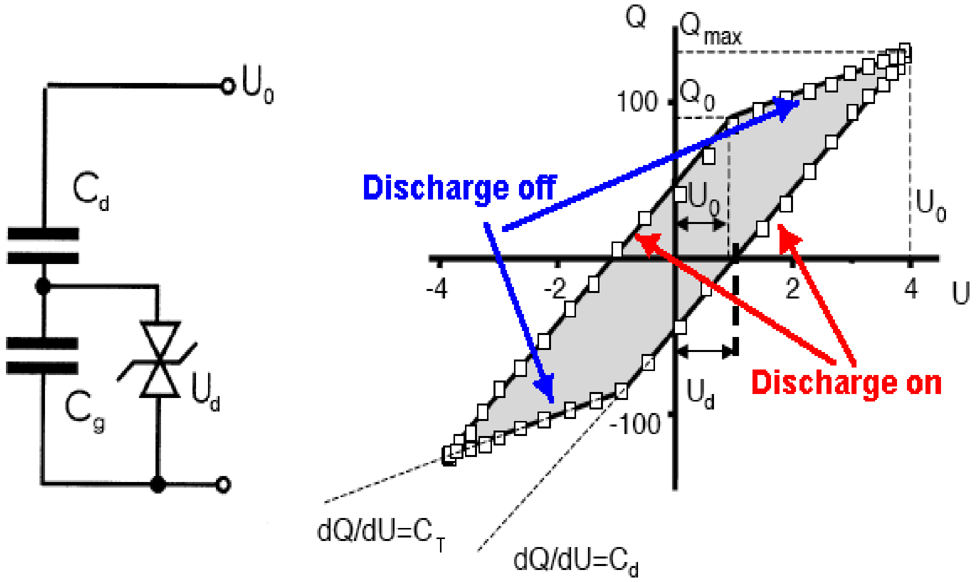

Fig 3 (a) Equivalent circuit for the DBD reactor and (b) resulting q-U Lissajous.

The equivalent circuit and q-U Lissajous is shown in figure 3 [3,5]. In Fig 3a C_d is the capacitance of the dielectric barrier and C_g is the capacitance of the air gap. When the voltage across the air gap exceeds U_d microdischarges start, this is represented by the bipolar zenner diode and continue to develop until the maximum voltage U_0.

The total capacitance, C_T, is given by

$$\frac{1}{C_T} = \frac{1}{C_g} + \frac{1}{C_d} \qquad (11)$$

During the discharge on period the current depend on the dielectric barrier capacitance alone, C_d, and during the off period it depends on the total capacitance, C_T. We have

$$\begin{aligned} \frac{dq}{dU} &= C_T = \frac{C_g C_d}{C_g + C_d} && \text{Discharge off} \\ \frac{dq}{dU} &= C_d && \text{Discharge on} \end{aligned} \qquad (12)$$

Cyclic integration

The energy in a cycle is given by the integral defined in Eqn 8. This corresponds to a cyclic integral in the U-q plane (i.e. q along the x axis and U along the Y axis – so the axes are transposed from those in Fig 3b).

Figure 4 shows the integration **A-B-C-D** – i.e. where **U** is +ve. From **A-B dq** is +ve and the shaded area in Fig. 4(i) is calculated. From **B-C-D dq** is –ve and the shaded area in Fig. 4(ii) will be subtracted from the shaded area in Fig. 4 (i) – leaving the shaded area in Fig. 4 (iii). The second half of the cycle does exactly the same for the negative **U** values. So the integral in Eqn 8 represents the area of the Lissajous figure.

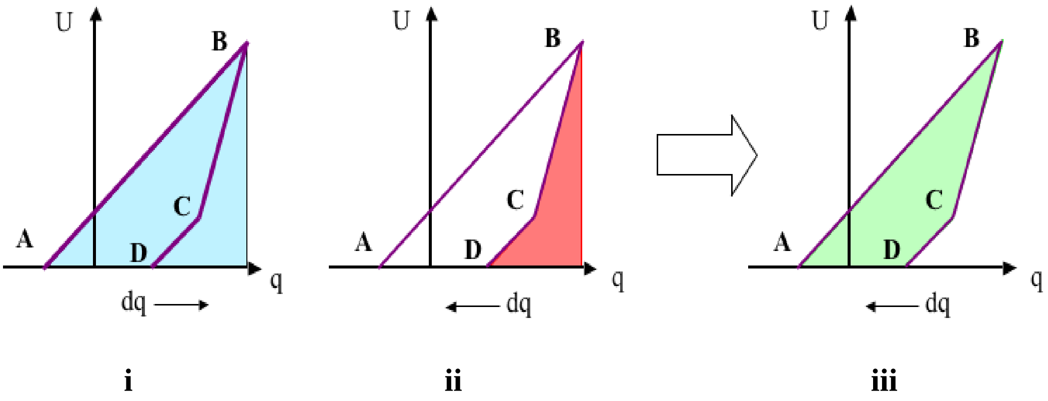

Fig 4 Energy integral defined in Eqn 8 over +ve **U** values

LabVIEW Implementation

The implementation in Labview is based on two channel ADC sampling using hardware from Picoscope (ADC200). This is used to record the high voltage waveform (via a 1000:1 reducing probe) and the voltage across the probe capacitance (typically 22 nF). The instrument interface is divided into two parts, a two channel sampling oscilloscope with signal averaging (upper part), and a Plasma Power section for evaluating Eqn 10 (lower part).

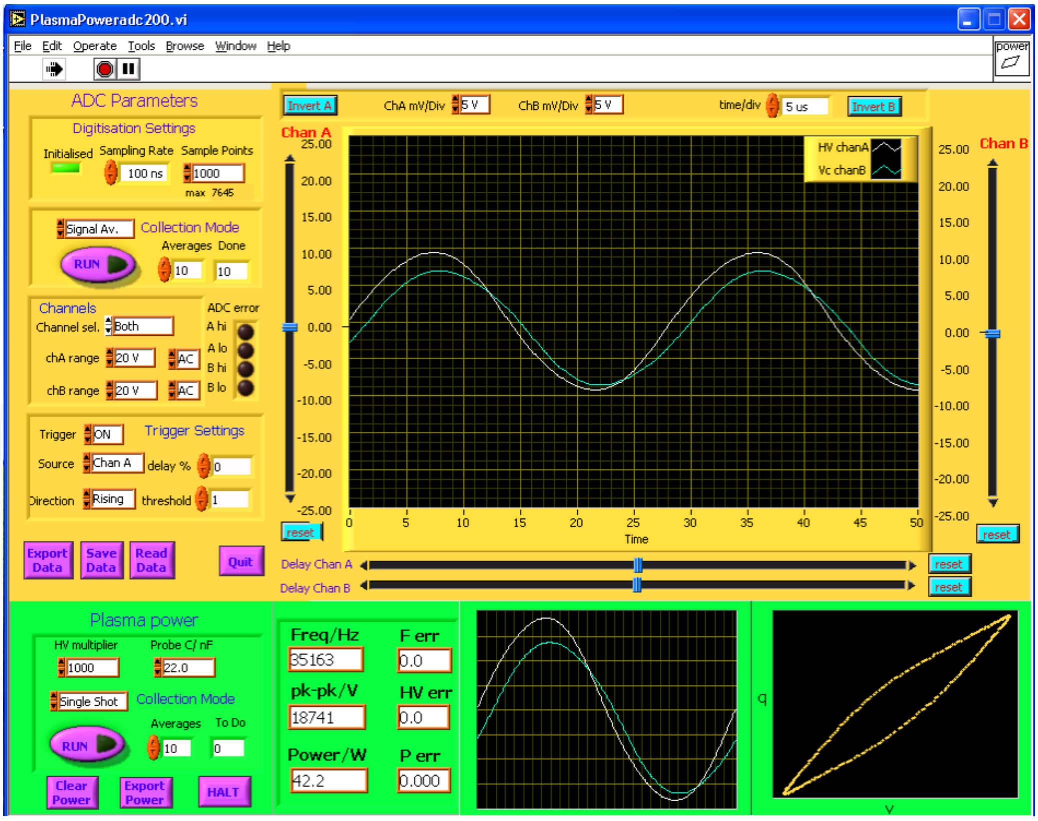

Initialised
Sampling Rate 100 ns
Sample Points 1000
max 7645

Collection Mode: Signal Av.
Averages 10
Done 10

Channel sel. Both
chA range 20 V AC
chB range 20 V AC

Trigger ON
Source Chan A
delay % 0
Direction Rising
threshold 1

ChA mV/Div 5 V
ChB mV/Div 5 V
time/div 5 us

HV multiplier 1000
Probe C/ nF 22.0
Collection Mode: Single Shot
Averages 10
To Do 0

Freq/Hz 35163
F err 0.0
pk-pk/V 18741
HV err 0.0
Power/W 42.2
P err 0.000

Fig 5 LabVIEW interface for plasma power determination

Picoscope ADC200 connections

Chan A: HV via 1000:1 reducing probe.

Chan B: V_c from probe capacitor.

Analysis methodology

The power is calculated from Eqn 8 using the numerical approximation of Eqn 10.

$$P = W \cdot f = f \sum_{k=1}^{n} \left(\frac{U_{k+1} + U_k}{2} \right) (q_{k+1} - q_k) \qquad (10)$$

This requires the frequency, ***f***, of the HV supply and a single cycle of data from ***U***(***t***) and $\boldsymbol{V_c(t)}$.

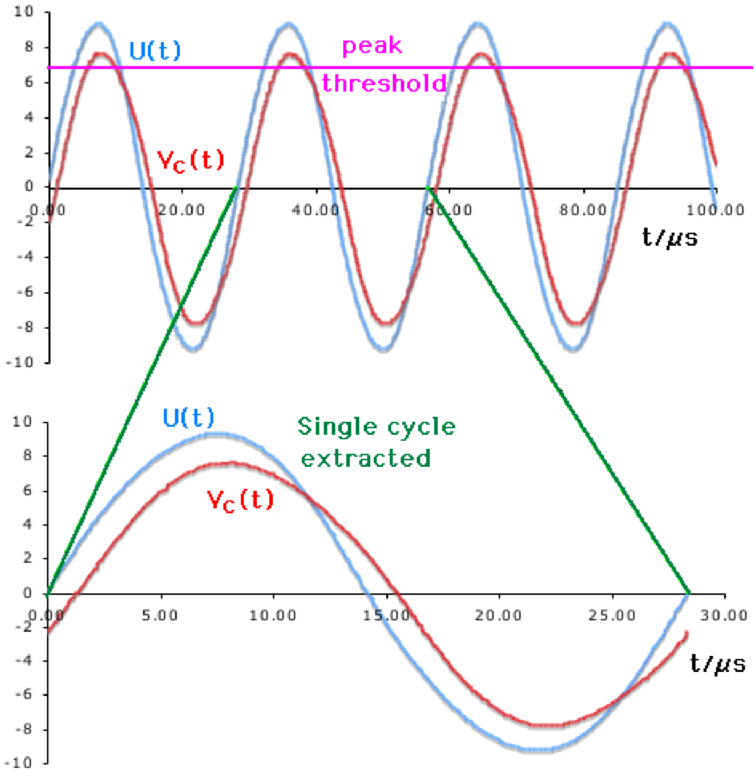

Fig 6 Suitable data sample (top trace) and extracted single cycle.

Determination of Frequency

In fact this is the major difficulty in the analysis and a multi-solution approach is performed.

3 – 5 cycle data limit

The evaluation of Eqn 10 requires a single complete cycle be extracted from the ***U*(*t*)** and **V_c(*t*)** data streams. The frequency analysis is performed in several stages which require **a minimum of 3 cycles and a maximum of 5 cycles** to be recorded. The power analysis section checks that the data in channel A (*U*(*t*)) has between 3-5 peaks above a threshold 75% of the maximum value and a peak width of at least 20 data points long. Analysis only proceeds if the data passes this test.

The sampling rate and the number of points must be set to ensure this is true.

Single tone analysis

An initial determination of the frequency is performed using *fast fourier transform* (FFT) techniques which requires that the $U(t)$ data have at least 3 full sine wave cycles for accurate values. The data processing is

Data → Hanning Window→ FFT→ Autopower Spectrum→ Fundamental Frequency

The fundamental frequency is accurate to 1-2 Hz for a pure sine wave without noise. However, the presence of noise can introduce uncertainties of 5-20 Hz in a 30 kHz signal. The approach also is unreliable with less than two cycles of data.

Three parameter least squares fit

The estimate of the frequency, $\boldsymbol{f_0}$, from the single tone analysis is used in a two-level least squares process to find a more robust estimate of the frequency. The signal $U(t)$ can be represented by

$$U(t) = A\sin(\omega t + \phi) \tag{13}$$

where $\omega = 2\pi f$.

We require to calculate least-squares estimates for A, ω, and φ by fitting $U(t)$ to Eqn 13 [6-8]. In terms of the N sampled data points we need to minimise the Least-Squares χ^2 value with respect to each parameter from

$$\chi^2 = \sum_{i=1}^{N} \left[U_i - A\sin(\omega t_i + \phi)\right]^2 \tag{14}$$

$$\frac{\partial \chi^2}{\partial A} = 0 \qquad \frac{\partial \chi^2}{\partial \omega} = 0 \qquad \frac{\partial \chi^2}{\partial \phi} = 0 \tag{15}$$

Unfortunately χ^2 is non-linear in ω and ϕ so there are no analytical expressions to these derivatives in Eqn 15. We can partially linearise the expression in Eqn 14 by expanding the sine expression.

$$\begin{aligned} U(t) &= A\sin(\omega t+\phi) = A\sin(\omega t)\cos(\phi) + A\cos(\omega t)\sin(\phi) \\ &= a\sin(\omega t) + b\cos(\omega t) \end{aligned} \qquad (16)$$

where $a = A\cos(\phi)$ and $b = A\sin(\phi)$

so $\phi = \tan^{-1}\left(\frac{b}{a}\right)$ and $A = \frac{a}{\cos(\phi)}$ (17)

And equations 14 and 15 become

$$\chi^2 = \sum_{i=1}^{N}\left[U_i - a\sin(\omega t_i) - b\cos(\omega t_i)\right]^2 \qquad (18)$$

$$\frac{\partial\chi^2}{\partial a} = 0 \qquad \frac{\partial\chi^2}{\partial b} = 0 \qquad \frac{\partial\chi^2}{\partial \omega} = 0 \qquad (19)$$

Now χ^2 is non-linear in **ω** only. We adopt a grid approach to determining **ω**. The single tone frequency $\mathbf{f_0}$ is used to calculate an intial guess $\boldsymbol{\omega_0}$ and Eqns 18 and 19 solved for this fixed $\boldsymbol{\omega_0}$. i.e. the *linear* least-squares is solved analytically for parameters **a** and **b** only (hence **ϕ** and **A** from Eqn 17).

This calculation is repeated at values of $\mathbf{f = f_0 \pm n\Delta f}$ where n =1…5 and typically Δf =20 Hz is used. The eleven χ^2 vs **f** values centred on $\mathbf{f_o}$ are then least-squares fitted to a parabola

$$\chi^2 = c_0 + c_1 f + c_2 f^2 \quad \text{yielding a minumum at } f_{\min} = -\frac{c_1}{2c_2} \qquad (20)$$

The process is then repeated on a finer grid with $\mathbf{f_0 = f_{min}}$ and **Δf =Δf /3**. The final estimate of the frequency is the $f_{\min}$ value from this second application. Finally **a** and **b** (hence **A** and **ϕ**) are found for this final value of $\mathbf{f_{min}}$. This is generally accurate to 1-3 Hz even for slightly noisy data.

Single cycle integration

The final least-squares parameters for **A**, **ω** and **ϕ** are then used to determine the start and end of a complete cycle. Since ***U*(*t*)** is used to trigger data collection **ϕ** will be a +ve number so we must start at ***U*(*t*) = 0** in the 2nd cycle.

$$t_{start} = \frac{2\pi - \phi}{\omega} \quad \text{and} \quad t_{end} = t_{start} + T \quad \text{where} \quad T = \frac{1}{f} \tag{21}$$

The single cycle can be converted to array indices simply from

$$n_{start} = \frac{t_{start}}{\Delta t} \quad \text{and} \quad n_{end} = \frac{t_{end}}{\Delta t} \quad \text{where } \Delta t = \text{ sampling period} \tag{22}$$

This single cycle is 'cut out' from $U(t)$ and $V_c(t)$ and the integration of Eqn 10 (via Eqn 7) performed.

Statistical Analysis

The power analysis section can be used to repeat the data collection + power determination for a number of samples. This allows determination of mean values for **A**, **f** and **P** with the associated uncertainties in their means:

$$\bar{f} = \frac{1}{N_S}\sum_{k=1}^{N_S} f_k \quad \text{where } N_S \text{ is the number of samples} \tag{23}$$

$$\sigma_{\bar{f}} = \sqrt{\frac{1}{N_S(N_S - 1)}\sum_{k=1}^{N_S}\left(f_k - \bar{f}\right)^2} \tag{24}$$

The equivalent quantities are also calculated for **A** and **P**.

File outputs – two channel oscilloscope

Datalog format

The data from the two channel oscilloscope section is stored in a proprietary LabVIEW format for retrieval at a later date. This also stores all running and display parameters. Such a file is also very useful as a way to configure the instrument for particular experimental conditions. The Power analysis settings and the current values of f, A and P (and errors) are also stored – but not the extracted waveform (since this can be easily extracted again by implementing a single analysis).

Export format

The voltage waveforms are saved in a tab-delimited text file suitable for reading into Excel. The three columns are:

Time/μs	**ChanA/V**	**ChanB/V**

These are simply the raw data returned by the Picoscope unit. No other information is exported.

File outputs – Plasma Power

Export format

The time, voltage waveform U(t) and charge q(t) are saved in a tab-delimited text file suitable for reading into Excel. Time is in microseconds and charge in microcoulombs. The three columns are:

Time/μs	**U/V**	**q/μC**

References

[1] "Nonthermal Plasma Technology" T Yamamoto and M Okubo vol 4 in "Handbook of Environmental Engineering", *ed* L K Wang, N C Pereira, Y-T Hung , Humana Press, 2007

[2] R. Feng and G.S.P. Castle, "Automated System for Power Measurement in the Silent Discharge," *IEEE. Trans. Indust. Appl.,* vol. 34, pp. 563–569,. 1998.

[3] H. E. Wagner, R. Brandenburg, K. V. Kozlov, A. Sonnenfeld, P. Michel, J. F. Behnke, "The barrier discharge: basic properties and applications to surface treatment", Vacuum, vol 71, 417-436, 2003.

[4] T. C. Manley, "The electric characteristics of the ozonator discharge," *Trans. Electrochem. Soc.,* vol. 84, 83–94,. 1943.

[5] K.P. Francke, R. Rudolph, H. Miessner, "Design and operating characteristics of a simple and reliable DBD reactor for use with atmospheric air", *Plasma chemistry and plasma processing,* 23, pp 47-57, 2003.

[6] J. Kuffel, T. R. McComb, and R. Malewski, "Comparative evaluation of computer methods for calculating the best-fit sinusoid to the digital record of a high-purity sine wave," IEEE *Trans. Instrum. Meas.,* vol. IM-36, pp.

418–422, June 1987.

[7] IEEE, “IEEE Standard for digitizing waveform recorders – *IEEE Std 1057-1994*”, Institute of Eletrical and Electronics Engineers, Inc., SH94245, December 1994.

[8] Handel, P., Properties of the IEEE-STD-1057 four-parameter sine wave fit algorithm. *IEEE Transactions on Instrumentation and Measurement*. v49. 1189-1193. 2000.

Appendix B: Calculation Methods for Electrical Parameters

Calculation of the gas voltage, U_g

The gas voltage, U_g can be calculated from equations A1 and A2:

$$U_g = U_{app} - U_d \qquad \text{(A1)}$$

$$U_c C_c = U_d C_d \qquad \text{(A2)}$$

Where U_{app} is the applied voltage, U_d is the voltage across the dielectric material, U_c is the voltage across a capacitor, C_c is the capacitance of the capacitor used and C_d is the capacitance of the dielectric material which is shown on Figure A1.

Calculation of the breakdown voltage, U_B

The breakdown voltage, U_B can be calculated from equations (A3 and A4):

$$U_B = U_{\min} \frac{1}{1 + C_g / C_d} \qquad \text{(A3)}$$

$$\frac{1}{C_t} = \frac{1}{C_g} + \frac{1}{C_d} \qquad \text{(A4)}$$

Where U_{min} is the minimum external voltage, which is depicted in Figure A1, C_g is the capacitance of the gas gap, C_d is the capacitance of the dielectric material and C_t is the total capacitance.

Measurement of the charge, Q and capacitance, C

The charge (Q_{pk-pk}), charge discharged (Q_d) and charge transferred per half cycle (Q_{trans}) are taken from a measurement of the Lissajous figure as shown in Figure A1.

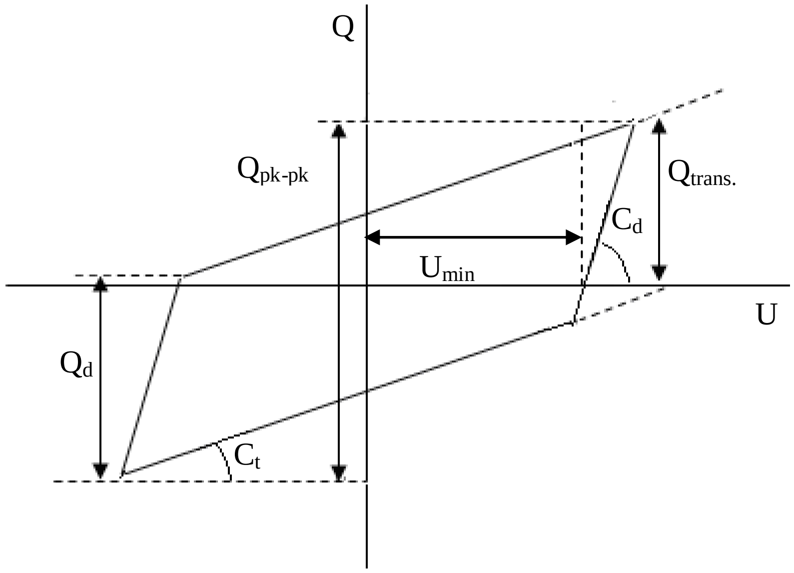

Figure A1: Schematic diagram showing the measurement of electrical parameters on a Lissajous figure.

Appendix C:

Publications

The following papers have been submitted and are awaiting publication:

- Helen. J. Gallon, Hyun-Ha Kim, Xin Tu, J. Christopher Whitehead, Microscope-ICCD Imaging of an Atmospheric Pressure CH_4 and CO_2 Dielectric Barrier Discharge, IEEE Transactions on Plasma Science, 2011.
- Xin Tu, Helen J. Gallon, J. Christopher Whitehead, Transition Behavior of Packed bed Dielectric Barrier Discharge in Argon, IEEE Transactions on Plasma Science, 2011.
- Xin Tu, Helen J. Gallon, J. Christopher Whitehead, Dynamic Behavior of an Atmospheric Argon Gliding Arc Plasma, IEEE Transactions on Plasma Science, 2011.
- Xin Tu, Helen J. Gallon, Martyn V. Twigg, Peter A. Gorry and J. Christopher Whitehead, Dry Reforming of Methane over a Ni/Al_2O_3 Catalyst in a Coaxial Dielectric Barrier Discharge Reactor, J. Phys. D: Appl. Phys, 2011.

Presentations have been made at the following conferences and meetings:

- Hakone XII. 12th International Symposium on High Pressure, Low Temperature Plasma Chemistry. Trenčianske Teplice, Slovakia, September 2010.
- Meetings of the Supergen XIV Consortium for Delivery of Sustainable Hydrogen. Leeds, April 2009, Glasgow, September 2009 and Cardiff, May 2010.
- National Institute for Advanced Industrial Science and Technology (AIST), Tsukuba, Japan, June 2009.

Posters have been presented at the following conferences:

- Technological Plasma Workshops. Belfast, December 2007, Milton Keynes, December 2008, Glasgow 2009 and Bristol 2011.
- Japan Society for Promotion of Science Summer Program. Sokendai, Japan, June 2009.

- Hakone XI. 11th International Symposium on High Pressure, Low Temperature Plasma Chemistry. Oléron Island, September 2008.
- Engineering and Physical Sciences Conference. Manchester, September 2008.